université PARIS-SACLAY

Planification et analyse d'expériences numériques pour la modélisation des tassements induits par le creusement mécanisé à partir de données de monitoring de surface

Design and analysis of computer experiments for numerical modeling of mechanized tunneling-induced settlements using surface monitoring data

Thèse de doctorat de l'Université Paris-Saclay

École doctorale n° 580, Sciences et Technologies de l'Information et de la Communication (STIC)
Spécialité de doctorat : Informatique mathématique
Graduate School : Sciences de l'ingénierie et des systèmes.
Référent : CentraleSupélec

Thèse préparée en partenariat avec le *Laboratoire des Signaux et Systèmes* (Université Paris-Saclay, CNRS, CentraleSupélec), le *Laboratoire de Mécanique de Paris-Saclay* (Université Paris-Saclay, CNRS, CentraleSupélec) et *Socotec Monitoring France*, sous la direction d'**Emmanuel VAZQUEZ**, Professeur des universités, et le co-encadrement de **Pierre JEHEL**, Maître de conférences, et **Maxime TATIN**, Docteur.

Thèse soutenue à CentraleSupélec, le 18 juin 2026, par

Boris KRATZ

Composition du jury

Membres du jury avec voix délibérative

Jean-Michel PEREIRA Professeur des universités, École des Ponts	Rapporteur et examinateur
Bruno SUDRET Professeur des universités, ETH Zurich	Rapporteur et examinateur
Olivier DECK Professeur des universités, Université de Lorraine, Mines de Nancy	Président
Daniel DIAS Professeur des universités, Université Grenoble Alpes	Examinateur
Nour EL SOUWAISSI Docteure, Eiffage Génie Civil	Examinatrice

THESE DE DOCTORAT

NNT : 2026UPAST071

université PARIS-SACLAY

ÉCOLE DOCTORALE
Sciences et technologies de l'information et de la communication (STIC)

Titre: Planification et analyse d'expériences numériques pour la modélisation des tassements induits par le creusement mécanisé à partir de données de monitoring de surface

Mots clés: Tunnelier, Tassement, Monitoring, Processus Gaussiens, Inversion d'ensemble

Résumé: Même si les tunneliers à front pressurisé, tels que les tunneliers à pression de terre (EPB), sont conçus pour limiter les mouvements de terrain induits par le creusement, des déformations peuvent néanmoins se produire. Celles-ci se propagent depuis le voisinage du tunnel vers la surface sous forme de déplacements verticaux du sol, appelés tassements, susceptibles d'affecter les structures.

En phase travaux, la maîtrise de ces tassements repose principalement sur le choix des conditions de pilotage du tunnelier (pression au front, pression d'injection, vitesse d'avancement, etc.). Ces paramètres constituent des leviers directs pour contrôler la réponse du sol, mais leur effet reste difficile à anticiper en raison des incertitudes sur les propriétés géotechniques et du caractère non linéaire et tridimensionnel du processus de creusement. La prise de décision nécessite ainsi un cadre prédictif capable de relier les paramètres de pilotage aux tassements attendus, tout en intégrant les incertitudes associées.

En pratique, ce choix est guidé par des modèles empiriques, analytiques ou numériques bidimensionnels, simples à mettre en œuvre mais fondés sur des hypothèses simplificatrices, en particulier l'hypothèse de déformation plane. Si ces approches permettent une estimation rapide des tassements, elles ne permettent pas de reproduire de manière réaliste la nature tridimensionnelle du processus de creusement, ni d'intégrer correctement les paramètres de pilotage du tunnelier.

À l'inverse, les modèles numériques tridimensionnels offrent une représentation plus fidèle des mécanismes physiques en jeu et permettent d'intégrer explicitement les conditions de pilotage. Cependant, leur coût de calcul élevé limite, d'une part, la réalisation d'analyses rapides en contexte opérationnel et, d'autre part, l'analyse des incertitudes affectant les paramètres d'entrée, en particulier les propriétés géologiques, dont la prise en compte nécessite généralement un grand nombre de simulations.

Dans ce contexte, cette thèse propose une méthodologie fondée sur le cadre de la *Planification et analyse d'expériences numériques* (DACE), qui consiste à considérer le modèle numérique comme un simulateur et à analyser son comportement à l'aide d'outils statistiques.

Un simulateur paramétrique tridimensionnel reposant sur la méthode des éléments finis est d'abord développé. Une stratégie de réduction précision-coût (*ACMR*) est proposée pour quantifier les artefacts numériques et sélectionner des configurations de calcul réduites à coût maîtrisé. Sur cette base, des métamodèles par processus gaussiens permettent de réaliser une analyse de sensibilité globale et d'identifier les paramètres d'entrée les plus influents.

Une chaîne de traitement et de reconstruction des champs de tassement est proposée afin de transformer des mesures ponctuelles bruitées en quantités d'intérêt dynamiques comparables aux sorties du simulateur.

Le calage du modèle est formulé comme un problème d'inversion bayésienne d'ensemble. Une adaptation de la *Bayesian subset simulation* (BSS), combinant métamodélisation par processus gaussiens et Monte Carlo séquentiel, est développée pour explorer efficacement l'ensemble admissible.

Appliqué au cas étudié, ce cadre réduit le coût des simulations par un facteur d'environ 5 à 10, met en évidence les paramètres dominants, et identifie des configurations compatibles avec les quantités d'intérêt observées.

université PARIS-SACLAY

ÉCOLE DOCTORALE
Sciences et technologies de l'information et de la communication (STIC)

Title: Design and analysis of computer experiments for numerical modeling of mechanized tunneling-induced settlements using surface monitoring data

Keywords: TBM, Settlement, Monitoring, Gaussian processes, Set inversion

Abstract: Even though pressurized-face tunnel boring machines (TBM), such as earth pressure balance (EPB) TBMs, are designed to limit ground movements induced by excavation, deformations may still occur. These deformations propagate from the vicinity of the tunnel toward the surface in the form of vertical ground displacements, referred to as settlements, which may affect surface structures.

During construction, the control of these settlements mainly relies on the choice of TBM operational parameters (face pressure, grouting pressure, advance rate, etc.). These parameters constitute direct levers to control the soil response, but their effects remain difficult to anticipate due to uncertainties in geotechnical properties and the nonlinear and three-dimensional nature of the excavation process. Decision-making therefore requires a predictive framework capable of relating operational parameters to the resulting settlements, while accounting for the associated uncertainties.

In practice, this choice is guided by empirical, analytical, or two-dimensional numerical models, which are simple to implement but rely on simplifying assumptions, in particular the plane strain assumption. While these approaches enable rapid estimation of settlements, they do not allow for a realistic representation of the three-dimensional nature of the excavation process, nor for a proper integration of TBM operational parameters.

In contrast, three-dimensional numerical models provide a more faithful representation of the underlying physical mechanisms and allow for an explicit incorporation of operational conditions. However, their high computational cost limits rapid analyses in operational contexts and the analysis of uncertainties affecting input parameters, particularly geological properties, whose consideration typically requires a large number of simulations.

In this context, this thesis proposes a methodology based on the *Design and Analysis of Computer Experiments* (DACE) framework, which consists of treating the numerical model as a simulator and analyzing its behavior using statistical tools.

A parametric three-dimensional finite element simulator is first developed. An *Accuracy-Cost Model Reduction* (ACMR) strategy is proposed to quantify numerical artefacts and select reduced computational settings with controlled cost. Gaussian process metamodels are then used to perform global sensitivity analysis and to identify the most influential input variables for model calibration.

A processing and reconstruction pipeline for settlement fields is proposed in order to transform noisy point measurements into dynamic quantities of interest that are consistent and comparable between observations and simulations.

Model calibration is formulated as a Bayesian set inversion problem. An adaptation of *Bayesian subset simulation* (BSS), combining Gaussian process metamodeling and sequential Monte Carlo techniques, is developed to efficiently explore the admissible set.

Applied to the case study, the framework reduces simulation cost by a factor of about 5 to 10, identifies the dominant parameters, and yields input configurations consistent with the observed quantities of interest.

Remerciements

C'est la fin d'une longue aventure qui, sans le soutien de mon entourage, aurait été bien plus difficile (voire impossible). Les mots qui suivent leur sont dédiés.

Tout d'abord, c'est à mon encadrement que vont mes premières pensées. Emmanuel, Maxime et Pierre, vous m'avez accordé votre confiance, fait preuve de patience, et m'avez énormément appris et soutenu au cours de ces quatre années. J'ai eu beaucoup de plaisir à travailler avec vous. Tout simplement, merci pour tout.

Ensuite, je suis très honoré qu'Olivier Deck, Daniel Dias, Nour El Souwaissi, Jean-Michel Pereira et Bruno Sudret aient accepté de lire, d'évaluer et de discuter mon travail de recherche. Je leur en suis sincèrement reconnaissant.

Mes remerciements vont également aux deux laboratoires (le Laboratoire des Signaux et Systèmes (L2S) et le Laboratoire de Mécanique de Paris-Saclay (LMPS)) ainsi qu'à leurs membres, qui m'ont accueilli et aidé lorsque j'en avais besoin. Il faut le dire : j'ai eu la chance d'y trouver un cadre de travail et des moyens sans lesquels il m'aurait été difficile de mener à bien mes travaux.

Je tiens aussi à remercier Socotec Monitoring pour la confiance accordée à mon travail, son soutien et les opportunités qui m'ont été offertes. Dans cette même lignée, je souhaite aussi remercier l'ANRT pour son aide financière.

Pour finir, que serais-je sans mes proches, qui m'ont accompagné tout au long de ce parcours ? Ils ont tous été là, par leur soutien, leur présence, leur compréhension lors de mes absences et les moments de qualité qui m'ont permis de respirer. Je pense à mes amis, à ma famille et à mes collègues de Socotec Monitoring (ils se reconnaîtront).

Parmi eux, j'ai une pensée toute particulière pour mes parents, qui ont su être là du début à la fin, dans les moments de doute comme dans ceux de réussite.

Enfin, je ne saurais terminer sans évoquer celle qui partage ma vie depuis (presque) le début de cette aventure. Sa présence et son soutien au quotidien m'ont énormément apporté, et je suis certain que, sans elle, je n'en serais pas là aujourd'hui. Je parle de toi, Justine.

À Justine.

Contents

1 Introduction **11**

1.1 Context of urban tunneling in Paris . . . 11

1.1.1 Mechanized tunneling using TBMs . . . 11

1.1.2 EPB TBM operation principles . . . 12

1.1.3 Sources of underground deformation . . . 13

1.1.4 Transmission of underground deformations to the surface . . . 14

1.1.5 Monitoring strategy . . . 15

1.2 Problem statement . . . 16

1.3 DACE methodology for TBM settlement modeling . . . 17

1.4 Proposed methodology . . . 18

1.5 Organization of the manuscript . . . 19

1.6 Summary of contributions . . . 21

2 Review of modeling approaches for TBM excavation in soils **23**

2.1 Mechanical modeling of soils . . . 23

2.1.1 Fundamental equations in geomechanics . . . 24

2.1.2 Pore pressure modeling . . . 24

2.1.3 In-situ stress initialization . . . 26

2.1.4 Soil rheology . . . 26

2.2 Review of boundary conditions for TBM simulation . . . 27

2.2.1 Numerical method . . . 27

2.2.2 Domain geometry . . . 28

2.2.3 Sequential boundary conditions for 3D TBM simulation . . . 30

2.3 Chapter conclusions . . . 35

3 A three-dimensional finite element model for EPB TBM excavation **37**

3.1 FE modeling assumptions . . . 37

3.1.1 Geological domain and boundaries . . . 37

3.1.2 Simulation procedure . . . 38

3.1.3 Material behavior . . . 39

3.2 Results from the 3D FE model . . . 42

3.2.1 Model setup . . . 42

3.2.2 Analysis of displacement and stress fields . . . 42

3.3 Computer code implementation . . . 48

3.3.1 Input taxonomy . . . 48

3.3.2 Outputs of interest . . . 50

3.3.3 Settlement QoIs . . . 51

3.4 Chapter conclusions . . . 58

4 Parameter influence analysis of the 3D TBM excavation model 61
4.1 Accuracy-cost model reduction . . . 61
4.1.1 ACMR framework . . . 63
4.1.2 ACMR results . . . 65
4.2 Global sensitivity analysis using Gaussian process metamodels . . . 71
4.2.1 Uncertainty-aware GSA approach . . . 72
4.2.2 GSA results using GP metamodels . . . 77
4.3 Discussion and conclusions . . . 82

5 Building Settlement Maps 91
5.1 Monitoring framework and settlement representations . . . 92
5.1.1 Surface settlement monitoring in urban tunneling . . . 92
5.1.2 Monitoring system and data limitations . . . 93
5.1.3 Coordinate system and settlement representations . . . 95
5.2 Longitudinal parametric model at the prism level . . . 98
5.2.1 Review of longitudinal parametric models . . . 98
5.2.2 Illustration of longitudinal parametric models . . . 99
5.3 Robust parameter estimation . . . 99
5.3.1 Estimation methodology . . . 101
5.3.2 Longitudinal model selection and robust estimation results . . . 102
5.4 Reconstruction of 2D total settlement maps . . . 110
5.4.1 Monitoring window definition . . . 110
5.4.2 GP reconstruction of total settlement maps . . . 110
5.4.3 Reconstructed total settlement maps . . . 111
5.5 Reconstruction of dynamic transverse settlement profiles . . . 113
5.5.1 Dynamic transverse settlement reconstruction algorithm . . . 113
5.5.2 Reconstructed dynamic transverse profiles . . . 114
5.6 Conclusions and discussions . . . 117

6 Bayesian subset simulation for set inversion 119
6.1 From inverse problem to set inversion . . . 119
6.2 Subset simulation, BSS, and set inversion . . . 121
6.2.1 SuS framework . . . 121
6.2.2 GP metamodel . . . 124
6.3 BSS for set inversion . . . 124
6.3.1 Set inversion procedure . . . 124
6.3.2 Adaptive design . . . 125
6.3.3 Illustration . . . 127
6.4 Set inversion uncertainty quantification . . . 129
6.4.1 Expected volume of the inversion set . . . 130
6.4.2 GP-induced uncertainty . . . 131
6.4.3 SMC-induced uncertainty . . . 132
6.4.4 Diagnostic interpretation and workflow . . . 132
6.5 Numerical experiments . . . 133
6.6 Case studies . . . 140

6.6.1 Protocol . . . 140
6.6.2 Hartmann 4 . . . 140
6.6.3 FE simulator - tunnel excavation . . . 146
6.7 Chapter conclusions . . . 150

7 Conclusion and Perspectives **151**

Appendices **157**

A Surface settlement and volume loss: Peck's formulation **159**

B Influence of depth on settlement **163**

C K_0 estimation **165**

D On the limitations of the K_0 procedure for stress initialization **167**

E Stress initialization examples **169**

F Supplementary review of 3D FEM and FDM TBM excavation models **171**

G Shield-soil contact interface models **175**

H Selection of operating pressures for TBM excavation **177**
H.1 Face support pressure . . . 177
H.2 Grout injection pressure . . . 178

I Evolution of grout stiffness during hardening **179**

J Tables of case study parameters **181**

K 3D simulation results: surface settlement profiles **185**

L Numerical fidelity framework **189**

M Full Sobol Indices Distribution per QoI **191**

N Robust regression framework **197**
N.1 Ordinary least squares (OLS) . . . 197
N.2 M-estimators . . . 198

O RANSAC algorithm **201**

P BSS for set inversion: additional details **203**
P.1 Definitions and notation . . . 203
P.2 Multi-output framework . . . 205
P.3 Theoretical proof . . . 206
P.4 Relaxation and stopping strategies . . . 207
P.5 Sampling criterion for GP metamodel . . . 210

Bibliography **213**

Chapter 1

Introduction

1.1 Context of urban tunneling in Paris

In densely populated metropolitan areas such as Paris, the expansion of underground transport networks is essential. The Grand Paris Express project, launched in 2010, includes about 200 km of new metro lines, with four entirely new lines and extensions of existing ones. Nearly 90 % of the network is built underground, with more than 20 Tunnel Boring Machines (TBM) operating and around 60 new stations under construction.

1.1.1 Mechanized tunneling using TBMs

Mechanized tunneling differs from conventional methods such as drilling and blasting by continuously removing soil or rock with mechanical cutters. According to the classification of the Association Française des Travaux en Souterrain (AFTES, AFTES (2000)), mechanized TBMs are grouped according to the type of support they provide during excavation: (i) without support, (ii) with lateral support, and (iii) with both frontal and lateral support.

Within the third category, pressurized-face tunnel boring machines (TBMs) operate in a closed and controlled environment. By regulating the face pressure to balance in-situ stresses, they limit ground deformations and reduce the risk of collapse. Two main technologies are used: earth pressure balance (EPB) shields and slurry shields. EPB machines use the excavated soil itself to transmit pressure to the face, while slurry shields use a bentonite suspension to maintain hydrostatic pressure. Hybrid systems combining both principles are also available. EPB-TBM are particularly suited for the heterogeneous soils and shallow covers typical of urban conditions such as those encountered in Paris. They also avoid the use of bentonite, which would otherwise require complex handling systems and additional cost. From now on, we will focus on EPB-TBM technology.

1.1.2 EPB TBM operation principles

The excavation process of an EPB TBM follows a cyclic sequence, as illustrated in Figure 1.1. Excavation is performed at the tunnel face by the rotating cutterhead (1), which cuts the soil and transfers the excavated material into the pressurized excavation chamber (2) located behind the cutterhead.

Pressure is continuously maintained within the chamber to prevent collapse of the soil at the face, thereby ensuring face stability. This pressure is controlled through the combined regulation of the screw conveyor (3) extraction rate, the TBM advance rate, and the rotational speed of the cutterhead. Laterally, the excavation is supported by a conical steel shield (7), which provides confinement of the surrounding soil during advance.

Inside the shield, prefabricated concrete lining segments (6) are assembled to form a complete lining ring. TBM advancement is achieved by hydraulic thrust jacks (4) reacting against the previously installed lining. As the machine advances, pressurized grout (5) is injected into the annular gap behind the lining to limit volume loss and provide long-term support.

This repeated sequence of excavation, lining installation, and grouting enables continuous
TBM advance. Despite the pressure-controlled excavation process, ground deformations are inevitably induced and are discussed in the following section.

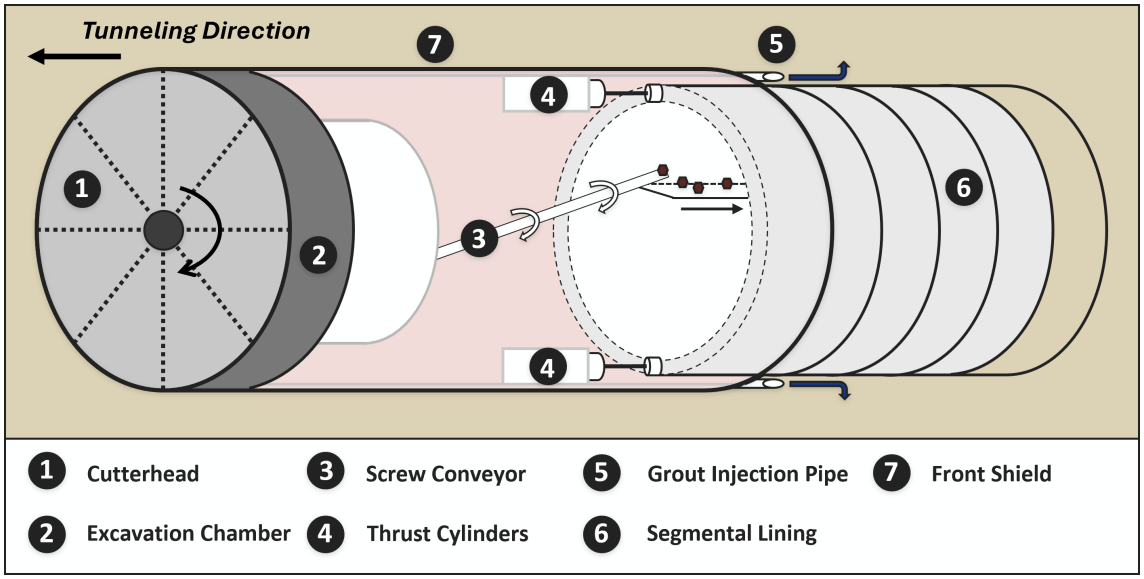

Figure 1.1: Tunnel boring machine - earth pressure balance illustration. The cutterhead (1) excavates soil into the pressurized excavation chamber (2), maintaining face stability. Excavated material is removed via a screw conveyor (3). Hydraulic thrust cylinders (4) advance the front shield (7) while grout (5) is injected into the annular gap behind the lining segments (6) to ensure soil support and surrounding soil stability. This process, excavation, spoil removal, grouting, lining installation, repeats continuously as the TBM advances.

1.1.3 Sources of underground deformation

Even though mechanized tunneling generally induces smaller soil movements than conventional methods (AFTES, 2000), significant deformations can still occur in the surrounding soil (Lee et al., 1992; Loganathan and Poulos, 1998; Lambrughi et al., 2012; Vanoudheusden, 2006; Kasper and Meschke, 2006a,b).

A classical framework introduced by Rowe and Kack (1983) and later formalized by Lee et al. (1992) identifies the main mechanisms responsible for these deformations through the so-called gap parameter (Figure 1.2). It includes three main contributions: the geometric gap between the excavation boundary and the lining, usually filled with grout; the soil loss caused by face deformation when the support pressure is insufficient; and the over-excavation effects associated with shield taper, cutterhead oversizing, and steering corrections.

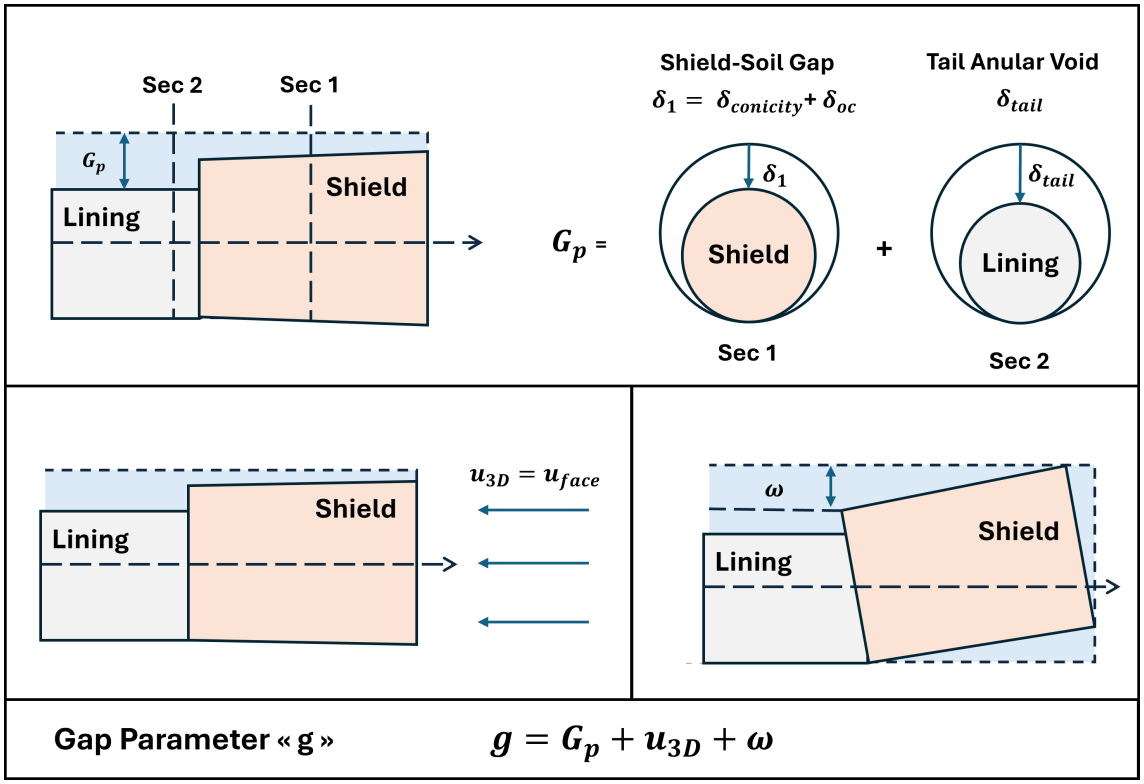

Figure 1.2: Definition of the gap parameter g, which combines (1) the geometric gap between the excavation boundary and the lining (G_p), (2) the soil loss due to face deformation and insufficient support pressure (u_{3D}), and (3) the over-excavation effects related to shield taper, cutterhead oversizing, and alignment corrections (ω) (adapted from Lee et al. (1992)).

In addition to these mechanisms, several operational and geological factors can further amplify soil movements. Temporary stoppages of the TBM during maintenance or shift changes may reduce face pressure and increase soil loss (Lambrughi et al., 2012). Geological heterogeneity, when the tunnel alignment crosses layers with contrasting stiffness or strength (mixed-face conditions) (Clough and Leca, 1993), as well as unexpected features such as cavities or aquifers, can also lead to localized instability.

In urban environments, tunneling operations are further challenged by loose soils, excavation below the groundwater table, shallow overburden, existing surface or underground structures, and the presence of foreign objects or abandoned utilities (Kovári, 2002).

1.1.4 Transmission of underground deformations to the surface

Urban tunnels are generally constructed at shallow depths, typically characterized by a cover-to-diameter ratio (C/D) below 5. Under such conditions, the deformation induced by tunneling can propagate through the soil and reach the surface, leading to measurable vertical displacements (see Appendix B).

The most common surface manifestation of these deformations is the vertical displacement of the ground surface, referred to as surface settlement (Figure 1.3). Engineers pay particular attention to differential settlements, as they are responsible for potential structural damage (Deck and Singh, 2012). Surface settlements are usually described using transverse profiles, measured perpendicular to the tunnel axis, and longitudinal profiles, which represent the evolution of settlement as the TBM advances. In addition, total and differential settlement values are used to evaluate the global deformation of the ground surface.

In extreme cases, excessive soil loss or insufficient face pressure can cause localized collapses known as sinkholes (Leca and Dormieux, 1990; Mollon et al., 2009, 2011). Such events highlight the importance of monitoring soil behavior during excavation, as discussed in the next section.

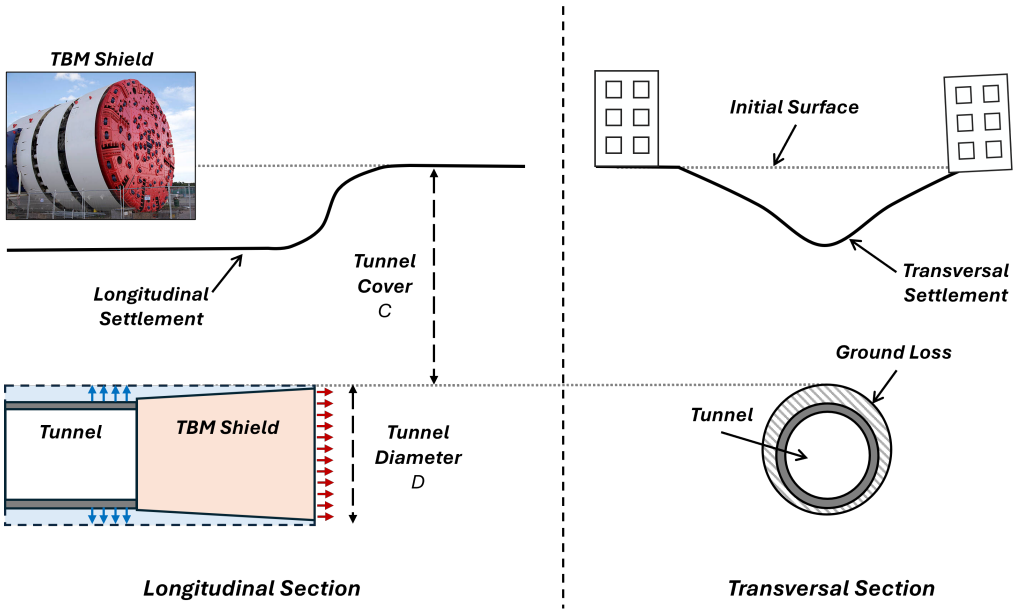

Figure 1.3: Surface settlements induced by TBM tunneling.

1.1.5 Monitoring strategy

Because of the surface deformations induced by TBM excavation and the associated risks, continuous monitoring of soil and structural movements is essential. To observe and quantify these deformations during tunneling, a dense monitoring system is implemented. Different sensors are deployed to track both soil movements and structural responses, with instruments installed inside the tunnel, in the surrounding soil, and at the surface to provide early warning of potential soil instabilities. Figure 1.4 illustrates a typical monitoring layout on a transverse section of the tunnel.

Two main approaches are generally distinguished for ground deformation monitoring. Geotechnical methods rely on borehole instruments such as inclinometers, which measure lateral displacement with depth, and extensometers, which record deformation between fixed anchors at different depths. Surface methods, on the other hand, often use total stations tracking survey prisms to measure surface displacements over time. Other techniques, including manual leveling and satellite-based interferometry, are also employed. Together, these approaches provide complementary data on both horizontal and vertical soil movements.

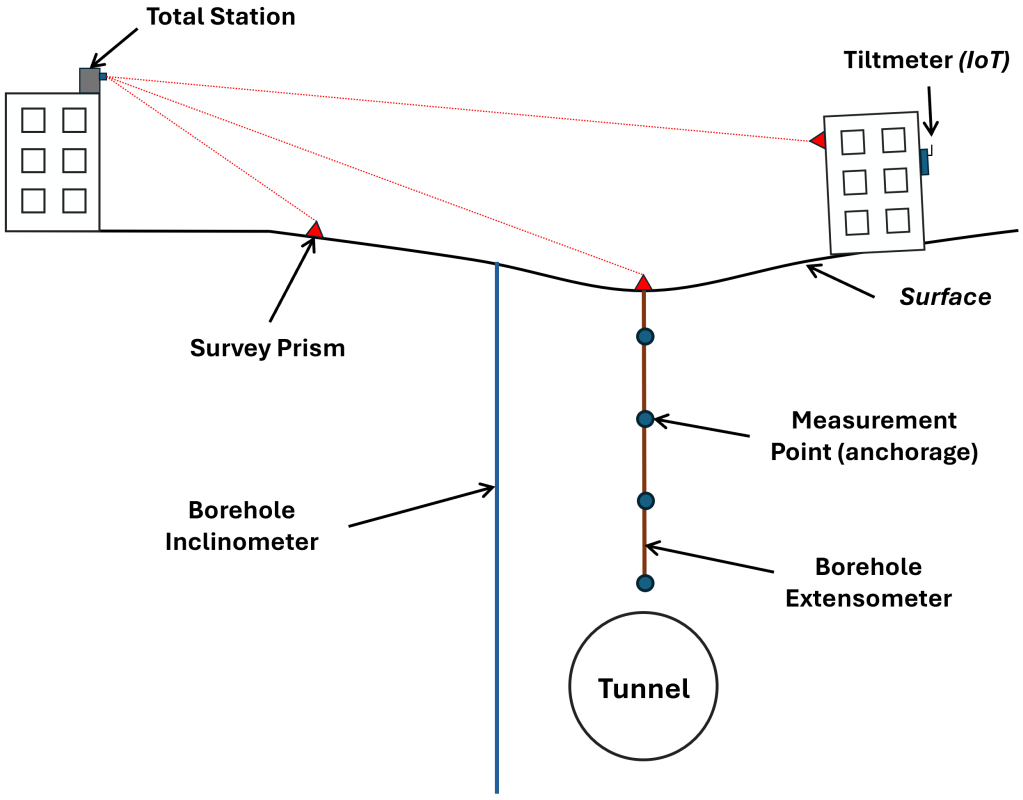

Figure 1.4: Typical monitoring instruments used during tunnel construction.

Regardless of the monitoring strategy, the gathered data consists of discrete points sensitive to urban activity, leading to noisy and sparse observations. In this study, we focus on surface settlement data obtained from vertical displacement measurements of

survey prisms, as urban tunneling projects are accompanied by dense surface monitoring networks designed to track soil and building deformations.

1.2 Problem statement

Even when using EPB technology, tunneling induces ground deformations that may affect buildings and infrastructure in dense urban environments.

At the design stage, tunnel alignment and design parameters, including the choice of geological layers to be excavated, are selected to balance ground displacements, local constraints, and project cost. During construction, settlement control relies on adjusting TBM operational parameters, such as face pressure, advance rate, and grouting injection, guided by real-time monitoring of surface settlements (Vanoudheusden, 2006).

In practice, these adjustments are commonly based on empirical (Peck, 1969; Celestino et al., 2000; Jacobsz et al., 2004; Vorster et al., 2005; Wang et al., 2022) or analytical models (Sagaseta, 1987; Verruijt and Booker, 1996; Loganathan and Poulos, 1998; Bobet, 2001; Park, 2004; Mair, 2008; Pinto and Whittle, 2014), as well as two-dimensional (2D) numerical simulations (Berthoz et al., 2020). However, these approaches are often constrained by simplifying assumptions such as plane strain conditions or soil homogeneity. Consequently, they offer limited capability to explicitly incorporate TBM operational parameters or to capture the inherently three-dimensional (3D) nature of the tunneling process. While 2D numerical models can better accommodate complex soil stratigraphy, they remain restricted by the same plane strain limitations (Janin et al., 2015).

As a recent alternative, data-driven approaches, including machine learning and deep learning methods, have been applied to settlement prediction (Kim et al., 2001; Zhou et al., 2017; Chen et al., 2019; Richa et al., 2024; Shang et al., 2024). Although such models can achieve good predictive performance on site-specific datasets, their transferability remains limited, and their physical interpretability is often reduced.

To better represent the physical mechanisms involved in TBM excavation, 3D numerical models are adopted, as they explicitly account for excavation sequences, soil-structure interaction, and operational conditions. However, their use is limited by parametric and modeling uncertainties, as well as high computational cost, which restrict their application in control-oriented settings requiring repeated simulations.

To address these limitations, this work proposes a methodology that leverages monitoring data to calibrate numerical predictions of surface settlements during excavation. By comparing observations with model outputs, the approach aims to reduce the uncertainty on the most influential parameters, identify admissible configurations consistent with observations, and provide a basis for subsequent predictive analyses under plausible TBM operating scenarios.

These objectives are difficult to achieve directly because 3D numerical models are computationally expensive, the number of uncertain input parameters is large, and monitoring data collected under urban conditions are sparse and noisy. This motivates the use of a design and analysis of computer experiments methodology.

1.3 DACE methodology for TBM settlement modeling

In this manuscript, this methodology is referred to as DACE. It treats parametric numerical models as simulators and analyzes them through controlled simulator evaluations, combining tools for metamodeling, sensitivity analysis, and inversion. In the statistical literature, an early occurrence of the exact phrase appears in the report of Currin et al. (1988), while the methodology is commonly associated with the foundational 1989 papers of Sacks and co-authors (Sacks et al., 1989a,b). The acronym DACE appears explicitly in later work (Park, 1991; Jones et al., 1998).

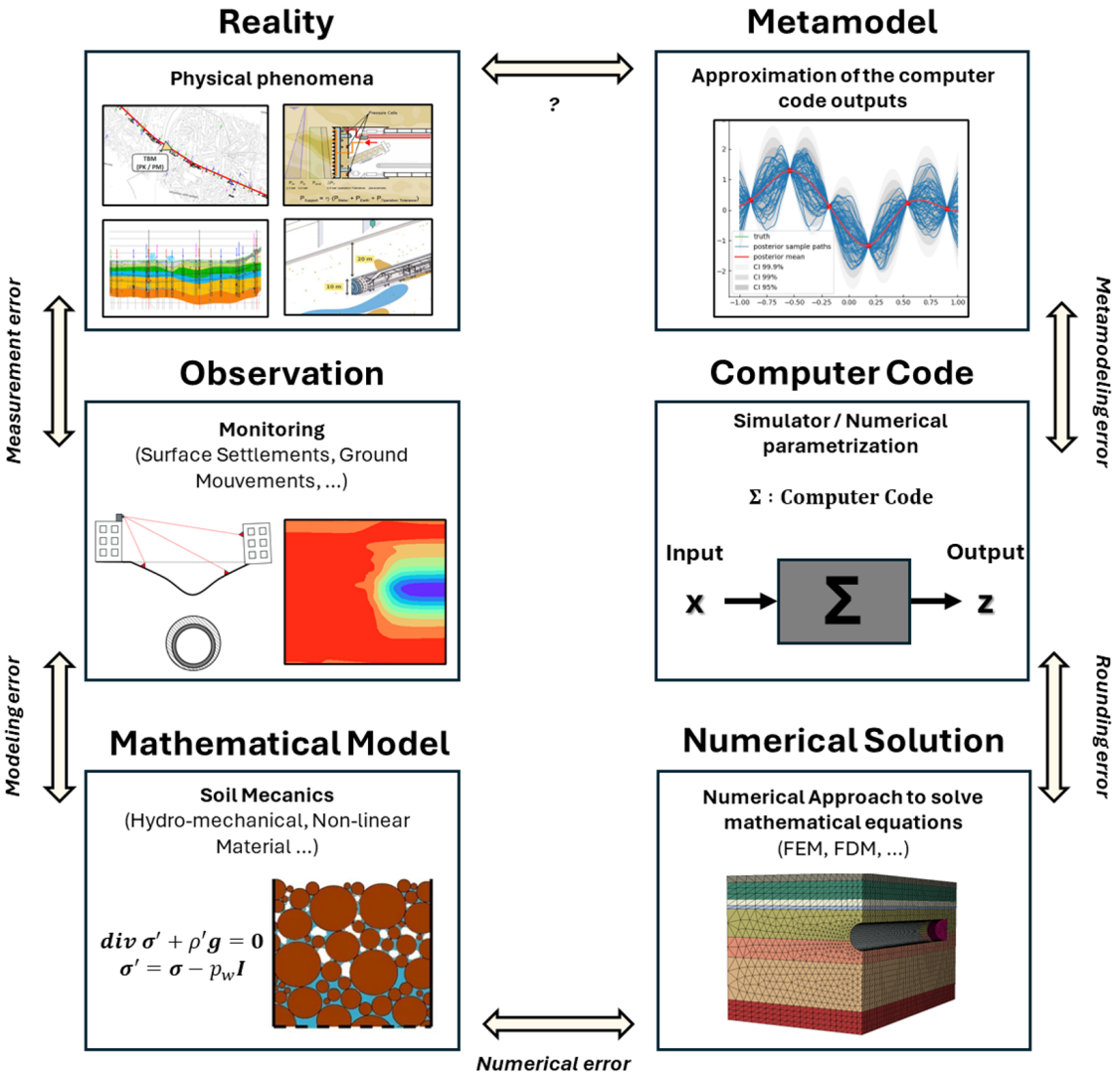

Figure 1.5: General framework of our DACE methodology applied to TBM modeling. The figure illustrates the sequence from physical reality to mathematical modeling, numerical approximation, computer simulation, and metamodel construction. Distinct sources of uncertainty are highlighted, including measurement, modeling, numerical, and metamodeling errors. Adapted from Le Gratiet (2013).

As illustrated in Figure 1.5, our DACE methodology identifies the different levels involved in TBM settlement estimation: (i) physical phenomena governing the system, (ii) their mathematical representation, (iii) the numerical scheme used to solve the resulting equations, (iv) the computer simulator that produces outputs for given inputs, and (v) a statistical approximation of this simulator, built from a set of simulation runs, referred to as a metamodel.

This sequenced representation clarifies where uncertainties and errors arise at each stage, including measurement noise, modeling assumptions, discretization errors, and metamodel approximation errors.

1.4 Proposed methodology

The methodology developed in this manuscript for TBM-induced settlement modeling is summarized in Figure 1.6.

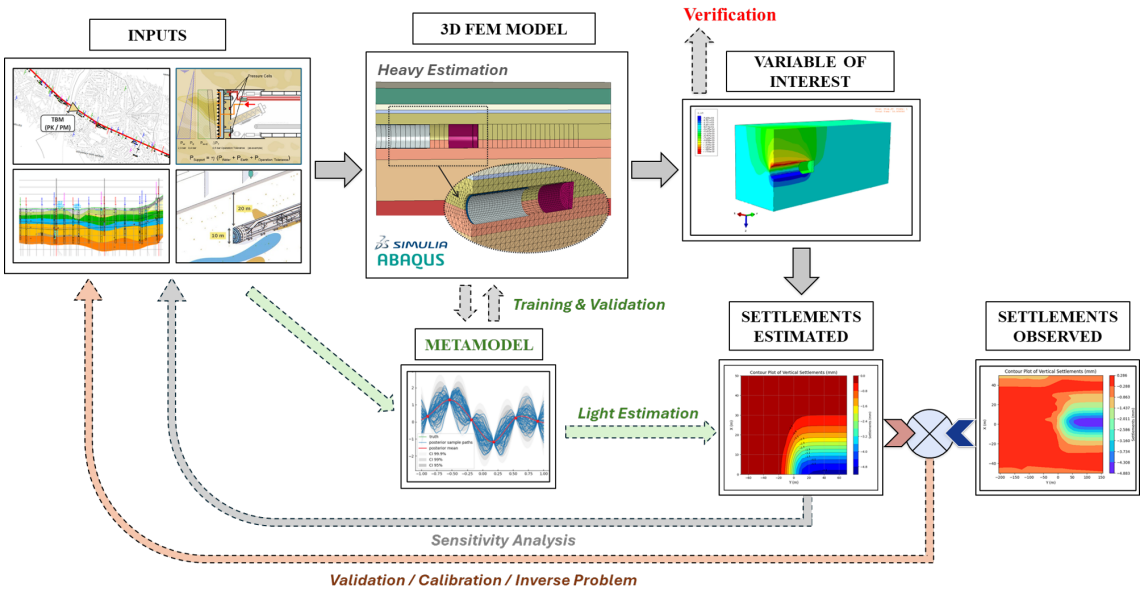

Figure 1.6: DACE-based workflow for TBM excavation modeling in urban areas, inspired by Blanchard et al. (2023). Inputs are defined according to the proposed taxonomy (environmental and control, physical, fixed, and modeling parameters). For a given input vector, the TBM simulator computes settlement-related quantities of interest. These quantities of interest are used to reconstruct settlement profiles and are compared with monitoring data from the corresponding tunnel section for validation, calibration, or back-analysis. The workflow also includes sensitivity analysis to reduce the input space, metamodel approximations to reduce the computational cost of numerical simulations, and inversion tools to identify input configurations consistent with observations.

The approach combines the following components:

Definition of a physics-based numerical model The mechanical behavior of the soil-TBM system is described by equilibrium equations, boundary conditions representing the excavation process, and constitutive laws for soil behavior. The resulting formulation is implemented as a parametric numerical simulator. Each simulator evaluation is regarded as a computer experiment.

Input-output taxonomy Input parameters are classified into operational, physical, numerical, and fixed project parameters. The outputs are defined as settlement-related quantities of interest, which may be scalar indicators or reduced representations of the surface settlement field.

Numerical verification and accuracy-cost analysis The numerical implementation is verified to ensure mechanical consistency of the results. Mesh density and domain size are selected to balance discretization accuracy and computational cost.

Construction of metamodels Because of the computational cost of the 3D simulator, a metamodel is introduced to approximate its response. Gaussian process metamodels are used to provide both predictive estimates and associated uncertainty (Williams and Rasmussen, 2006). Their construction relies on a set of simulator evaluations generated through a Design of Experiments (DoE).

Global sensitivity analysis Given the high dimensionality of the input space, global sensitivity analysis is used to identify the parameters that most influence settlement estimations and to reduce the dimensionality of the calibration problem.

Calibration against monitoring data The simulator is calibrated against field monitoring data to estimate uncertain parameters and improve prediction accuracy. This step supports back-analysis.
The guideline followed in this work is to propose a methodological framework for settlement prediction using numerical models.

1.5 Organization of the manuscript

The manuscript is organized as follows.

Chapter 2 Chapter 2 develops the concepts introduced above by
reviewing the main numerical approaches used to simulate TBM excavation and estimate tunneling-induced settlements. It examines how the mechanical equilibrium equations and boundary conditions defined in the physical model are implemented through numerical methods, focusing on 3D finite element modeling. The chapter discusses the initialization of in-situ stresses, the choice of constitutive soil models, and the sequential representation of excavation stages, including face pressure, shield, and grouting effects. It also reviews numerical strategies and boundary condition formulations commonly adopted for TBM simulations in urban soils, with a particular focus on EPB technology.

Part of this review was presented at the *World Tunnel Congress 2023* in Athens, under the title *"3D Numerical Simulation of TBM Excavation for Predicting Surface Settlements - State of the Art"* (Kratz et al., 2023a).

Chapter 3 Following the review of numerical approaches to simulate TBM EPB excavation, Chapter 3 presents a 3D numerical parametric model based on finite element methods. Some results are analyzed to verify the consistency of stress and displacement fields. The chapter first introduces the numerical parametric model and defines its variable inputs, including geological parameters, geometry, and numerical settings such as meshing parameters. Based on this parametrization, the simulator computes the displacement fields induced by the excavation process. Quantities of interest are then defined to characterize surface settlements and serve as the outputs of the simulator. This parametric finite element simulator then serves as the reference model for the simulations performed throughout this PhD work.

Chapter 4 Chapter 4 studies the influence of modeling parameters and physical inputs on the settlement-related quantities of interest computed by the TBM simulator. First, the numerical assumptions are verified by analyzing the effects of mesh density and domain size on the settlement quantities of interest. The objective is to achieve a balance between numerical accuracy and computational efficiency. An Accuracy-Cost Model Reduction approach is proposed and applied to select a reduced numerical configuration that maintains sufficient accuracy while reducing computational time. A global sensitivity analysis is performed to quantify the influence of input parameters on the settlement-related quantities of interest. Due to the high computational cost of the reduced numerical configuration, this analysis relies on Gaussian process metamodel combined with Sobol' indices. It enables the quantification of the contribution of design, operational, and physical parameters to the variability of the quantities of interest. The results identify the most influential parameters and define a reduced parameter space, which is used to focus subsequent calibration and back-analysis.
This work was published in *Computers and Geotechnics* under the title *"Parameter Influence Analysis in a 3D TBM Model via Sensitivity Analysis and GP Metamodels"* (Kratz et al., 2026).

Chapter 5 Chapter 5 focuses on the processing of surface monitoring data to enable consistent comparison with numerical simulations. In practice, monitoring data consist of point measurements (e.g., prisms automatically targeted by total stations), which are often spatially sparse, noisy, and not perfectly aligned with geotechnical cross-sections, making direct comparison with finite element simulation results difficult. To compare the simulated settlements with observations, a method is proposed to reconstruct continuous settlement fields from pointwise sensor data. First, each monitoring point is fitted using a robust longitudinal empirical model to mitigate the influence of local anomalies. Then, for each TBM position, a non-parametric Gaussian Process regression is applied to interpolate these values and reconstruct 2D settlement maps. By combining these maps, the evolution of transverse settlement profiles can be reconstructed and directly compared with the simulated ones. This approach enables direct comparison with 3D finite element simulations and supports the interpretation of settlement evolution as the TBM advances.

Chapter 6 Chapter 6 introduces a probabilistic framework for model calibration and inversion based on Bayesian set inversion using subset simulation. Traditional inverse approaches, formulated as point estimation problems such as Maximum a Posteriori (MAP) or Maximum Likelihood (ML), may lead to non-unique or unstable solutions in high-dimensional settings and in the presence of observational noise. In such cases, set inversion offers an alternative by characterizing all input configurations that produce outputs within a target region, which is particularly relevant in geotechnical applications where uncertainties often lead to non-uniqueness in plausible scenarios explaining observed behavior. The proposed Bayesian subset simulation method combines Gaussian process metamodeling with sequential Monte Carlo sampling. Particles are iteratively propagated through adaptive relaxation levels toward the target inversion set. Diagnostic quantities, such as the expected volume of the inversion set and its uncertainty, are introduced to assess Gaussian process and sequential Monte Carlo errors and to adaptively refine the sampling strategy.

This framework allows model calibration and back-analysis using a Gaussian process metamodel of the TBM-induced settlement simulator. It also enables the metamodel to be iteratively improved based on inversion-set diagnostics.

1.6 Summary of contributions

The main methodological and technical contributions of this work are summarized as follows.

(1) A parametric three-dimensional finite element simulator of TBM excavation is developed to represent the main mechanisms governing ground deformations. The simulator maps a high-dimensional set of input parameters, including geotechnical properties, TBM operational parameters, and geometrical variables, to settlement-related quantities of interest defined through a parametric representation of surface settlements.

(2) To enable its use in uncertainty quantification settings, an Accuracy-Cost Model Reduction (ACMR) method is introduced. This approach identifies reduced numerical configurations that achieve a controlled trade-off between discretization accuracy and computational cost, making large-scale simulation campaigns tractable.

(3) Based on the reduced simulator, Gaussian process metamodels are constructed for each quantity of interest and used to perform global sensitivity analysis using Sobol' indices, while accounting for metamodel uncertainty. This analysis identifies the most influential parameters and defines a reduced parameter space for subsequent calibration.

(4) A dedicated methodology is proposed to process monitoring data and reconstruct settlement-related quantities of interest consistent with simulator outputs. This enables a coherent comparison between observations and simulations and supports the calibration of the model.

(5) A Bayesian set inversion framework is introduced, combining Gaussian process metamodeling with sequential Monte Carlo methods. This approach characterizes the set of input configurations consistent with observations, rather than a single optimal solution, and provides diagnostic quantities to assess inversion reliability. The methodology is applied to the TBM settlement case study using metamodels defined on the reduced parameter space.

Publications

Journal Articles Kratz, B., Jehel, P., Tatin, M., & Vazquez, E. (2026). *Parameter influence analysis in a 3D TBM model via sensitivity analysis and GP metamodels. Computers and Geotechnics*, 189, 107650.

Conference Articles Kratz, B., Jehel, P., & Tatin, M. (2023). *3D numerical simulation of TBM excavation for predicting surface settlements - state of the art. Expanding Underground - Knowledge and Passion to Make a Positive Impact on the World*, 2757-2765.

Kratz, B., Jehel, P., Tatin, M., & Vazquez, E. (2023, May). *Kriging metamodels for 2D finite element simulations of the settlements induced by TBM excavation in urban areas.* In *Congrès Français du Génie Civil 2023.*

Communications

Kratz, B., Jehel, P., Tatin, M., & Vazquez, E. (2023, April). *Metamodeling of finite element simulations of TBM excavation.* Géoressources Seminar 2023, Université de Lorraine, Nancy, France.

Kratz, B., Jehel, P., & Tatin, M. (2023, May). *3D Numerical Simulation of TBM Excavation for Predicting Surface Settlements - State of the Art.* World Tunnel Congress 2023, ITA-AITES, Athens, Greece. (Poster)

Kratz, B., Jehel, P., Tatin, M., & Vazquez, E. (2023, May). *Kriging Metamodels for 2D Finite Element Simulations of Settlements Induced by TBM Excavation in Urban Areas.* Congrès Français du Génie Civil 2023, Association Française de Génie Civil, Gif-sur-Yvette, France.

Kratz, B., Jehel, P., Tatin, M., & Vazquez, E. (2023, October). *Calibrating a 3D Finite Element Model of TBM Excavation Using Monitoring Data Through Bayesian Approaches.* ETICS2023, Research Network on Uncertainty Quantification (RT-UQ).

Chapter 2

Review of modeling approaches for TBM excavation in soils

Chapter overview. Representing soil complexity and the inherently three-dimensional (3D) nature of TBM excavation using analytical models is challenging, particularly in multilayered soils exhibiting non-linear mechanical behavior. Numerical modeling, and in particular finite element (FE) method, therefore provide a more appropriate framework to account for complex geometries, non-linear soil constitutive laws, groundwater effects, and the sequential nature of mechanized tunneling. This chapter recalls the key soil mechanics concepts and governing equations relevant to TBM excavation, and reviews the main numerical strategies used to simulate the excavation process. It also presents common procedures for modeling excavation sequences and boundary conditions. The numerical model presented in Chapter 3 is developed based on the concepts and modeling strategies reviewed in this chapter. Building on previous reviews (Niu et al., 2023; Zhou et al., 2024) and the doctoral work of (El Jirari, 2021), the focus is placed on 3D FE modeling strategies.

Notation. Throughout this manuscript, scalar quantities are denoted by italic letters (e.g., p, z, E). Vectors are denoted by bold symbols (e.g., $\boldsymbol{u}$). The stress and strain tensors are denoted by bold symbols (e.g., $\boldsymbol{\sigma}$ and $\boldsymbol{\epsilon}$). The vertical coordinate z is taken positive downward from the ground surface (z=0).

2.1 Mechanical modeling of soils

Before presenting numerical strategies for TBM excavation modeling, we introduce key concepts, namely soil as a porous medium, the governing equilibrium equations, in-situ stress initialization, and soil rheology. The initial stress state controls the soil response and convergence phenomena, while the soil stress-strain constitutive behavior is essential for estimating deformations induced by tunnel advancement.

In this chapter, the soil domain is idealized as a parallelepiped, with a horizontal ground surface and a horizontal tunnel axis. The tunnel axis is aligned with the y-direction, the transverse direction is denoted by x, and the vertical coordinate z represents depth.

2.1.1 Fundamental equations in geomechanics

Numerical models in geotechnical engineering are based on the equations of continuum mechanics, solved under appropriate boundary and initial conditions. Soils are treated as a porous medium composed of a solid skeleton and one or more fluid phases (air and water). Depending on the presence of water, soil permeability, and excavation advance rate, the soil is assumed to be either drained, when pore pressures dissipate within the time scale of the loading process, or undrained, when excess pore pressures develop during construction and cannot dissipate within the considered time step.

In saturated soils, the effective stress represents the portion of the total stress carried by the solid skeleton. Total and effective stresses are related through Terzaghi's principle (Terzaghi, 1943), expressed as

$$\boldsymbol{\sigma} = \boldsymbol{\sigma}' + p_w \mathbf{I}, \tag{2.1}$$

where $\boldsymbol{\sigma}'$ and $\boldsymbol{\sigma}$ denote the effective and total stress tensors, respectively, p_w is the pore water pressure, and $\mathbf{I}$ is the identity tensor. In dry soils, $p_w = 0$ and total stresses are equal to effective stresses.

In the static or quasi-static regime, the mechanical equilibrium of a continuous soil medium is expressed as

$$\boldsymbol{\nabla} \cdot \boldsymbol{\sigma} + \boldsymbol{f}_b = \mathbf{0}, \tag{2.2}$$

where $\boldsymbol{\sigma}$ is the total stress tensor and $\boldsymbol{f}_b = \rho_s \mathbf{g}$ denotes the body force per unit volume (bulk total unit weight), with ρ_s being the soil density. The gravitational acceleration vector is defined as $\mathbf{g} = g\boldsymbol{e}_z$, where g is the gravitational acceleration and $\boldsymbol{e}_z$ is the unit vector along the vertical axis, z, which is taken positive downward. The operator $\boldsymbol{\nabla}\cdot$ represents the divergence operator and, in a Cartesian coordinate system (x, y, z), $\boldsymbol{\nabla} = \left(\frac{\partial}{\partial x}, \frac{\partial}{\partial y}, \frac{\partial}{\partial z}\right)$, where x and y denote the horizontal coordinates and z the depth.

Substituting Eq. (2.1) into Eq. (2.2) leads to the equilibrium equation expressed in terms of effective stresses

$$\boldsymbol{\nabla} \cdot \boldsymbol{\sigma}' + \boldsymbol{\nabla} p_w + \boldsymbol{f}_b = \mathbf{0}, \tag{2.3}$$

where the gradient of pore water pressure $\boldsymbol{\nabla} p_w$ acts as an additional body-force term.

2.1.2 Pore pressure modeling

The modeling strategy adopted in practice depends on how the pore-pressure term $\boldsymbol{\nabla} p_w$ in Eq. (2.3) is treated.

Drainage condition and modeling framework. In geotechnical engineering, the terms drained and undrained describe the ability of pore pressures to dissipate during loading. This behavior is governed by the ratio between the characteristic time scale of pore-pressure dissipation, t_c, and the loading or excavation time scale, t_{load}. Drained conditions correspond to $t_c \ll t_{\text{load}}$, whereas undrained conditions correspond to $t_c \gg t_{\text{load}}$.

In a quasi-static framework, time is not explicitly resolved and loading is represented as a sequence of equilibrium states. As a result, the drainage condition is not captured by the mechanical formulation and must be prescribed a priori based on engineering judgment.

In contrast, fully coupled hydromechanical formulations explicitly account for time by solving the evolution of pore pressure together with mechanical equilibrium. These approaches allow a consistent description of transient drainage conditions, but are significantly more computationally demanding.

Numerical formulations. Based on these considerations, four main numerical formulations can be distinguished (CFMS, 2023; Berthoz et al., 2020).

(i) Total-stress formulation. In this approach, pore pressures are not explicitly modeled and mechanical equilibrium is written in terms of the total stress tensor $\boldsymbol{\sigma}$. The effects of pore pressure are implicitly incorporated into the constitutive parameters. This formulation is often adopted for undrained analyses in a quasi-static framework.

(ii) Fully coupled hydromechanical formulation. In this case, mechanical equilibrium is solved together with Darcy's law and mass conservation equations, introducing time explicitly into the simulation (Kasper and Meschke, 2004; Meschke et al., 2011; Nagel and Meschke, 2010). This formulation allows the transient evolution of pore pressure to be captured and provides the most consistent representation of hydromechanical interactions.

(iii) Decoupled hydromechanical formulation. In this approach, the mechanical problem and the pore-pressure field are treated as two decoupled calculations. The pore-pressure field p_w is first computed independently based on the assumed hydraulic conditions (e.g., permeability, drainage regime, and characteristic time scales), and is then introduced as a prescribed field in the mechanical problem. The equilibrium equations are solved in terms of effective stresses $\boldsymbol{\sigma}'$, with the total stress given by Eq. 2.1. This formulation can be interpreted as a simplified approximation of the fully coupled hydromechanical problem, in which the temporal evolution of the pore-pressure field is not considered, and p_w is assumed to be fixed for a given characteristic time scale.

(iv) Mixed drained-undrained formulation. This formulation corresponds to a particular case of the decoupled approach applied to heterogeneous soil profiles, where different layers are assigned distinct drainage conditions. In practice, effective-stress formulations are used in permeable layers, where pore-pressure dissipation occurs within the considered time scale, while total-stress formulations are adopted in low-permeability layers, where pore-pressure dissipation is negligible. The pore-pressure field is typically prescribed, often assuming a hydrostatic distribution in permeable layers. This mixed formulation, illustrated in Appendix E and in Berthoz et al. (2020), provides a practical approximation of the initial stress state without resorting to fully coupled hydromechanical analyses.

Hydrostatic assumption. In the effective-stress formulation with prescribed pore pressure, the pore-pressure field is often assumed to follow a hydrostatic distribution:

$$p_w(z) = \begin{cases} \gamma_w(z - z_w), & z > z_w, \\ 0, & z \leq z_w, \end{cases} \tag{2.4}$$

where γ_w is the unit weight of water and z_w is the groundwater level. This assumption is appropriate when hydraulic gradients induced by excavation are neglected.

2.1.3 In-situ stress initialization

The in-situ stress state prior to excavation must be initialized in order to account for both gravity loading and the geological stress history of the soil mass.

Assuming that the initial principal stress directions are aligned with the Cartesian axes (x, y, z), the vertical stress σ_z is first obtained by solving the self-weight equilibrium problem.

Under effective-stress conditions with prescribed hydrostatic pore pressure, the submerged unit weight $\gamma'_s = \gamma_s - \gamma_w$ is used below the groundwater level, whereas in total-stress formulations the total unit weight γ_s is adopted. This gravity step provides the vertical stress profile $\sigma_z(z)$ (total or effective, depending on the formulation).

In subsurface soils, the in-situ stress state is generally anisotropic, so that the vertical and horizontal effective stresses differ ($\sigma'_z \neq \sigma'_x$ and $\sigma'_z \neq \sigma'_y$). The horizontal effective stresses are usually evaluated using the at-rest earth pressure condition (K_0 procedure), defined by

$$\sigma'_x = K_{0x}\sigma'_z, \qquad \sigma'_y = K_{0y}\sigma'_z.$$

If horizontal isotropy is assumed, $K_{0x} = K_{0y} = K_0$.

Remark. Common empirical formulations for estimating K_0 are provided in Appendix C.

Remark. In complex geological or urban contexts (e.g. inclined strata, surface loads, or variable water tables), direct K_0-based procedures may lead to unrealistic stress fields. More detailed discussions and examples are provided in (Ochmański et al., 2018; CFMS, 2023) and in Appendix D-E.

The following subsection examines soil rheology and its role in governing stress redistribution and ground deformations during excavation.

2.1.4 Soil rheology

The mechanical response of the soil skeleton is described by a constitutive relation linking stress and strain. In effective-stress formulations, this relation is written in terms of effective stresses as

$$\boldsymbol{\sigma}' = \mathbf{M}(\boldsymbol{\epsilon}), \tag{2.5}$$

where $\mathbf{M}$ denotes the constitutive operator associated with the chosen soil model (elastic, elastoplastic, or hardening models), and $\boldsymbol{\epsilon}$ is the strain tensor.

In elastoplastic models commonly used in geotechnical engineering, the total strain tensor is decomposed into elastic and plastic parts,

$$\boldsymbol{\epsilon} = \boldsymbol{\epsilon}_e + \boldsymbol{\epsilon}_p,$$

where $\boldsymbol{\epsilon}_e$ denotes the recoverable elastic strain tensor, and $\boldsymbol{\epsilon}_p$ the irreversible plastic strain tensor. This additive decomposition constitutes a fundamental assumption of small-strain plasticity models.

Near the tunnel face, stress redistribution may locally exceed the yield surface, leading to plastic strains. Although many constitutive models have been developed to represent soil behavior, capturing plasticity, hardening, small-strain stiffness, and anisotropy, no single model can reproduce all aspects of soil response with a limited number of parameters (Potts et al., 2001). In practice, constitutive models must be calibrated using laboratory tests, which becomes increasingly challenging as model complexity and the number of parameters increase.

For this reason, simple elastoplastic models are commonly used in geotechnical engineering practice. The Mohr-Coulomb (MC) model remains widely used due to its simplicity, limited input requirements, and computational efficiency (Gilleron et al., 2021; Tyrer et al., 2023).

However, the MC model assumes constant stiffness and does not account for higher unloading-reloading stiffness, nor for strain hardening and small-strain nonlinearity, which limits its ability to reproduce realistic stress-strain behavior (Obrzud, 2010; Tjie-Liong, 2014; Chen et al., 2016; Tyrer et al., 2023).

More advanced constitutive laws, such as the Hardening Soil (HS) model and its small-strain extension (HSS), address these limitations by introducing stress-dependent stiffness and plastic hardening (Schanz et al., 2019), at the cost of a larger number of model parameters.

Remark. A review of soil behavior and geological modeling approaches used in TBM excavation is provided in Appendix F.

2.2 Review of boundary conditions for TBM simulation

To approximate the equilibrium equations under realistic boundary and initial conditions, numerical models are required. Such models are now used throughout all steps of tunneling projects, from preliminary design to construction and post-construction monitoring. Typical applications include tunnel face stability assessment (Mollon et al., 2013), soil-structure interaction analysis (Mroueh and Shahrour, 2003; Jenck and Dias, 2004), segmental lining design (Kavvadas et al., 2017), inverse modeling (Zhao et al., 2015), and uncertainty quantification (Zhao et al., 2015; Mollon et al., 2013).

This section reviews numerical strategies for TBM excavation, with a focus on boundary condition formulations in 3D analyses.

2.2.1 Numerical method

In 3D tunneling simulations, excavation is commonly modeled through a sequence of quasi-static steps within a Lagrangian framework. Excavation is represented by deactivating the excavated zone, updating boundary conditions at the tunnel face, and activating support elements such as the lining and annular grout. This approach is widely used in tunneling analyses and is well suited to the low to moderate deformation levels expected during EPB TBM excavation Lambrughi et al. (2012); Migliazza et al. (2009); Mollon et al. (2013);

Kavvadas et al. (2017); Zhao et al. (2015); Ochmański et al. (2018); Nematollahi and Dias (2019).

Alternative formulations, including Eulerian and hybrid approaches such as Coupled Eulerian-Lagrangian methods or automatic remeshing, have been proposed to address large-deformation problems (Lee et al., 2016; El Jirari, 2021; Kim, 2021). These approaches are not considered further in this chapter.

Several numerical methods can be used to solve the governing equations in mechanized tunneling, including the finite element (FE), the finite difference (FD), and the discrete element (DE) methods. Given the moderate deformation regime expected during EPB TBM excavation and the demonstrated effectiveness of FE modeling in the literature Kasper and Meschke (2004, 2006b,a); Zhao et al. (2015); Kavvadas et al. (2017); Ochmański et al. (2018); Nematollahi and Dias (2019), a Lagrangian FE modeling framework is adopted in the following. The review therefore focuses on FE modeling, with limited reference to FD modeling due to similar assumptions regarding boundary conditions.

2.2.2 Domain geometry

In numerical simulations of TBM excavation, the soil domain is modeled as a finite domain rather than as an infinite medium. The model boundaries must be placed sufficiently far from the tunnel to minimize boundary effects on the computed response, and suitable boundary conditions must be prescribed at these limits.

Most models exploit symmetry about the vertical plane $x = 0$, reducing the analysis to a half-domain defined by the half-width X_{lim}, length Y_{lim}, and depth Z_{lim}. This assumption, however, may be invalid in the presence of surface structures or heterogeneous soil conditions.

Figures 2.1 and 2.2 present the transverse and longitudinal sections of the 3D finite domain, together with the boundary conditions applied on the model boundaries.

Several guidelines have been proposed in the literature to determine minimum model dimensions $(X_{\text{lim}}, Y_{\text{lim}}, Z_{\text{lim}})$ as functions of the tunnel depth H_t and diameter D_t. Dimensions are given in the order $(X_{\text{lim}}, Y_{\text{lim}}, Z_{\text{lim}})$ and refer to a half-domain in the transverse direction x (symmetry with respect to the vertical plane $x = 0$).

- Rodriguez (2000): $(3H_t; H_t + 3D_t; H_t + 4D_t)$
- Möller (2006):

$$\left(D_t\left(1+\frac{H_t}{D_t}\right); D_t\left(13+\frac{11}{3}+\frac{H_t}{D_t}\right); (1.1-2.5)D_t\right)$$

- Ochmański et al. (2018): $(3H_t; 5H_t; 3H_t)$
- Lambrughi et al. (2012); Nematollahi and Dias (2019): $(2(H_t{+}4D_t); 2(H_t{+}4D_t); 3H_t)$
- Kavvadas et al. (2017): $(11D_t; 21D_t; H_t + 3D_t)$

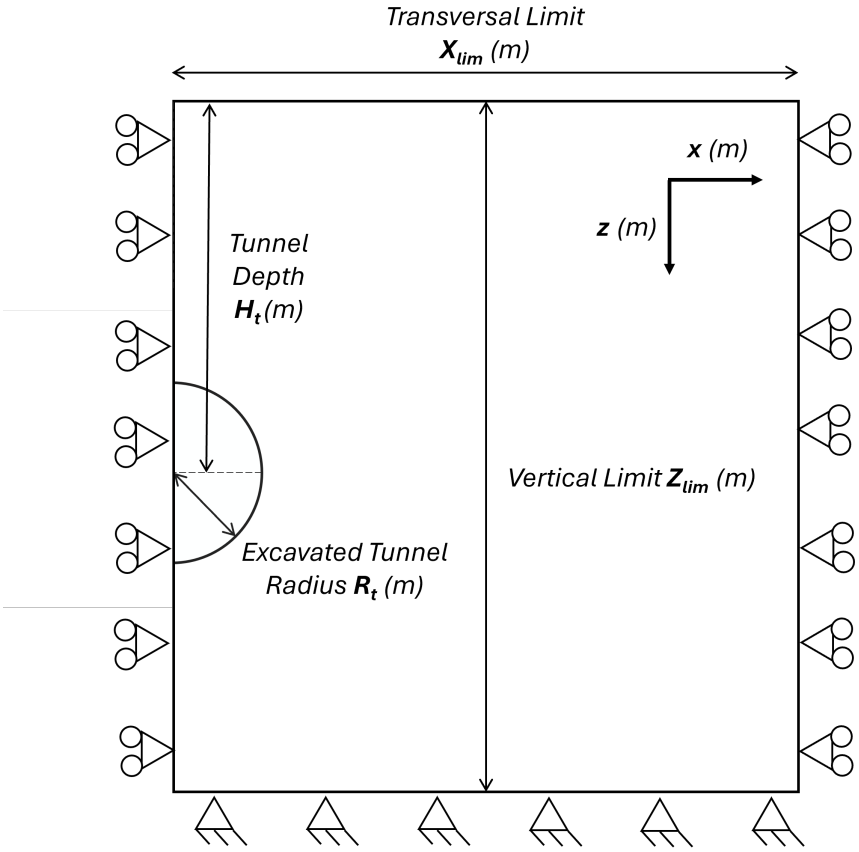

Figure 2.1: Transverse section ($y = 0$) of the finite domain in 2D plane-strain analyses. Horizontal displacement is fixed ($u_x = 0$) at $x = X_{\text{lim}}$ and $x = 0$, while all degrees of freedom are fixed at the base ($z = Z_{\text{lim}}$).

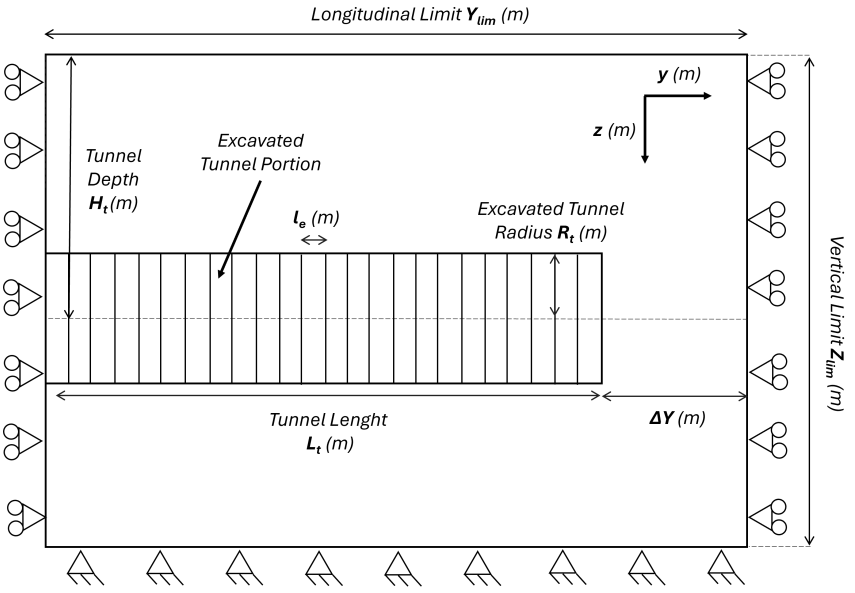

Figure 2.2: Longitudinal section ($x = 0$) of the finite domain in 3D analyses. Horizontal displacement is fixed ($u_y = 0$) at $y = Y_{\text{lim}}$ and $y = 0$, while all degrees of freedom are fixed at the base ($z = Z_{\text{lim}}$).

2.2.3 Sequential boundary conditions for 3D TBM simulation

As discussed in Section 2.2.1, the step-by-step method is commonly used to reproduce TBM advancement through discrete, quasi-static steps. In this section, excavation is represented as a sequence of discrete equilibrium states, each corresponding to an excavation step.

Within this formulation, time-dependent processes are not modeled explicitly. Instead, excavation steps act as a pseudo-time variable, and all physical processes (loading, support installation, and material evolution) are approximated through their evolution with respect to these steps.

The procedure starts with the initialization of the in-situ stress state under gravity loading, accounting for both saturated and unsaturated conditions in order to define the vertical effective stresses (Section 2.1.3). Excavation then proceeds step-by-step.

To model the excavation process at step t, several phenomena must be represented simultaneously through different boundary conditions applied to different elements of the mesh, in order to capture realistic soil-tunnel interactions.

In what follows, we summarize the main numerical strategies used to simulate (1) the application of face pressure to ensure low ground deformation at the tunnel face, (2) the TBM conical shield and its interaction with the surrounding soil, represented through boundary conditions, (3) grout injection to fill the void between the lining and the excavated soil at the end of the tail, (4) grout hardening during the step, (5) lining installation, and (6) soil-structure interaction.

Modeling of face pressure

During tunneling, the Tunnel Boring Machine (TBM) shield is designed to apply a pressure on the excavation front (also called tunnel face), to prevent collapse onto the cutterhead. This face pressure is a critical parameter influencing surface settlements and overall soil response (Lee et al., 1992; Kasper and Meschke, 2006a).

Closed-face TBM technologies have been developed to actively control this pressure. Slurry TBMs stabilize the chamber by injecting a mixture of excavated material and slurry, while EPB TBMs retain the excavated soil itself to pressurize the face. In numerical modeling, this face pressure is typically represented as a horizontal load applied at the tunnel face (Kasper and Meschke, 2006a; Losacco and Viggiani, 2019; Ochmański et al., 2018).

In a total-stress formulation, the applied face pressure is prescribed as a total pressure and must balance both the in-situ horizontal total stress and the groundwater pressure. To account for the vertical variation of stresses, a hydrostatic distribution is commonly assumed, given by

$$p_f(z) = p_{f,0} + \gamma_f \left(z - H_t\right), \tag{2.6}$$

where $p_{f,0}$ denotes the total face pressure at the tunnel axis level ($z = H_t$), z is the depth coordinate (positive downward), H_t is the tunnel axis depth, and γ_f is the unit weight of the excavated material, which may differ from the in-situ soil unit weight γ_s.

Remark. In an effective-stress formulation with prescribed hydrostatic pore pressure, the effective face pressure is obtained by subtracting the pore pressure from the total face pressure. It may therefore be expressed as

$$p'_f(z) = p_{f,0} + \gamma_f \left(z - H_t\right) - \gamma_w \left(z - z_w\right), \tag{2.7}$$

where $p_{f,0}$ denotes the total face pressure at the tunnel axis level ($z = H_t$), γ_w is the unit weight of water, H_t is the tunnel axis depth, and z_w denotes the groundwater level.

TBM monitoring data indicate that face pressure does not always vary linearly with depth (Lambrughi et al., 2012). Consequently, uniform pressure distributions have been adopted in some studies (Migliazza et al., 2009; Lambrughi et al., 2012; Founta et al., 2013; Mirhabibi and Soroush, 2013). Some modeling approaches, such as Jenck and Dias (2004), instead represent face stability by constraining horizontal displacements at the excavation front rather than applying an explicit pressure load.

Remark. To choose the face pressure, engineers often rely on empirical relations (see Appendix H.1).

Shield-soil interaction

The TBM shield generally has a conical shape that reduces friction with the surrounding soil and facilitates advancement. Combined with overcutting at the excavation face, this geometry creates voids around the shield and behind the tail, which influence soil displacements and settlement development. An appropriate representation of shield-soil interaction is therefore required in numerical simulations.

In the literature, shield-soil interaction is commonly modeled using approaches that can be grouped into four main categories.

First, the supporting effect of the shield may be represented by applying an equivalent radial pressure (Neumann boundary conditions) along the excavation boundary over the shield length (Mroueh and Shahrour, 2003, 2008), sometimes established using the convergence-confinement approach (Panet and Sulem, 2021).

Second, displacement boundary conditions (Dirichlet boundary conditions) can be imposed along the excavation boundary to mimic the kinematic effect of the conical shield and overcut (Jenck and Dias, 2004; Founta et al., 2013; Zhang et al., 2016), or by blocking displacements (Mollon et al., 2013).

Third, the annular void created by the shield conicity may be represented by introducing a thin low-stiffness zone between the excavated soil mesh elements and the shield mesh elements (Lambrughi et al., 2012).

Finally, the shield can be explicitly modeled, with contact laws defining the mechanical interaction between the soil and the shield (Zhao et al., 2015; Kavvadas et al., 2017; Ochmański et al., 2018; Losacco and Viggiani, 2019). See Appendix G for more details.

Modeling of TBM weight and thrust jack

Although the TBM weight generally has a limited impact on surface settlements compared to other factors (Kasper and Meschke, 2006a), its contribution to local stress and strain

fields should be considered for completeness. It also affects shield tilt, which can increase the annular gap at the tunnel crown (Lee et al., 1992). When the TBM is explicitly modeled with surface or volume elements, its density is defined to represent the mass of the shield, the excavated chamber, and associated equipment (Kavvadas et al., 2017). Alternatively, its weight can be approximated in the model by applying distributed vertical loads along the excavation boundary or on the lining structure to simulate the backup train (Kasper and Meschke, 2004; Ochmański et al., 2018; Zhang et al., 2016; Nematollahi and Dias, 2019).

Thrust jacks ensure TBM advancement and guidance and, like the shield weight, affect the shield tilt and consequently the annular gap between the shield and the excavated soil (Lee et al., 1992). In numerical models, these forces are typically represented as horizontal loads applied at the circumferential interface between the tail skin and the last installed lining ring (Do et al., 2014; Founta et al., 2013; Ochmański et al., 2018, 2020; Nematollahi and Dias, 2019). This representation is often combined with frictional contact laws to capture interactions between the shield and the surrounding soil (Kasper and Meschke, 2004; Meschke et al., 2011; Ochmański et al., 2018).

Modeling of grout injection

After the passage of the TBM shield, pressurized grout is injected to fill the annular void between the tail and the segmental lining. This operation provides support to the excavated soil, mitigates surface settlements, and ensures effective load transfer to the lining structure.

In numerical modeling, grout pressure is often introduced as a radial surface load applied along the tunnel circumference and activated shortly behind the TBM tail (Lambrughi et al., 2012).

Alternatively, the grout can be represented as an elastic volumetric material occupying the annular gap, with internal pore pressure simulating the injection force (Kavvadas et al., 2017; Ochmański et al., 2018), or by imposing displacements at the injection interface to reproduce volume loss effects (Viggiani et al., 2004).

To account for the weight of the liquid grout and its variation with depth, a hydrostatic distribution of pressure is frequently adopted (Ochmański et al., 2018),

$$p_g(z) = p_{0,g} + \gamma_g(z - z_{\text{crown}}), \tag{2.8}$$

where $p_{0,g}$ is the reference pressure at the tunnel crown level, z is the vertical coordinate, and γ_g denotes the unit weight of the grout. Eq. (2.8) represents the injected grout pressure under undrained conditions (total stress state). For drained conditions, the formulation is similar to that used for the face pressure (Eq. (2.7)).

While this distribution is physically consistent, many models simplify the injection by assuming a uniform radial pressure (Founta et al., 2013; Kavvadas et al., 2017; Lambrughi et al., 2012; Losacco and Viggiani, 2019).

Remark. To choose the grouting pressure, engineers use empirical relations (see Appendix H.2).

Modeling of grout hardening

As the TBM advances, freshly injected grout evolves from a pressurized liquid phase to a solid with no internal pore pressure. This hardening process is critical for modeling excavation support, since the consolidated grout transfers loads from the surrounding soil to the lining.

In numerical simulations, grout is typically introduced as an elastic material with properties E_g and ν_g, tied to both the excavated soil and the lining to ensure consistent load transfer.

Hardening is generally represented as a multi-stage process in which the mechanical properties evolve with time or excavation steps. The Young's modulus progressively increases (Kasper and Meschke, 2004; Lambrughi et al., 2012; Ochmański et al., 2018), while the Poisson's ratio may decrease from 0.5 (incompressible) to about 0.2 during consolidation (Demagh et al., 2008, 2013).

Simplified two-stage models also exist, in which grout initially behaves as a pressurized liquid before abruptly adopting hardened properties Nematollahi and Dias (2019). More refined approaches use empirical laws to describe the time-dependent evolution of $E_g(t)$ (CEB-FIB, 1993; FIB, 2013; Lambrughi et al., 2012) (see Appendix I).

Since these approaches require linking stiffness evolution to excavation progress, the TBM advance rate is a key parameter. In a step-by-step quasi-static approach, the number of hardening steps can be estimated from the distance excavated during the characteristic hardening time as

$$n_h = \left\lfloor \frac{V_{\mathrm{TBM}}\, t_{\mathrm{hardening}}}{l_{\mathrm{step}}} \right\rfloor,$$

where V_{TBM} is the advance rate, $t_{\mathrm{hardening}}$ is the characteristic hardening time, and l_{step} is the excavation step length.

Remark. Operational pauses may affect the effective excavation time and thus the number of hardening steps. Their influence could be incorporated through an adjusted advance rate or an effective excavation time, although this is not considered here.

Two modeling strategies are generally adopted within a step-by-step quasi-static framework. The first explicitly updates stiffness according to the actual advance rate and step length, thereby reproducing the evolution of $E_g(t)$, which is discretized with respect to excavation steps. This approach provides an accurate representation of grout hardening but may require many steps for slow-hardening mixes, thus increasing computational cost. The second strategy uses a fixed number of steps n_h, condensing the hardening process into fewer steps. This approximation improves computational efficiency while maintaining sufficient engineering accuracy. These strategies are compared in Figure 2.3.

Modeling of lining

Behind the TBM tail, precast concrete lining rings are assembled to provide structural support and ensure tunnel impermeability. In numerical analyses, the lining is generally represented using 2D shell or 3D solid FE, with elastic properties defined by a modulus E_l and a Poisson's ratio ν_l. Connection to the surrounding grout is most often modeled using tie constraints, which enforce no relative displacement at the interface and simplify the

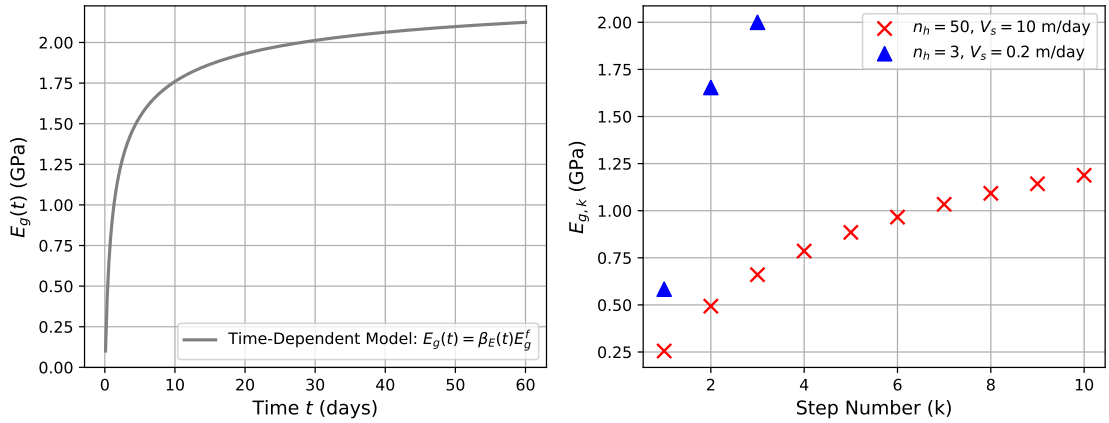

Figure 2.3: Comparison between continuous and discrete representations of the FIB grout hardening model (FIB, 2013). Red markers indicate a stepwise model with stiffness updates at each excavation step assuming a 10 m/day advance rate with $l_e = 2$m. Blue markers illustrate a simplified three-stage approximation using a fictitious hardening length.

contact behavior. Alternative approaches employ surface-to-surface contact formulations without tie conditions to capture possible relative movements between lining and grout (Ninić and Meschke, 2017).

The lining is commonly modeled as a continuous structure, neglecting joints between rings or segments. Several studies have shown that this simplification has limited influence on predicted soil displacements (Do et al., 2013, 2014). However, joints reduce the overall stiffness and allow for local rotations, which become non-negligible when evaluating internal stresses and strains (Litsas et al., 2015; Kavvadas et al., 2017; Nematollahi and Dias, 2019; Nematollahi et al., 2020).

To account for the reduced stiffness of a segmented lining without explicitly modeling individual joints, a reduction factor α_{red} can be applied to the Young's modulus of the concrete segments E_{seg} (Koyama, 2003; Demagh et al., 2008). The effective modulus assigned in the numerical model is then given by

$$E_l = \alpha_{\text{red}} E_{\text{seg}}. \tag{2.9}$$

Soil-structure interaction

The interaction between tunneling and surface structures (buildings, piles, foundations) influences both the magnitude and distribution of soil settlements. Structural stiffness redistributes deformations, generally reducing settlements beneath buildings but sometimes increasing them near foundations or in twin-tunnel configurations (Jenck and Dias, 2004; Mirhabibi and Soroush, 2013; Viggiani et al., 2004; Cheng et al., 2007; Afifipour et al., 2011; Nematollahi and Dias, 2019). These effects depend on structural geometry and mechanical properties, often uncertain for existing buildings.

Explicitly modeling structural stiffness in 3D FE analyses provides more accurate estimates of tunneling-induced loads than applying free-field soil movements directly to

structures (Mroueh and Shahrour, 2003). Including the buildings' self-weight in the initial stress state is also important to avoid underestimating these loads.

2.3 Chapter conclusions

This chapter has reviewed numerical strategies for simulating TBM excavation in urban environments, with a particular focus on boundary condition formulations within a 3D FE framework.

Key aspects include the initialization of in-situ stress states, soil rheology models, and detailed interactions between the TBM, tunnel components, and the surrounding soil, including face pressure, shield geometry, grout injection and hardening, lining installation, and soil-structure interaction.

This chapter constitutes the first step of the design and analysis of computer experiments (DACE) framework, in which the mathematical and numerical formulations are reviewed to establish the finite element (FE) simulator used to model the process and estimate TBM-induced settlements.

Chapter 3 implements this framework to build a parametric 3D FE model and to express it as a mapping between input variables and settlement-related outputs, thereby enabling its integration within a DACE framework.

Chapter 3

A three-dimensional finite element model for EPB TBM excavation

Chapter overview. This chapter presents the three-dimensional (3D) finite element (FE) simulator developed to model Earth Pressure Balance (EPB) shield tunneling and to estimate the resulting surface settlements. The model is based on the state-of-the-art FE approaches reviewed in Chapter 2 and incorporates the assumptions required for EPB TBM excavation in urban conditions.

3.1 FE modeling assumptions

This section presents the mechanical and geometrical assumptions of the numerical simulator.

3.1.1 Geological domain and boundaries

A 3D FE simulator was developed using the Abaqus software (Abaqus, 2011). The same coordinate system as in Chapter 2 is adopted. The geological domain is modeled as a rectangular parallelepiped defined in a Cartesian coordinate system (x, y, z), where x denotes the transverse direction (perpendicular to the tunnel axis), y the longitudinal direction (along the tunnel axis), and z the vertical direction. The ground surface corresponds to $z = 0$, and depth is taken positive downward.

Symmetry is imposed with respect to the vertical plane $x = 0$, which contains the tunnel axis aligned with the y-direction (see Figure 3.1). Only half of the domain is simulated for efficiency.

The computational domain Ω is defined by its half-width X_{lim}, length Y_{lim}, and depth Z_{lim} as

$$\Omega = [0, X_{\text{lim}}] \times [0, Y_{\text{lim}}] \times [0, Z_{\text{lim}}].$$

The soil, TBM, lining, and grout are discretized using independent meshes: C3D4 elements for the soil (with fine and coarse densities), S8 shell elements for the TBM and lining, and C3D8 elements for hardened grout. Boundary conditions fix the bottom, restrict normal displacements laterally, and leave the surface free.

The main geometrical parameters of the model, including the domain size, tunnel geometry, and mesh densities, are illustrated in Figure 3.1.

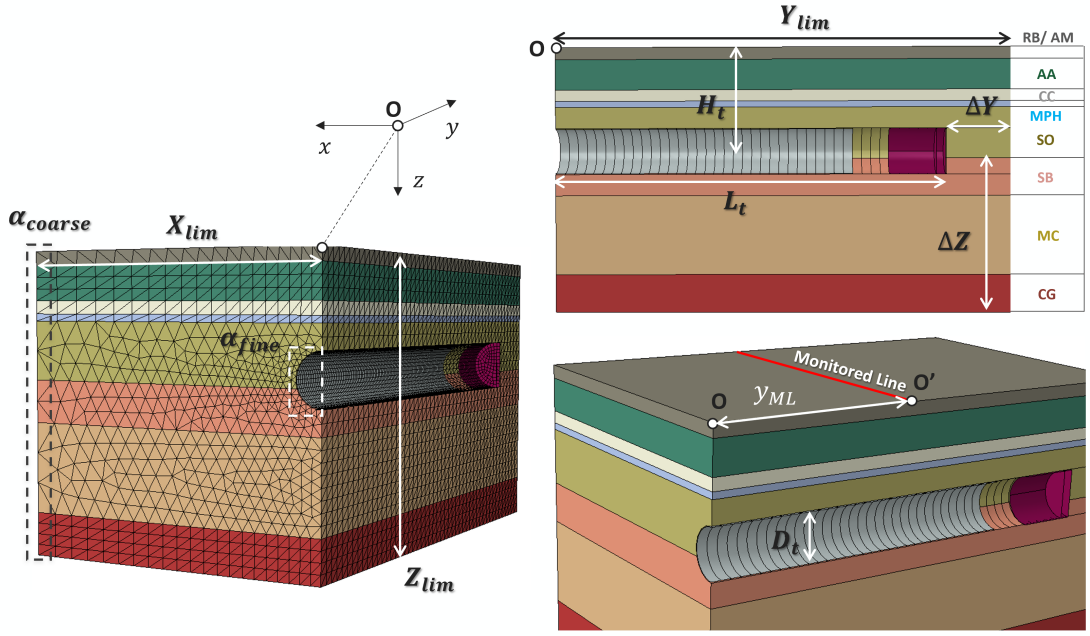

Figure 3.1: FE model domain size and meshing parameters definition. The geological domain is characterized by key modeling parameters. These include the transverse extent of the domain (X_{lim}), the distance between the first excavation slice and the longitudinal limit (Y_{lim}), the tunnel length (L_t), the tunnel depth (H_t), the offset between the tunnel end and the longitudinal boundary (ΔY), the depth of the domain (Z_{lim}), the tunnel diameter (D_t), and the distance from the first slice to the monitored line (y_{ML}). All parameters are in meters. Additionally, α_{coarse} and α_{fine} denote the mesh density far from and near the tunnel, respectively.

3.1.2 Simulation procedure

The TBM excavation is simulated as a sequence of quasi-static steps under small-deformation assumptions, using a Lagrangian formulation. Each step models excavation, shield advance, grout injection, lining installation, and grout hardening at different positions along the tunnel.

The full simulation procedure is summarized in Algorithm 1 and illustrated in Figure 3.2.

In contrast to mixed formulations (Section 2.1.2), all soil layers are assumed fully drained with hydrostatic pore pressure. The mechanical response is therefore governed by effective stresses. This assumption is consistent with long-term conditions and remains representative for permeable soils or slow TBM advance rates (Zhao et al., 2015; Berthoz et al., 2020).

The initial stress state is defined from self-weight for vertical stresses, and from at-rest earth pressure coefficients K_0 for horizontal stresses. These coefficients are specified in

both transverse (K_{0x}) and longitudinal (K_{0y}) directions to account for stress anisotropy (see Section 2.1.3 for further details).

At each step, soil elements are excavated (deactivated), the TBM shield advances, and the lining is installed with pressurized grout injection. Face and grout pressures are modeled as hydrostatic profiles, defined by a reference pressure at the tunnel axis and a vertical gradient:

$$p_\alpha(z) = p_\alpha^0 + p_\alpha^{\text{grad}}(z - z_0), \tag{3.1}$$

where $\alpha = \text{f}$ and $\alpha = \text{g}$ correspond to the face and grout pressures, respectively. The term p_α^0 denotes the pressure defined at the reference depth $z = z_0$.

Remark. Under drained conditions, $p_\alpha(z)$ is defined as an effective pressure obtained by subtracting the pore water pressure at depth z, assuming a hydrostatic groundwater field. To ensure physical consistency, the effective pressure $p_\alpha(z)$ is typically constrained to be non-negative ($p_\alpha(z) \geq 0$).

The TBM-soil interface is modeled using an exponential overclosure contact law (see Section 2.2.3 and Appendix G), while the grout-soil and lining-grout interfaces are represented by tie constraints. To account for the weight of surface structures, a uniform surface load is applied (see Section 2.2.3).

The simulation begins either with TBM entry (first slice excavation) or with the initial shield already embedded in the domain. Excavation proceeds until the TBM reaches its final position at $L_t = Y_{\text{lim}} - \Delta Y$. After the last step, the shield may remain in place until grout hardening is complete or be progressively moved out of the domain to reduce soil-shield interaction while allowing adequate grout hardening.

Remark. In Algorithm 1, at excavation step k, the face pressure is applied to the newly excavated slice, corresponding to position $k + 1$ in the discretized mesh (see Figure 3.2). Grout injection, lining activation, and hardening are defined relative to the shield position through indices such as $k - n_{\text{tbm}}$ and $k - n_{\text{tbm}} - n_g$. For early excavation stages, when these indices become non-positive, the corresponding operations are not activated until the relevant slices exist in the computational domain.

Remark. The numerical model does not include explicit soil-structure interaction (SSI) at the ground surface, nor does it account for the thrust jack pressures of the TBM. However, an equivalent uniform surface load is applied to represent the weight of surface structures.

3.1.3 Material behavior

In this study, we adopt the Mohr-Coulomb elastoplastic model with a non-associated plastic flow rule, characterised by Young's modulus E, Poisson's ratio ν, friction angle ϕ, cohesion c, and dilatancy angle $\Psi = \phi - 30°$ (Brinkgreve, 2004).

Despite its limitations, the MC model remains well suited for mechanised tunneling with low volume loss, where plasticity is mainly confined near the tunnel face (Gilleron et al., 2021). Field observations also confirm its good estimation performance for surface settlements (Migliazza et al., 2009; Ring and Comulada, 2018; Beghoul and Demagh, 2019; Ahmed et al., 2021; M Saleh et al., 2022; Zerdia et al., 2024).

Algorithm 1 TBM Excavation Process Simulation

Input:
    Tunnel length L_t, excavation step length l_e, shield length l_s, grout injection length l_g, grout hardening length l_h.
    Face pressure profile $p_f(z)$, grout pressure profile $p_g(z)$, initial grout modulus E_g^i.
Initialization:
    Compute the number of excavation steps: $N_{\text{excavation}} = \lfloor L_t/l_e \rfloor$.
    Determine the number of slices for TBM shield n_{tbm}, grout injection n_g, and grout hardening n_h.
    Geostatic Step:
        Initialise stress and strain fields: $\boldsymbol{\sigma}_0$, $\boldsymbol{\epsilon}_0 = \mathbf{0}$.
for $k = 1$ to $N_{\text{excavation}}$ **do**
    Excavation:
        Remove soil slice at step k.
        Apply face pressure p_f at step $k + 1$.
        Advance TBM shield to $k + 1$ and enforce contact laws at the interface.
    Grout Injection:
        Inject grout at slice $k - n_{\text{tbm}}$ with pressure p_g over n_g slices.
        Initiate solidification at slice $k - n_{\text{tbm}} - n_g$ with modulus E_g^i.
    Lining Installation:
        Activate lining at slice $k - n_{\text{tbm}} - n_g$ and tie it to the grout layer.
    Grout Hardening:
    for $i = 1$ to n_h **do**
            Update grout modulus at slice $k - n_{\text{tbm}} - n_g - i$ using the selected hardening law.
    end for
    Update Fields:
        Solve for stress, strain, and displacement fields: $\boldsymbol{\sigma}_k$, $\boldsymbol{\epsilon}_k$, $\mathbf{u}_k$.
end for

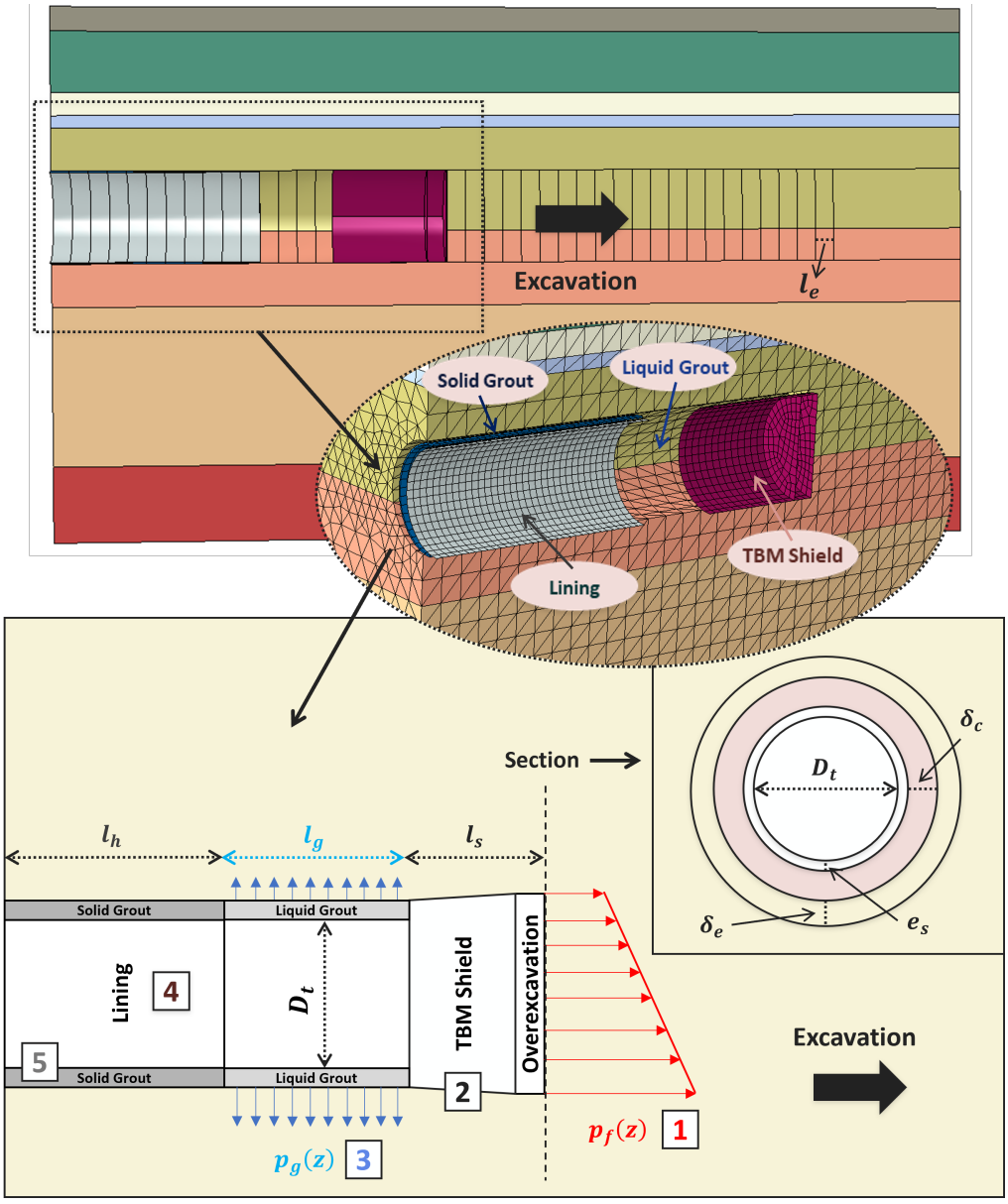

Figure 3.2: Boundary conditions applied during a quasi-static step in the simulation. The upper schema illustrates the multi-step quasi-static process, where different meshing components are defined, including the lining, grout, soil, and TBM shield. The lower figure provides details on the boundary conditions applied at each step of the excavation process: (1) the face pressure, (2) the contact law based on the distance between soil nodes and TBM shield nodes, (3) the injected grout pressure, (4) the lining installation, and (5) the hardening grout law, modeled by progressively increasing its rigidity throughout the simulation. Key parameters can be defined, such as the number of soil slices interacting with the TBM shield $n_s = l_s/l_e$, the number of slices where grout pressure is applied $n_g = l_g/l_e$, and the number of slices over which grout rigidity increases $n_h = l_h/l_e$. Additionally, several geometric characteristics are defined, including the over-excavation ratio δ_e, the conicity δ_c, the thickness of the TBM shield e_s, and the tunnel diameter D_t.

To further reduce potential discrepancies, several refined stiffness definitions have been proposed, such as replacing E with the unloading-reloading modulus E_{ur} (Tjie-Liong, 2014; Tyrer et al., 2023), or using an equivalent small-strain modulus E_0 calibrated from field data (Miliziano and de Lillis, 2019).

Remark. In undrained geological layers analyzed under total stress conditions, it is common practice to use $\nu = 0.49$, $\phi = 0°$, and $c = c_u$ (the undrained shear strength). This assumption corresponds to a short-term analysis in saturated fine soils where pore pressures are not explicitly modeled. In contrast, for drained soils, pore pressures are assumed to dissipate, and the soil behavior is described in terms of effective stresses using the parameters ϕ' and c' obtained from drained laboratory tests.

The TBM shield, lining, and hardened grout are modeled as elastic materials. Their self-weight (TBM, Grout and Lining) is accounted for through gravity loading based on their respective densities. Grout hardening is represented by a step-dependent evolution of Young's modulus (Eq. (I.1)) (FIB, 2013), reflecting the progressive increase in stiffness during construction (see Section 2.2.3 and Appendix I).

Lining stiffness is modeled via its effective Young's modulus, accounting for joints between segments as described by Eq. (2.9).

3.2 Results from the 3D FE model

3.2.1 Model setup

To verify the numerical model, a simulation was performed. The analysis follows the domain size recommendations presented in Section 2.2.2, with the following dimensions: $X_{\text{lim}} = 10D_t \approx 100\text{m}$, $Y_{\text{lim}} = 15D_t \approx 150\text{m}$, $L_t = 115\text{m}$, $H_t = 32\text{m}$, $\Delta Z = 3D_t \approx 30\text{m}$, and $Y_{\text{ML}} = 65\text{m}$, where D_t is the tunnel diameter.

The geological context is multilayered and fully drained; all stresses are therefore expressed in terms of effective stresses. The input parameters are defined in Appendix J, with values taken at the midpoints of their respective ranges. Both the effective face and grout pressures are set to constant values $p'_{f,0} = p'_{g,0} = 0$ kPa (see Eq. (2.7)), assuming a groundwater level $z_w = 0$ m.

The displacement and effective stress fields obtained from this reference simulation are analysed below to describe the overall mechanical behavior. To describe the displacement and stress fields, standard tunnel terminology is adopted, including the crown, invert, and springline, which are defined in Figure 3.3.

3.2.2 Analysis of displacement and stress fields

This section analyzes displacement and stress fields at selected excavation stages and TBM positions.

Remark. In this part, we denote the vertical displacement by $U_3 = u_z$ and the displacement magnitude by U_{magn}.

The vertical displacement field U_3 (Figure 3.4) shows that settlements initiate ahead of the shield and reach their maximum behind it, resulting from the combined effects of

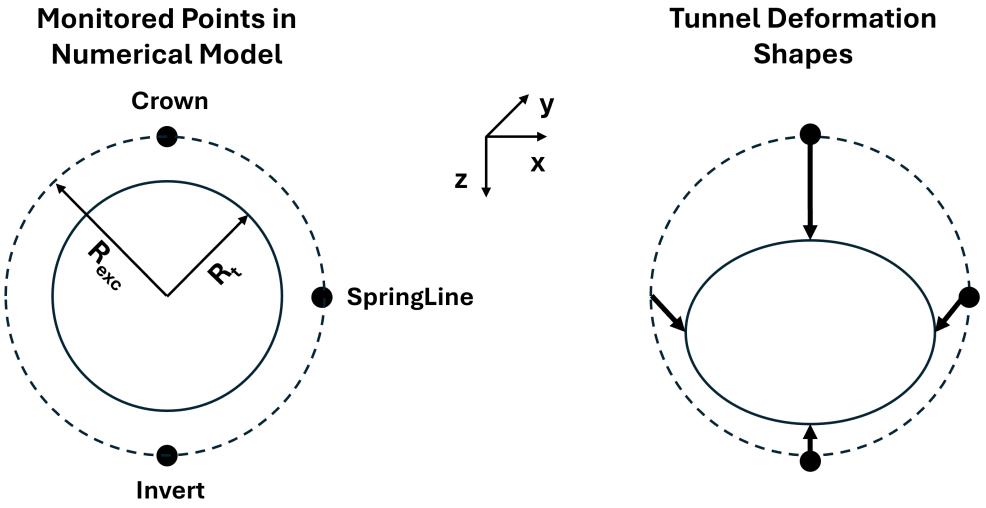

Figure 3.3: Definition of reference points and geometrical quantities around the tunnel cross-section: tunnel radius R_t, excavation radius R_{excv}, crown, invert, and springline.

face and grout pressures and shield conicity. An asymmetric response is observed, with larger displacements at the crown than at the invert. This deformation propagates to the ground surface, forming a settlement pattern centred above the tunnel axis, while vertical displacements remain minimal at the springline.

The total displacement magnitude $\|\mathbf{U}\|$, shown in Figures 3.5 (longitudinal section, $X = 0$) and 3.6 (transverse section, $Y =$ constant), confirms the anisotropic deformation pattern. Radial displacements are dominant at the crown, followed by the invert and the springline (see Figure 3.3), leading to an ovalisation of the tunnel cross-section. This behavior is consistent with gap-based descriptions (Lee et al., 1992), such as the profiles proposed by Loganathan and Poulos (1998), and reflects the combined effects of in-situ stress anisotropy ($K_0 < 1$) and asymmetric loading induced by the TBM shield.

In addition, vertical discontinuities observed in both the vertical displacement field and the displacement magnitude field can be attributed to contrasts in stiffness and in-situ stress ratios (K_0) between geological layers. Figures 3.4, 3.5, and 3.6 correspond respectively to Step 20, Step 29, and Step 44 of the excavation sequence.

Figures 3.7, 3.8, 3.9, and 3.10 show the effective stress fields at different excavation stages: σ'_{xx} in the transverse direction, σ'_{yy} in the longitudinal direction, and σ'_{zz} in both longitudinal and transverse sections. In all these figures, effective stresses are expressed in kPa, with negative values corresponding to compressive stresses.

Far from the tunnel boundary, the stress state remains close to the initial condition. The vertical effective stress σ'_{zz} increases with depth following a gravity-controlled profile, while the horizontal stresses are governed by the initial at-rest conditions and soil stratification. These regions are not affected by excavation-induced unloading or shield-soil interaction, indicating that boundary effects are negligible for the present geometrical configuration.

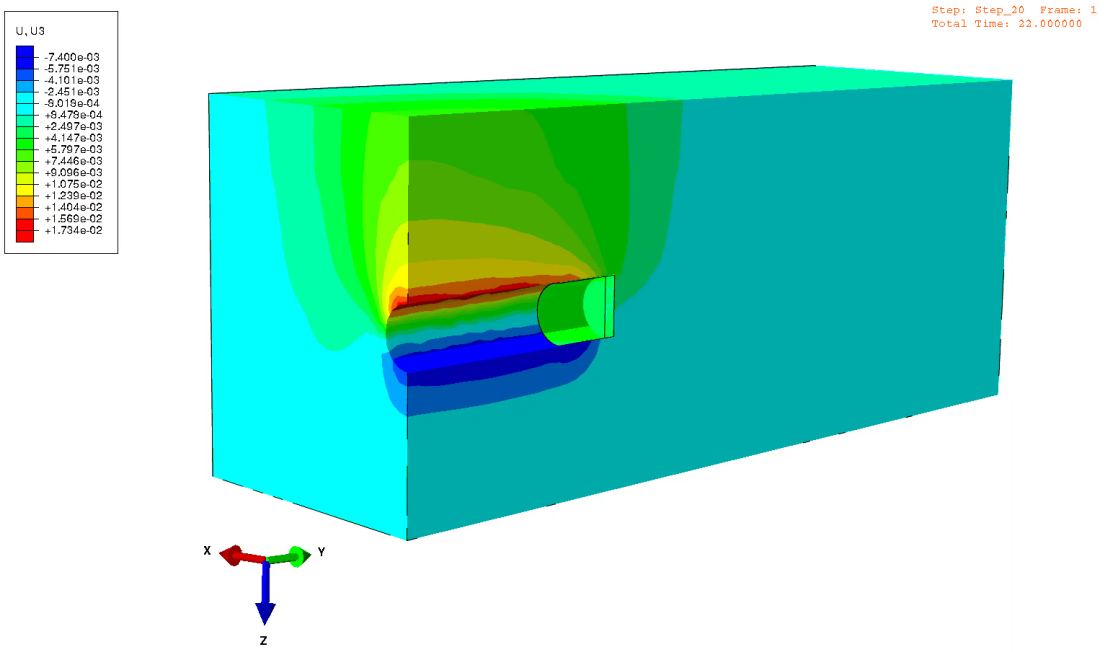

Figure 3.4: Vertical displacement field U_3 (m) at Step 20. Settlements initiate ahead of the TBM and reach their maximum behind the shield, with peak values at the crown. The deformation reflects the combined effects of shield conicity, gravity loading, and the absence of face and grout pressures.

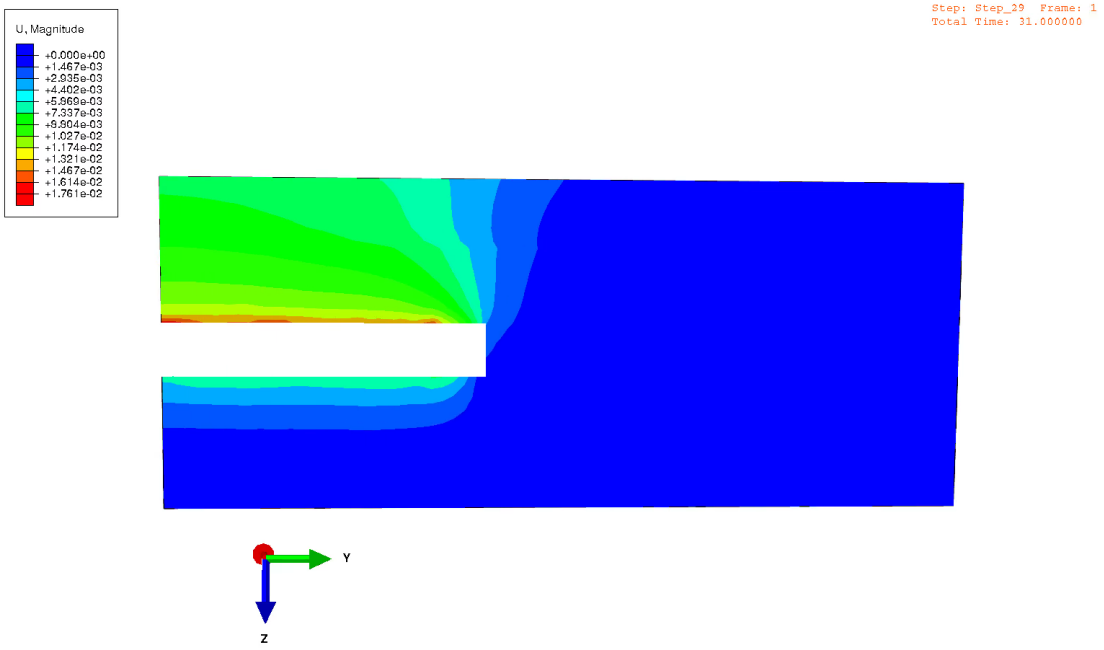

Figure 3.5: Displacement magnitude $\|\mathbf{U}\|$ (m) at Step 29 in the longitudinal section ($X = 0$). Deformation is dominated by crown settlement and extends behind the TBM, illustrating the progressive development of the settlement field during shield advance.

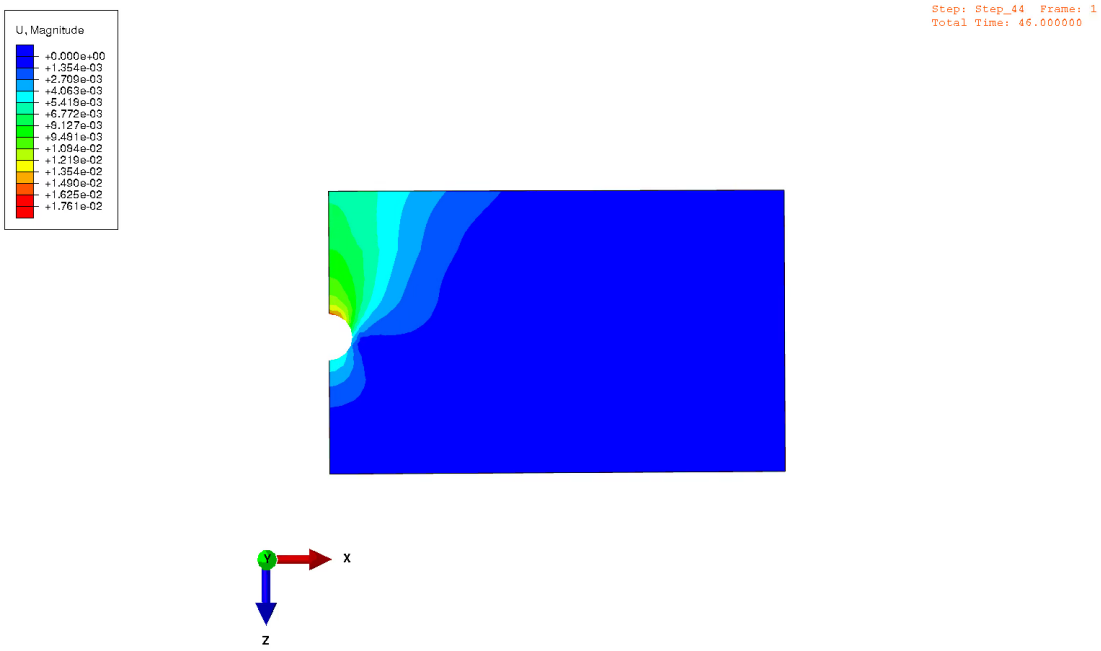

Figure 3.6: Displacement magnitude $\|\mathbf{U}\|$ (m) at Step 44 in a transverse section (Y = constant) after shield passage. The deformation pattern is asymmetric, with maximum displacements at the crown, moderate at the invert, and minimal at the springline, reflecting radial contraction under $K_0 < 1$ conditions.

Near the excavation boundary, the stress fields are modified by face pressure, shield-soil interaction, grout injection, and hardening, which induce confinement loss and subsequent stress redistribution.

The horizontal effective stress σ'_{xx} (Figure 3.7) shows a redistribution around the tunnel. A decrease in σ'_{xx} is observed near the springline and in the immediate vicinity of the tunnel, reflecting excavation-induced loss of lateral confinement. Above the crown, a localized increase in σ'_{xx} is observed, indicating stress transfer and the development of arching within the surrounding soil.

The longitudinal effective stress σ'_{yy} (Figure 3.8) shows a decrease ahead of the TBM face, reflecting longitudinal stress release induced by excavation and the absence of full face support. Near the shield-soil interface, localized variations are observed, associated with the interaction between the soil and the advancing shield. Behind the TBM, σ'_{yy} stabilizes at values lower than the initial state, indicating persistent excavation-induced unloading.

The vertical effective stress σ'_{zz} (Figures 3.9 and 3.10) shows, after TBM passage, a decrease around the tunnel, with lower stresses near the crown and in the vicinity of the tunnel due to excavation-induced unloading.

Remark. Local irregularities observed near the excavation boundary are mainly attributed to the mesh resolution at the TBM shield interface. These effects are discussed in Section 4.1.2, with examples provided in Figures 4.3 and 4.7. They could be mitigated by adopting adaptive meshing strategies.

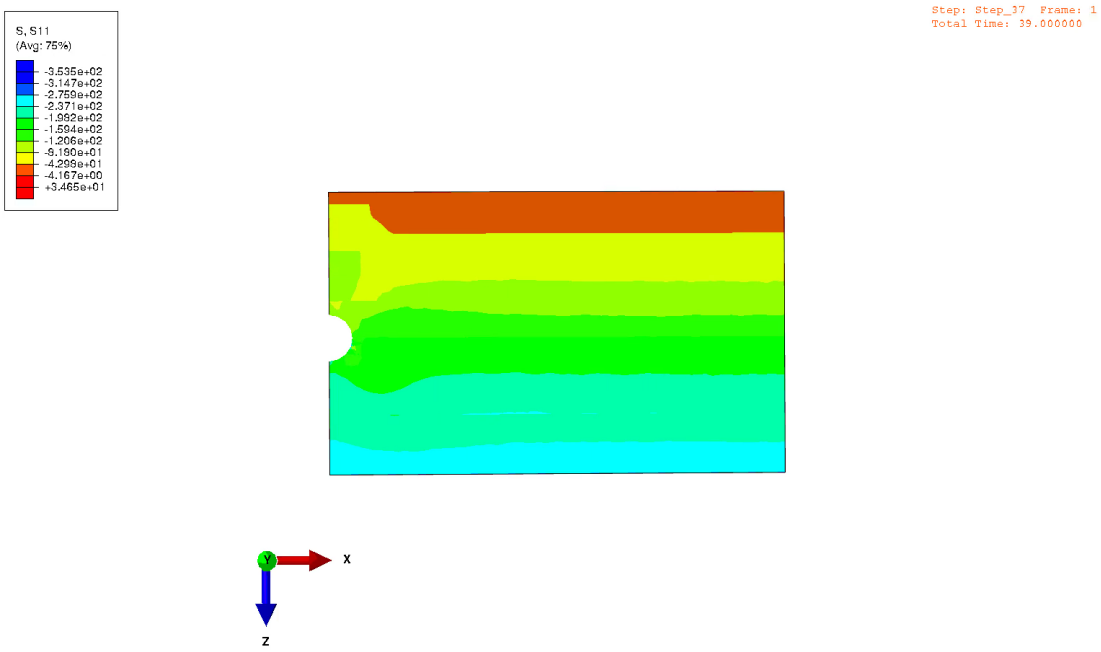

Figure 3.7: Horizontal effective stress σ'_{xx} (kPa) at Step 37, shown in a transverse section (Y = constant) after lining installation. Stress redistribution occurs around the tunnel, with a decrease near the springline and localized increases above the crown. Stratification and anisotropy effects remain visible across layers.

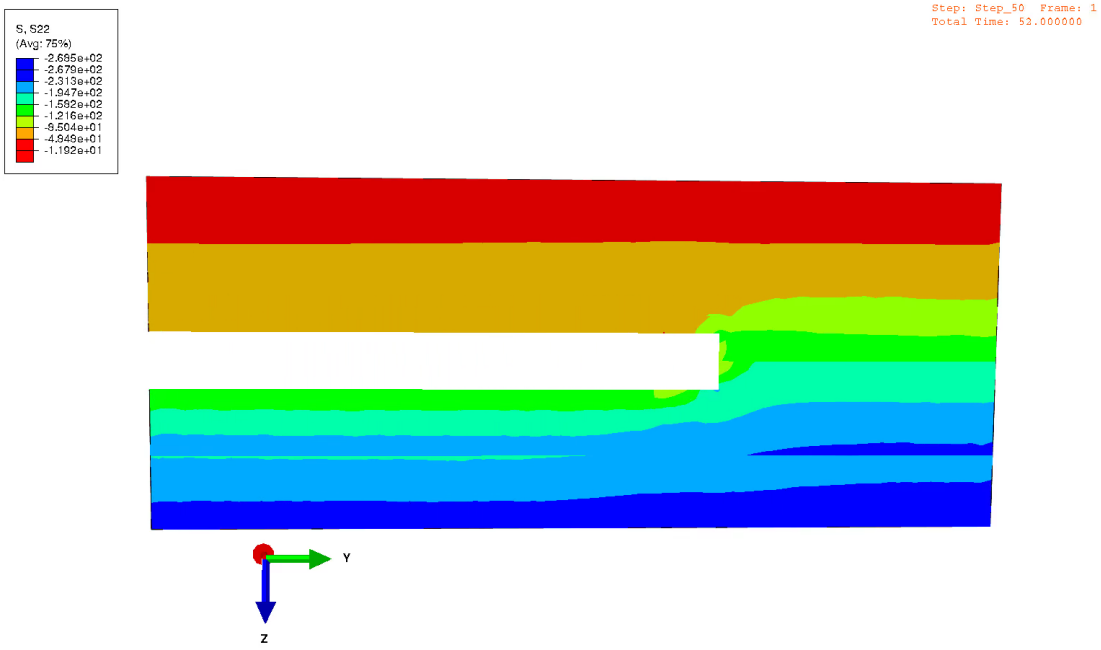

Figure 3.8: Longitudinal effective stress σ'_{yy} (kPa) at Step 50, shown in the longitudinal section ($X = 0$). A stress decrease is observed ahead of the TBM face, followed by localized variations near the shield-soil interface, particularly close to the crown and invert.

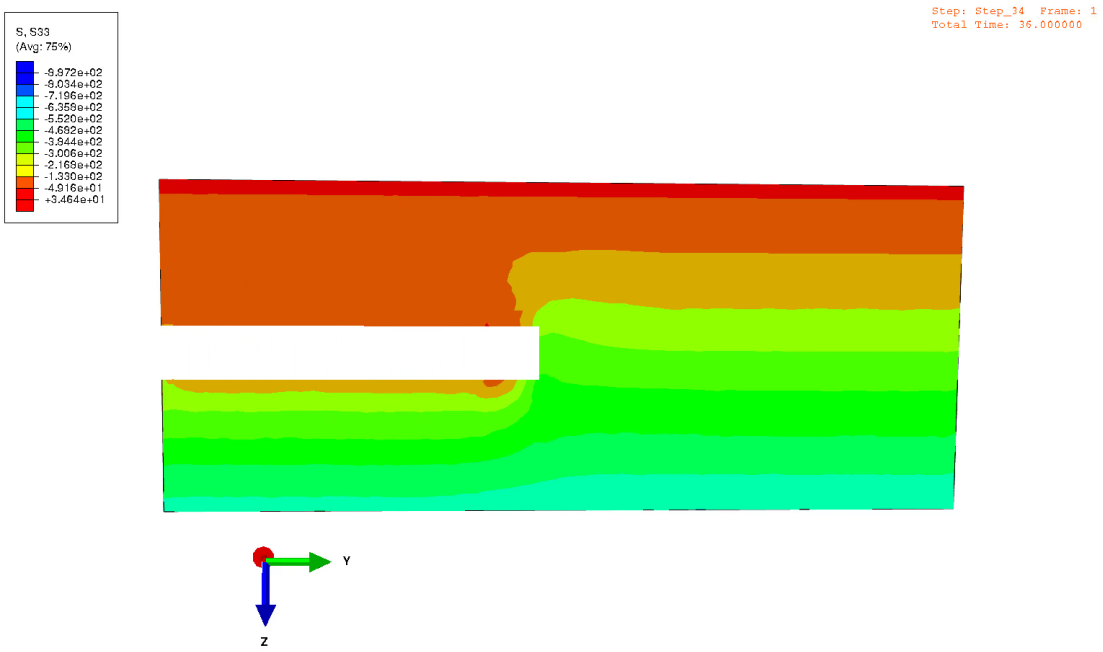

Figure 3.9: Vertical effective stress σ'_{zz} (kPa) at Step 34, shown in the longitudinal section ($X = 0$). A decrease in vertical stress is observed around the tunnel due to excavation-induced unloading.

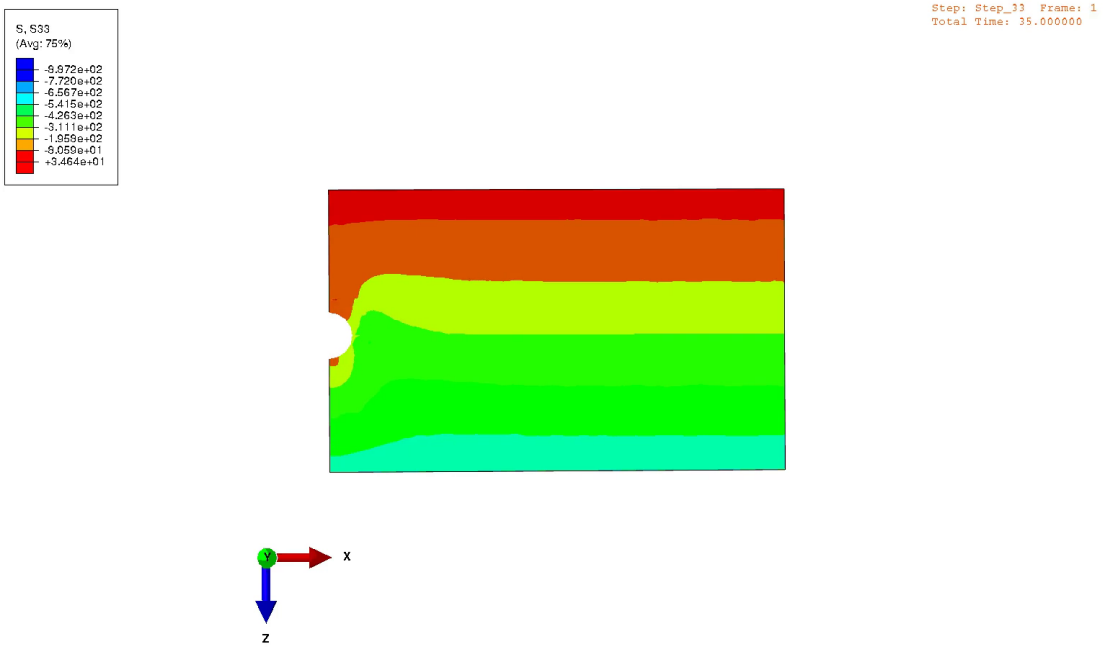

Figure 3.10: Vertical effective stress σ'_{zz} (kPa) at Step 33, shown in a transverse section (Y = constant) after lining installation. Reduced stresses near the crown and in the vicinity of the tunnel reflect excavation-induced unloading.

Remark. All effective stress components (σ'_{xx}, σ'_{yy}, σ'_{zz}) remain negative throughout the domain, confirming a fully compressive state consistent with gravity loading. Apparent tensile zones in the color plots are post-processing artefacts caused by interpolation near zero and autoscaling effects.

Overall, the results at this excavation stage reproduce the main features of TBM advancement: progressive soil deformation, stress redistribution, and excavation-induced unloading. Away from the tunnel, effective stresses follow a gravity-induced profile, modulated by stratification and initial anisotropy.

3.3 Computer code implementation

The 3D TBM excavation model introduced in the previous section is hereafter considered as a black-box numerical simulator. Its internal structure is not detailed; only the mapping between input variables and the resulting surface settlements is considered.

The simulator is treated as a deterministic mapping

$$f : \mathcal{X} \subset \mathbb{R}^d \to \mathbb{R}^q,$$

where $\mathbf{x}$ gathers the physical, operational, and geometrical input parameters, and $\mathbf{z} = f(\mathbf{x})$ denotes the corresponding vector of quantities of interest describing the settlement response.

In the following sections, the input and output variables used for further analyses are explicitly defined.

3.3.1 Input taxonomy

Following the taxonomy proposed in Blanchard et al. (2023), inputs can be grouped into four categories: (i) *modeling parameters*, related to discretization, solver settings, domain size, and modeling choices such as the soil constitutive law; (ii) *physical parameters*, which describe geological conditions (soil layering, hydromechanical properties), TBM, lining and grout mechanical properties, and soil-TBM interactions; (iii) *operational parameters*, describing the excavation scenario (TBM controls, advance rate); and (iv) *geometrical and fixed parameters*, which define the tunnel geometry, TBM design, and other project-specific features that remain constant.

These categories and their representative input variables are listed in Table 3.1.

In the following, we distinguish between two types of parameters. *Input parameters* encompass the physical, TBM operational, and geometrical quantities defining a simulation scenario, as detailed in Table 3.1. In contrast, *modeling parameters* refer to numerical and discretization choices that control the behavior of the simulator itself, such as mesh density, domain extent, or algorithmic settings. These are also reported in Table 3.1.

Remark. Accuracy is defined here as the sensitivity of simulation results to variations in modeling parameters. For instance, a simulation is considered accurate if the settlement response is relatively insensitive to changes in mesh density or domain size, indicating that numerical artefacts are minimal.

Table 3.1: Classification of input parameters according to the adopted taxonomy.

Category	**Typical parameters**
(i) Modeling parameters	Domain dimensions (width, length, depth), mesh densities (coarse and fine), excavation step length, solver settings, boundary conditions, numerical scheme (FD, FE, 2D, 3D), constitutive model choice.
(ii) Physical parameters	Soil properties (elastic modulus, Poisson's ratio, cohesion, friction angle, dilation angle, density, layer thickness, at-rest earth pressure coefficients K_{0x} and K_{0y}), hydraulic conditions (groundwater level, pore pressure distribution), grout properties (reference pressure, stiffness, hardening behavior), TBM-soil contact law parameters, and lining mechanical properties.
(iii) TBM operational parameters	Face pressure (reference pressure, vertical gradient), injected grout control (pressure, volume, vertical gradient), TBM advance rate, over-excavation ratio, and other process control variables defining the excavation scenario.
(iv) Geometrical and fixed parameters	Tunnel geometry (depth, diameter, slope), TBM structure (shield thickness, total length, face and tail diameters), lining behavior (thickness, stiffness, joint flexibility factor), and project-specific design parameters.

The next step is to define the prior space associated with each input parameter, i.e. its range of variation and probability distribution. The input vector $\mathbf{x} \in \mathcal{X} \subset \mathbb{R}^d$ gathers all input parameters, except modeling parameters, and defines a simulation case of the 3D TBM numerical simulator. The domain $\mathcal{X}$ reflects prior knowledge and engineering plausibility and defines the space over which sensitivity analysis is performed.

This domain is detailed in Appendix J, in Tables J.1-J.2.

3.3.2 Outputs of interest

After defining the input space, we now turn to the model outputs and the corresponding quantities of interest (QoIs). Surface settlements constitute the key observable for linking numerical simulations to field data in calibration and inversion analyses.

Following previous studies (Ochmański et al., 2018, 2020; Kavvadas et al., 2017; Lambrughi et al., 2012; Losacco and Viggiani, 2019), settlements in 3D simulations are typically analyzed along two orthogonal directions: the transverse axis (perpendicular to the tunnel axis) and the longitudinal axis (parallel to the tunnel axis).

In this work, a *monitored line* (ML) is defined at the ground surface, perpendicular to the tunnel axis. The ML is located at longitudinal position $y_{\mathrm{ML}} = \frac{L_t}{2}$, so that its coordinates in the global frame are $(x, y, z) = (x, y_{\mathrm{ML}}, 0)$, where x varies along the transverse direction and $z = 0$ corresponds to the ground surface (see Figure 3.1 in Chapter 3). For convenience, a translated coordinate system is introduced, with origin $O' = (0, y_{\mathrm{ML}}, 0)$, so that all results are expressed relative to the monitored line.

In this translated frame, the longitudinal coordinate becomes $\tilde{y} = y - y_{\mathrm{ML}}$, and displacement fields are therefore evaluated at coordinates $(x, \tilde{y}, z)$.

Then, at simulation step k, the vertical surface displacement along the monitored line ($\tilde{y} = 0$) is defined as

$$s_v(x; y_k) := u_z^{(k)}(x, 0, 0), \tag{3.2}$$

where $u_z^{(k)}(x, y, z)$ denotes the vertical component of the displacement field evaluated at point (x, y, z) at step k, and y_k denotes the position of the TBM face relative to the monitored line at step k.

The position of the TBM face relative to the monitored line (ML) at step k is defined as

$$y_k := k l_e - y_{\mathrm{ML}}, \tag{3.3}$$

where l_e is the excavation advance per step and y_{ML} is the longitudinal coordinate of the ML in the original frame. A negative value of y_k indicates that the TBM face is located upstream of the ML (pre-crossing phase), while a non-negative value indicates that it has passed the ML (post-crossing phase).

Equivalently, the settlement field can be written as a function of the TBM face position:

$$s_v(x; y_k) := u_z(x, 0, 0; y_k), \tag{3.4}$$

where y_k is the signed distance from the TBM face to the ML. This formulation facilitates direct comparison with monitoring data from surface sensors, typically installed at fixed transverse positions along the tunnel alignment.

Figure 3.11 illustrates the evolution of the settlement profile $s_v(x; y_k)$ along the ML for different TBM positions y_k, using the simulation dataset described in Section 3.2. The color map provides a global view of settlement evolution during excavation.

Remark: Examples of outputs extracted at the monitored-line (ML) mesh nodes are provided in Appendix K.

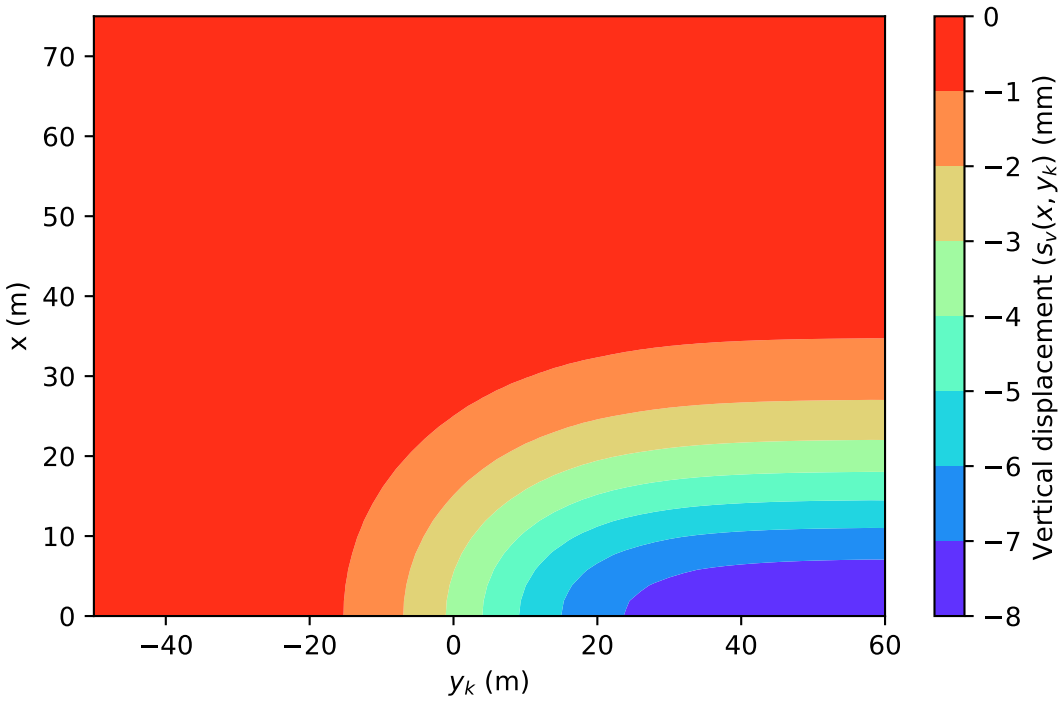

Figure 3.11: Evolution of the vertical surface settlement profile $s_v(x; y_k)$ along the monitored line for various TBM face positions y_k. The color map shows settlement magnitude as a function of transverse coordinate x and TBM position during excavation (relative to the monitored line).

The raw simulation outputs vary in size depending on the number of nodes, in the FE mesh along the monitored line, the transverse domain width X_{lim}, the mesh resolution, and the number of excavation steps. Although tunnel length, domain geometry, and meshing strategy are not systematically varied, they may change in specific studies dedicated to assessing the influence of modeling parameters. As a result, the settlement field $s_v(x; y_k)$ can differ in both resolution and spatial extent, making direct comparisons difficult. To enable consistent comparison across simulations and reduce output dimensionality, the full field $s_v(x; y_k)$ is summarized by a limited set of QoIs, whose construction is discussed in the next section.

3.3.3 Settlement QoIs

Different strategies can be used to reduce the number of output variables from numerical simulations. A first approach consists in extracting simple scalar descriptors from the displacement field, such as the maximum settlement, the trough width, or other statistical

measures (e.g., mean, standard deviation) (Mollon et al., 2013; Zhao et al., 2015; Liu et al., 2017). While this approach facilitates comparison between simulations, it may discard part of the spatial information contained in the original settlement field.

A second approach relies on dimensionality reduction techniques such as Principal Component Analysis (PCA) or Proper Orthogonal Decomposition (POD), which project the settlement fields onto a reduced basis. This method preserves global variability but results in abstract coordinates that are less directly interpretable from an engineering perspective.

In this work, a third and more interpretable strategy is adopted. The settlement field $s_v(x; y_k)$ is approximated by a parametric function fitted to each simulation output. The parameters of this function, which describe the main shape and amplitude characteristics of the settlement trough, constitute the set of QoIs. This approach maintains the physical meaning of the outputs while reducing their dimensionality, making it well suited for subsequent sensitivity or inversion analyses.

The following section presents the construction and validation of this parametric representation, and the selection of the most appropriate functional forms for both transverse and longitudinal settlement profiles.

Review of parametric models for settlement profile representation

To build a compact and interpretable representation of the simulated settlements, the two-dimensional settlement field is first assumed to be decomposable into independent transverse and longitudinal components. It is then expressed as the sum of a deterministic part $\bar{s}_v(x, y_k)$, represented by an empirical parametric model, and a residual term $\varepsilon(x, y_k)$ accounting for local discrepancies between the model and the numerical simulation. This can be written as

$$s_v(x, y_k) = \bar{s}_v(x, y_k) + \varepsilon(x, y_k) = s_{\max} s_v^{\mathrm{t}}(x) s_v^{\mathrm{l}}(y_k) + \varepsilon(x, y_k), \tag{3.5}$$

where $s_{\max}$ denotes the maximum surface settlement, and $s_v^{\mathrm{t}}(x)$ and $s_v^{\mathrm{l}}(y_k)$ are normalized functions describing the transverse and longitudinal shapes, respectively.

Remark. The parametric model (Eq. (3.5)) assumes a multiplicative separation between the transverse (x) and longitudinal (y) components of the settlement field. This separability assumption is empirical and is supported by the goodness-of-fit results reported in Table 3.3.

The next step consists in identifying suitable empirical forms for $s_v^{\mathrm{t}}(x)$ and $s_v^{\mathrm{l}}(y_k)$. To this end, several empirical formulations were reviewed from the literature, each describing the normalized shape of settlement profiles using a few physically interpretable parameters. Table 3.2 summarizes the most common expressions used in tunneling applications.

Selection of a parametric settlement model using numerical simulations

To compare the different parametric formulations, each two-dimensional candidate model was fitted to the settlement profiles produced by the numerical simulator, and its performance was evaluated according to several statistical criteria. The unknown parameters

Table 3.2: Normalized empirical settlement formulas for transverse and longitudinal profiles

Normalized Formula	Axis of Settlements	Reference
$e^{\frac{-(x-x_0)^2}{2i_x^2}}$	Transverse ($s_v^t(x)$)	Peck (1969)
$\frac{1}{1+\lvert\frac{x-x_0}{i_x}\rvert^b}$	Transverse ($s_v^t(x)$)	Celestino et al. (2000)
$e^{-\frac{1}{2}\left(\frac{\lvert x-x_0\rvert}{i_x}\right)^{1.5}}$	Transverse ($s_v^t(x)$)	Jacobsz et al. (2004)
$\frac{\eta}{(\eta-1)+e^{\alpha(\frac{x-x_0}{i_x})^2}}$	Transverse ($s_v^t(x)$)	Vorster et al. (2005)
$(1+(\frac{(x-x_0)}{i_x})^2)^{-5}$	Transverse ($s_v^t(x)$)	Wang et al. (2022)
$\frac{1}{1+e^{-\frac{(y-y_0)}{i_y}}}$	Longitudinal ($s_v^l(y)$)	–
$\int_{-\infty}^{y}\frac{1}{i_y\sqrt{2\pi}}e^{-\frac{(\eta-y_0)^2}{2i_y^2}}d\eta$	Longitudinal ($s_v^l(y)$)	Attewell et al. (1986)

Note: i_x and i_y are expressed in meters and represent characteristic influence lengths for the transverse and longitudinal profiles, respectively.

Table 3.3: Performance of fitted 2D settlement models: combinations of transverse and longitudinal formulas, with number of parameters and R^2 statistics over 366 simulations.

Transverse	Longitudinal	# Param.	# Sim. $R^2 < 0.99$	R^2 (5%)
Peck (1969)	Sigmoid	4	65	0.9782
Celestino et al. (2000)	Sigmoid	5	23	0.9881
Jacobsz et al. (2004)	Sigmoid	4	39	0.9832
Vorster et al. (2005)	Sigmoid	6	22	0.9896
Wang et al. (2022)	Sigmoid	4	35	0.9834
Peck (1969)	Attewell et al. (1986)	4	328	0.4965
Celestino et al. (2000)	Attewell et al. (1986)	5	291	0.4964
Jacobsz et al. (2004)	Attewell et al. (1986)	4	302	0.4967
Vorster et al. (2005)	Attewell et al. (1986)	6	287	0.5103
Wang et al. (2022)	Attewell et al. (1986)	4	303	0.4969

of $\bar{s}_v(x, y_f)$ (see Table 3.2) were estimated from $s_v(x; y_k)$ using nonlinear least squares (`curve_fit` function in `SciPy` (Virtanen et al., 2020)).

These include: (i) the number of simulations with a coefficient of determination $R^2 < 0.99$; (ii) the 5th percentile of the R^2 distribution, used to assess robustness in the presence of low-quality fits; and (iii) the total number of parameters required by each model.

For this analysis, a dataset of 366 simulated settlement profiles was used, generated by the numerical simulator described in Section 4.2.2 of the Chapter 4 (see Appendix J for the corresponding input parameters).

Table 3.3 summarizes the results in terms of fitting accuracy and model complexity.

Results show that the sigmoid function provides a better representation of longitudinal settlements than the normal cumulative distribution function (CDF) proposed by Attewell et al. (1986). For the transverse direction, the formulation of Vorster et al. (2005) offers the highest fitting quality but requires six parameters. The model by Wang et al. (2022) achieves comparable accuracy with only four parameters, offering a better trade-off between precision and simplicity.

Remark. A similar analysis, focused on longitudinal settlements, was performed on monitoring data in Chapter 5.

Remark. The Gaussian profile proposed by Peck (1969) is widely used in tunneling

practice to represent transverse surface settlements; however, in the present study, it provides a less accurate fit to the settlement shapes obtained from the numerical simulations.

Selected parametric model for the settlement profile

The comparison metrics summarized in Table 3.3 and the histogram of R^2 values in Figure 3.12 show that, among the tested formulations, the combination of the transverse model proposed by Wang et al. (2022) and a sigmoid function for the longitudinal direction provides the best compromise between accuracy and simplicity.

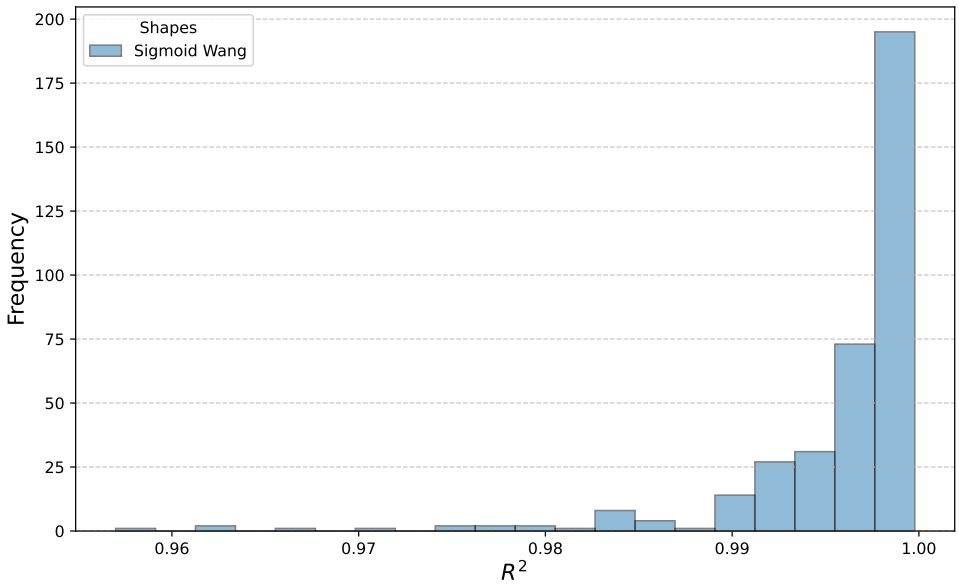

Figure 3.12: Histogram of R^2 values resulting from fitting the settlement profile using the proposed parametric model (see (3.5)) to 366 simulation cases.

The corresponding parameterized form is

$$\bar{s}_v(x; y_k) = s_{\max} \left(1 + \left(\frac{x}{r_0}\right)^2\right)^{-5} \frac{1}{1 + \exp\left(-\frac{y_k - y_0}{i_y}\right)}, \tag{3.6}$$

where $s_{\max}$ is the maximum settlement, r_0 the transverse radius of influence, y_0 the longitudinal inflection point, and i_y a characteristic slope controlling the transition from pre- to post-crossing phases. At $y_k = y_0$, the derivative of the longitudinal function satisfies

$$\frac{\mathrm{d}s_v^{\mathrm{l}}}{\mathrm{d}y_k}(y_0) = \frac{1}{4i_y},$$

Parameter i_y controls the steepness of the transition from pre-crossing to post-crossing phases. Figures 3.13 and 3.14 illustrate these two normalized components of the model, namely the longitudinal ($s_v^l(y_k)$) and transverse ($s_v^t(x)$) settlement profiles.

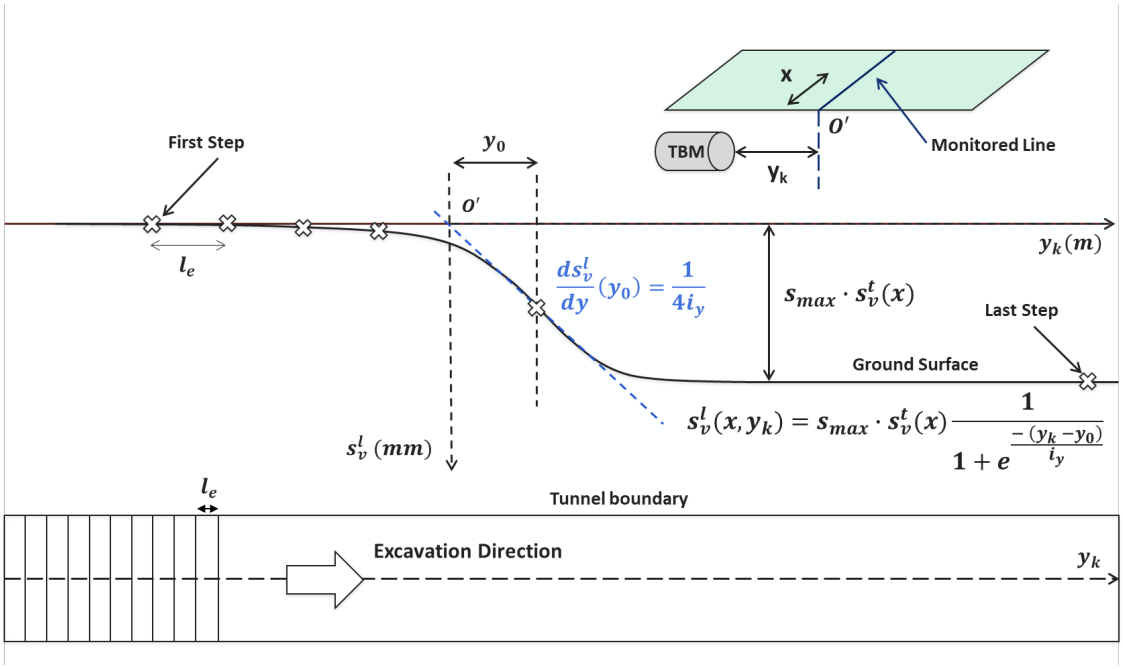

Figure 3.13: Longitudinal settlement profile. The vertical displacement at the monitored line is plotted as a function of the TBM face position y_k relative to the ML. The observed profile follows a sigmoid shape: before passage ($y_k \ll 0$), settlements are near zero; after passage ($y_k \gg 0$), they reach a plateau. The curve is parameterized by its inflection point y_0, its steepness i_y, and an amplitude $s_{\max} s_v^t(x)$, which depends on the transverse location x.

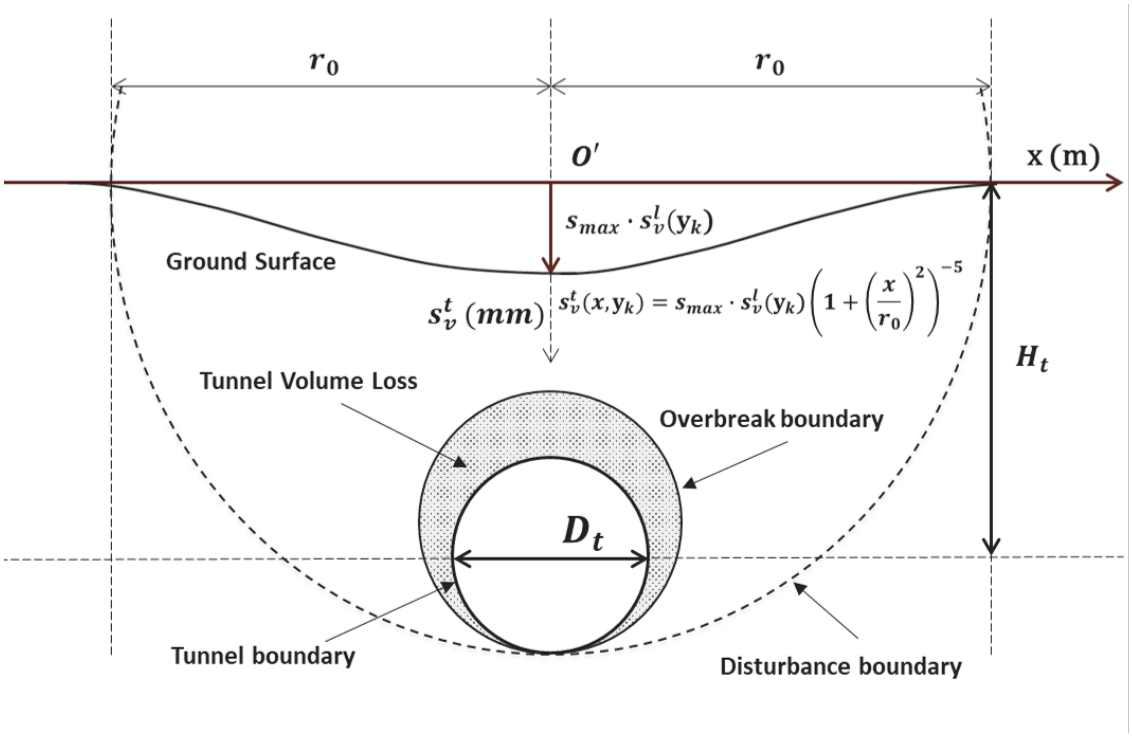

Figure 3.14: Transverse settlement profile. For a fixed TBM position y_k, the transverse surface displacements along x (OX direction) are modeled using Wang's formula Wang et al. (2022), with r_0 representing the radius of influence. The normalized transverse shape $s_v^t(x)$ is scaled by the longitudinal factor $s_v^l(y_k)$, which captures the evolution of settlements during excavation.

3.4 Chapter conclusions

In this chapter, a 3D FE simulator of TBM excavation in stratified soil layers was presented. The excavation process is modeled step-by-step, including face pressure application, soil-TBM interactions, lining installation, and grout injection and hardening. The simulator outputs full 3D displacement and stress fields, from which surface settlements are extracted along a monitored line perpendicular to the tunnel axis.

The simulator is then considered as a black-box function mapping input parameters to settlement-related QoIs, as illustrated in Figure 3.15. The input parameters are summarized in Table 3.1, while detailed parameter values required for a single simulation are provided in Tables J.3, J.1, and J.2 (in Appendix J).

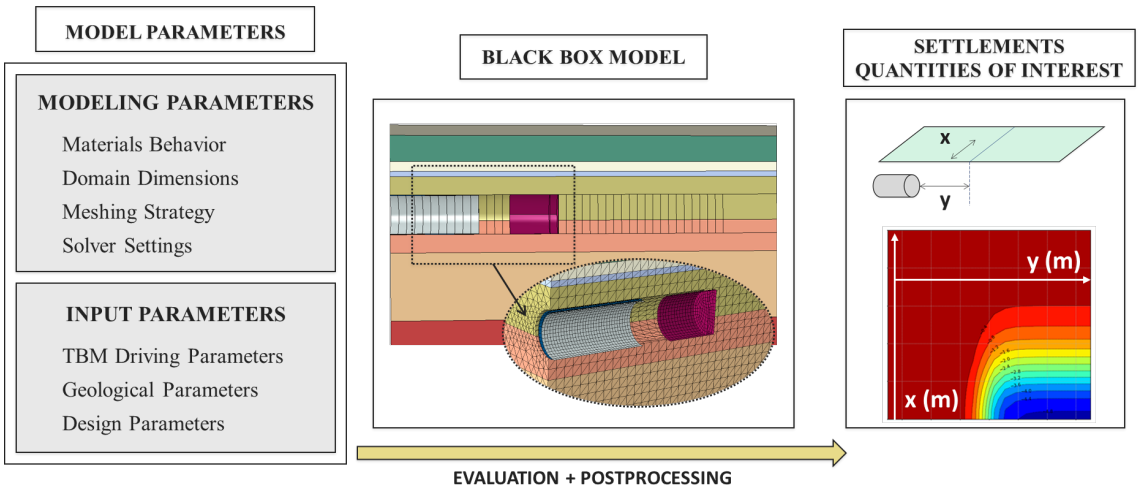

Figure 3.15: Black-box representation of the 3D TBM excavation simulator. For each input vector (geological parameters, TBM control variables, and design features), the simulator produces settlement-related QoIs obtained from a parametric fit of the surface settlement field. Modeling parameters such as domain size and mesh resolution are not included in the input space, but are treated as numerical configuration parameters.

After investigating several parametric formulations for the settlement profile, a compromise between model complexity and fitting accuracy is selected. The retained formulation combines Wang's transverse settlement model with a sigmoid longitudinal function, as defined in Eq. (3.6).

Each simulation output is then summarized by a vector of fitted parameters,

$$\mathbf{z} = (z_1, z_2, z_3, z_4) := (s_{\max}, r_0, i_y, y_0),$$

which defines the four QoIs used in the subsequent analyses (Table 3.4).

Based on this simulator setup, various analyses can now be performed to investigate the influence of input parameters on settlement behavior and to enable model calibration against field data. Before conducting such analyses, it is necessary to identify suitable modeling parameters governing both the accuracy and the computational cost of the FE

Table 3.4: QoIs extracted from the fitted settlement profile

Vector Component	Symbol	Unit	Description
z_1	$s_{\max}$	mm	Maximum surface settlement
z_2	r_0	m	Radius of transverse influence
z_3	i_y	m	Steepness of the longitudinal profile at the inflection point
z_4	y_0	m	Position of the longitudinal inflection point

simulations. These parameters control the discretization resolution and the spatial extent of the geological domain, which must be sufficiently large to limit artificial boundary effects.

The next chapter introduces a systematic approach, referred to as the *Accuracy-Cost Model Reduction* (ACMR), designed to determine an appropriate numerical configuration while maintaining a balance between computational efficiency and numerical accuracy.

A sensitivity analysis is then performed to identify the most influential input parameters affecting settlement behavior, allowing a reduction of model complexity and facilitating subsequent analyses such as calibration.

Chapter 4

Parameter influence analysis of the 3D TBM excavation model

Chapter overview. The 3D TBM simulator introduced in Chapter 3 is used here to analyse the influence of input parameters on the predicted surface settlements. The simulator is computationally expensive and involves many uncertain inputs, which motivates a sensitivity analysis prior to any direct calibration. First, an Accuracy-Cost Model Reduction (ACMR) approach is introduced to identify numerical settings that balance discretization error and computational cost. A simulation dataset is then generated using this reduced configuration, and a Gaussian process (GP) metamodel is constructed to approximate the mapping between inputs and settlement-related quantities. Finally, Sobol' indices are computed from the metamodel to quantify parameter influence at a reduced computational cost.

4.1 Accuracy-cost model reduction

Running a three-dimensional FE simulation requires defining several modeling parameters related to boundary conditions, mesh resolution, and solver settings. In geomechanical applications, numerical estimates are affected by several sources of error: (i) artificial boundary effects due to the finite domain size, (ii) discretization errors related to mesh density, and (iii) constitutive model formulation and its numerical implementation. These factors jointly influence the predicted mechanical response of the ground.

In tunneling simulations, numerical effects can significantly influence the computed quantities of interest (QoIs), defined in Table 3.4 (Section 3.3), even when apparently conservative configurations are used (for instance, a large domain but a coarse mesh).

In this section, we focus on the first two sources of error: boundary effects and discretization errors. These sources directly affect the accuracy of settlement estimates and computational cost, yet do not have a direct physical meaning.

Specifically, we investigate the influence of domain dimensions that control the geological model size in the transverse (X_{lim}), longitudinal (Y_{lim}), and vertical (Z_{lim}) directions, as well as the excavation length (L_t), which determines the number of excavation steps and helps limit longitudinal boundary effects.

In addition, two meshing parameters (α_{fine}, α_{coarse}) are considered to control the mesh density near the tunnel and in the far field, respectively (see Figure 3.1).

Increasing the domain dimensions, refining the mesh, or extending the tunnel length generally improves the physical accuracy of the numerical estimates. A larger domain reduces boundary effects, while a finer mesh provides a better approximation of the continuum. However, these improvements also come with longer computation times and greater memory requirements.

In current tunneling practice, modeling parameters such as domain size are typically selected based on engineering judgment or on general guidelines available in the literature (see Section 2.2.2 in Chapter 3). Only a few studies have explicitly quantified their impact on simulation accuracy or computational cost (Miro et al., 2014; Zhao et al., 2015).

Illustration of numerical effects: In FE modeling, it is common to assess the impact of modeling parameters through a one-at-a-time (OAT) analysis. Starting from a high-fidelity reference configuration (large domain, refined mesh), each parameter is varied independently while keeping the others fixed, enabling the evaluation of its influence on the QoIs.

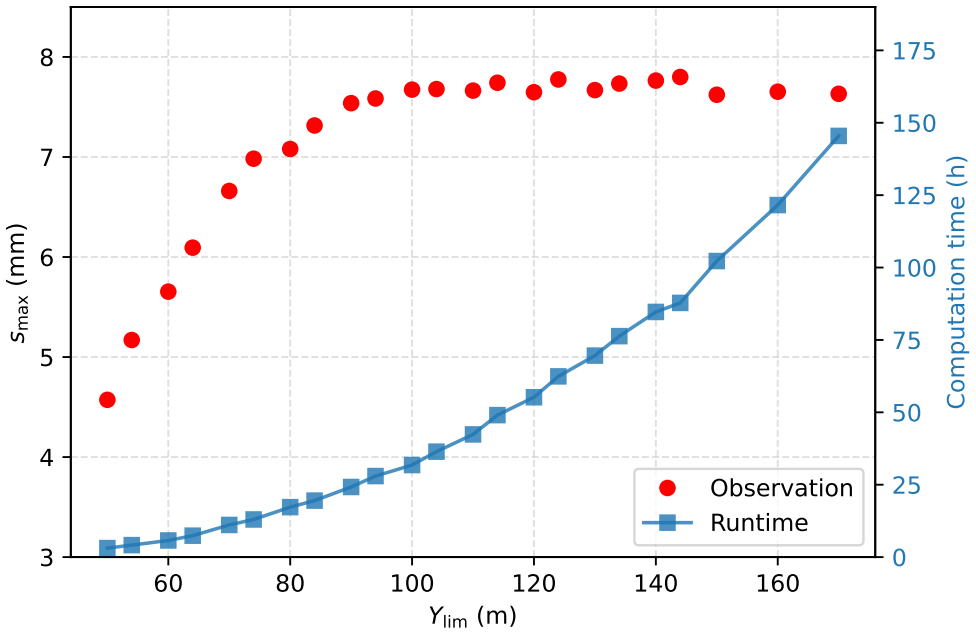

Figure 4.1: Illustrative OAT analysis of the effect of the lateral domain extent Y_{lim} on the maximum surface settlement s_{max}. As Y_{lim} decreases, boundary effects increase and settlement predictions deviate from the reference value, while computation time decreases. Red scatter points represent simulation results $(Y_{\text{lim}}, s_{\text{max}})$ for different domain extents, while blue points indicate the corresponding computation times in hours.

Figure 4.1 illustrates this approach by showing the influence of the lateral domain extent Y_{lim} on the maximum surface settlement s_{max}. As expected, smaller domain extents

amplify boundary constraints, increasing numerical artefacts and altering the estimated settlements, while simultaneously reducing computation time. The relationship between $s_{\max}$ and $Y_{\lim}$ appears to follow an exponential decay.

During the parametric study conducted to identify mesh and domain configurations that balance numerical accuracy and computational cost, it appears that the reference high-fidelity configuration does not fully eliminate discretization effects.

To exploit the simulation results obtained in this parametric study and estimate an ideal reference solution, the Accuracy-Cost Model Reduction (ACMR) methodology is introduced. Within this framework, an empirical numerical error model is defined and fitted using the available simulation data. This calibration enables the extrapolation of an ideal reference, which is not accessible in practice, against which candidate numerical configurations are compared to identify the best compromise between accuracy and computational cost.

4.1.1 ACMR framework

The ACMR approach is inspired by verification principles originally developed for verification and validation (V&V) in computational fluid dynamics (CFD) (Roy and Oberkampf, 2011), notably Roache's Grid Convergence Index (GCI) (Roache, 1994), to quantify numerical artefacts in soil mechanics. Our adaptation, referred to as the ACMR framework, consists of seven steps, presented below.

Step 1: Large-domain reference model. We start from a large-domain reference configuration $M_{\text{large_ref}}$, chosen with margins on all domain dimensions that are several times larger than the observed settlement extent, and with the finest mesh that fits in memory. This corresponds to the high-cost model that would be used without ACMR.

Step 2: Controlled variation of modeling parameters. From $M_{\text{large_ref}}$, we reduce domain dimensions one at a time while keeping all other parameters fixed. For each reduced domain, the mesh density is varied in the vicinity of that of $M_{\text{large_ref}}$; smaller domains allow us to test finer discretizations within the same computer memory limit.

Step 3: Multi-fidelity error modeling. The variations in domain dimensions and mesh densities from Step 2 produce a collection of simulator evaluations at multiple resolutions and domain sizes. We interpret these configurations as different "fidelity levels" in the sense that they have different numerical error magnitudes with respect to the (unknown) continuum solution.

To relate the QoI z to the modeling parameters, we assume that the two main sources of error act independently and additively on the asymptotic value z_∞ reached for an infinitely fine mesh in an infinite domain. Possible interaction effects between truncation and discretization errors are therefore neglected

The discretization error is modeled by a power law in the element size, following Richardson extrapolation

$$\Delta z_{\text{mesh}}(h) = C_h h^{p_h}, \tag{4.1}$$

where h denotes the element size, C_h is a constant, and $p_h > 0$ is the apparent order of convergence. This choice is consistent with grid convergence theory, (Roache, 1994), where the apparent order of convergence p_h depends both on the interpolation order of the FE discretization and on the regularity of the solution.

Remark. In the remainder of this chapter, mesh refinement is parameterized through the surface node densities α_{fine} and α_{coarse}. These quantities are defined as inverse measures of the characteristic element size, such that $\alpha \propto \frac{1}{h}$. Consequently, increasing α corresponds to mesh refinement (smaller element size and higher node density), whereas decreasing α leads to a coarser discretization.

The boundary truncation error is modeled by an exponential decay with respect to a distance L between the excavation and the domain boundary,

$$\Delta z_{\text{bound}}(L) = C_L \exp\big(-\frac{L}{L_0}\big), \tag{4.2}$$

where L_0 denotes a characteristic boundary extent beyond which further increases in the domain size have a negligible effect on the solution. The exponential decay reflects the attenuation of stress and displacement fields away from the excavation. This functional form is motivated by (i) analytical solutions (Loganathan and Poulos, 1998; Serratrice and Magnan, 2002) and (ii) the OAT sensitivity analysis illustrated in Figure 4.1.

Assuming four independent domain dimensions $(X_{\text{lim}}, Y_{\text{lim}}, L_t, Z_{\text{lim}})$ and two independent mesh sizes $(h_{\text{fine}}, h_{\text{coarse}})$, the combined error model is expressed as the sum of boundary truncation errors associated with each domain dimension (Eq. (4.2)) and mesh discretization errors associated with each mesh size (Eq. (4.1)), and reads:

$$z(\mathbf{L}, \mathbf{h}) = z_\infty + \sum_{i=1}^{4} C_{L_i} \exp\left(-\frac{L_i}{L_{i,0}}\right) + \sum_{j=1}^{2} C_{h_j} h_j^{p_{h_j}}. \tag{4.3}$$

The parameters $(z_\infty, C_{L_i}, L_{i,0}, C_{h_j}, p_{h_j})$ are identified separately for each QoI by nonlinear least squares fitting to the dataset from Step 2 (Virtanen et al., 2020). This parametric form is an adaptation of the framework of Roache (1994) for grid convergence and domain independence, extended here to multiple independent domain dimensions and separate refined and coarse mesh zones.

Step 4: Virtual high-fidelity model. From the fitted model (4.3), the asymptotic value z_∞ is extracted for each QoI. These asymptotic values correspond to the limit of infinite mesh density and very large domain dimensions. Their collection defines a *virtual* high-fidelity configuration M_∞, which is not computable in practice but serves as a reference in the sense of Roache's Grid Convergence Index methodology.

Step 5: Error computation. The error associated with a configuration $(\mathbf{L}, \mathbf{h})$ is defined with respect to z_∞ as

$$\varepsilon(\mathbf{L}, \mathbf{h}) = |z(\mathbf{L}, \mathbf{h}) - z_\infty|. \tag{4.4}$$

Errors are computed for each QoI and aggregated using the ℓ_1 norm. This approach is consistent with established verification practices (Roache, 1994; Roy and Oberkampf, 2011).

Step 6: Accuracy-cost trade-off. Each configuration is evaluated in terms of error, measured with respect to the reference solution M_∞, and computational cost (wall-clock time). Plotting error against runtime enables a direct comparison between configurations. The Pareto front corresponds to the set of configurations that achieve the best compromise between accuracy (error minimization) and computational cost (runtime).

Step 7: Selection of baseline configuration. From the Pareto set, we select a configuration that achieves a low error relative to M_∞ while satisfying practical runtime constraints. This configuration is adopted as the baseline for all subsequent GP metamodel construction and GSA (Section 4.2.1).

Remark. While our procedure is conceptually related to multi-fidelity optimisation strategies (e.g., Stroh et al., 2022), we do not combine several fidelity levels in a single metamodel. Instead, we first identify an accuracy-cost-optimal single-fidelity configuration and then train GP metamodels on this fixed setup (see Appendix L for further details). Alternative error modeling approaches include Bayesian extrapolation methods such as GP regression (Bect et al., 2021; Oates et al., 2025), which offer a probabilistic description of numerical errors.

4.1.2 ACMR results

Following the ACMR procedure detailed below, we apply this framework to the case study introduced in Section 3.2, in order to assess the influence of modeling parameters on the QoIs defined in Section 3.3.3.

We apply the first step of the ACMR framework by defining a large-domain configuration $M_{\text{large_ref}}$ identical to that adopted in Section 3.2. The second step is then applied by varying $(X_{\text{lim}}, Y_{\text{lim}}, Z_{\text{lim}}, L_t, \alpha_{\text{fine}}, \alpha_{\text{coarse}})$ over the ranges listed in Table J.3, thereby generating a dataset of 69 simulations. Here, the parameters α_{fine} and α_{coarse} denote the surface node densities of the mesh in the near-tunnel and far-field zones, respectively.

Remark. In this section, the regression is performed in terms of the mesh densities α_{fine} and α_{coarse}, whereas the theoretical formulation of the discretization error is expressed in terms of the characteristic element size h. The two parameterizations are related through $\alpha \propto 1/h$.

This dataset provides the input-QoI pairs required for error-model regression and enables the quantification of numerical errors relative to an inaccessible high-fidelity reference.

For each QoI, the multi-parameter model (4.3) is fitted by nonlinear least squares (Virtanen et al., 2020). A Huber loss is used for robustness to outliers; for z_2, a weighted ℓ_2 loss improves sensitivity to X_{lim} variations. The fitted models are then extrapolated to the asymptotic limit $z_{i,\infty}$, defining the *virtual* high-fidelity reference configuration M_∞ used for error computation.

Regression performance. Figure 4.2 compares the predicted errors obtained from the error model (Eq. (4.4)) with the simulated QoI errors with respect to M_∞. All QoIs achieve $R^2 > 0.9$ and low RMSE values, indicating that the model captures the dominant dependencies of the QoIs on domain size and mesh density.

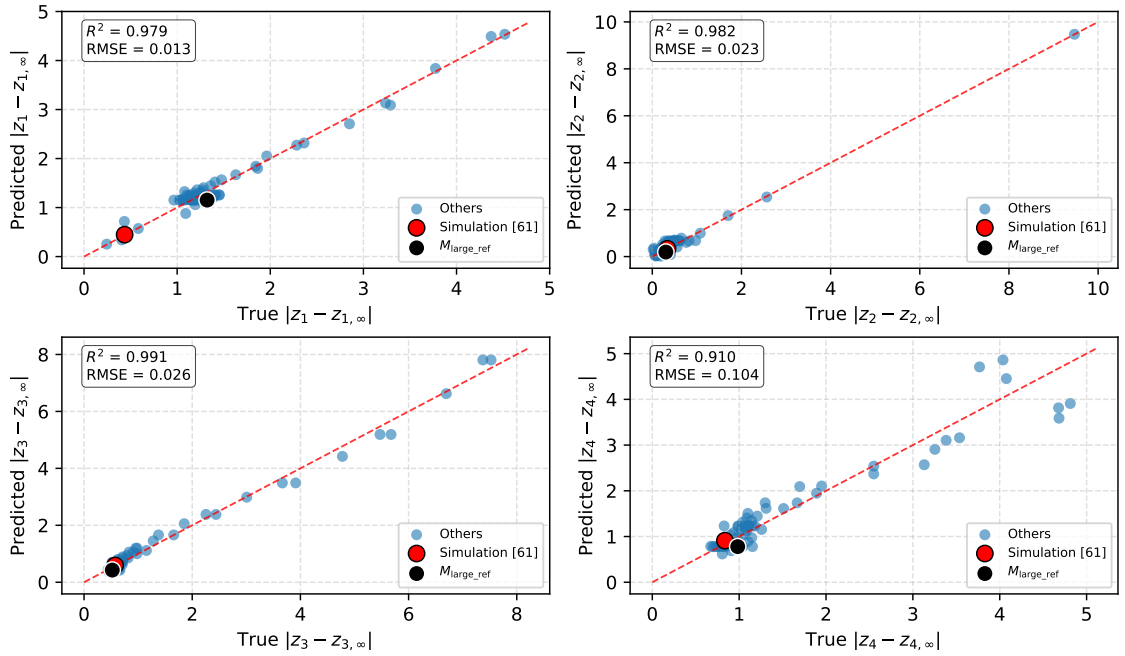

Figure 4.2: True vs predicted errors relative to M_∞ $|z_i - z_{i,\infty}|$ for the four QoIs. Red: model 61 (GP baseline), which shows lower errors than the large-domain reference $M_{\text{large_ref}}$ (black). Dashed line: perfect agreement. Reported R^2 and normalized RMSE indicate good predictive accuracy.

Figures 4.3–4.6 illustrate these dependencies for the different QoIs. For z_1 (maximum settlement), the error is primarily driven by L_t, Y_{lim}, and α_{fine}, with the accuracy stabilizing for $L_t > 80$ m and $\alpha_{\text{fine}} \gtrsim 1$ node/m^2. For z_2 (transverse influence radius), X_{lim} is the dominant parameter: values below $z_{2,\infty}$ lead to a sharp increase in error, while Z_{lim} has a secondary effect when reduced below approximately 15 m. For z_3 (longitudinal profile steepness at the inflection point) and z_4 (longitudinal inflection point position), the error is mainly controlled by L_t and Y_{lim}, with α_{fine} also influencing z_4.

Remark. In Figures 4.3-4.6, vertical alignments can be observed due to the OAT sampling strategy. For a fixed value of a given parameter, the remaining inputs vary, leading to multiple QoIs values for the same abscissa.

Pareto analysis and baseline selection. Using the fitted error models, absolute errors $|z_i - z_{i,\infty}|$ are computed for each configuration and combined with runtime to construct the accuracy-cost Pareto front (see Figure 4.7). As expected, heavily reduced models run faster but have higher errors, while high-fidelity configurations are accurate but slower. Applying QoIs-specific tolerances ($z_1 = 0.5$ mm, $z_2 = 1.0$ m, $z_3 = 1.0$ m,

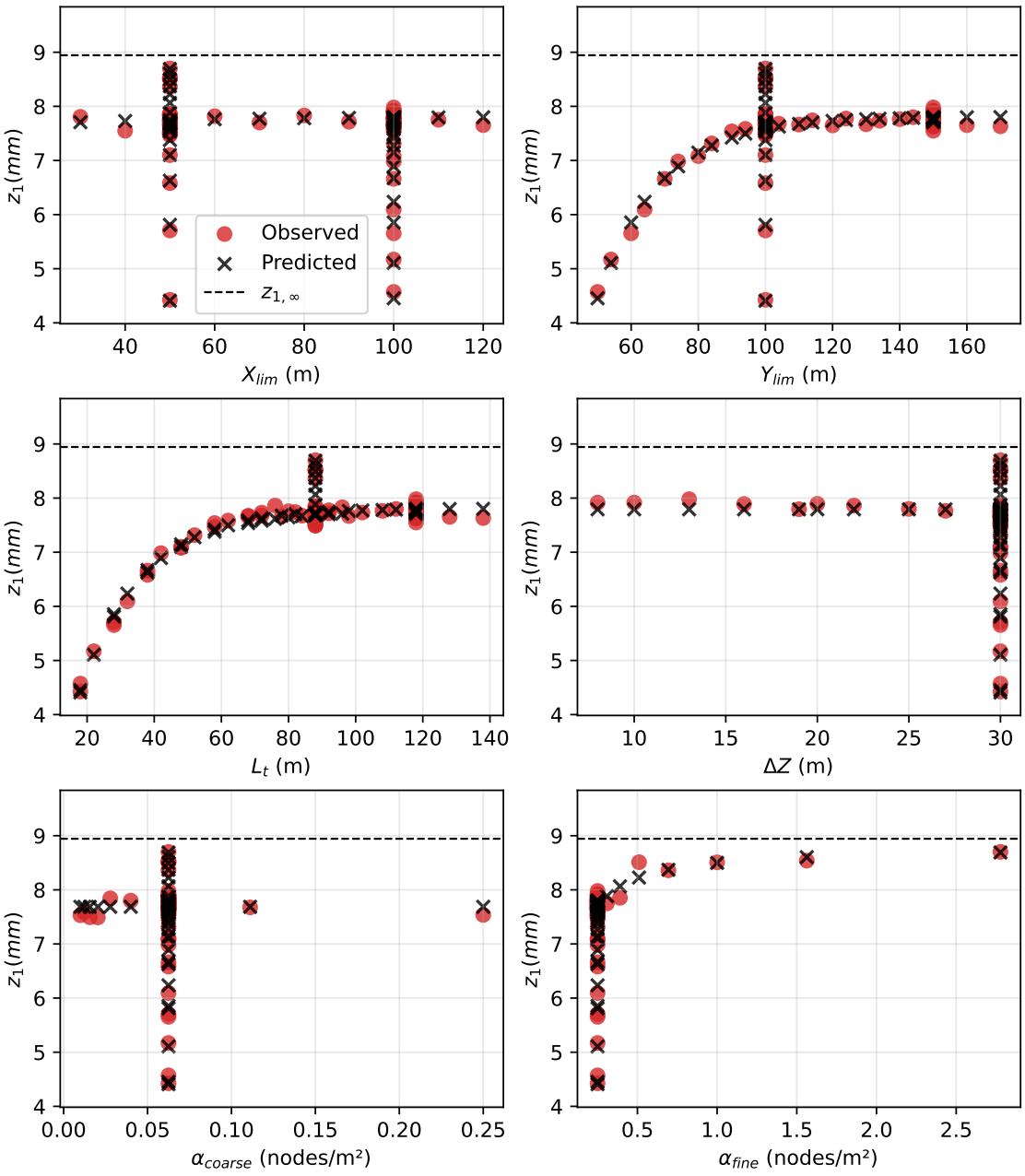

Figure 4.3: Model error surface response for z_1. Red points are simulation results, black crosses model predictions. The dashed line marks $z_{1,\infty}$. The largest-domain simulation does not converge to $z_{1,\infty}$, mainly due to coarse near-tunnel mesh. L_t, Y_{lim} and α_{fine} dominate the error; accuracy stabilizes for $L_t > 80$ m and $\alpha_{\text{fine}} \gtrsim 1$ node/m².

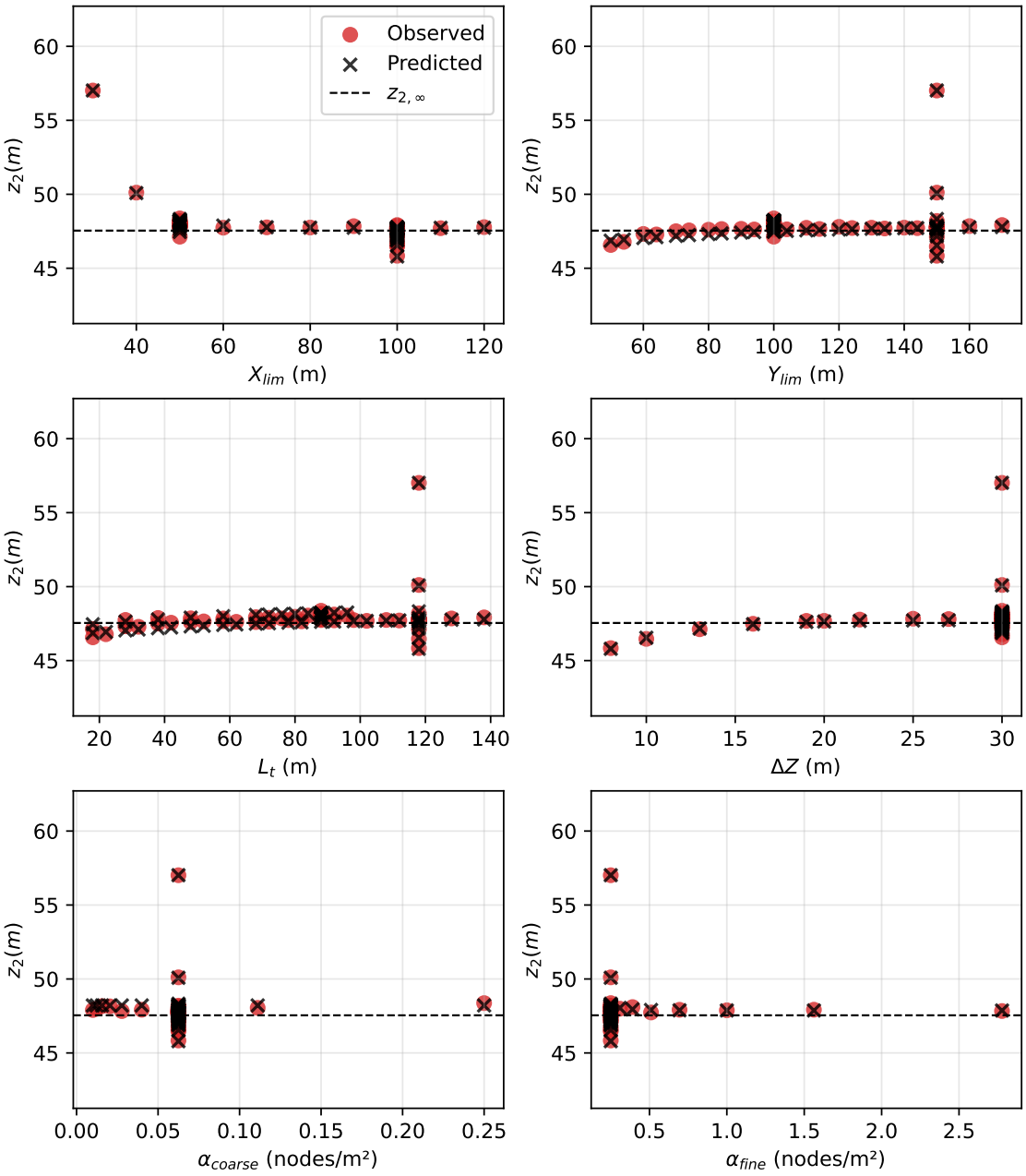

Figure 4.4: Model error surface response for z_2 (see Figure 4.3 for details). X_{lim} dominates the error: values below $z_{2,\infty}$ cause sharp increases. Z_{lim} (recall that $Z_{\text{lim}} = \Delta Z + H_t$) also has a secondary impact when reduced below approximately 15m.

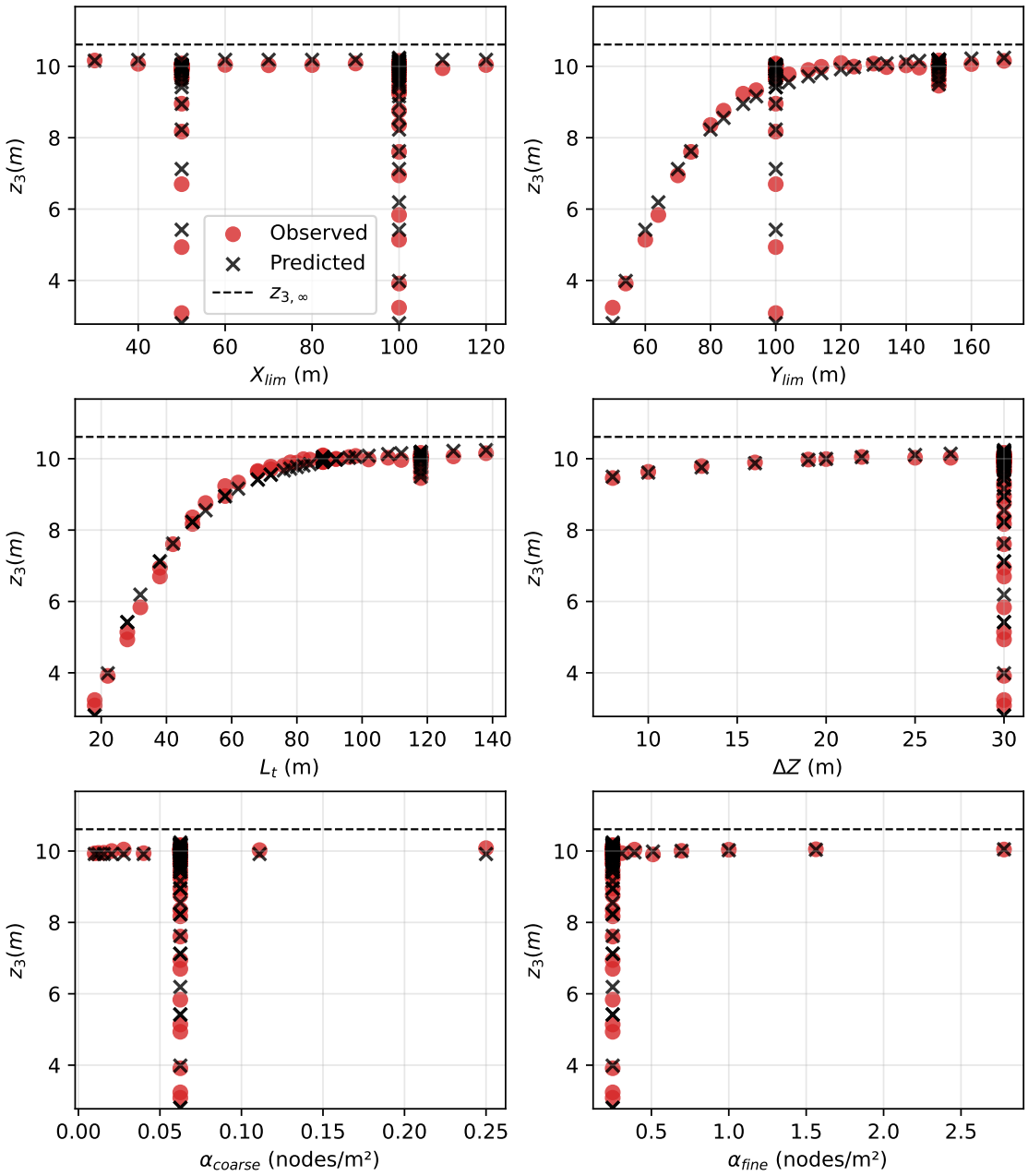

Figure 4.5: Model error surface response for z_3 (see Figure 4.3 for details). L_t and Y_{lim} dominate the error, with Z_{lim} (with $Z_{\text{lim}} = \Delta Z + H_t$) also contributing.

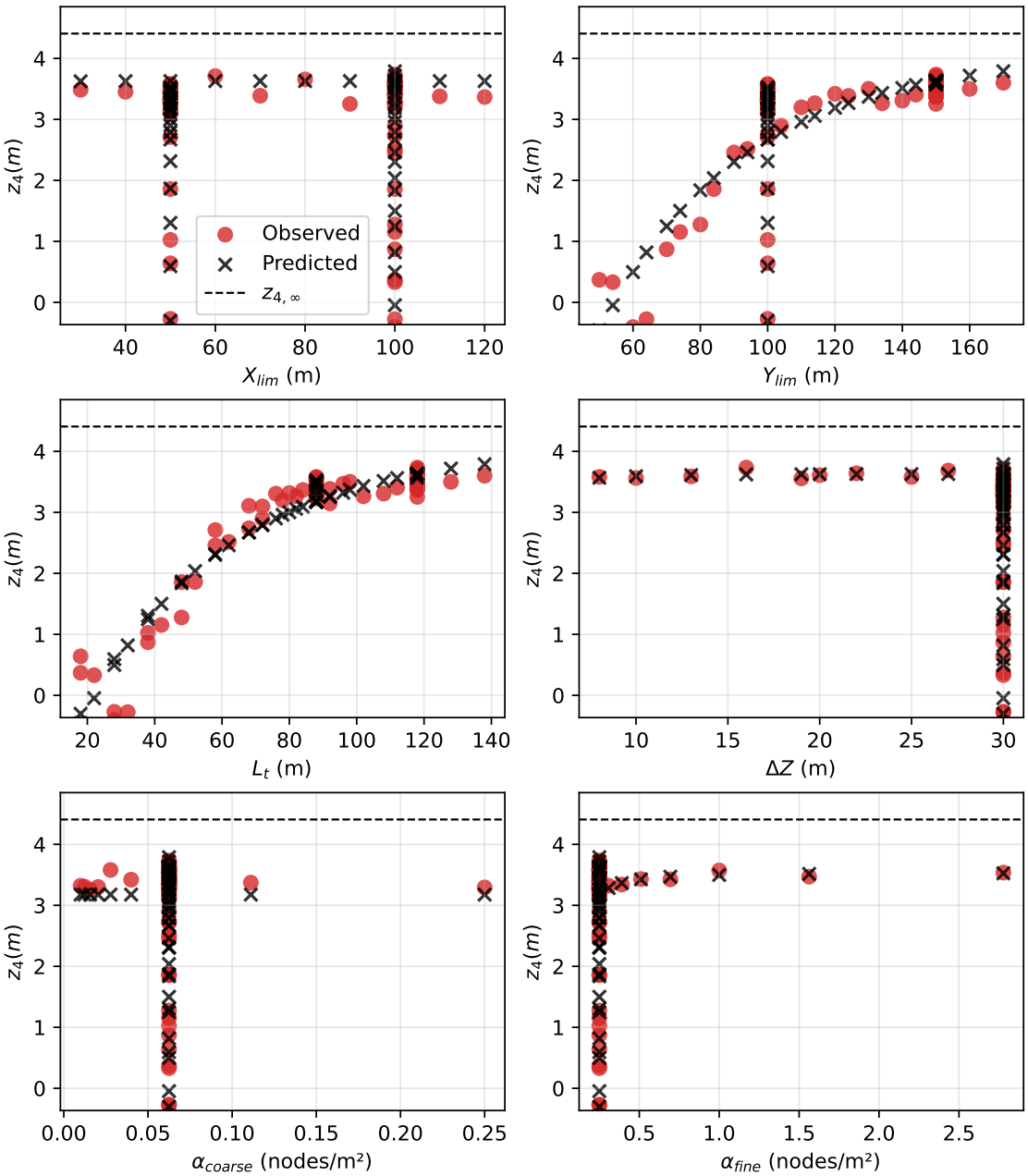

Figure 4.6: Model error surface response for z_4 (see Figure 4.3 for details). L_t and Y_{lim} dominate, with α_{fine} also influencing accuracy.

$z_4 = 1.0$ m) and a 40-hour runtime limit yields three acceptable configurations, namely, models 59, 60 and 61.

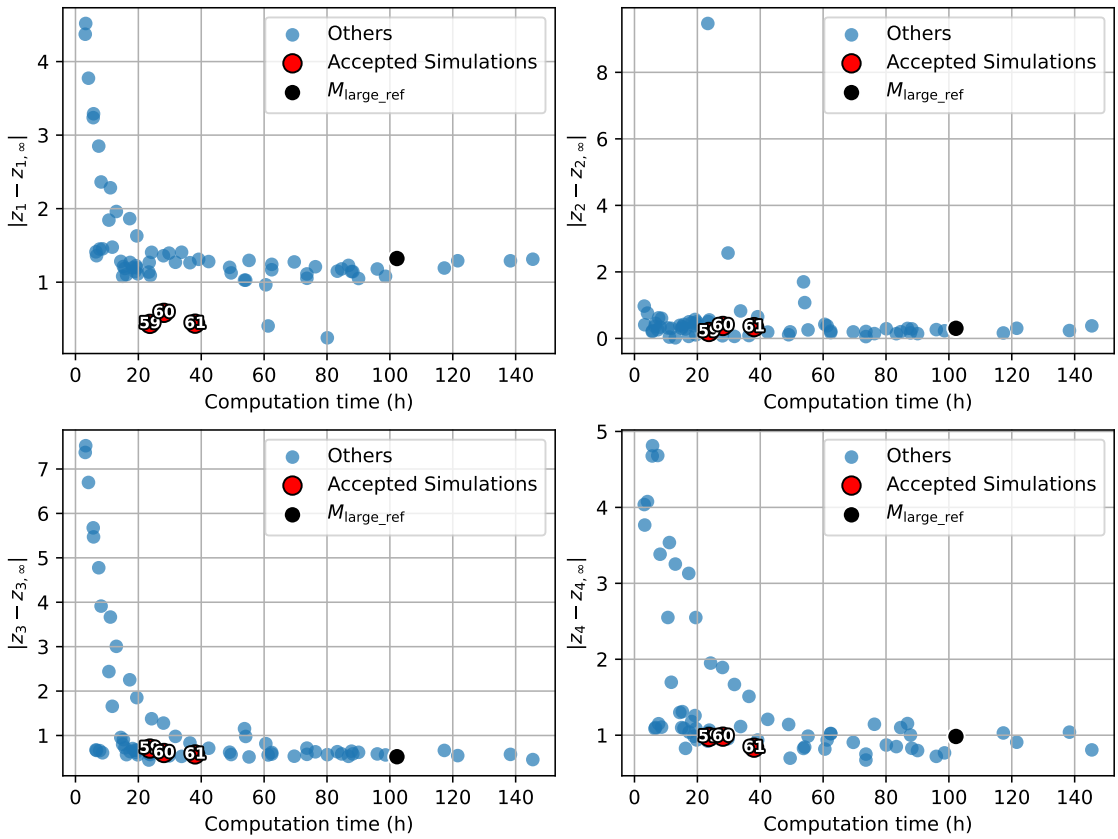

Figure 4.7: Pareto plot of runtime vs errors relative to M_∞ $|z_i - z_{i,\infty}|$ for the four QoIs (69 simulations). Applying thresholds $z_1 = 0.5$ mm, $z_2 = z_3 = z_4 = 1.0$ m and a 40 h limit selects three configurations (59, 60, 61), identical except for $\alpha_{\text{fine}} \in \{0.5, 0.7, 1.0\}$. Model 61 was chosen as the baseline to build the GP metamodel because it yields lower errors than $M_{\text{large_ref}}$ while keeping a reasonable runtime. See Figure 4.2.

Model 61 was retained as the baseline configuration. It increases X_{lim} to reduce geomechanical bias on z_1, while coarsening the far-field mesh to limit computational cost. This setup matches or exceeds the performance of $M_{\text{large_ref}}$ and is therefore used for all subsequent GP metamodeling and sensitivity analyses.

The reduced numerical configuration adopted for the following simulations is: $X_{\text{lim}} = 60$ m, $Y_{\text{lim}} = 100$ m, $Z_{\text{lim}} = 60$ m, $\Delta Y = 20$ m, $\alpha_{\text{fine}} = 1.0$ nodes/m^2, and $\alpha_{\text{coarse}} = 0.0625$ nodes/m^2.

4.2 Global sensitivity analysis using Gaussian process metamodels

Given the reduced numerical configuration obtained from the ACMR analysis (Section 4.1), we now turn to studying the influence of physical input parameters on the QoIs defined

in Table 3.4 (Section 3.3).

To study the influence of inputs, several approaches exist, ranging from local sensitivity analysis (LSA) to global sensitivity analysis (GSA) (Blanchard et al., 2023).

LSA evaluates how small perturbations in the inputs affect the outputs in the vicinity of a reference configuration. However, it is limited to local effects and depends on the chosen point of analysis.

This motivates the use of global sensitivity analysis (GSA), which quantifies the contribution of each input variable to the overall output variability across the entire input domain (Iooss and Lemaître, 2015).

GSA provides a global ranking of input importance and accounts for both individual and interaction effects, making it well-suited for complex, high-dimensional tunneling simulations.

However, because of the high computational cost of the 3D FE simulator and the large number of input parameters, performing GSA directly on the simulator is prohibitively expensive. To overcome this limitation, a metamodel can be used to approximate the simulator outputs. Each QoI is analyzed separately, and an independent metamodel can be constructed for each of them.

The following sections first introduce Sobol' indices as the chosen measure of input influence and the methodology used to perform uncertainty-aware GSA, based on Sobol' indices computed from GP metamodels.

Finally, we present and discuss the results, including GP construction and validation, Sobol' index estimation, and interpretation of the most influential parameters for model simplification and tunneling practice.

4.2.1 Uncertainty-aware GSA approach

GSA common practices in tunnels numerical modeling.

GSA aims to quantify how variations in the input parameters $\mathbf{x} = (x_1, x_2, \ldots, x_d)$ contribute to the variability of the QoIs.

Different GSA methods have been developed in the literature, including: (i) variance-based approaches such as Sobol' indices (Sobol', 1993; Saltelli, 2002); (ii) screening methods, notably the Morris method (Morris, 1991; Campolongo et al., 2007); (iii) spectral techniques such as the Fourier Amplitude Sensitivity Test (FAST) (Cukier et al., 1973; Saltelli et al., 1999); (iv) kernel-based dependence measures like the Hilbert-Schmidt Independence Criterion (HSIC) (Gretton et al., 2005); and (v) machine-learning-based approaches such as SHAP values derived from Shapley theory (Lundberg and Lee, 2017).

Among these, variance-based methods, and particularly Sobol' indices, are commonly used in geotechnical and tunneling applications because they provide an interpretable decomposition of output variance into main and interaction effects (Miro et al., 2014; Rohmer, 2014; Zhao et al., 2015; Liu et al., 2017; Noubissi et al., 2024). For this reason, Sobol' indices are adopted in this work.

Sobol' indices

Sobol' indices are among the most classical and widely used methods for GSA. The starting point is to adopt a probabilistic framework, where the input vector $\mathbf{x} = (x_1, x_2, \ldots, x_d)$ is treated as a set of independent random variables $\mathbf{X}$, and the output, previously denoted $\mathbf{z}(x_1, x_2, \ldots, x_d)$, is represented by a vector of random variables $\mathbf{Z}$. This perspective makes it possible to analyze how variability in the inputs propagates through the simulator and to measure the influence of each input on the outputs by decomposing the variance of a given QoI Z_i.

For a QoI Z_i with $\mathbb{V}[Z_i] > 0$, the *first-order Sobol' index* $S_j^{(i)}$ measures the fraction of variance of Z_i explained by X_j alone:

$$S_j^{(i)} = \frac{\mathbb{V}_{X_j}\left[\mathbb{E}(Z_i \mid X_j)\right]}{\mathbb{V}[Z_i]}, \tag{4.5}$$

where $\mathbb{E}[\cdot]$ denotes expectation, $\mathbb{V}[\cdot]$ variance, and $\mathbb{V}_{X_j}[\cdot]$ variance with respect to X_j.

The *total-effect index* $S_{T,j}^{(i)}$ measures the overall effect of X_j, including all its interactions:

$$S_{T,j}^{(i)} = 1 - \frac{\mathbb{V}_{\mathbf{X}_{-j}}\left[\mathbb{E}(Z_i \mid \mathbf{X}_{-j})\right]}{\mathbb{V}[Z_i]}, \tag{4.6}$$

where $\mathbb{E}[\cdot \mid \mathbf{X}_{-j}]$ denotes the conditional expectation given all inputs except X_j, and $\mathbf{X}_{-j}$ denotes all inputs except X_j.

Then to estimate these indices, we use the pick-and-freeze Monte Carlo scheme, detailed next.

Pick-and-freeze Monte Carlo estimation

Given d independent inputs $\mathbf{X} = (X_1, \ldots, X_d)$ with joint distribution $p(\mathbf{x})$ and a scalar QoI $Z = f(\mathbf{X})$, the classical Monte Carlo approach to estimating Sobol' indices (Sobol', 1993; Saltelli, 2002; Saltelli et al., 2010) uses two independent sampling matrices:

$$A = \left[\mathbf{a}^{(1)}, \ldots, \mathbf{a}^{(N_S)}\right]^\top \in \mathbb{R}^{N_S \times d},$$
$$B = \left[\mathbf{b}^{(1)}, \ldots, \mathbf{b}^{(N_S)}\right]^\top \in \mathbb{R}^{N_S \times d},$$

where $N_S \in \mathbb{N}$ is the number of Monte Carlo samples and each row is an independent draw from $p(\mathbf{x})$.

For each $j = 1, \ldots, d$, a third matrix $A_B^{(j)}$ is constructed by replacing the j-th column of A with the j-th column of B, so that $A_B^{(j)}$ shares all variables with A except X_j, which is taken from B.

With this convention, a standard estimator of the first-order index (Eq. 4.5) is the Saltelli estimator:

$$\hat{S}_j = \frac{\frac{1}{N_S}\sum_{n=1}^{N_S} f(\mathbf{b}^{(n)})\left(f(\mathbf{a}_B^{(j),(n)}) - f(\mathbf{a}^{(n)})\right)}{\hat{V}}, \tag{4.7}$$

where $\bar{f}_A = \frac{1}{N_S}\sum_{n=1}^{N_S} f(\mathbf{a}^{(n)})$ and

$$\hat{V} = \frac{1}{N_S}\sum_{n=1}^{N_S} f(\mathbf{a}^{(n)})^2 - \bar{f}_A^2 \tag{4.8}$$

is the Monte Carlo estimator of the output variance.

Using the same sampling design, the total-effect index (Eq. 4.6) is estimated by the Jansen estimator:

$$\hat{S}_{T,j} = \frac{\frac{1}{2N_S}\sum_{n=1}^{N_S}\left(f(\mathbf{a}^{(n)}) - f(\mathbf{a}_B^{(j),(n)})\right)^2}{\hat{V}}. \tag{4.9}$$

This scheme requires $(d+2)N_S$ simulator runs for each set of indices (Janon et al., 2014), where d is the number of input parameters and N_S the base sample size. For computationally expensive models such as the 3D FE simulator used in this work, this cost is often prohibitive.

To overcome this limitation, we construct a metamodel that approximates the simulator's QoIs responses from a limited number of evaluations, enabling an efficient estimation of Sobol' indices.

Metamodels for expensive simulators in geotechnical engineering.

In geotechnical engineering, metamodels are widely used to approximate computationally intensive simulators. Common approaches include polynomial chaos expansions (PCE) (Mollon et al., 2013), polynomial chaos kriging (PCK) (Kratz et al., 2023b; Man et al., 2024), support vector machines (SVM) (Liu et al., 2017, 2018), proper orthogonal decomposition combined with radial basis functions (POD-RBF) (Khaledi et al., 2014; Zhao et al., 2015; Mahmoudi et al., 2019), and artificial neural networks (ANN) (Ninić and Meschke, 2015; Obel et al., 2020; Choi and Lee, 2022).

Most existing applications operate in low-dimensional input spaces (fewer than 20 parameters), selected through expert judgment or preliminary sensitivity analysis (Liu et al., 2017; Zhao et al., 2015). They also often assume homogeneous soil layers to simplify the simulator and reduce computational costs (Mollon et al., 2013; Khaledi et al., 2014; Miro et al., 2014; Ninić and Meschke, 2015). Model outputs are usually reduced to scalar QoIs (e.g., maximum settlement) or displacements at selected nodes.

In this work, we adopt a GP metamodel (Williams and Rasmussen, 2006), a widely used probabilistic approach for approximating computational models (Sacks et al., 1989a; Santner et al., 2003; Gramacy, 2020). Unlike deterministic metamodels, GP regression provides a full probabilistic description of the model response, quantifying epistemic uncertainty through its posterior distribution. This uncertainty information is particularly valuable for subsequent sensitivity analysis and model simplification, yet it is generally not addressed in tunneling studies that rely on deterministic metamodels.

Gaussian process regression.

A GP treats the simulator output as a realization of a stochastic process, $\xi \sim \mathcal{GP}(m, k)$ with mean function $m(\mathbf{x})$ and covariance function $k(\mathbf{x}, \mathbf{x}')$. One independent GP is fitted for each QoI.

The mean function is chosen as constant or linear:

$$m(\mathbf{x}) = \beta^\top \phi(\mathbf{x}), \tag{4.10}$$

where $\phi(\mathbf{x})$ is a vector of basis functions and β the corresponding coefficients. The covariance function models the correlation between two outputs as a function of the distance between their inputs. A popular choice is the Matérn kernel (Williams and Rasmussen, 2006). In this work, we adopt the Matérn 5/2 kernel:

$$k(\mathbf{x}, \mathbf{x}') = \sigma^2 r\left(\|\mathbf{x} - \mathbf{x}'\|_l\right), \tag{4.11}$$

with process variance σ^2, correlation lengths $l = (l_1, \ldots, l_d)$,
$\|\mathbf{x} - \mathbf{x}'\|_l^2 = \sum_{i=1}^{d} \left((x_i - x_i')/l_i\right)^2$, and $r : \mathbb{R}_+ \to \mathbb{R}$ a correlation function.

Let $\mathcal{D}_n = \{(\mathbf{x}_i, f(\mathbf{x}_i))\}_{i=1}^n$ denote the set of n simulator evaluations used to fit the GP model, and let $\mathbf{F}_n = \big(f(\mathbf{x}_1), \ldots, f(\mathbf{x}_n)\big)^\top$ be the corresponding vector of simulator outputs.

Given these data, the GP yields at any $\mathbf{x}$ an estimated mean value

$$m_n(\mathbf{x}) = m(\mathbf{x}) + \mathbf{k}(\mathbf{x})^\top K^{-1}(\mathbf{F}_n - \mathbf{m}), \tag{4.12}$$

and an associated variance

$$\sigma_n^2(\mathbf{x}) = k(\mathbf{x}, \mathbf{x}) - \mathbf{k}(\mathbf{x})^\top K^{-1}\mathbf{k}(\mathbf{x}), \tag{4.13}$$

where $K = (k(x_i, x_j))_{i,j}$ is the $n \times n$ covariance matrix of the data points ($\mathcal{D}_n$), $\mathbf{k}(\mathbf{x}) = (k(\mathbf{x}_i, \mathbf{x}))_i$ is their covariance vector with $\mathbf{x}$, and $\mathbf{m} = (m(x_i))_i$ is the mean vector.

The quantity $m_n(\mathbf{x})$ is the GP estimate of $f(\mathbf{x})$, while $\sigma_n(\mathbf{x})$ quantifies the associated uncertainty. These correspond to the predictive (kriging) mean and standard deviation, also referred to as the GP posterior mean and variance. Accordingly, the GP posterior ξ_n satisfies, for any $\mathbf{x} \in \mathcal{X}$, $\xi_n(\mathbf{x}) \sim \mathcal{N}\big(m_n(\mathbf{x}), \sigma_n^2(\mathbf{x})\big)$.

Illustration. Figure 4.8 shows a one-dimensional GP fit to a smooth target function, obtained with the gpmp Python package (Vazquez, 2025) with a constant mean and a Matérn 5/2 kernel. Red squares are the simulator evaluations, the blue line is the GP posterior mean function, and the shaded band is the 95% confidence interval. Gray curves are conditional sample paths drawn from the GP; these represent possible simulator behaviors consistent with the data. Adding more evaluation points improves the estimate and reduces uncertainty.

Hyperparameter estimation. The parameters $\theta = \{\beta, l, \sigma\}$ are determined by maximizing the GP log-likelihood:

$$\log \mathcal{L}(\theta) = -\tfrac{1}{2}(\mathbf{F}_n - \mathbf{m})^\top K^{-1}(\mathbf{F}_n - \mathbf{m}) - \tfrac{1}{2}\log|K| - \tfrac{n}{2}\log(2\pi), \tag{4.14}$$

using gradient-based optimization (e.g., L-BFGS). Other criteria such as restricted maximum likelihood (REML) or cross-validation can also be used.

Model validation. We assess GP predictive accuracy using leave-one-out (LOO) cross-validation (Petit et al., 2023). Let $\mathcal{D}_n = (\mathbf{x}_i, f(\mathbf{x}_i))_{i=1}^n$ be the n simulator evaluations. For each i, the LOO estimate $m_{n,-i}(\mathbf{x}_i)$ is obtained from a GP fitted to all data points except

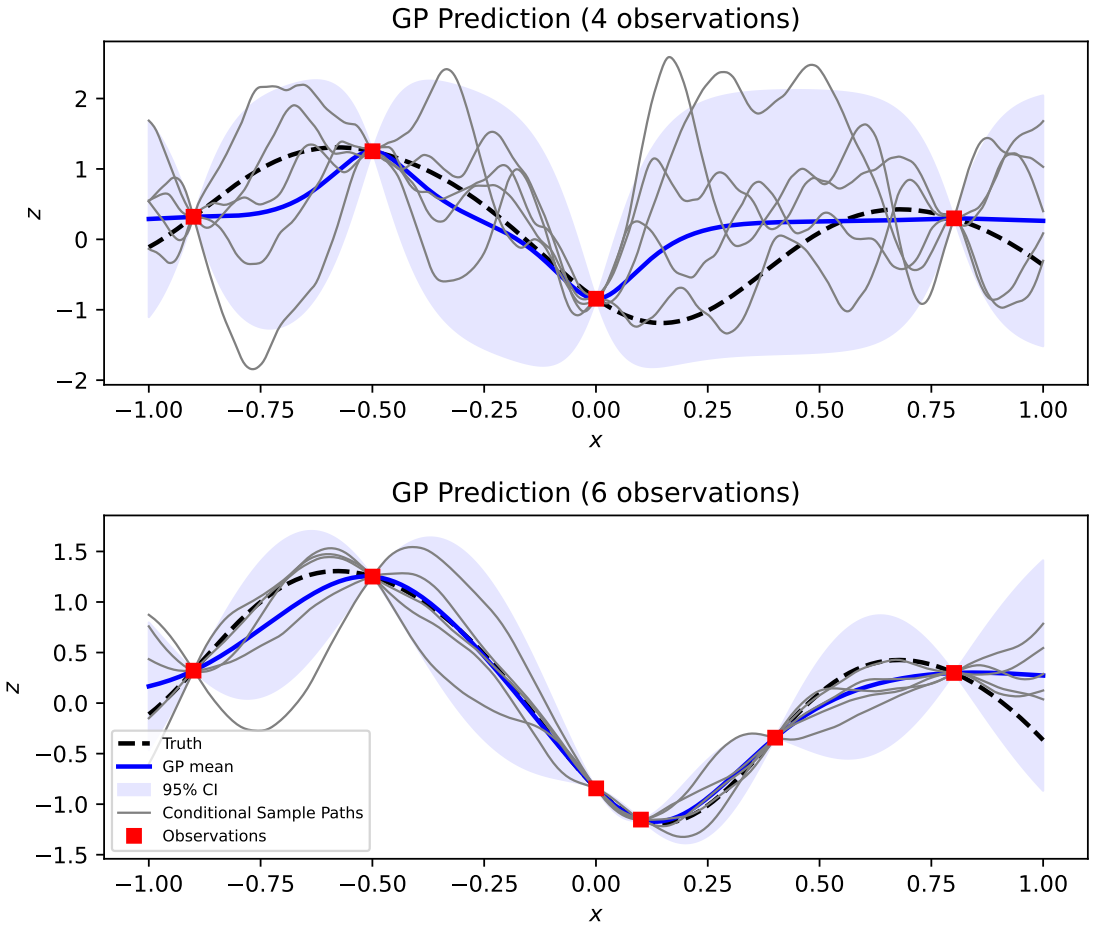

Figure 4.8: Illustrative example of a one-dimensional GP regression using a constant mean function and a Matérn 5/2 covariance kernel to approximate an unknown target function (dashed black line). The simulator outputs (red squares) are interpolated by the GP posterior mean (solid blue line), with the associated 95% confidence intervals shown as a shaded blue area. Five conditional sample paths drawn from the GP posterior distribution are plotted in grey.

$(\mathbf{x}_i, f(\mathbf{x}_i))$. Closed-form LOO formulas yield $m_{n,-i}(\mathbf{x}_i)$ and its variance $\sigma^2_{n,-i}(\mathbf{x}_i)$ without recomputing n separate fits.

The LOO root mean squared error is

$$\text{LOO-RMSE} = \sqrt{\frac{1}{n}\sum_{i=1}^{n}\left(f(\mathbf{x}_i) - m_{n,-i}(\mathbf{x}_i)\right)^2}. \tag{4.15}$$

The LOO coefficient of determination is

$$Q^2 = 1 - \frac{\sum_{i=1}^{n}\left(f(\mathbf{x}_i) - m_{n,-i}(\mathbf{x}_i)\right)^2}{\sum_{i=1}^{n}\left(f(\mathbf{x}_i) - \bar{f}_n\right)^2}, \tag{4.16}$$

where $\bar{f}_n = \frac{1}{n}\sum_{i=1}^{n} f(\mathbf{x}_i)$ is the sample mean output.
High Q^2 and low LOO-RMSE indicate that the GP reproduces the simulator output well.

Monte Carlo estimation of Sobol' indices using GP

Sobol' indices can be estimated from GP metamodels using two complementary approaches. The first, known as the *plug-in* approach, replaces the simulator $f(\cdot)$ by the GP predictive mean $m_n(\mathbf{x})$, and computes Sobol' indices with the classical Monte Carlo pick-and-freeze scheme (see Section 4.2.1). This method is computationally efficient but ignores the uncertainty due to metamodel approximation.

The second, *uncertainty-aware* approach, propagates the epistemic uncertainty of the GP by drawing conditional sample paths from the GP posterior process. Over the finite Monte Carlo design, the corresponding vector of evaluations follows a multivariate Gaussian distribution with posterior mean vector and posterior covariance matrix induced by the GP. For each sample path, Sobol' indices are computed using the same Monte Carlo procedure (see Eqs. 4.7–4.9). Their distributions are then summarized by posterior means and credible intervals (Oakley and O'Hagan, 2004; Marrel et al., 2009; Gratiet et al., 2016):

1. Generate conditional sample paths $\{\hat{\xi}^{(r)}(\cdot)\}_{r=1}^{R}$ from the GP posterior over the Monte Carlo design $\{\mathbf{A}, \mathbf{B}, \mathbf{A}_{\mathbf{B}}^{(j)}\}$.
2. For each path $\hat{\xi}^{(r)}$, compute $\hat{S}_j^{(r)}$ and $\hat{S}_{T,j}^{(r)}$ using the standard Monte Carlo formulas.
3. Aggregate the results to obtain posterior means and credible intervals for all indices.

Workflow. Then, the complete procedure adopted in this work (Algorithm 2) is applied independently to each QoI: (i) generate a Saltelli sampling design, (ii) draw conditional sample paths from the GP posterior and evaluate them at the design points, (iii) compute Sobol' indices using Monte Carlo estimators, and (iv) summarize the resulting distributions by their medians and credible intervals.

4.2.2 GSA results using GP metamodels

We now apply the uncertainty-aware GSA procedure to the 3D tunneling case study. The analysis assumes a multi-layer Île-de-France geological context where the TBM operates

Algorithm 2 Sobol' indices estimation using GP conditional sample paths

Inputs: number of Monte Carlo samples N_S; Saltelli sampling design $\{\mathbf{A}, \mathbf{B}, \mathbf{A}_{\mathbf{B}}^{(j)}\}_{j=1}^{d} \subset \mathbb{R}^{N_S \times d}$; GP models $\{\xi^{(i)}\}_{i=1}^{q}$ (one per QoI); number of conditional sample paths R; design of experiments $\mathcal{D}_n = \{(\mathbf{x}_\ell, f(\mathbf{x}_\ell))\}_{\ell=1}^{n}$.
for $i = 1$ to q **do** ▷ Loop over QoIs
  for $r = 1$ to R **do** ▷ Loop over GP conditional paths
    Draw a conditional sample path $\hat{\xi}^{(i,r)}(\cdot) \sim \xi_n^{(i)}$.
    Evaluate $\hat{\xi}^{(i,r)}$ on all rows of $\{\mathbf{A}, \mathbf{B}, \mathbf{A}_{\mathbf{B}}^{(j)}\}_{j=1}^{d}$.
    Compute first-order and total-effect Sobol' indices $\hat{S}_j^{(i,r)}$ and $\hat{S}_{T,j}^{(i,r)}$ using standard Monte Carlo estimators.
  end for
  Summarize $\{\hat{S}_j^{(i,r)}\}_{r=1}^{R}$ and $\{\hat{S}_{T,j}^{(i,r)}\}_{r=1}^{R}$ by posterior medians and credible intervals.
end for
Output: posterior distributions (or summaries) of Sobol' indices $\{S_j^{(i)}, S_{T,j}^{(i)}\}$ for all QoIs.

under mixed-face conditions across two distinct soil layers, consistent with the monitoring data presented in Chapter 5. The corresponding geological and operational parameters are detailed in Tables J.1-J.3 in Appendix J. The input space includes both geological and operational variables.

Experimental design. The analysis considers $d = 66$ independent input parameters covering construction controls (e.g., face pressure, grout pressure, tunnel lining stiffness), geological properties (e.g., Young's modulus E, cohesion c, friction angle ϕ, lateral earth pressure coefficients K_{0x}, K_{0y}, layer thickness, unit weight), and loading conditions (e.g., surface surcharge q_s). More details about parameter bounds are given in Tables J.1-J.3 in Appendix J.

A pseudo-maximin Latin hypercube sampling (Pronzato and Müller, 2012) of size $n \approx 5d = 370$ is generated using the GPmp Python package (Vazquez, 2025), providing space-filling coverage under uniform marginal distributions. The reduced numerical configuration identified in Section 4.1.2 is used for all runs: $X_{\text{lim}} = 60$ m, $Y_{\text{lim}} = 100$ m, $Z_{\text{lim}} = 60$ m, $\Delta Y = 20$ m, $\alpha_{\text{fine}} = 1.0\text{nodes/m}^2$, $\alpha_{\text{coarse}} = 0.0625\text{nodes/m}^2$.

Of the 370 simulations, 366 completed successfully, while 4 failed to converge due to excessive mesh distortion during the simulation. Each simulation requires, on average, 17 hours. Figure 4.9 presents the distributions of the four QoIs (z_1, z_2, z_3, and z_4), obtained by post-processing the simulated displacement fields using the parametric settlement model defined in Eq. (3.5).

GP construction and validation. GP construction is carried out using the GPmp Python package (Vazquez, 2025). Each QoI component z_i is modeled by an independent GP with constant mean and Matérn-5/2 covariance kernel. Hyperparameters are estimated by maximizing the restricted log-likelihood. Predictive accuracy is assessed using exact closed-form leave-one-out formulas (`GPmp` implementation) to compute LOO-RMSE

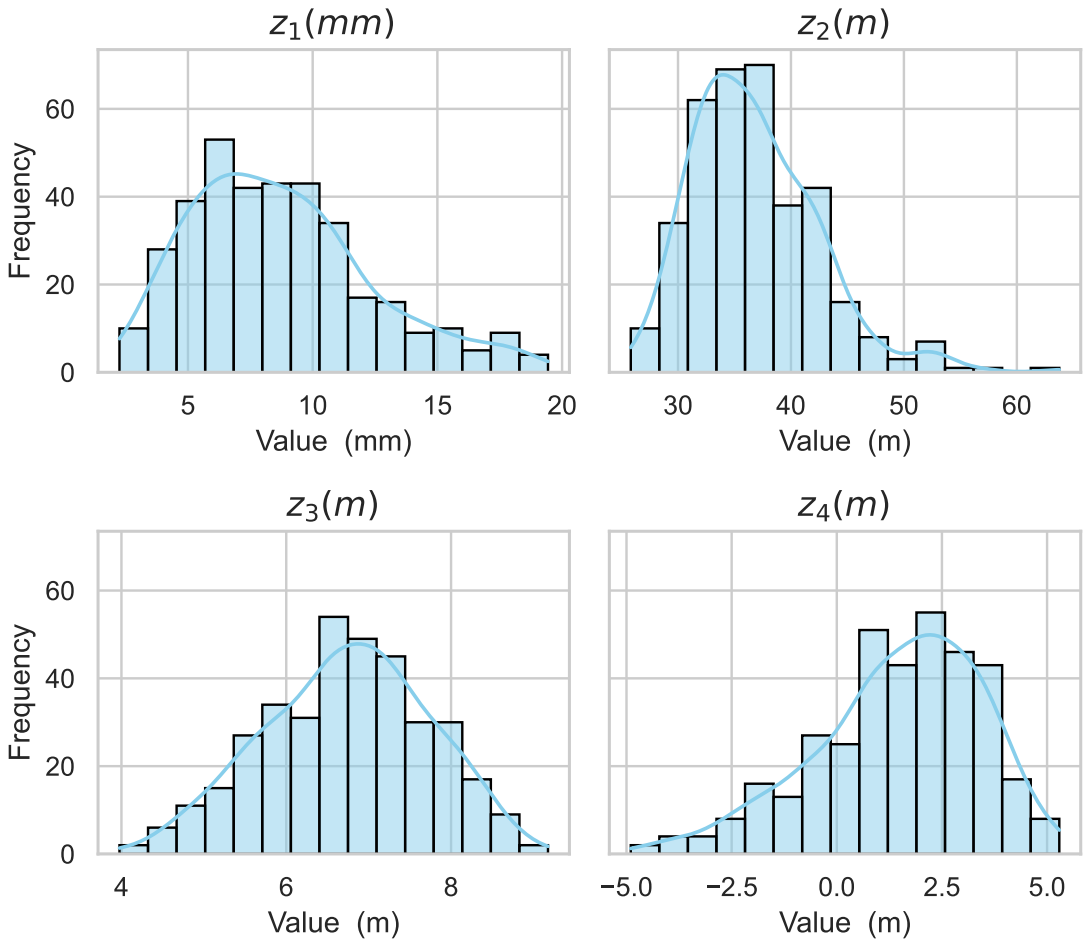

Figure 4.9: Histograms of the four QoIs (z_1, z_2, z_3, and z_4) defined in Table 3.4 in Chapter 3.

and Q^2 scores. Figure 4.10 shows good alignment with the $y = x$ line, indicating accurate metamodel behavior.

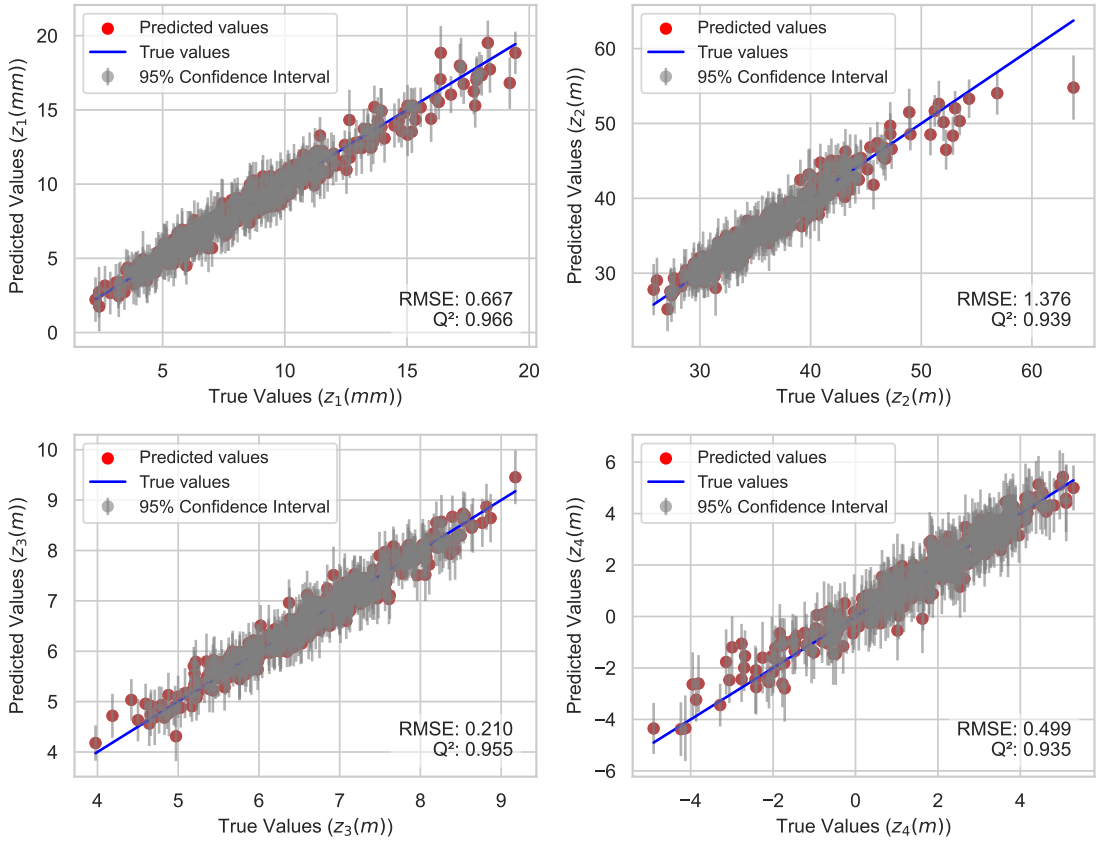

Figure 4.10: Validation of GP metamodel performance using leave-one-out cross-validation for each QoI z_i. This validation process removes each simulation point $(\mathbf{x}_t, z_t)$ from $\mathcal{D}_n$ to train GP metamodels on the remaining data. Each metamodel is then evaluated at $\mathbf{x}_t$, providing mean and variance predictions. This procedure is repeated for the entire simulation dataset $\mathcal{D}_n$. The predictions and true values are plotted with 95% confidence intervals. Perfect performance would align predictions with the $y = x$ line. Here, the models demonstrate satisfactory performance, with predictions well-distributed around $y = x$, as evidenced by LOO-RMSE and Q^2 metrics.

Sobol' index estimation. Global sensitivity analysis follows Algorithm 2. For each QoI, $N_{\text{scp}} = 200$ conditional sample paths are drawn from the GP posterior. Saltelli sampling with $N_S = 128$ yields $n = N_S \times (d+2) = 8704$ evaluations per path. First-order (S_1) and total-order (S_T) Sobol' indices are computed with SaLib (Herman and Usher, 2017; Iwanaga et al., 2022), producing index distributions across sample paths.

Interpretation of results. The 20 most influential inputs are identified from the maxima of the 95th percentiles of the Sobol' indices across all QoIs (Figs. 4.11-4.14).

More precisely, the ranking is based on the maximum of the 95th percentiles of the first-order $S_j^{(i)}$ and total-effect $S_{T,j}^{(i)}$ indices over all QoIs. The first-order index $S_j^{(i)}$ quantifies the main effect of input X_j on QoI Z_i, while the total-effect index $S_{T,j}^{(i)}$ accounts for both its main effect and all interaction effects. When $S_{T,j}^{(i)} \approx S_j^{(i)}$, interactions involving X_j are negligible, and its contribution to the output variance is mainly additive. Results are analyzed for each QoI $(z_1, \ldots, z_4)$, whose physical meaning is summarized in Table 3.4 in Chapter 3.

Geological parameters. Soil mechanical properties primarily control the variability of the QoIs: E, ϕ, c, K_{0x}, and K_{0y} are among the most influential parameters. Their impact is mainly concentrated in the layers intersected by the tunnel (SO and SB), which is consistent with the stress redistribution and deformation processes occurring in the vicinity of the excavation.

Remark. The excavation is performed under mixed-face conditions within the SO layer (Saint-Ouen limestone), while the SB layer (Beauchamp sand) lies below (see Figure 3.1).

Layer-specific effects are observed. The SO layer tends to have a stronger influence on the settlement amplitude z_1 and the longitudinal QoIs (z_3 and z_4), suggesting that the upper layer plays a predominant role in both the magnitude and the longitudinal development of settlements. In comparison, the SB layer appears to have a relatively greater influence on z_2, which characterizes the transverse extent of the settlement trough. The stiffness of the overlying MPH layer, through its Young's modulus, also contributes to z_2, indicating that overburden stiffness influences the lateral extent of the settlement trough.

An anisotropic response is observed: K_{0x} significantly affects z_1 and z_2, which are related to transverse settlement characteristics. This is consistent with empirical relationships linking settlement trough geometry to lateral stress conditions (Peck, 1969) (see Appendix A). In contrast, K_{0y} has a weaker overall influence but contributes to the longitudinal QoIs (z_3, z_4).

The influence of K_{0x} and K_{0y} must be interpreted with care, as wide variability ranges are considered in this GSA. These ranges are chosen to reflect uncertainty in the in-situ stress state, particularly in the horizontal stress components represented by K_{0x} and K_{0y}. However, since these parameters control horizontal confinement and therefore influence deformation around the excavation, their impact remains physically consistent.

Remark. K_{0x} and K_{0y} are key calibration variables, as they are commonly used to estimate face pressure through empirical relationships (see Appendix H).

Soil stiffness E and strength parameters ϕ and c mainly affect amplitude-related QoI (z_1), as they govern deformability and yielding. The lower influence of c compared to ϕ depends on the prescribed uncertainty ranges and should be interpreted cautiously.

Overall, these trends are consistent with previous studies (Mollon et al., 2013; Zhao et al., 2015; Miro et al., 2014; Liu et al., 2017).

Face pressure. Face pressure parameters (p_f^0, p_f^{grad}) primarily influence the longitudinal QoI z_3, with negligible impact on z_1, z_2, and z_4. This indicates that face support mainly controls the longitudinal evolution of settlements, as captured by the steepness parameter

z_3, rather than the final settlement magnitude (z_1) or the transverse trough shape (z_2). This observation is consistent with the role of face pressure in maintaining front stability and limiting short-term deformations ahead of the excavation (Mollon et al., 2010).

However, this result contrasts with some field observations (Vanoudheusden, 2006) and numerical studies (Kasper and Meschke, 2006a), which report a more significant contribution to the final settlement amplitude. This discrepancy may be attributed to modeling assumptions, in particular the representation of the excavation process through a prescribed static face pressure, without accounting for pore pressure-induced deformation. In addition, volume loss mechanisms occurring at the tunnel face are not explicitly modeled but only indirectly controlled through face pressure boundary conditions, which limits the ability of the model to capture their contribution to settlement amplitude (z_1).

Grout behavior. Grout pressure (p_g^0, p_g^{grad}) and the extent of the liquid grout zone (n_g) influence all QoIs, with a weaker effect on z_2. This is consistent with the role of tail void processes in settlement control (Kasper and Meschke, 2006a; Kavvadas et al., 2017). While p_g^0 limits cavity convergence, n_g controls the longitudinal extent of support before hardening.

Surface loading and tunnel depth. Surface surcharge q_s influences all QoIs, highlighting the importance of load characterization in urban environments. Tunnel depth H_t mainly affects z_2 and z_3, with limited impact on z_1 and z_4, consistent with theoretical expectations (see Appendix B).

Interactions. Significant differences between S_1 and S_T for K_{0x}, K_{0y}, ϕ, c, and H_t indicate non-negligible interaction effects, reflecting the coupling between stress state, soil strength, and tunnel geometry.

Remark. These conclusions are conditional on the assumed prior distributions of the 66 input parameters.

Remark. The complete distributions of total Sobol' indices for all 66 input parameters are provided in the Supplementary Material (SM 1) associated with this chapter.

Input dimension reduction. Figure 4.15 shows that the metamodel accuracy, measured by Q^2, exceeds 0.8 when about 15 input parameters are retained, and surpasses 0.9 beyond 20. The improvement then stabilizes after approximately 40 inputs.

Three main observations can be made: (i) dimensions below three are unstable in this setting; (ii) sharp gains occur when adding strongly interacting variables; (iii) for z_4, adding inputs can degrade Q^2, suggesting noise-like effects.

Remark. In Figure 4.15, dimensionality reduction is performed independently for each QoI using Sobol' indices (Figures 4.11-4.14). The least influential inputs for the QoI under consideration are progressively removed, and model performance is evaluated using R^2 and RMSE at each step.

4.3 Discussion and conclusions

Overall, this chapter presents a reproducible framework that integrates (i) the ACMR methodology to optimize numerical settings, (ii) GP metamodeling to approximate the

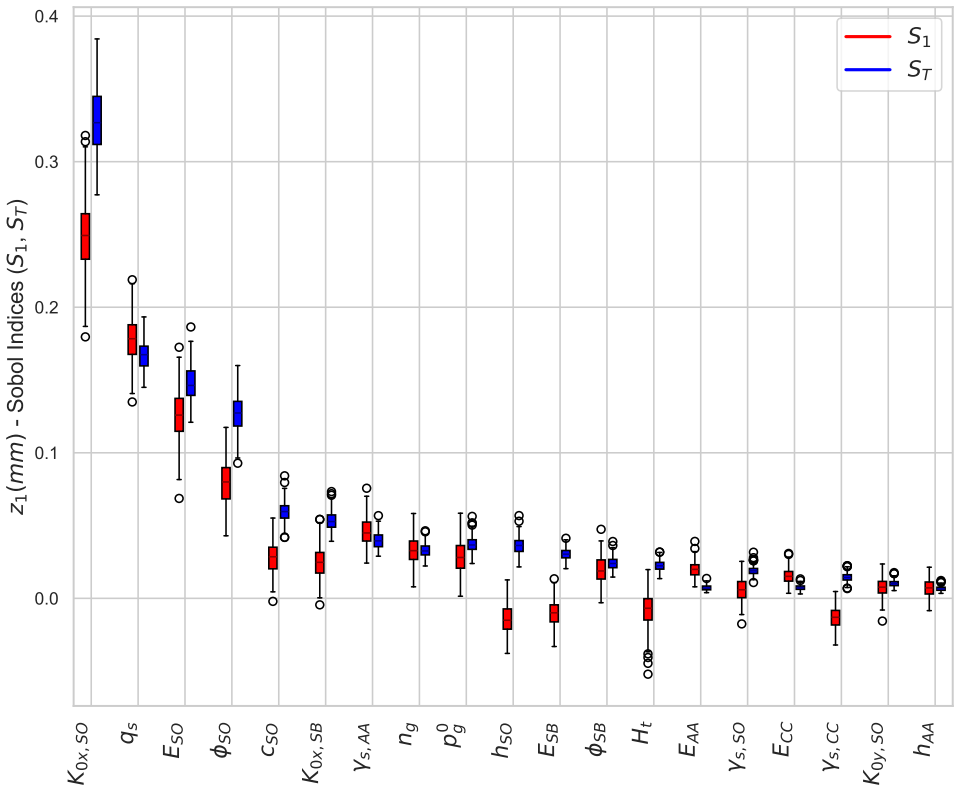

Figure 4.11: Influence of the 20 Most Influential Input Parameters on the maximum settlement value $z_1 = s_{\max}$. The box plots represent the distribution of the Sobol indices for the first-order (red) and total-order (blue) sensitivity analysis. These indices were estimated using 200 conditional sample paths of the GP posterior. The 20 most influential input parameters were selected by comparing the maximum 95th quantile of the Sobol first-order and total-order distributions for each input parameter. For the maximum surface settlement, the mechanical properties of the soil layers (SO and SB) where the TBM is excavating have a greater influence on the maximum settlement compared to other input parameters. The grouting injection pressure also plays an important role in this QoI.

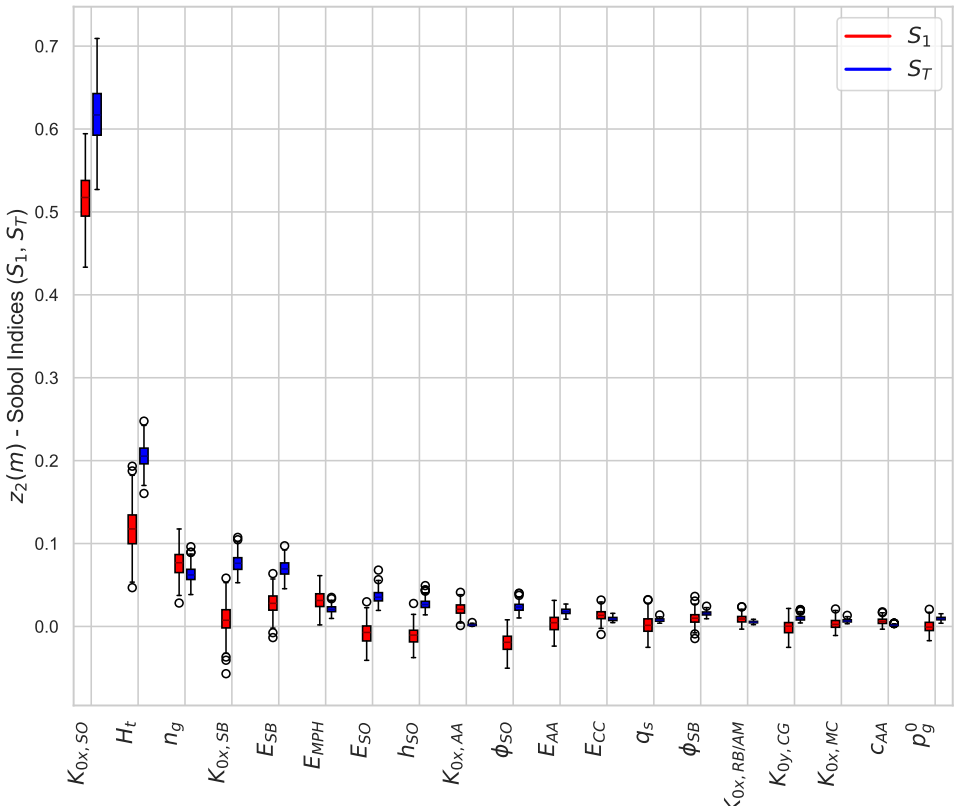

Figure 4.12: Influence of the 20 Most Influential Input Parameters on the transverse settlement width $z_2 = r_0$. The box plots represent the same information as Figure 4.11, with the same Sobol indices color scheme and comparison method. $z_2(r_0)$ is mainly influenced by the transverse earth coefficient at rest K_{0x} in the soil layers where the TBM is excavating and the tunnel depth H_t. The Young's modulus of the soil layers above the tunnel also plays a key role. The grout injection pressure p_g^0 and the length over which it is applied after the shield tail n_g also appears to impact this QoI.

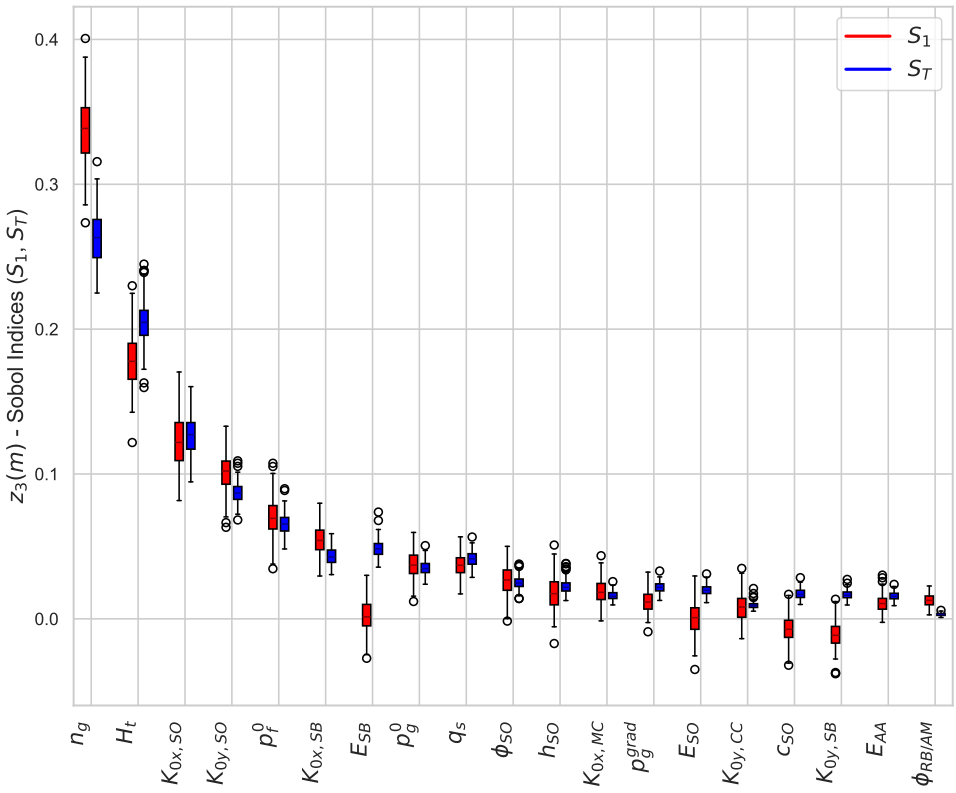

Figure 4.13: Influence of the 20 Most Influential Input Parameters on the longitudinal settlement steepness $z_3 = i_y$. The box plots represent the same information as Figure 4.11, with the same Sobol indices color scheme and comparison method. The same observation can be made as in Figure 4.12 regarding the geological properties and their influence on this QoI, but with a significant contribution from the length over which the grout injection pressure is applied after the shield tail n_g. The face pressure applied to maintain the excavated soil also shows a non-negligible influence on the steepness of the longitudinal settlement.

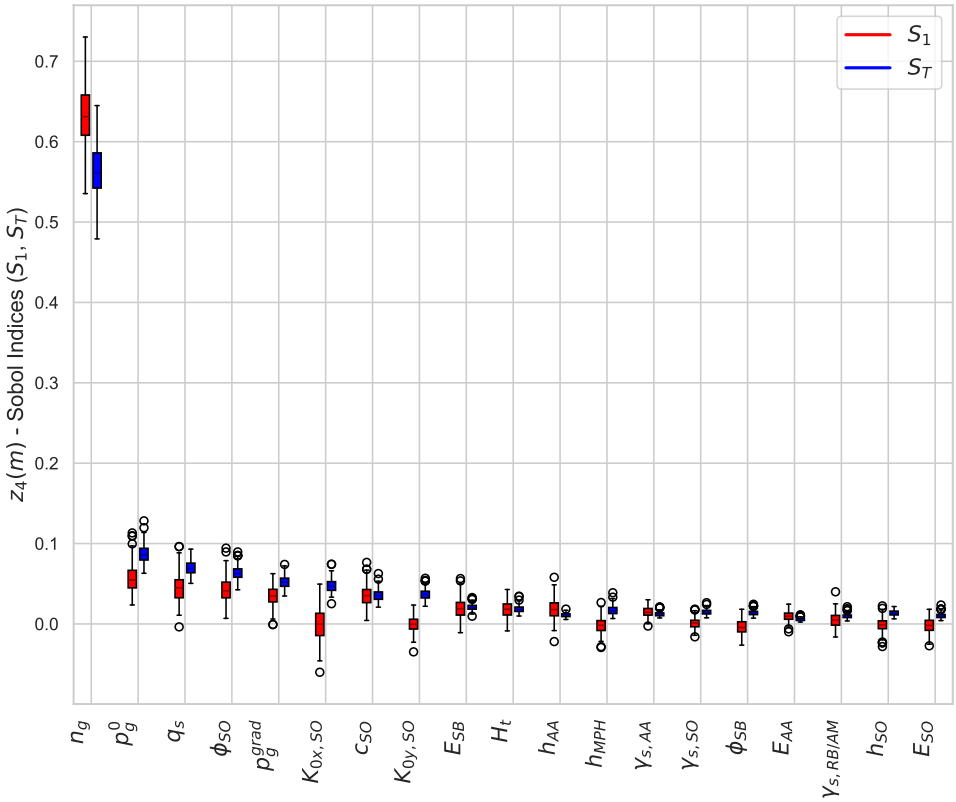

Figure 4.14: Influence of the 20 Most Influential Input Parameters on the longitudinal settlement inflection point $z_4 = y_0$. The box plots represent the same information as Figure 4.11, with the same Sobol indices color scheme and comparison method. This QoI is mainly sensitive to the length over which the grout injection pressure is applied after the shield tail n_g. The same observations as before (Figures 4.11 and 4.12, 4.13) can be made.

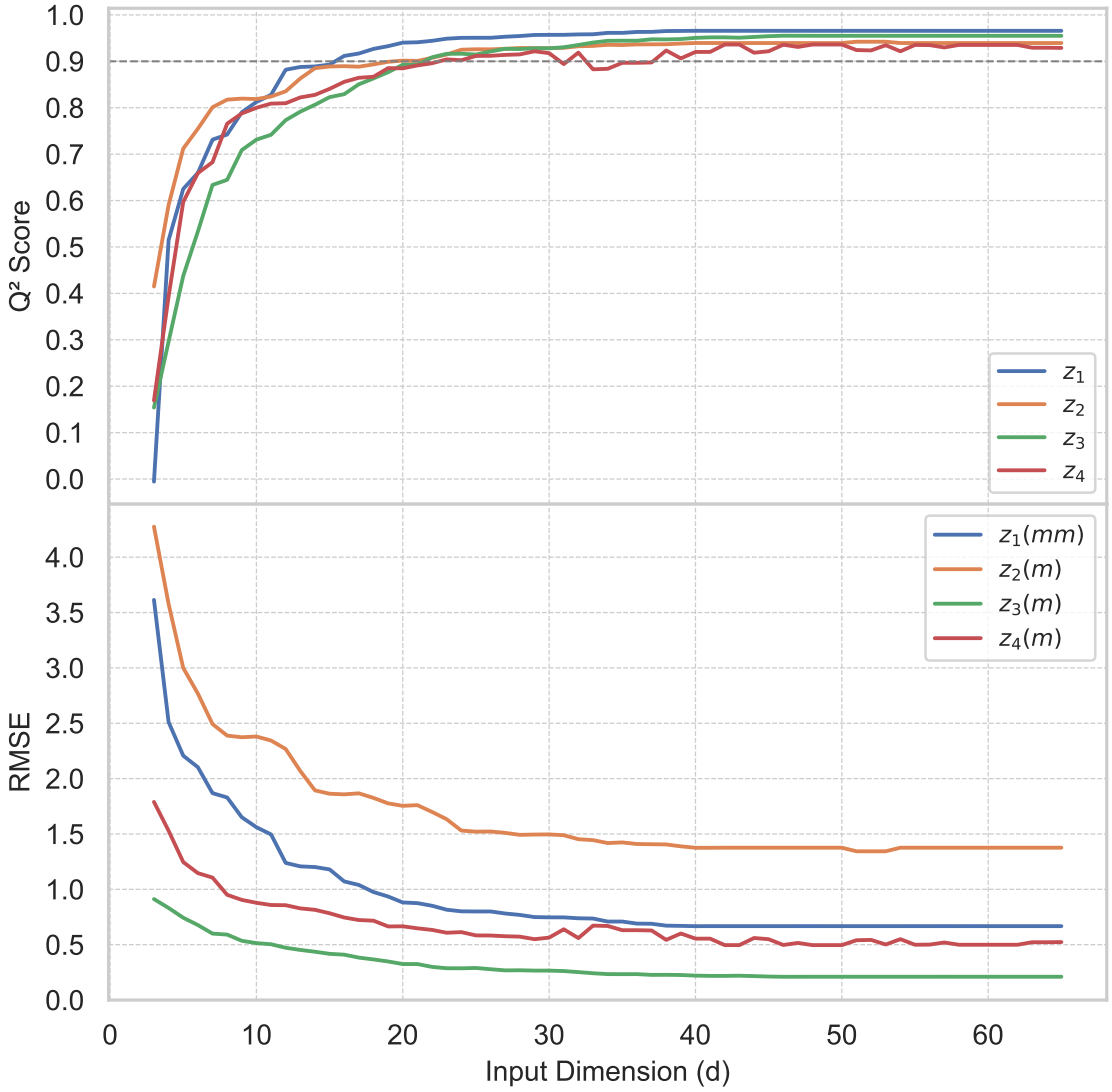

Figure 4.15: Impact of input parameter reduction on metamodel accuracy using Sobol' indices. Sobol' indices, estimated with Gaussian process metamodels, are used to rank input parameters by their influence, allowing the removal of low-impact variables. Reduced-dimension metamodels are trained on the same simulation database $\mathcal{D}_n$ used for GP training, and their performance is evaluated using Q^2 and RMSE metrics through leave-one-out cross-validation (Figure 4.10). Metamodels retaining the 20 most influential parameters already achieve satisfactory accuracy ($Q^2 > 0.75$ for all QoIs), while adding further parameters gradually improves performance, converging toward that of the full 66-input model. These results confirm that Sobol' indices derived from GP metamodels provide an effective basis for dimensionality reduction while preserving predictive accuracy.

computationally expensive FE simulator, and (iii) uncertainty-aware global sensitivity analysis using Sobol' indices derived from the GP posterior distributions.

We now summarize and discuss the main results of this chapter through several key aspects.

QoIs Using QoIs extracted from FE results and physically linked to an empirical parametric settlement model clarifies the interpretation of sensitivity indices. In addition, the fitted model is stable across mesh refinements and domain settings. Errors induced by the parametric fit (see Section 3.3.3 in Chapter 3) could be incorporated into the GP model as an additional observation-noise term.

Guidelines for domain and mesh settings. Simulation cost is highly sensitive to both domain size and mesh resolution. Using the proposed ACMR methodology, we quantified how these parameters influence prediction accuracy and runtime. The empirical error-model analysis confirms that an exponential form is well suited for estimating domain-truncation errors, while a power-law form is appropriate for discretization-error studies. Coupling ACMR with Pareto-front analysis provides an effective tool to identify a reduced-model baseline with lower computation cost. However, this methodology has some limitations. First, the findings are site-specific and remain theoretically valid only within the considered framework (see Appendix L for further details); thus, the analysis would need to be reapplied for different geotechnical contexts. Second, the total dataset in this study was restricted to 69 simulations. This computational effort could be further optimized by implementing an adaptive design strategy to achieve an even better compromise between accuracy and cost.

Based on our results, we recommend the following practical choices: set the transverse half-width greater than the expected radius of influence (r_0), the total model length to at least 100m, and the base depth to at least 20m below the tunnel axis. Use a refined mesh near the tunnel, with a density of approximately 0.5-1.0nodes/m^2, and reduce the density to below 0.1 nodes/m^2 in the far field. For 100m-long models, a longitudinal buffer ΔY of about 20m is generally sufficient to limit boundary effects. With these settings, simulation time decreases from about 140h to 15-30h without compromising accuracy.

Metamodel-based GSA. A direct Sobol' analysis using Saltelli's method would require 8704 simulations, equivalent to 1-3 $\times$ 10^{5}CPU-h, even with mesh and domain size optimisation. To make this tractable, we construct a GP metamodel using 366 simulations sampled via latin hypercube sampling ($\approx$ 5 points per variable over 66 inputs) and validated it using leave-one-out cross-validation. The GP posterior yields Sobol' indices with credible intervals, reducing GSA cost by a factor of 10-20. Further gains are possible by restricting the analysis to 10-20 dominant inputs, as in earlier work (Mollon et al., 2013; Miro et al., 2014; Zhao et al., 2015; Liu et al., 2017). Parallel execution reduces wall-clock time without extra license usage. The computational budget saved can be reallocated to reliability analysis, inverse modeling, or additional metamodel training.

Key parameters. Sobol' indices reveal that a small group of variables drives most of the output variance: the lateral earth pressure coefficients K_{0x} and K_{0y}, Young's modulus E, and the cohesion c and friction angle ϕ of the layers intersected by the TBM (Mollon et al., 2013; Miro et al., 2014; Zhao et al., 2015; Liu et al., 2017). In the specific geotechnical context of this study (two layers intersected), maximal settlements (z_1) and longitudinal QoIs (z_3 and z_4) tend to be more influenced by the upper layer (SO), whereas

the transverse settlement width (z_2) appears to be more influenced by the properties of the lower layer (SB). As these parameters remain uncertain, they should be prioritized in further calibration strategies.

Regarding TBM operation, grouting pressure affects all outputs, with a limited effect on z_2, while face pressure mainly influences the longitudinal slope z_3. This shows the inherent difficulty in numerically capturing the impact of face pressure on final surface settlement magnitudes. However, it must be noted that these sensitivity results depend on the chosen intervals of variation (Appendix J). Therefore, the findings must be interpreted specifically within the context of these uncertainty ranges.

The proposed workflow supports model simplification by retaining only the most influential and uncertain input parameters. This reduction then facilitates model validation, calibration, and inverse analysis through comparisons between simulated and observed data. The next chapter presents the monitoring data and describes its processing to enable direct comparison with the numerical simulator QoIs.

Chapter 5

Building Settlement Maps

Chapter overview. This chapter introduces a workflow to transform raw monitoring data into representations compatible with numerical simulations for calibration.

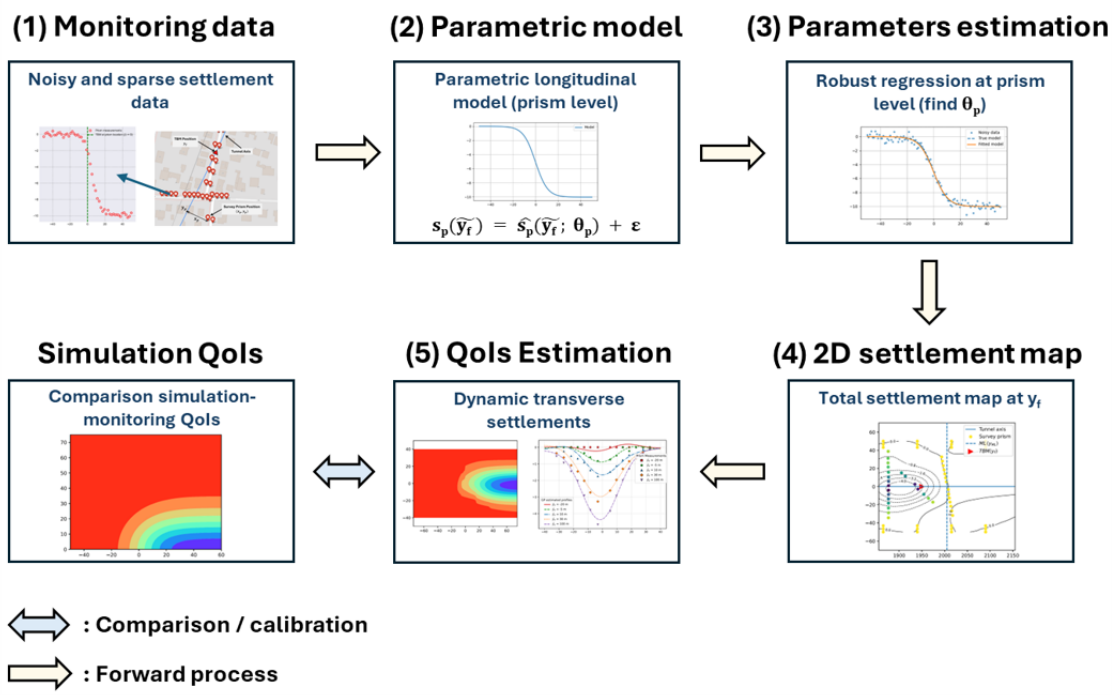

Figure 5.1: Processing workflow from raw monitoring data to quantities of interest used for comparison with numerical simulations. Starting from noisy and sparse surface settlement measurements (1), a longitudinal parametric model is introduced to represent the settlement evolution at the prism level (2). The parameters of this model are then estimated for each prism (one set of parameters per prism) using robust regression methods (3). These calibrated models are subsequently used to reconstruct a continuous two-dimensional settlement field (4), from which dynamic transverse settlement profiles (5) are extracted. Finally, the resulting quantities of interest are compared with the outputs of the TBM numerical simulator.

The workflow is organized into five steps, each described in a dedicated section (Figure 5.1).

Section 1: Monitoring system and settlement representations. This section describes the instrumentation deployed during urban tunnel construction and introduces the coordinate system and settlement representations used in this work. The input data consist of sparse settlement time series as a function of TBM position, which are affected by noise, outliers, and missing values due to disturbances in urban environments.

Section 2: Longitudinal parametric model at the prism level. To extract the underlying settlement behavior, a parametric model of the longitudinal evolution, defined as the settlement at a prism as a function of TBM position, is introduced.

Section 3: Robust parameter estimation. The model parameters are calibrated for each prism using robust estimation methods to mitigate the impact of corrupted measurements.

Section 4: Reconstruction of 2D total settlement maps. Based on these calibrated models, local total settlement maps are reconstructed in a tunnel-centred coordinate system. Gaussian process (GP) regression is used to interpolate the settlement field between sensors and obtain continuous spatial representations.

Section 5: Reconstruction of dynamic transverse settlement profiles. A transverse monitoring line is defined to extract dynamic transverse settlement profiles. These profiles are used to estimate the quantities of interest (QoIs) and enable comparison with the outputs of the numerical simulator.

Scope. This methodology is illustrated using surface settlement data from a geological context matching the parameters in Chapter 4 and Appendix J.

5.1 Monitoring framework and settlement representations

In this section, we aim to answer the following questions: how are surface settlements monitored, and which representations are standard for analysing surface deformations beyond the prism level?

5.1.1 Surface settlement monitoring in urban tunneling

In urban tunneling projects, surface settlement monitoring is central to risk management because it provides direct observations of excavation-induced ground movements at the surface.

Several monitoring techniques are available to measure surface settlements, including topographic surveys, satellite-based Interferometric Synthetic Aperture Radar (InSAR), and fiber-optic sensing systems AFTES (2005); Bilotta (2024); Vanoudheusden (2006).

While fiber-optic systems involve high installation costs, InSAR often lacks the temporal frequency and accuracy required to capture rapid ground movements during TBM passage. Furthermore, GNSS-based methods frequently suffer from insufficient vertical resolution for precise settlement tracking. Consequently, topographic monitoring remains the most widely deployed technique in practice.

Topographic monitoring is based on the measurement of discrete points installed at the ground surface, referred to as survey prisms. By reflecting a laser signal emitted by a theodolite, these prisms allow the three-dimensional position of surface points to be measured relative to stable reference points, with typical vertical uncertainties within ± 0.5 mm under favourable conditions.



Figure 5.2: Automated total station deployed for real-time surface settlement monitoring on a tunneling project.

Two acquisition modes are commonly used. Manual surveys provide low-frequency measurements and require on-site intervention, which limits their applicability for dense monitoring networks. Automatic systems rely on robotic theodolites (total stations, illustrated in Figure 5.2) that perform measurements at regular intervals and provide near real-time access to the data, at the cost of requiring stable reference points, continuous power supply, and network connectivity. In both cases, the measurements consist of sparse three-dimensional displacement data.

In urban tunneling projects, where surface deformations evolve continuously with TBM advance and monitoring networks extend over large areas, automatic total station systems are generally preferred. In the following, we focus on data acquired from automatic topographic monitoring systems.

5.1.2 Monitoring system and data limitations

System Installation Before excavation reaches a monitored area, the monitoring system must be calibrated by defining a reference state in which relative displacements are

set to zero. This calibration phase aims at verifying that no systematic offsets are present in the measurements. To this end, several reference prisms are installed in areas where no ground deformation is expected. The stability of these reference prisms is critical, as any movement of a reference point affects all recorded displacements.

The locations of survey prisms, reference prisms, and total stations are defined by engineers based on the identification of a geotechnical zone of influence (GZI), within which excavation-induced soil movements are expected (see Figure 5.3). Reference prisms must be installed outside the GZI in order to ensure the reliability of the reference frame used for displacement measurements.

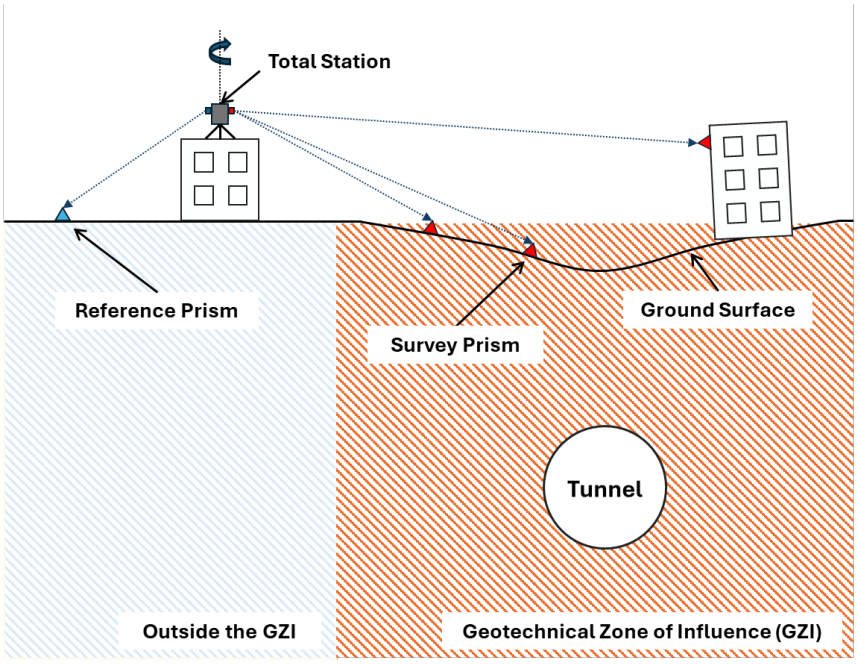

Figure 5.3: Setup of a surface settlement monitoring system using automatic total stations. Reference prisms are installed outside the expected GZI, including a safety margin, in order to ensure a stable reference frame. Survey prisms are distributed within the GZI to directly monitor surface deformations induced by tunneling.

Data limitations Although automatic total station systems provide high-accuracy measurements, their reliability in dense urban environments is often limited when compared to numerical models. Data quality can be affected by urban activity, line-of-sight obstructions, or prism damage, leading to missing values and outliers. Furthermore, site constraints often prevent an ideal spatial distribution of reference points, and precision naturally decreases with long-distance measurements. It is also critical to note that reference prisms outside the GZI may not be perfectly stable, which may introduce additional errors. For these reasons, raw settlement data must be carefully preprocessed before being compared with simulations.

5.1.3 Coordinate system and settlement representations

Tunnel-centred coordinate system

Before introducing settlement representations, we first define the notations and the coordinate system used in this section.

Settlement measurements are expressed in a curvilinear coordinate system defined with respect to the tunnel axis, as illustrated in Figure 5.4. The position of the TBM face along the tunnel axis is denoted by y_f. Each survey prism p is described by coordinates (x_p, y_p), where x_p denotes the orthogonal position relative to the tunnel axis (also called the transverse coordinate) and y_p the longitudinal coordinate of its projection onto the axis.

For longitudinal analyses, a relative coordinate $\tilde{y}_f = y_f - y_p$ can be introduced, representing the signed distance between the TBM face and the prism. By convention, $\tilde{y}_f < 0$ indicates that the TBM face is located before the prism along the tunnel axis, while $\tilde{y}_f > 0$ indicates that it has passed beyond it.

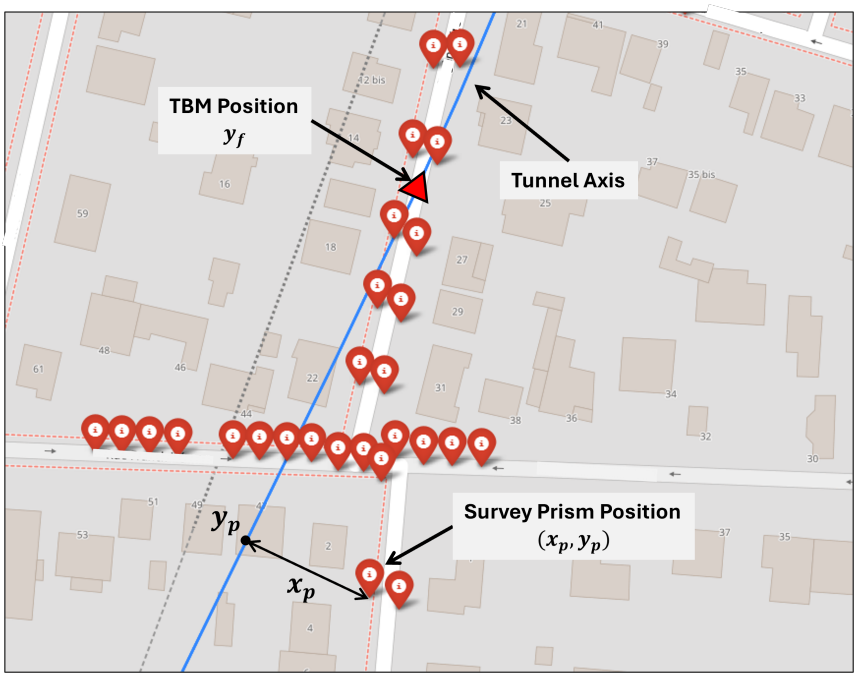

Figure 5.4: Tunnel-centred coordinate system used to describe surface settlement measurements. The tunnel axis defines the longitudinal direction y, while x denotes the transverse coordinate to the axis. The position of the TBM face is indicated by y_f. Each surface monitoring prism p is located by its coordinates (x_p, y_p).

For a relative TBM position $\tilde{y}_f$, the vertical settlement recorded at prism p is denoted by $s_p(\tilde{y}_f)$ and defined by $s_p(\tilde{y}_f) = u_z(x_p, y_p; \tilde{y}_f)$, where u_z denotes the vertical displacement field evaluated at the prism location (x_p, y_p).

In this coordinate system, the geological context described in Chapter 4 and Appendix J is defined over the chainage interval 2000 ± 250 m.

Standard settlement representations

Settlement data are then organised into standard representations used in tunneling practice.

Surface settlement data are available at discrete prism locations and time instants. Depending on the objectives, these data are synthesised into complementary one- and two-dimensional representations.

One-dimensional representations Transverse settlement profiles describe vertical surface displacements along a cross-section orthogonal to the tunnel axis at a given TBM position,as a function of the distance from the tunnel axis, denoted by x. They are commonly used to characterise the shape and width of the settlement trough and to compare observations with analytical or empirical transverse models (some empirical references are given in Table 3.2 in the previous chapter and analytical references (Loganathan and Poulos, 1998; Verruijt and Booker, 1996; González and Sagaseta, 2001; Sagaseta, 1987)).

Longitudinal settlement profiles describe the evolution of surface settlement at a fixed prism location as a function of the relative TBM position $\tilde{y}_f$. This representation is suited for analysing the temporal development of settlements during tunnel excavation and is directly used to calibrate longitudinal settlement models.

Figure 5.5 illustrates these two representations using real monitoring data.

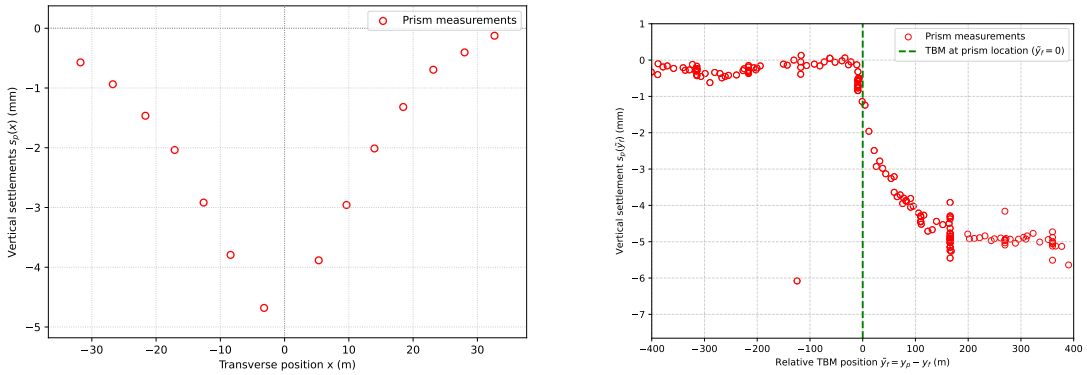

(a) Transverse settlement profile

(b) Longitudinal settlement profile

Figure 5.5: One-dimensional settlement profiles derived from monitoring data. *Left*: transverse settlement profile along a monitored line (ML) at $y_{ML} = 2005$ m for a TBM position $y_f \approx 2200$ m. This corresponds to a relative position $\tilde{y}_f \approx 195$ m, with slight variations between individual prisms. The profile exhibits the typical settlement trough, with maximum settlement near the tunnel axis (x=0) and decreasing deformation away from it. *Right*: longitudinal settlement profile at prism `STA3_22`, represented as a function of the relative TBM position $\tilde{y}_f = y_f - y_p$. The evolution follows a characteristic S-shaped behavior, with negligible deformation ahead of the TBM, a sharp increase during passage, and progressive stabilization behind the face.

Two-dimensional representations Two-dimensional settlement representations provide a spatial description of surface deformations over an area of interest. Total settlement maps represent surface vertical displacements at a given TBM position, while instantaneous settlement maps represent incremental displacements induced by individual excavation steps. These instantaneous maps isolate the contribution of each excavation stage to the total settlement. In particular, they provide information on the position of the settlement center, which can be related to the excavation process: a location behind the TBM may be associated with shield conicity or grouting issues, whereas a location ahead of the face may be associated with insufficient face pressure. They can be defined as the difference between successive total settlement maps (Serratrice and Magnan, 2002; Möller, 2006; Janin et al., 2015). Examples based on synthetic measurements are given in Figure 5.6.

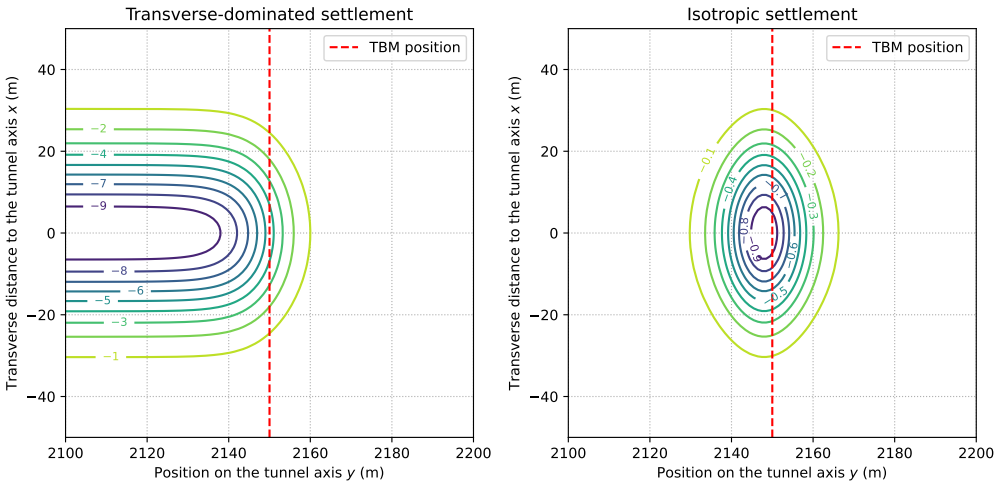

Figure 5.6: Synthetic example of two-dimensional settlement representations. *Left*: total settlement map showing the surface vertical displacements at a given TBM position. *Right*: instantaneous settlement map representing incremental surface displacements associated with a single excavation stage.

In addition, a dynamic transverse settlement representation is introduced. It describes the evolution of transverse settlement profiles at a fixed cross-line (referred to as the ML in Figure 3.1) as a function of TBM advance. This representation corresponds to the outputs of the FE simulator for TBM excavation, presented in Chapter 3, where an illustrative example is shown in Figure 3.11. Additional transverse, longitudinal, and dynamic transverse profiles of the simulation outputs are provided in Appendix K.

This framework is then used to reconstruct dynamic transverse profiles and to estimate the QoIs defined in Section 3.3.3, and to compare them with numerical simulations.

5.2 Longitudinal parametric model at the prism level

To filter out measurement noise and outliers, we propose a parametric model that represents settlement evolution at the prism level. This model serves as a robust substitute for raw measurements when generating total settlement maps. The key question addressed here is: which longitudinal models are best suited to represent this evolution?

5.2.1 Review of longitudinal parametric models

Using a parametric formulation, the longitudinal settlement at a given prism p is modeled as:

$$s_p(\tilde{y}_f) = \hat{s}_p(\tilde{y}_f; \boldsymbol{\theta}_p) + \varepsilon_{\text{longi}}, \tag{5.1}$$

where $\tilde{y}_f = y_f - y_p$ is the signed distance between the TBM face and prism p. The quantity $s_p(\tilde{y}_f)$ denotes the observed vertical settlement, $\hat{s}_p(\tilde{y}_f; \boldsymbol{\theta}_p)$ the parametric function, and $\varepsilon_{\text{longi}}$ the combined modeling and measurement error. A constant offset term may also be included in $\hat{s}_p$ to account for initial measurement bias.

In this coordinate system, surface settlements are expressed as a function of the relative TBM position $\tilde{y}_f = y_f - y_p$. Settlements remain negligible ahead of the TBM face ($\tilde{y}_f < 0$), increase as the face approaches and passes the prism ($\tilde{y}_f \approx 0$), and progressively stabilize behind it ($\tilde{y}_f > 0$). A longitudinal shift parameter y_0 may be introduced to account for the offset between the TBM position and the onset of surface deformation.

Below, we evaluate several candidates for the parametric function $\hat{s}_p$. Based on the QoIs definitions in Section 3.3.3, we compared two empirical models used to represent longitudinal settlement in numerical simulations: the Gaussian cumulative model by Attewell and Woodman (1982) and the sigmoid empirical shape. Consequently, we include these models in the following comparative analysis to evaluate their suitability for representing the longitudinal profiles obtained from monitoring data.

The Gaussian cumulative model proposed by Attewell and Woodman (1982) is defined as

$$\hat{s}_p^{At}(\tilde{y}_f; s_{\max}, i_y, y_0) = s_{\max} \frac{1}{i_y\sqrt{2\pi}} \int_{-\infty}^{\tilde{y}_f} \exp\left(-\frac{(t-y_0)^2}{2i_y^2}\right) \mathrm{d}t, \tag{5.2}$$

where $s_{\max}$ is the maximum settlement at prism p, and i_y is a characteristic longitudinal influence distance.

The sigmoid formulation is defined as

$$\hat{s}_p^{sig}(\tilde{y}_f; s_{\max}, y_0, i_y) = \frac{s_{\max}}{1 + \exp\left(-\dfrac{\tilde{y}_f - y_0}{i_y}\right)}, \tag{5.3}$$

where i_y controls the steepness of the settlement curve along the tunnel axis.

We also include an analytically derived shape based on ground volume loss (V_s) in an elastic half-space. Sagaseta (1987) derived the following closed-form expression:

$$\hat{s}_p^{Sa}(\tilde{y}_f; V_s, H_t, y_0) = \frac{V_s}{2\pi H_t^2} \left(1 + \frac{\tilde{y}_f - y_0}{\sqrt{(\tilde{y}_f - y_0)^2 + H_t^2}}\right), \tag{5.4}$$

where H_t is the tunnel depth. In this study, V_s is interpreted as an effective fitting parameter for each prism rather than a direct physical measurement.

While these models effectively characterize numerical simulator outputs, monitoring data in some cases, such as the one shown in Figure 5.5, exhibit asymmetry: settlements remain negligible well ahead of the TBM, increase sharply near the face ($\tilde{y}_f \approx 0$), and then reach a steady state through a second phase of more progressive evolution.

To capture this asymmetric behavior, we introduce a double-sigmoid formulation:

$$\hat{s}_p^{dsig}(\tilde{y}_f; s_{\max}, y_0, y_1, i_{y0}, i_{y1}) = s_{\max}\hat{s}_p^{sig}(\tilde{y}_f; 1, y_0, i_{y0})\hat{s}_p^{sig}(\tilde{y}_f; 1, y_0 + y_1, i_{y1}), \tag{5.5}$$

subject to $y_1 > 0$ and $i_{y0}, i_{y1} > 0$. The first sigmoid governs the settlement increase as the TBM approaches the prism, while the second captures the more gradual stabilization behind it. In practice, the second transition occurs after the first because it is centered at $y_0 + y_1$.

Additionally, two asymmetric models from the literature are considered. Serratrice and Magnan (2002) proposed:

$$\hat{s}_p^{Se}(\tilde{y}_f; c, H_t, R_t, y_0, a) = \begin{cases} 4cR_t^2 \left[1 - \frac{H_t^2}{H_t^2 + (\tilde{y}_f - y_0)^2} \exp\left(-\frac{a(\tilde{y}_f - y_0)^2}{(H_t + R_t)^2}\right)\right], & \tilde{y}_f > y_0, \\ 0, & \text{otherwise}, \end{cases} \tag{5.6}$$

where a (typically 0.25) controls the profile shape and c defines the steady-state level.

Finally, the piecewise formulation by Hajjar et al. (2015) is included:

$$\hat{s}_p^{Ha}(\tilde{y}_f; s_{\max}, i_y, y_0) = \begin{cases} s_{\max} \exp\left(-\dfrac{(\tilde{y}_f - y_0 + i_y)^2}{2i_y^2}\right), & \tilde{y}_f \leq y_0 - i_y, \\ s_{\max}, & \tilde{y}_f > y_0 - i_y, \end{cases} \tag{5.7}$$

with $i_y > 0$. Written in this form, the model is consistent with the convention $\tilde{y}_f = y_f - y_p$: settlements are small ahead of the prism and approach a plateau after TBM passage.

5.2.2 Illustration of longitudinal parametric models

After introducing several standard longitudinal parametric models, illustrative examples are provided for a reference case ($s_{\max} = 10$ mm, $R_t = 4.9$ m, $H_t = 15$ m, and $y_0 = 0$ m) to compare their respective behaviors in Figure 5.7.

Based on the trends observed in Figures 5.5 and 5.7, the Serratrice and Magnan (2002) model and the double-sigmoid formulation appear to be better suited for capturing the asymmetric settlement evolution typically observed at the prism level.

Remark. Figure 5.9 provides a detailed comparison of these six models for a single prism. A broader analysis of their performance is available in Section 5.3.2.

5.3 Robust parameter estimation

At this stage, the parameters of the longitudinal parametric models are unknown and must be estimated for each prism. Two questions are addressed in this section: how can the longitudinal model parameters be estimated robustly for each prism? and, after parameter estimation, which longitudinal model best represents the monitoring data?

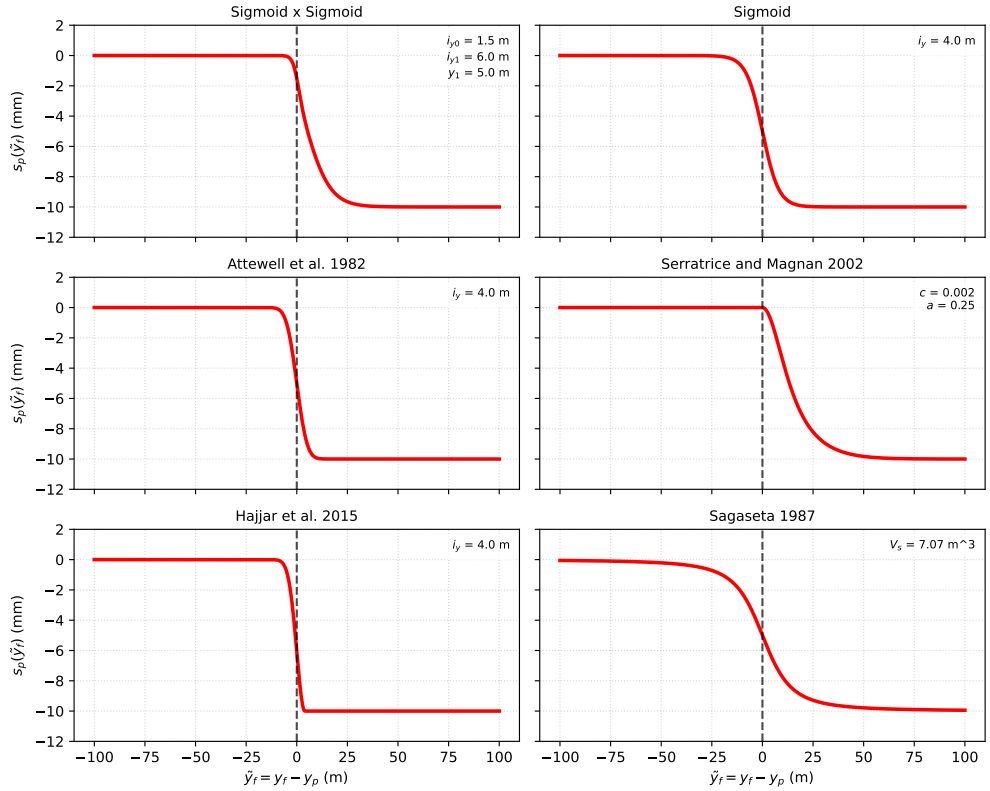

Figure 5.7: Comparison of longitudinal settlement models as a function of the relative TBM position $\tilde{y}_f = y_f - y_p$. Symmetric models, such as Sagaseta (1987), the sigmoid formulation, and Attewell and Woodman (1982), produce identical behaviors before and after TBM passage. In contrast, the Serratrice and Magnan (2002), double-sigmoid, and Hajjar et al. (2015) formulations account for asymmetric responses. As observed in Figure 5.5, observed longitudinal profiles may be asymmetric, with a sharp transition during TBM passage followed by progressive stabilization.

5.3.1 Estimation methodology

To perform this estimation, a regression problem is formulated based on the measured settlement data, as given in Eq. (5.1).

Ordinary least squares

Given a set of longitudinal settlement observations $\{(\tilde{y}_i, s_i)\}_{i=1}^n$ at a given prism, the regression problem derived from Eq. (5.1) is written as:

$$s_i = \hat{s}(\tilde{y}_i; \boldsymbol{\theta}) + \varepsilon_i, \tag{5.8}$$

where $\hat{s}(\cdot; \boldsymbol{\theta})$ denotes the candidate parametric longitudinal settlement model and ε_i represents the measurement and modeling error.

Assume an additive error model with $\varepsilon_i \sim \mathcal{N}(0, \sigma^2)$, independent and identically distributed (i.i.d.). Under this assumption, maximizing the Gaussian likelihood is equivalent to minimizing the sum of squared residuals. The maximum likelihood estimator (MLE) of $\boldsymbol{\theta}$ therefore coincides with the least-squares estimator: it reduces to ordinary least squares (OLS) when the model is linear in $\boldsymbol{\theta}$, and to nonlinear least squares otherwise:

$$\hat{\boldsymbol{\theta}} = \arg\min_{\boldsymbol{\theta}} \sum_{i=1}^{n} \left(s_i - \hat{s}_p(\tilde{y}_i; \boldsymbol{\theta})\right)^2. \tag{5.9}$$

When $\hat{s}_p(\cdot; \boldsymbol{\theta})$ is nonlinear in $\boldsymbol{\theta}$, the estimation problem falls into the nonlinear least-squares framework. Under the assumption of additive i.i.d. Gaussian errors with constant variance, this estimator coincides with the MLE and is statistically efficient. In practice, least-squares estimation is often applied even when these assumptions are violated; however, efficiency may be lost, and uncertainty quantification should then rely on robust approaches, such as heteroscedasticity-robust covariance estimators or robust regression methods.

Robust regression

In practice, measurements may contain outliers due to monitoring disturbances (complex urban environments). To reduce their influence on regression results, robust estimation strategies are considered as alternatives to OLS, which is known to be sensitive to outliers.

M-estimator Among robust regression methods, M-estimators aim to limit the influence of outlying observations by replacing the quadratic loss function with robust loss functions such as Huber or Soft-L1 losses (Huber, 1973; Fox and Weisberg, 2002; Filzmoser and Nordhausen, 2021). In contrast to the quadratic loss, which assigns increasing weight to large residuals, robust loss functions bound the influence of large errors.

The M-estimator is defined as

$$\hat{\boldsymbol{\theta}}_M = \arg\min_{\boldsymbol{\theta}} \sum_{i=1}^{n} \rho(e_i), \tag{5.10}$$

where $e_i = s_i - \hat{s}_p(\tilde{y}_i; \boldsymbol{\theta})$ denotes the residual and $\rho(\cdot)$ is a loss function (e.g. Huber, Soft-L1, or the quadratic L_2 loss, which recovers the OLS estimator).

Remark. Further details on M-estimators are provided in Appendix N.

Random Sample Consensus (RANSAC) For sensors affected by a high proportion of corrupted measurements, M-estimators may be insufficiently robust to ensure reliable parameter estimation. In such cases, an alternative strategy is to use the RANSAC algorithm, which estimates model parameters from repeated OLS fits performed on small random subsets of the data.

The underlying idea is to identify a set of inliers consistent with the assumed parametric model, while discarding observations that strongly deviate from it. At each iteration, a minimal subset of observations is randomly selected, with its size controlled by a parameter p defining the proportion of data used for initial model fitting. Model parameters are then estimated, and the number of observations whose residuals fall below a predefined tolerance threshold is counted. The solution associated with the largest inlier set is retained, and a final OLS fit is performed using these inliers only.

Remark. The pseudo-code of the RANSAC algorithm is provided in Appendix O.

5.3.2 Longitudinal model selection and robust estimation results

Longitudinal model selection

To identify the most suitable parametric longitudinal settlement model, each model presented in Section 5.2.1 is fitted to the monitoring data using OLS.

The analysis is carried out on two datasets: (i) a subset of selected prisms with low noise and no significant outliers (22 prisms), and (ii) the full monitoring dataset (634 prisms).

In addition, the fitted responses of the six models are illustrated on two representative prisms from the low-noise dataset, in order to provide a qualitative comparison of their behavior.

For each model, parameter estimation is performed using the nonlinear least-squares routine `least_squares` from the `scipy` library (Virtanen et al., 2020), with a quadratic loss function, which is equivalent to the OLS estimator.

Once the model parameters are estimated for each prism, the quality of the fitted longitudinal settlement profiles is evaluated using three metrics that compare model predictions with observed measurements: the coefficient of determination (R^2), the root mean square error (RMSE), and the mean absolute error (MAE), defined as

$$\mathrm{RMSE} = \sqrt{\frac{1}{n}\sum_{i=1}^{n}\left(s_i - \hat{s}_p(\tilde{y}_i)\right)^2}, \qquad \mathrm{MAE} = \frac{1}{n}\sum_{i=1}^{n}\left|s_i - \hat{s}_p(\tilde{y}_i)\right|,$$

and

$$R^2 = 1 - \frac{\sum_{i=1}^{n}\left(s_i - \hat{s}_p(\tilde{y}_i)\right)^2}{\sum_{i=1}^{n}\left(s_i - \bar{s}\right)^2},$$

where s_i denotes the observed settlement at relative TBM position $\tilde{y}_i$, $\hat{s}_p(\tilde{y}_i)$ the corresponding model prediction, $\bar{s}$ the mean of the observed settlements, and n the number of observations.

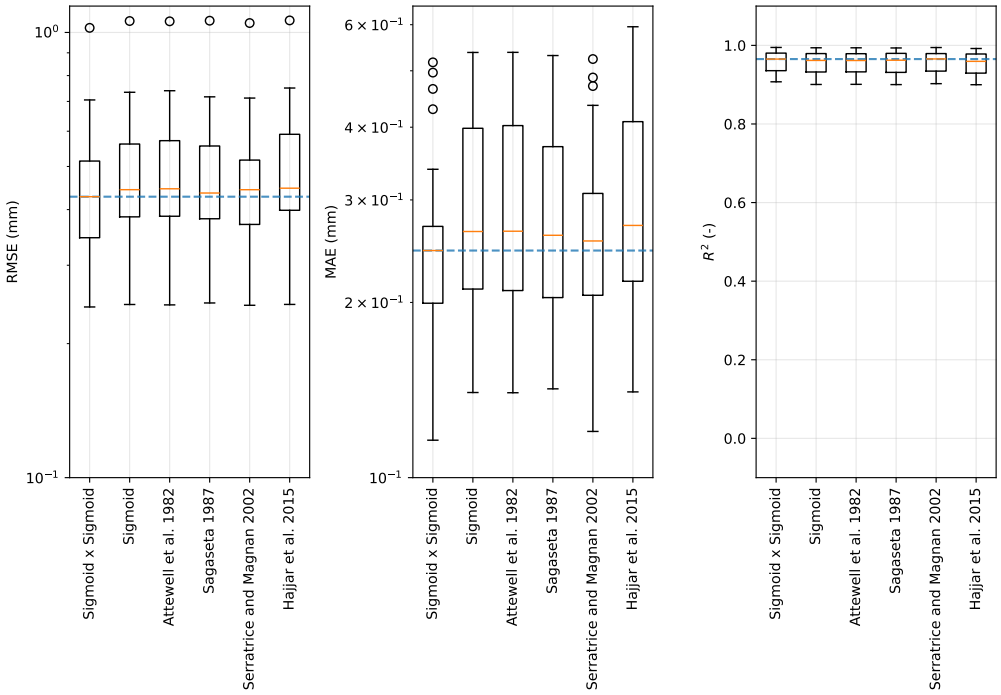

Figure 5.8: Comparison of longitudinal settlement models on a subset of prisms with low noise and no significant outliers (22 prisms). Boxplots of RMSE, MAE, and R^2 are shown for each model. The orange marker indicates the median value for each model. The dashed blue horizontal line corresponds to the median performance of the double-sigmoid model, which is used as a reference. Overall, the double-sigmoid model (Eq. (5.5)) provides the best performance on this dataset.

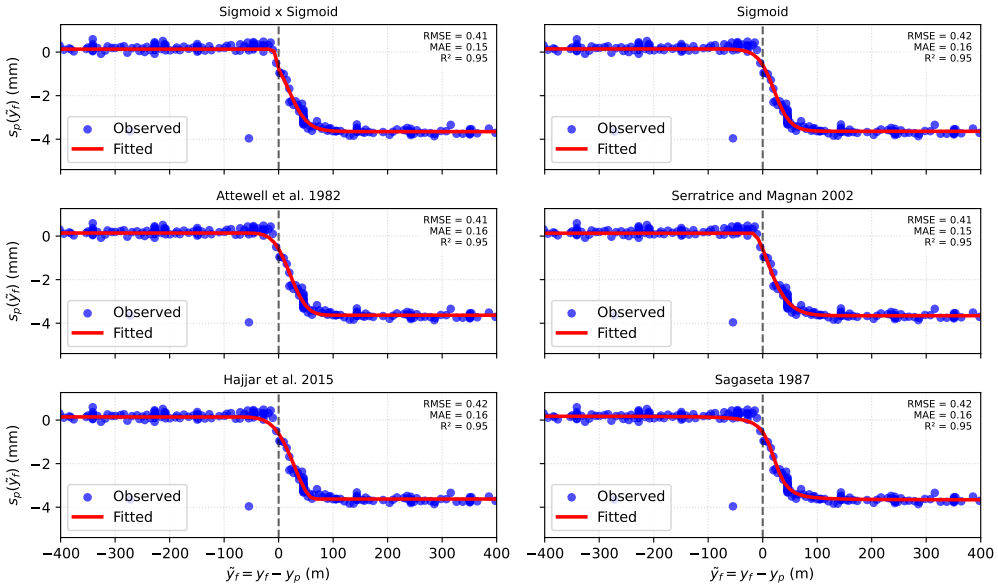

Figure 5.9: Observed longitudinal settlements at the prism `STA32_7` (blue dots) as a function of the relative TBM position $\tilde{y}_f = y_f - y_p$. The evolution follows a characteristic S-shaped pattern: negligible deformation ahead of the face ($\tilde{y}_f \ll 0$), a sharp drop near $\tilde{y}_f \approx 0$, and progressive stabilization toward steady-state. The double-sigmoid (Eq. (5.5)) and Serratrice (Eq. (5.6)) models demonstrate better accuracy in capturing the transition zone and post-face stabilization compared to symmetric formulations.

Figure 5.9 illustrates representative estimation results for prism `STA32_7`. Both the Serratrice model (Eq. (5.6)) and the double-sigmoid formulation (Eq. (5.5)) better capture the asymmetric settlement evolution.

Specifically, they represent the sharp transition during TBM passage and the subsequent gradual stabilization phase, which are often over-smoothed by symmetric formulations.

However, the benchmark results obtained on the low-noise dataset (Figure 5.8) show that the double-sigmoid model consistently achieves the best overall performance. It is therefore retained as the reference longitudinal settlement model in the following.

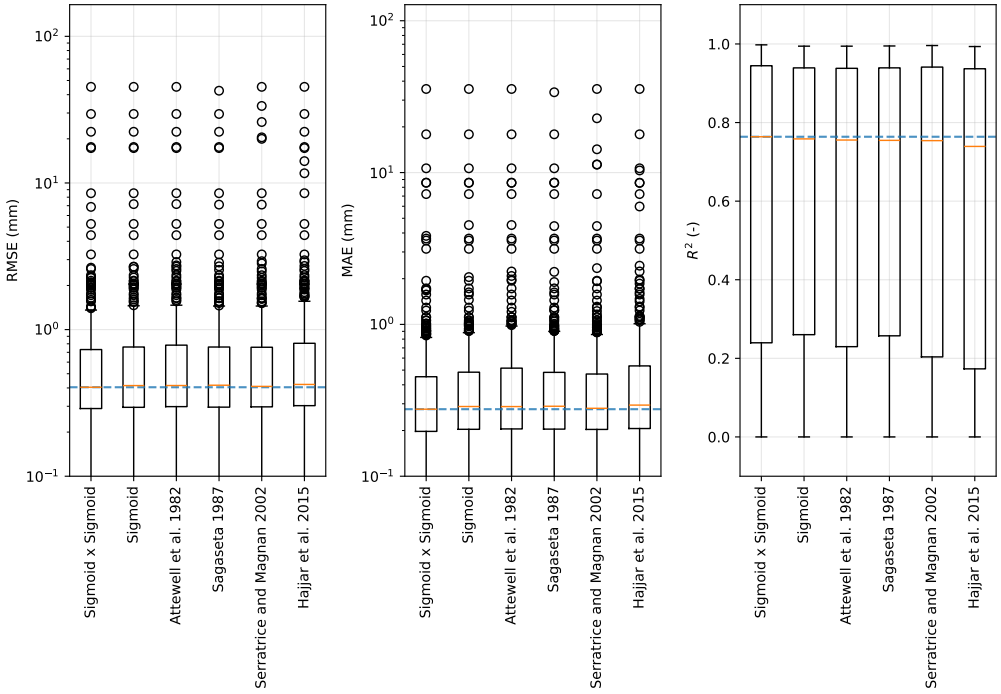

Figure 5.10: Comparison of longitudinal settlement models on the full monitoring dataset (634 prisms). The description is identical to that of Figure 5.8. For this dataset, the performance metrics exhibit a high variability across all models, indicating that some prisms are well fitted while others are not.

The results obtained on the full dataset (Figure 5.10) show a large variability in fit quality across prisms when using OLS. This variability is mainly driven by noise, outliers, and, more rarely, severely corrupted measurements, rather than by intrinsic limitations of the longitudinal models.

This motivates the use of M-estimators and, for the most severely corrupted prisms, the application of the RANSAC algorithm.

Robustness to noise and outliers

To address the limitations of OLS in the presence of noise and outliers, we compare several regression strategies. Four estimators are considered: OLS, M-estimation with a Huber loss function, M-estimation with a Soft-L1 loss function, and the RANSAC algorithm.

Four representative prisms are selected to illustrate the behavior of the regression strategies. A first prism without corrupted measurements is analyzed (Figure 5.11), followed by three prisms affected by significant noise and outliers, selected from the most degraded measurement cases (Figures 5.12, 5.13, and 5.14).

For the RANSAC-based regression, the following parameters are used in the presented examples: a residual threshold of 1.25 mm to classify observations as inliers, a minimum inlier ratio of 75%, and a sampling proportion $p = 30\%$ of the initial dataset. The number of iterations is set to $n_{\text{iter}} = 5000$ to ensure a high probability of selecting an outlier-free subset.

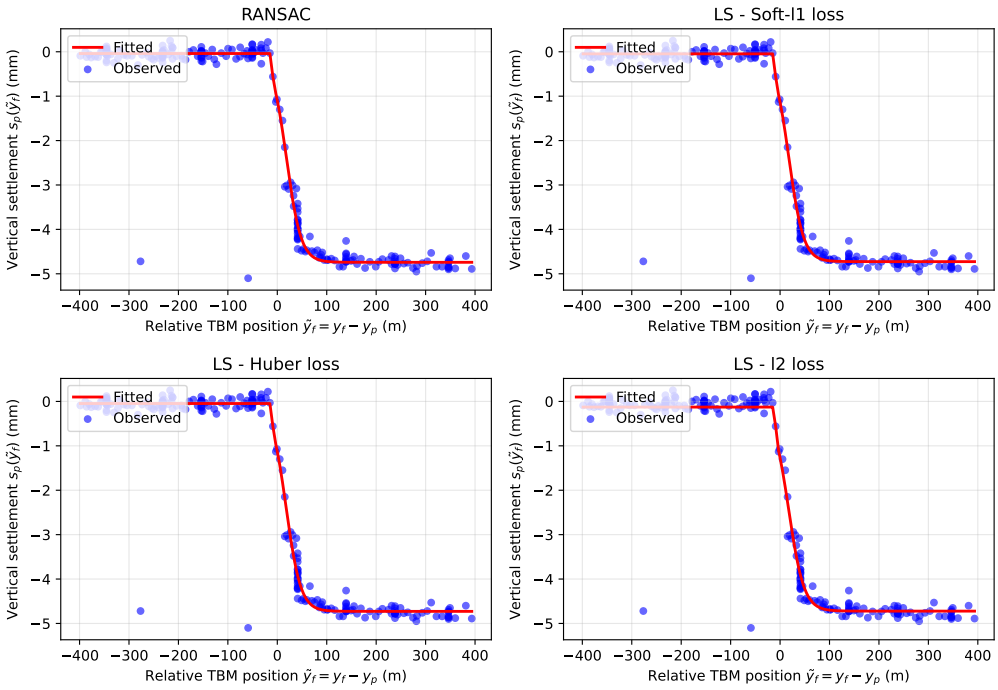

Figure 5.11: Example 1 - Comparison of regression strategies for prism `STA32_9`, in the absence of corrupted measurements. Observed settlements are shown in blue, and fitted longitudinal models in red. OLS (L2 loss), M-estimators (Huber and Soft-L1), and RANSAC all successfully recover the settlement trend for this prism.

Figure 5.11 indicates that, in a low-noise setting, all considered regression strategies lead to comparable and satisfactory fits.

In the presence of noise and outliers, OLS performance degrades. Figure 5.14 shows that OLS rapidly deteriorates and fails to capture the settlement evolution.

M-estimation generally improves robustness and remains satisfactory in moderately corrupted cases, as illustrated in Figure 5.14. However, when the level of corruption increases, such as in Figures 5.12 and 5.13, M-estimators are no longer able to recover the underlying settlement trend.

RANSAC can, in some situations, recover the expected behavior, as observed for prisms `STA8_26` (Figure 5.13). Nevertheless, its performance is not consistent, and it may also

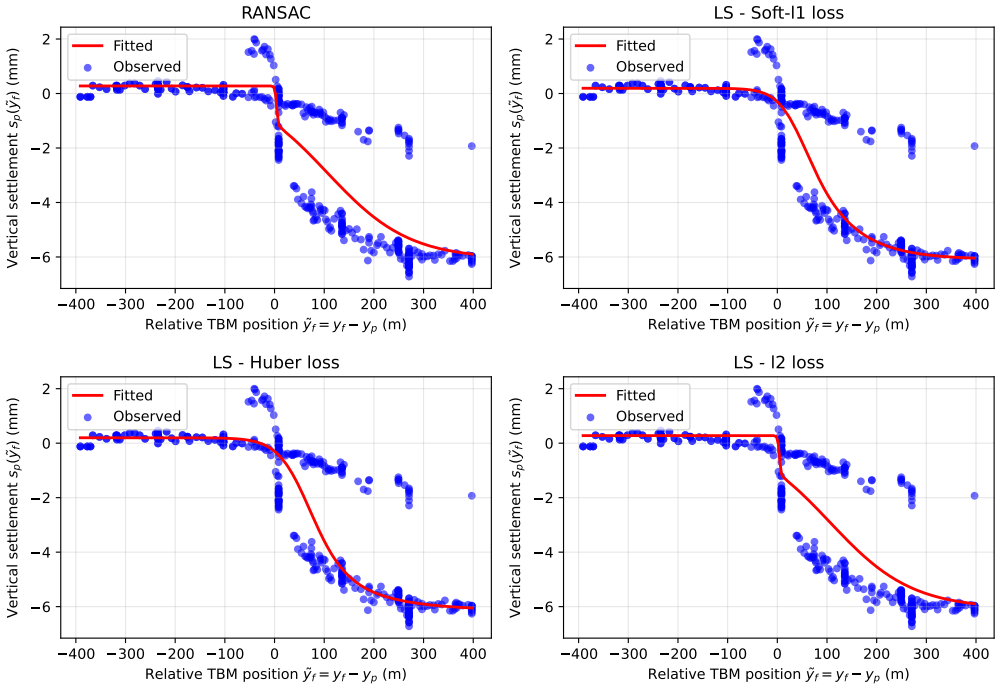

Figure 5.12: Example 2 - Comparison of regression strategies for prism `STA8_25`, affected by corrupted measurements. Observed settlements are shown in blue, and fitted longitudinal models in red. OLS (L2 loss), M-estimators (Huber and Soft-L1), and RANSAC fail to provide satisfactory fits for this prism. RANSAC hyperparameters may require adjustment.

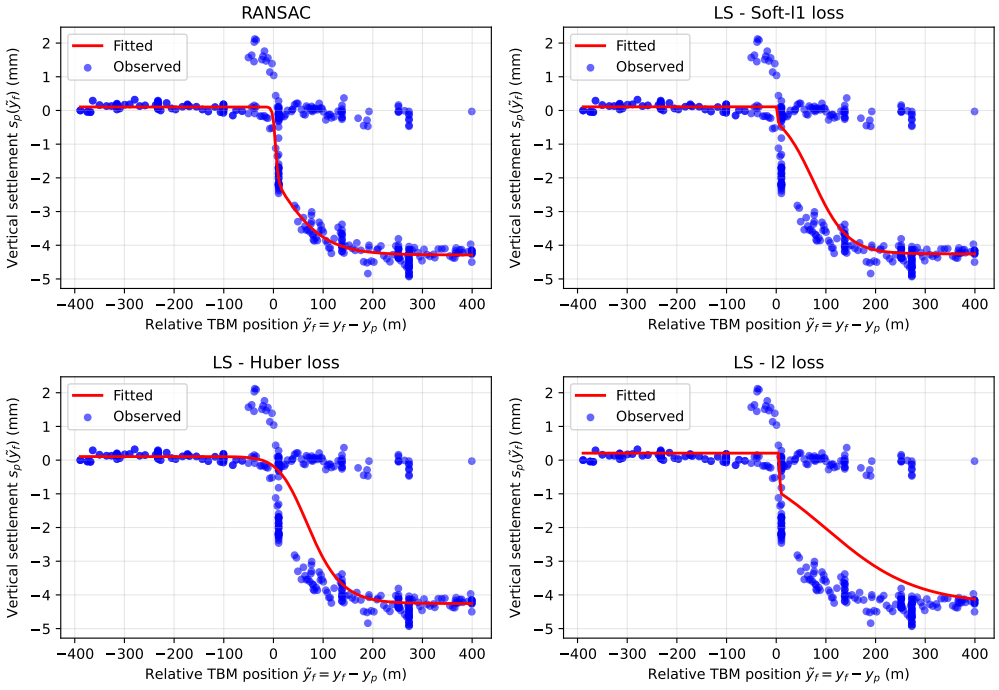

Figure 5.13: Example 3 - Comparison of regression strategies for prism `STA8_26`, affected by corrupted measurements. Observed settlements are shown in blue, and fitted longitudinal models in red. OLS (L2 loss) and M-estimators (Huber and Soft-L1) remain influenced by outliers, whereas RANSAC successfully retrieves the settlement trend for this prism.

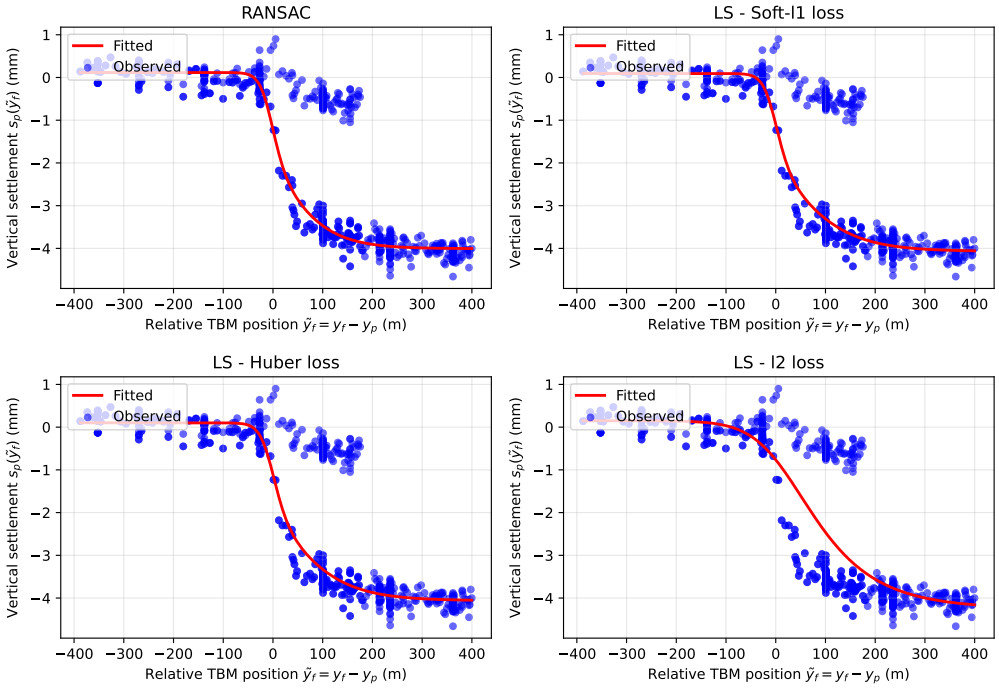

Figure 5.14: Example 4 - Comparison of regression strategies for prism `STA9_30`, affected by corrupted measurements. Observed settlements are shown in blue, and fitted longitudinal models in red. OLS (L2 loss) remains influenced by outliers. In contrast, M-estimation and RANSAC provide the best fit, regardless of whether the Soft-L1 or Huber loss function is used.

fail to provide a satisfactory fit, as shown in Figure 5.12. This variability is mainly due to its sensitivity to user-defined parameters, in particular the sampling proportion p and the residual threshold.

As a result, RANSAC requires case-specific tuning, which limits its use as a general processing strategy across all prisms. Based on these results, the processing strategy relies on M-estimators with a Huber loss function for the calibration of longitudinal settlement models. The Soft-L1 loss yields very similar results and is therefore not considered separately. RANSAC is only applied in a second stage to a limited number of prisms for which M-estimation fails, typically due to a high proportion of corrupted measurements.

5.4 Reconstruction of 2D total settlement maps

At this stage, each survey prism is associated with a calibrated longitudinal settlement model $s_p(\tilde{y}_f; \hat{\boldsymbol{\theta}}_p)$, obtained using the regression strategies described in the previous sections.

The question addressed in this section is: how to reconstruct a continuous surface settlement field at a given TBM position y_f?

5.4.1 Monitoring window definition

To analyse the evolution of settlements, a surface monitoring line is defined at a reference position y_{ML} along the tunnel axis. This definition is consistent with the outputs of the numerical simulation (see Section 3.3.2) and enables direct comparison.

To retain only the monitoring data relevant to this section, a rectangular selection window is introduced around the monitoring line (Figure 5.15). The window is defined by a longitudinal half-length d_{box} and a transverse half-width l_{box}. Only survey prisms located inside this window are retained for the reconstruction of transverse settlement profiles.

The reconstruction is performed at discrete TBM positions $y_f(k) = y_k$, sampled at a constant longitudinal increment δy_f, where k denotes the discrete position index. In the following, $\delta y_f = 2$ m is adopted, consistent with the excavation step used in the numerical simulations. The initial TBM position is chosen such that the excavation face lies outside the monitoring window, ensuring negligible predicted settlements at the beginning of the reconstruction.

5.4.2 GP reconstruction of total settlement maps

At each TBM position y_k, prism settlements are evaluated as $s_p^{(k)} = s_p(y_k - y_p; \hat{\boldsymbol{\theta}}_p)$, yielding the scattered dataset $\{(x_p, y_p, s_p^{(k)})\}_p$.

A GP is used to reconstruct a continuous settlement field from prism-level estimates. A zero-mean GP prior is assumed for the latent settlement field, such that

$$s_v(\cdot, \cdot; y_f) \sim \mathcal{GP}\left(0, k((x, y), (x', y'))\right),$$

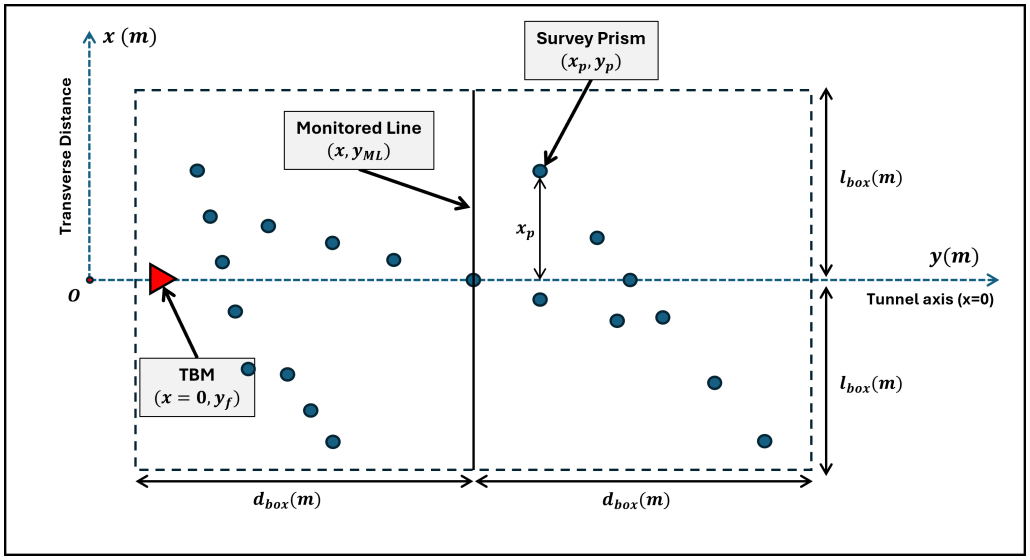

Figure 5.15: Definition of the transverse monitoring window. The monitoring line is located at abscissa y_{ML} along the tunnel axis. A rectangular window, defined by a longitudinal half-length d_{box} and a transverse half-width l_{box}, is used to select the prisms contributing to the reconstruction of dynamic transverse settlement profiles.

and the prism-level observations are modeled as noisy evaluations of this latent field. For any spatial position (x, y),

$$s_v^{\text{obs}}(x, y; y_f) = s_v(x, y; y_f) + \varepsilon(x, y),$$

where $\varepsilon(x, y)$ is a zero-mean noise term with variance σ^2_{noise}. In matrix form, this corresponds to adding a nugget term $\sigma^2_{\text{noise}}\mathbf{I}$ to the covariance of the observations.

An anisotropic squared exponential covariance kernel is adopted:

$$k((x, y), (x', y')) = \sigma^2 \exp\left(-\frac{(x - x')^2}{2\ell_x^2} - \frac{(y - y')^2}{2\ell_y^2}\right),$$

where σ^2 denotes the process variance, controlling the overall amplitude of the settlement field, and ℓ_x and ℓ_y are the transverse and longitudinal length-scale parameters, respectively.

The GP hyperparameters are fixed rather than estimated by likelihood maximisation. In practice, the transverse length-scale ℓ_x is chosen to be of the same order of magnitude as the transverse influence distance i_x of the settlement trough (Peck, 1969).

Along the longitudinal direction, the monitoring data are sparse, with large gaps between sensors. A large longitudinal correlation length is prescribed to stabilize the reconstruction ($\ell_y = 50$ m).

5.4.3 Reconstructed total settlement maps

Once all longitudinal settlement models have been calibrated, each survey prism p is associated with a parameter vector $\hat{\boldsymbol{\theta}}_p$ defining its longitudinal settlement evolution, here illustrated using the double-sigmoid model (Eq (5.5)).

As a reminder, the ML is defined at position $y_{ML} = 2005$ m along the tunnel axis in the coordinate system considered, selected to represent the numerical simulation context. A rectangular selection window is introduced around this line, with a longitudinal half-length $d_{box} = 200$ m and a transverse half-width $l_{box} = 40$ m.

Surface settlements are reconstructed using a zero-mean GP regression model with an anisotropic squared exponential covariance kernel. The correlation length-scales are fixed to $\ell_x = 20$ m in the transverse direction and $\ell_y = 50$ m in the longitudinal direction, the latter being chosen sufficiently large to preserve long-range longitudinal correlations. A measurement noise variance of 0.01 is assumed, and the process variance is set to $\sigma^2 = 1$. GP regression is implemented using the `GPy` library (GPy, since 2012).

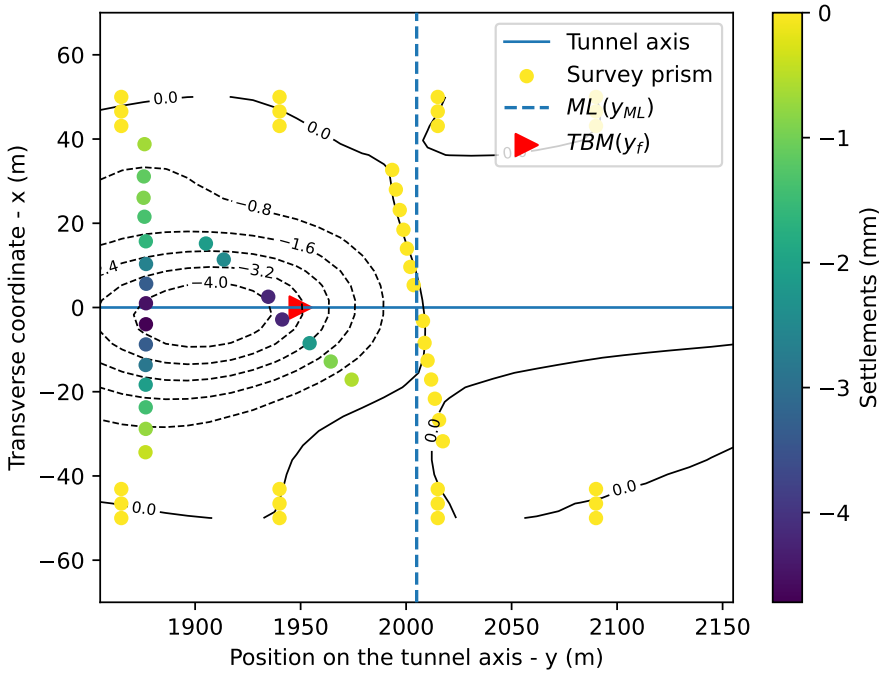

Figure 5.16: Total settlement map reconstructed at TBM position $y_f = y_{ML} - 55$ m. Survey prisms are shown as colored points according to their vertical settlement values (in millimetres). Iso-settlement contours correspond to the posterior mean of the GP. The triangle indicates the TBM position, with excavation progressing in the positive longitudinal direction. The dashed line denotes the monitored transverse section located at $y = y_{ML}$. At this stage, the TBM has not yet passed the ML.

Figures 5.16 and 5.17 illustrate examples of reconstructed total settlement maps obtained using GP regression, before and after TBM passage.

Based on these total settlement maps at different TBM positions y_k, the next step is to reconstruct dynamic transverse settlement profiles in order to estimate the QoIs.

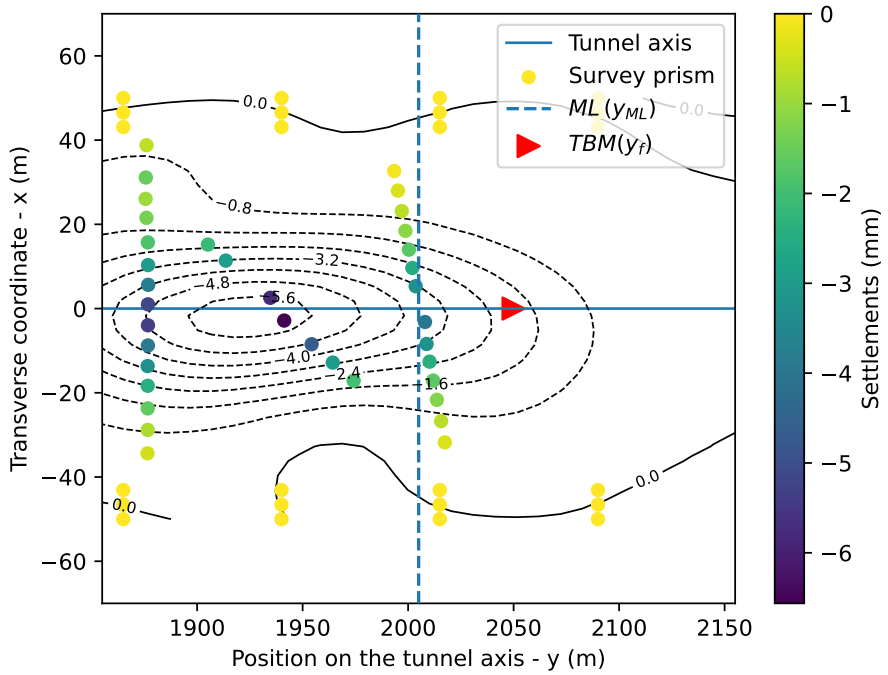

Figure 5.17: Total settlement map reconstructed at TBM position $y_f = y_{ML} + 45$ m. Same description as Figure 5.16. At this stage, the TBM has passed the ML.

5.5 Reconstruction of dynamic transverse settlement profiles

The question addressed in this section is the following: how can dynamic transverse settlement profiles be reconstructed from these maps in a way that is consistent with the representations used in numerical simulations?

This section focuses on a reference transverse position y_{ML} along the tunnel axis, at which dynamic settlement profiles are constructed and compared with numerical simulation results.

5.5.1 Dynamic transverse settlement reconstruction algorithm

Using a sequence of total settlement maps at different TBM positions y_k, dynamic transverse settlement profiles are reconstructed along the monitoring line (see Figure 5.15).

The reconstruction procedure is summarized in Algorithm 3. At each TBM position y_k, settlement estimates at the prism locations are obtained from the calibrated longitudinal models and used to condition a GP. The posterior GP mean is then evaluated along the transverse monitoring line $y = y_{ML}$ (see Eq. (4.12) of Section 4.2.1 for the analytical expression of the GP posterior mean, also referred to as the kriging predictor).

This procedure yields a dynamic transverse settlement field $\hat{s}_v(x, y_{ML}; y_f)$. This field

is then used to estimate the QoIs in the same manner as for the surface settlement outputs of the numerical simulator (see Section 3.3.3).

Algorithm 3 Dynamic transverse settlement reconstruction algorithm

Require: Prism locations (x_p, y_p), calibrated longitudinal models $s_p(\cdot; \hat{\boldsymbol{\theta}}_p)$, reference section y_{ML}, window sizes (d_{box}, l_{box}), TBM step δy_f, GP hyperparameters $(\sigma, \sigma_{\text{noise}}, \ell_x, \ell_y)$

Ensure: Dynamic transverse settlement profiles $\hat{s}_v(x, y_{ML}; y_f)$

1: Select survey prisms located within the monitoring window
2: **for** each TBM position y_k **do**
3: **for** each selected prism p **do**
4: $\tilde{y}_{k,p} = y_k - y_p$
5: $s_p^{(k)} \leftarrow s_p(\tilde{y}_{k,p}; \hat{\boldsymbol{\theta}}_p)$
6: **end for**
7: Construct the training dataset $\mathcal{D}^{(k)} = \{(x_p, y_p, s_p^{(k)})\}_p$
8: Define a GP prior with zero mean and covariance $k(\cdot, \cdot; \sigma, \ell_x, \ell_y)$
9: Evaluate the posterior GP mean (conditioned on $\mathcal{D}^{(k)}$) $m_n(x_i, y_{ML})$, with n the size of $\mathcal{D}^{(k)}$.
10: **end for**
11: **return** dynamic transverse settlement profiles $\{\hat{s}_v(x_i, y_{ML}; y_k)\}_{i,k}$

5.5.2 Reconstructed dynamic transverse profiles

The reconstruction algorithm is applied to the same area as that considered in Section 4.2.2, where the numerical simulations are performed, in the considered coordinate system at the reference chainage y_{ML}. The same GP hyperparameters as in Section 5.4.3 are used.

In the coordinate system considered, the TBM position varies from $y_k = y_{ML} - 200$ m to $y_k = y_{ML} + 200$ m, with a sampling step of 2 m. A sequence of transverse settlement profiles is thus obtained, which defines a dynamic transverse settlement representation.

Figures 5.18 and 5.19 present this representation at the ML y_{ML}, using two different transverse length-scales, namely $\ell_x = 20$ m and $\ell_x = 5$ m. In each figure, the left panel shows selected transverse settlement profiles at specific TBM positions, while the right panel displays the evolution of settlements at the ML as a color map with a finer longitudinal resolution ($\delta y_f = 2$ m). Both representations describe the same settlement evolution at the ML y_{ML}.

Comparing Figures 5.18 and 5.19 shows that using a smaller transverse length-scale ℓ_x increases the variability of the reconstructed transverse settlement profiles. While this leads to shapes closer to the observed settlement troughs, it also increases sensitivity to measurement noise and complicates comparison with numerical simulations, which do not explicitly account for all sources of spatial heterogeneity.

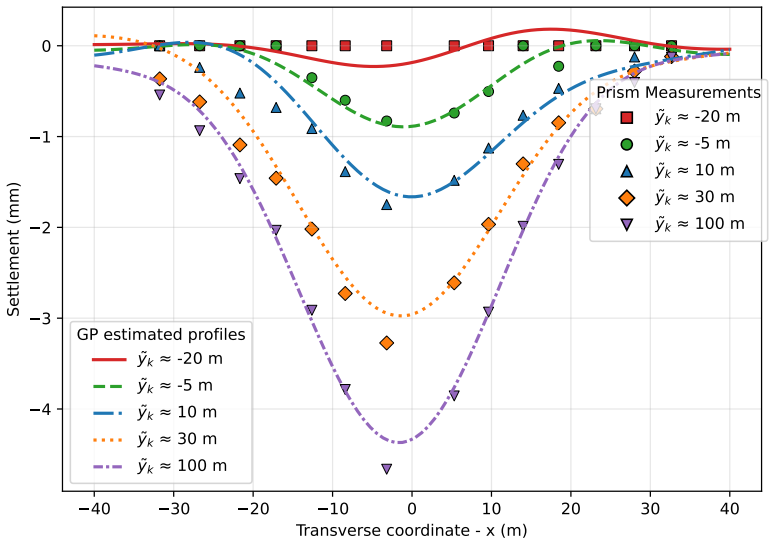

(a) Five transverse settlement profiles at y_{ML} for five selected TBM positions.

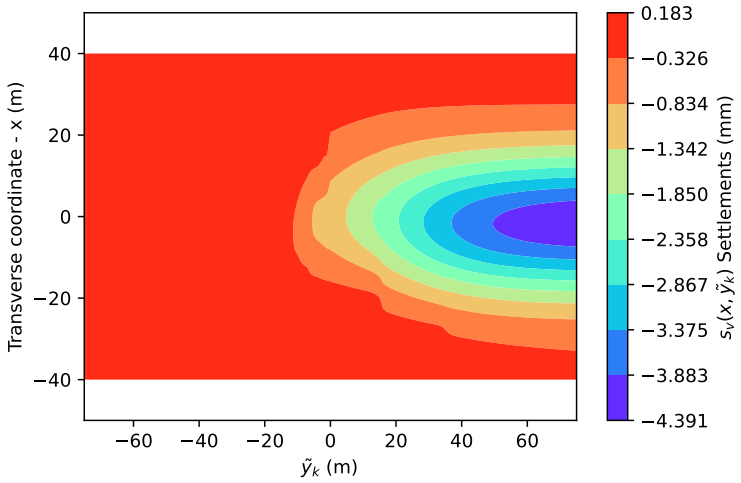

(b) The color plot of longitudinal settlement evolution at y_{ML} = 2005 m.

Figure 5.18: Two representations showing the same settlement evolution at the monitoring line y_{ML}. In the left figure, five transverse settlement profiles are shown for selected TBM positions. Each line corresponds to a given TBM position and represents the estimate provided by the posterior mean of the GP, together with the corresponding prism observations used for the reconstruction. Here, a larger transverse length-scale $\ell_x = 20$ m is used to increase smoothness in the transverse direction. The other parameters remain unchanged. The GP hyperparameters are fixed and not optimized. The resulting GP prediction provides a representative estimate of the settlement trough at each TBM position, consistent with the observed prism settlements.

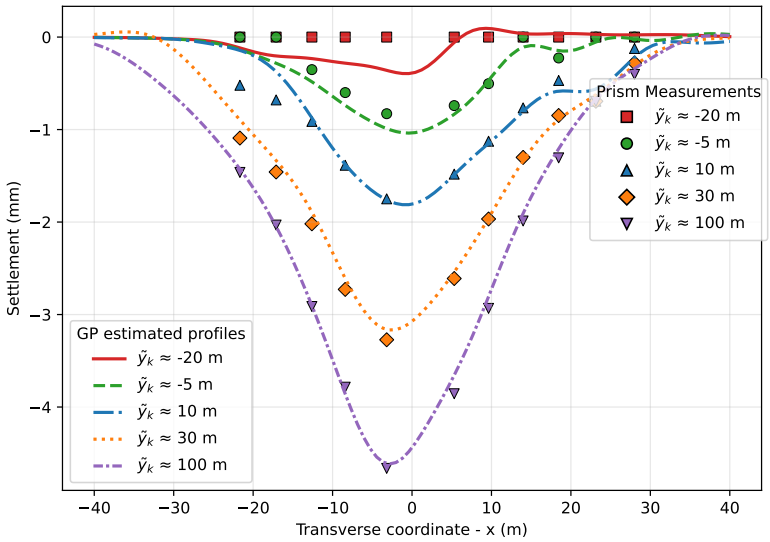

(a) Five transverse settlement profiles at $y_{ML} = 2005$ m for selected TBM positions.

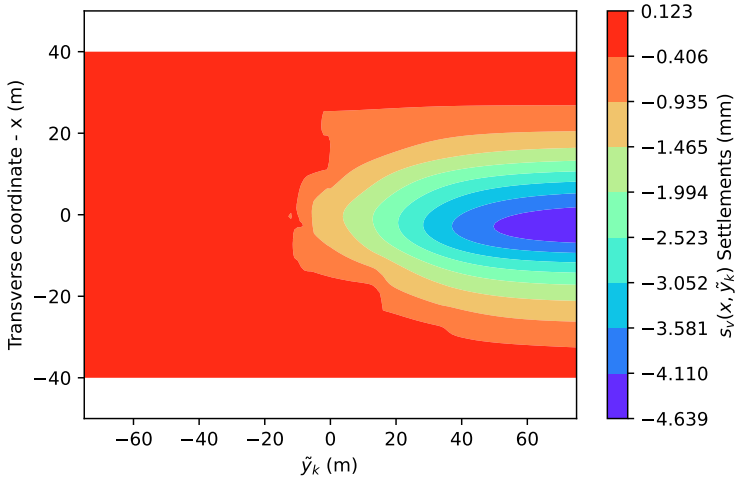

(b) Dynamic longitudinal representation of settlements at $y_{ML} = 2005$ m.

Figure 5.19: Same representation as Figure 5.18, using a smaller transverse length-scale $\ell_x = 5$ m. All other parameters are unchanged.

5.6 Conclusions and discussions

This chapter presents a comprehensive processing methodology designed to construct settlement representations for direct comparison with FE simulator results.

Among the reviewed parametric longitudinal settlement models, the double-sigmoid formulation (Eq. (5.5)) is selected as the most representative for fitting longitudinal monitoring data, as it accurately reproduces the asymmetric behavior observed before and after the TBM passage. These models are calibrated at the prism level using M-estimation with a Huber loss function to mitigate the influence of noise and outliers. In cases where M-estimation fails to provide satisfactory results, the RANSAC algorithm is applied as a robust alternative.

Based on the resulting fitted models, GP regression is used to reconstruct total settlement maps. By repeating this reconstruction at successive TBM positions, a dynamic representation of transverse settlement is obtained for a given ML. An illustrative example is presented for a ML located at y_{ML}, corresponding to the geotechnical context analyzed in Section 4.2.2 of Chapter 4.

Using the dynamic transverse profiles shown in Figures 5.18 and 5.19, the QoIs defined in Section 3.3.3 of Chapter 3 are estimated. The estimation follows the same approach as that described in Section 3.3.3. Along the ML, the estimated values are $z_{1,\text{obs}} = 4.5$ mm, $z_{2,\text{obs}} = 37$ m, $z_{3,\text{obs}} = 12.9$ m, and $z_{4,\text{obs}} = 18.6$ m.

These values are compared with the design of experiments performed with the numerical simulator for this specific ML (see Figure 4.9 in Chapter 4). While the maximum settlement (z_1) and the settlement width (z_2) lie within the boundaries of the design of experiments, the longitudinal QoIs (z_3 and z_4) fall outside this range.

In addition to the discrepancies between the simulated (z_3, z_4) and observed ($z_{3,\text{obs}}, z_{4,\text{obs}}$) values, a structural difference in longitudinal behavior is identified: the numerical simulator results are well-represented by a standard sigmoid function (see Section 3.3.3 of Chapter 3), whereas the monitoring data are better described by a double-sigmoid formulation. This suggests that the FE simulator does not capture the asymmetric longitudinal evolution observed during the TBM excavation.

However, as $z_{1,\text{obs}}$ and $z_{2,\text{obs}}$ remain within the design of experiments boundaries, the objective is now to identify the ranges of geological properties for the SO and SB layers that yield these specific observations. To achieve this, the following chapter introduces Bayesian Subset Simulation for set inversion.

Chapter 6

Bayesian subset simulation for set inversion

Chapter overview. This chapter addresses Bayesian set inversion for an expensive tunnel-excavation simulator. The objective is to identify the set of input configurations consistent with observed quantities of interest (QoIs), rather than a single optimal parameter vector. The proposed approach adapts Bayesian subset simulation to set inversion by combining a Gaussian process (GP) metamodel with a sequential Monte Carlo scheme. A sequence of relaxation levels progressively concentrates a particle population toward the target inversion set, yielding a stochastic approximation of the admissible set. A key contribution is the introduction of diagnostic metrics that separate GP-induced and SMC-induced uncertainties. These metrics quantify inversion accuracy and guide the selection of model enrichment strategies, particle population size, and relaxation scheduling.

The chapter is organized as follows. Section 6.1 introduces the set inversion framework. Section 6.2 recalls the main ingredients of BSS adapted to this context. Section 6.3 details the proposed inversion procedure. Section 6.4 presents the diagnostic metrics. Section 6.5 provides numerical illustrations on a one-dimensional test case, and Section 6.6 presents applications to the Hartmann 4 function and to a three-dimensional (3D) finite element (FE) tunnel model. Section 6.7 concludes the chapter.

6.1 From inverse problem to set inversion

Using the processed settlement monitoring data (see Chapter 5), we aim to identify the set of input parameters of the TBM FE simulator that are consistent with the observed soil response.

Classical inverse methods estimate a single parameter vector by minimizing a mismatch between observations and model outputs (Maximum Likelihood Estimator (MLE) / Maximum A Posteriori (MAP) formulations) (Kaipio and Somersalo, 2005; Stuart, 2010). In many geotechnical applications, however, the inverse problem suffers from identifiability issues due to the large number of uncertain parameters: distinct parameter combinations can produce very similar responses and explain the data almost equally well.

To address this issue, we adopt a *set inversion* viewpoint (Jaulin and Walter, 1993). Instead of searching for a single optimum, the objective is to recover the admissible set of

inputs that satisfy output constraints.

The link with the inverse problem is straightforward. Assume that an observed QoIs $\mathbf{z}_{\text{obs}}$ is available and that model outputs are deemed acceptable when they fall within a prescribed tolerance box $\mathcal{B}_{\text{target}}$ around $\mathbf{z}_{\text{obs}}$. The calibration problem is then no longer "find the best $\mathbf{x}$", but rather "find all $\mathbf{x}$ such that $f(\mathbf{x}) \in \mathcal{B}_{\text{target}}$". This is precisely a set inversion problem.

In the deterministic case, the associated admissible set is defined as

$$\mathbf{\Gamma} = \{\mathbf{x} \in \mathcal{X} : \ f(\mathbf{x}) \in \mathcal{B}_{\text{target}}\}. \tag{6.1}$$

When the tolerance box is narrow relative to the range of possible simulator outputs, the admissible set $\mathbf{\Gamma}$ is typically small relative to the input domain $\mathcal{X}$.

If $\mathcal{X}$ is equipped with an input distribution $P_{\mathcal{X}}$, the probability mass of the admissible set defined in Eq. (6.1) is

$$\alpha = \mathbb{P}_{\mathcal{X}}(\mathbf{\Gamma}). \tag{6.2}$$

When $\mathbf{\Gamma}$ has a small probability mass (Eq. (6.2)) under $P_{\mathcal{X}}$, direct Monte Carlo exploration becomes inefficient for two reasons. First, if one samples $\mathbf{x} \sim P_{\mathcal{X}}$ and checks whether $\mathbf{x} \in \mathbf{\Gamma}$, successful samples are rare, so a large number of samples is required to estimate α with acceptable precision. The coefficient of variation of a crude Monte Carlo estimator $\hat{\alpha}$ satisfies $\text{cv}(\hat{\alpha}) \approx \sqrt{\frac{1-\alpha}{N\alpha}}$, where N is the number of samples. For instance, if $\alpha = 10^{-3}$, about $N = 10^5$ samples are required to achieve a coefficient of variation close to 10%.

Second, in the present setting, each sample may require an expensive FE simulation, making such sample sizes impractical. Subset simulation (SuS) (Au and Beck, 2001), implemented through sequential Monte Carlo (SMC) methods (Cérou et al., 2012), was originally introduced to estimate small probabilities of excursion or failure by replacing a rare event with a sequence of less rare nested events. In contrast to standard Monte Carlo approaches based on independent samples $\mathbf{x} \sim P_{\mathcal{X}}$, SMC relies on a population of N_p **particles** $\{Y^{(i)}\}_{i=1}^{N_p}$, which are sequentially propagated across a sequence of intermediate distributions associated with these nested events of increasing rarity. As a result, the particle population progressively concentrates in the region corresponding to the rare event of interest.

Bayesian subset simulation (BSS) (Bect et al., 2017) adds a GP metamodel and a sequential design strategy, so that the expensive simulator is evaluated only at selected design points while the SMC scheme is mainly driven by the metamodel.

In this chapter, we adapt this machinery from probability estimation to set reconstruction. The objective is not only to estimate the probability mass of the inversion set, but also to characterize its geometry in the input space, i.e., to reconstruct the inverse image of a target output set.

To this end, we introduce a sequence of relaxed output sets and use SuS/BSS to progressively concentrate particles toward the target inversion set. Related probabilistic formulations have also been proposed (Ait Abdelmalek-Lomenech et al., 2025).

6.2 Subset simulation, BSS, and set inversion

Before presenting the proposed method, it is useful to distinguish SuS from BSS. Subset simulation (SuS) is a particle-based strategy for rare-event estimation: a difficult target event is replaced by a sequence of nested events, and a population of particles is successively reweighted, resampled, and moved from one level to the next. BSS (Bect et al., 2017) keeps this sequential structure but replaces the true simulator by a GP metamodel over most of the input space, while an adaptive design strategy selects additional simulator evaluations in regions where the metamodel must be improved.

In standard reliability applications, the main output of SuS or BSS is a scalar probability associated with a failure or excursion event. Here, the object of interest is instead a set. This section therefore recalls the SuS and BSS ingredients and explains how they are reformulated for set inversion. For clarity, the exposition starts with the scalar-output case $f : \mathcal{X} \to \mathbb{R}$. The presentation is organized in three steps. We first recall the SuS idea of replacing one difficult target set by a sequence of nested relaxed sets. We then explain how SMC propagates a particle population through these levels. Finally, we introduce the GP coverage function, which replaces exact set-membership tests when the simulator is expensive. In the present context, the set of interest $\mathbf{\Gamma}$ is defined as the set of inputs producing simulator outputs within prescribed bounds $\mathcal{B}_{\text{target}} = [a_{\text{target}}, b_{\text{target}}] \subset \mathbb{R}$. Consistently with Eq. (6.1), it reads

$$\mathbf{\Gamma} = \{\mathbf{x} \in \mathcal{X} : f(\mathbf{x}) \in \mathcal{B}_{\text{target}}\}. \tag{6.3}$$

Remark. The framework naturally extends to excursion set problems, where the target set is defined by a one-sided constraint (e.g., $f(\mathbf{x}) > u$). Such formulations are particularly relevant in the context of TBM excavation in urban areas, where the objective is to quantify the probability of exceeding prescribed surface settlement thresholds and to characterize the associated inversion set in order to identify the corresponding input configurations.

Remark. The extension to multi-output problems $f : \mathcal{X} \to \mathbb{R}^q$ is detailed in Appendix P.2.

6.2.1 SuS framework

In this chapter, we present the SuS framework for set inversion. The target region $\mathbf{\Gamma}_T$ is decomposed into a sequence of nested intermediate events, defined through a family of relaxed output sets

$$\mathcal{B}_0 \supset \cdots \supset \mathcal{B}_T,$$

parameterized by a monotone relaxation parameter λ_t,

$$\mathcal{B}_t = [a_{\lambda_t}, b_{\lambda_t}], \qquad 0 = \lambda_0 < \cdots < \lambda_T = 1.$$

Each level induces an input-space set

$$\mathbf{\Gamma}_t = \{\mathbf{x} \in \mathcal{X} : f(\mathbf{x}) \in \mathcal{B}_t\}, \tag{6.4}$$

with $\mathbf{\Gamma}_0 \supset \cdots \supset \mathbf{\Gamma}_T$.

The interest of this construction is that it replaces a difficult target set $\mathbf{\Gamma}_T$, which may have a small probability mass under the input distribution, by a sequence of easier intermediate sets. These intermediate sets are easier to explore because they are less selective than the final one: more particles fall into $\mathbf{\Gamma}_t$ than into $\mathbf{\Gamma}_T$, so the corresponding conditional probabilities are larger and can be estimated with less weight degeneracy and lower Monte Carlo variance. In standard SuS, this makes the estimation problem more stable because the probability of the final set can be factorized as a product of conditional probabilities between successive levels, each chosen to be much less extreme than the final event. As a result, particles that have already reached $\mathbf{\Gamma}_{t-1}$ are much more likely to provide information about $\mathbf{\Gamma}_t$ than particles sampled directly from the initial distribution.

This sequential construction is also what makes SuS effective computationally. Rather than repeatedly sampling the whole input space and wasting most simulations in regions that are clearly outside the target set, the algorithm progressively reallocates the particle population toward the regions that remain compatible with the current relaxation level. The reweight-resample-move steps of SMC then maintain a particle cloud concentrated near the current set while preserving diversity.

In the present set inversion framework, the final target set $\mathbf{\Gamma}_T$ may be small, but the intermediate sets $\mathbf{\Gamma}_t$ are introduced precisely so that the successive transitions are less extreme. SuS is therefore used as a progressive refinement mechanism, where successive relaxation levels correspond to increasing inversion-set accuracy.

The successive levels are explored using a sequential Monte Carlo (SMC) procedure (Cérou et al., 2012; Del Moral et al., 2006; Bect et al., 2017). Starting from an initial population of N_p particles sampled from the input distribution $P_{\mathcal{X}}$ with density $\pi_{\mathcal{X}}$, the particles are iteratively reweighted, resampled, and moved across the relaxation levels according to their membership in $\mathbf{\Gamma}_t$. This process progressively concentrates the particle system toward the target inversion region $\mathbf{\Gamma}_T$.

SMC in a nutshell. SMC can be viewed as a sequential importance-sampling strategy applied to a population of particles. At a given level, each particle receives a weight that measures how compatible it is with the current target set: particles with large weights are likely to belong to the relevant region, whereas particles with small weights are likely to be discarded. A resampling step then replicates the most relevant particles and removes the least relevant ones. Since resampling creates duplicates, a move step is added to perturb the replicated particles and restore diversity while keeping them in regions that are plausible under the current level. Repeating these three operations across relaxation levels yields a particle cloud that progressively tracks the nested sets from $\mathbf{\Gamma}_0$ to $\mathbf{\Gamma}_T$. Figure 6.1 illustrates the SuS logic across two relaxation levels, whereas Figure 6.2 details the three SMC operations at a fixed level.

The resulting particle distribution provides a stochastic approximation of the regions of the input space with high posterior probability of belonging to the inversion set, and forms the main output of the set inversion procedure.

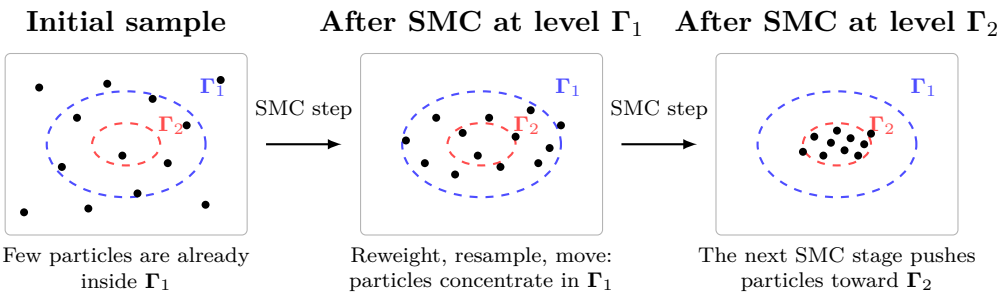

Figure 6.1: Illustration of SuS with two nested subsets, $\mathbf{\Gamma}_2 \subset \mathbf{\Gamma}_1 \subset \mathcal{X}$. Starting from an initial sample drawn in $\mathcal{X}$, an SMC step concentrates the particle population in $\mathbf{\Gamma}_1$. A second SMC step then pushes the particles toward the smaller target set $\mathbf{\Gamma}_2$. At each stage, reweighting favors particles compatible with the current set, resampling replicates the most relevant ones, and the move step restores diversity.

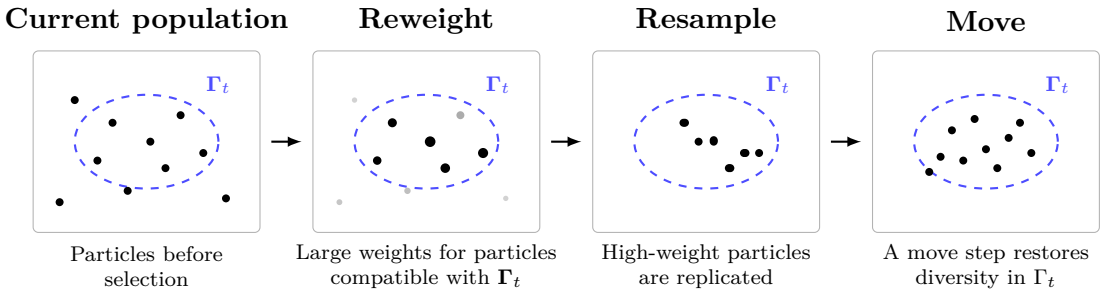

Figure 6.2: Illustration of one SMC transition at a fixed relaxation level $\mathbf{\Gamma}_t$. Reweighting assigns larger weights to particles that are more compatible with the current target set, resampling replicates the most relevant particles, and the move step disperses these replicated particles to restore diversity while keeping them in plausible regions.

6.2.2 GP metamodel

In the Bayesian framework, the simulator f is modeled as a realization of a GP $\xi \sim \mathcal{GP}(m, k)$ with mean function $m(\cdot)$ and covariance kernel $k(\cdot, \cdot)$ encoding prior assumptions (Williams and Rasmussen, 2006; Santner et al., 2003). Given n evaluations at design points $\mathbf{x}_1, \ldots, \mathbf{x}_n$ with outputs $\mathbf{F}_n = \big(f(\mathbf{x}_1), \ldots, f(\mathbf{x}_n)\big)$, the GP posterior is denoted $\xi_n = \xi(\cdot \mid \mathcal{D}_n)$, where $\mathcal{D}_n = \{(\mathbf{x}_i, f(\mathbf{x}_i))\}_{i=1}^n$.

In SuS, membership in the set $\mathbf{\Gamma}_t$ is determined by the indicator $\mathbf{1}_{\mathbf{\Gamma}_t}(\mathbf{x})$. In the present framework, the true simulator output is unknown away from the design points, and classification must rely on the GP model.

To this end, we introduce the posterior coverage function

$$g_{t,n}(\mathbf{x}) = \mathbb{P}\big(\xi(\mathbf{x}) \in \mathcal{B}_t \mid \mathcal{D}_n\big), \tag{6.5}$$

which represents the posterior probability that $f(\mathbf{x})$ lies in the relaxed output set $\mathcal{B}_t$. An analytical expression for $g_{t,n}(\mathbf{x})$ in our setting is provided in Appendix P.1.

The function $g_{t,n}(\mathbf{x})$ acts as a probabilistic classifier of the event $\{f(\mathbf{x}) \in \mathcal{B}_t\}$, encoding the posterior uncertainty of the GP. It can be interpreted as the probabilistic analogue of the indicator function $\mathbf{1}_{\{f(\mathbf{x}) \in \mathcal{B}_t\}}$. In practice, $g_{t,n}(\mathbf{x})$ is used to assess whether a given input $\mathbf{x}$ is likely to belong to the current relaxed inversion set.

6.3 BSS for set inversion

6.3.1 Set inversion procedure

In Algorithm 4, we perform set inversion within the BSS framework under a fixed experimental design $\mathcal{D}_n$, meaning that the GP metamodel is not updated during the SMC stages. This can be viewed as applying a SuS scheme to the GP metamodel conditioned on the fixed design.

A sequence of relaxation parameters $\{\lambda_t\}_{t=0}^T$ defines progressively finer target sets $\mathcal{B}_t$ and associated inversion regions $\mathbf{\Gamma}_t$. The procedure initializes a particle population from the prior distribution and propagates it through successive relaxation levels using SMC steps, while relying on the GP-based coverage function defined at Eq. 6.5.

At a practical level, the aim is simple: at each relaxation level, we want the particles to concentrate in input regions that remain plausible under the prior and are likely, according to the GP, to belong to the current relaxed inversion set. The density introduced below formalizes this idea.

At relaxation level t, the particle system targets the density

$$q_{t,n}(\mathbf{x}) \propto g_{t,n}(\mathbf{x}) \pi_{\mathcal{X}}(\mathbf{x}), \tag{6.6}$$

where $\pi_{\mathcal{X}}$ denotes the density of the input distribution $P_{\mathcal{X}}$ and $g_{t,n}(\mathbf{x})$ is the GP-based coverage function associated with $\mathcal{B}_t$. Intuitively, $q_{t,n}$ gives more weight to input regions that are both probable under the prior and likely, according to the GP, to belong to the current relaxed inversion set.

In other words, $q_{t,n}$ is the auxiliary sampling distribution used by the SMC algorithm at level t. It steers the particle cloud toward the part of the input space that is most relevant for the current relaxed inversion set. Points that are implausible under $P_{\mathcal{X}}$ or unlikely to belong to $\mathbf{\Gamma}_t$ receive little weight under $q_{t,n}$.

This interpretation becomes particularly clear in the ideal case where the GP classification is exact, so that $g_{t,n}(\mathbf{x}) = \mathbf{1}_{\mathbf{\Gamma}_t}(\mathbf{x})$. Then $q_{t,n}$ reduces, up to normalization, to $\mathbf{1}_{\mathbf{\Gamma}_t}(\mathbf{x})\pi_{\mathcal{X}}(\mathbf{x})$, that is, the input distribution restricted to the set $\mathbf{\Gamma}_t$. The density $q_{t,n}$ can therefore be viewed as a metamodel-based approximation of the input distribution conditioned on the current relaxed inversion set.

Remark. The notation $\propto$ emphasizes that, for the SMC steps, the target density (Eq. (6.6)) only needs to be known up to a multiplicative normalizing constant. In practice, reweighting depends on ratios of successive target densities, so these constants cancel out. They become explicit only when introducing the normalized density $q_{t,n}$ through $\alpha_{t,n}$ in Section 6.4.

This choice directly explains the SMC reweighting step. Indeed, when moving from level $t-1$ to level t, the importance ratio between successive target densities satisfies

$$\frac{q_{t,n}(\mathbf{x})}{q_{t-1,n}(\mathbf{x})} \propto \frac{g_{t,n}(\mathbf{x})}{g_{t-1,n}(\mathbf{x})}. \tag{6.7}$$

The particle weights are therefore updated using the ratio $g_{t,n}/g_{t-1,n}$, after which resampling and move steps generate a diversified population approximately distributed according to $q_{t,n}$.

Assuming that the GP provides an accurate representation of the simulator in the region of interest, the particle population generated by the algorithm progressively concentrates near the target inversion region $\mathbf{\Gamma}_T$.

Remark. The initial relaxation set $\mathcal{B}_0$ is chosen wide so that $g_{0,n}(\mathbf{x}) \approx 1$ over most of the input space. This ensures well-defined importance weight ratios at the first relaxation step.

Remark. The relaxation sequence (λ_t) should balance conditional probabilities between successive levels so that they are large enough to prevent null weights in SMC reweighting, while avoiding an excessive number of intermediate stages.

Remark. As in Bect et al. (2017), Algorithm 4 may be embedded in an outer adaptive loop to progressively improve the approximation of the inversion set. The relaxation parameter λ_t can be selected adaptively, for instance by prescribing a fixed conditional probability between successive levels (see Appendix P.4) or by using an Effective Sample Size criterion (Del Moral et al., 2012). Additional model evaluations may also be introduced during the procedure until predefined stopping criteria are satisfied (see Appendix P.4). These adaptive extensions are not developed in the present section, which focuses on the fixed-design inversion procedure. They are only discussed as possible outer-loop extensions, or considered comparatively before and after metamodel refinement.

6.3.2 Adaptive design

Once the fixed-design inversion procedure has been specified, the next question is how to enrich the GP when the current design is not sufficiently informative. To this end,

Algorithm 4 BSS for Set Inversion

Goal: progressively concentrate a particle population from $P_{\mathcal{X}}$ toward the target distribution $q_{T,n}$.

Initialization (stage $t = 0$):
Load initial design of experiments $\mathcal{D}_n = \{(\mathbf{x}_i, f(\mathbf{x}_i))\}_{i=1}^n$
Specify the input distribution $P_{\mathcal{X}}$ with density $\pi_{\mathcal{X}}$
Generate N_p i.i.d. particles $\mathbf{Y}_0 = \{Y_0^{(i)}\}_{i=1}^{N_p} \sim P_{\mathcal{X}}$
Define $\mathcal{B}_0$, $\mathcal{B}_T$, and the relaxation grid $\{\lambda_t\}_{t=0}^T$
Compute $\hat{\alpha}_0 \leftarrow \frac{1}{N_p} \sum_{i=1}^{N_p} g_{0,n}(Y_0^{(i)})$
$t \leftarrow 1$
while $t \leq T$ **do**
    Define $\mathcal{B}_t$ and $g_{t,n}(\cdot)$ from λ_t
    SMC step: reweight, resample, and move the particle population
    Reweight:
    Compute unnormalized weights

$$w_t^{(j)} \propto \frac{g_{t,n}(Y_{t-1}^{(j)})}{g_{t-1,n}(Y_{t-1}^{(j)})}$$

    Normalize weights: $\tilde{w}_t^{(j)} = w_t^{(j)} \Big/ \sum_{k=1}^{N_p} w_t^{(k)}$
    Resample:
    Draw $\tilde{\mathbf{Y}}_t$ from $\{Y_{t-1}^{(j)}\}$ according to weights $\tilde{w}_t^{(j)}$
    Move:
    Apply a Markov kernel invariant with respect to $q_{t,n}$ to $\tilde{\mathbf{Y}}_t$ to obtain $\mathbf{Y}_t$
    Increment t
end while
Output: particle population approximately distributed according to

$$q_{T,n}(\mathbf{x}) \propto g_{T,n}(\mathbf{x}) \pi_{\mathcal{X}}(\mathbf{x})$$

new simulator evaluations can be added sequentially. Two main acquisition families are commonly employed: stepwise uncertainty reduction (SUR) (Bect et al., 2012, 2019), which is effective under a limited evaluation budget but computationally demanding, and maximal uncertainty reduction (MUR), which is less effective but cheaper computationally. Since the present chapter focuses on a practical BSS-based set inversion procedure, we adopt an MUR strategy rather than SUR.

In the original BSS setting, adaptive enrichment is coupled with the metamodel-based sequential simulation scheme. In this chapter, however, the roles are separated: the inner SuS/SMC loop is run on a fixed GP conditioned on the current design, and enrichment is considered only outside this loop, between two runs of the set inversion procedure.

MUR targets regions where the GP uncertainty on the inversion set is maximal. In this work, we propose a MUR-based criterion that combines the misclassification measure of Bryan et al. (2005) with the GP posterior variance (weighted MSE). This promotes exploration in regions where the GP uncertainty is high and the inversion boundary is poorly defined. The sampling criterion is

$$G_{t,n}(\mathbf{x}) = \big(\tau_{t,n}(\mathbf{x})\big)^{\beta_1} \big(\sigma_n^2(\mathbf{x})\big)^{\beta_2}, \tag{6.8}$$

where $\sigma_n(\mathbf{x})$ is the GP posterior standard deviation and $\tau_{t,n}(\mathbf{x}) = \min\{g_{t,n}(\mathbf{x}), 1 - g_{t,n}(\mathbf{x})\}$, with $g_{t,n}(\mathbf{x})$ the coverage function defined in Eq. (6.5).

The next design point is selected as

$$\mathbf{x}_{n+1} = \arg\max_{\mathbf{x}\in\mathcal{X}} G_{t,n}(\mathbf{x}). \tag{6.9}$$

Further details and sensitivity analyses regarding the choice of (β_1, β_2) are provided in Appendix P.5. These results indicate that the setting $(\beta_1, \beta_2) = (0.5, 1)$ provides a good trade-off between misclassification and GP uncertainty.

Remark. When multiple evaluations can be performed in parallel, batch sampling strategies may be employed to refine the model by selecting and evaluating several design points simultaneously. The criterion in Eq. (6.8) can be extended accordingly for batch selection (see Appendix P.5).

6.3.3 Illustration

To illustrate Algorithm 4 and to analyze the resulting particle distribution, as well as the evaluation of the coverage function (Eq. (6.5)) and the sampling criterion (Eq. (6.8)) on the particle population, we apply the method to a one-dimensional test function with two different initial designs of experiments, kept fixed throughout the procedure. This example is used to quantify the accuracy and limitations of the proposed method in the absence of informative metrics to characterize the quality of the inversion set.

Test function. It is defined as

$$f(x) = -\big(0.7x + \sin(5x + 1) + 0.1\sin(10x)\big),$$

with f defined on $\mathcal{X} = [-1, 1]$. The inverse problem targets the interval $\mathcal{B}_{\text{target}} = [0.85, 1.15]$ starting from the initial interval $\mathcal{B}_{\text{initial}} = [-2.0, 2.0]$.

Initial design of experiments. To sample the initial design and the particles, we consider a uniform prior $p_{\mathcal{X}} = \mathcal{U}([-1, 1])$.

GP metamodel. For this illustration, and throughout the remainder of this section, the unknown function f is treated as a realisation of a GP prior with constant mean and a Matérn-5/2 covariance kernel. At each update the GP hyperparameters are re-estimated by restricted maximum likelihood (REML) (Stein, 1999), and a small nugget term (10^{-6}) is added to the diagonal of the covariance matrix to ensure numerical stability.

Protocol. Two initial designs of experiments Ξ_{n_0} with $n_0 \in \{7, 10\}$ are generated using a maximin Latin hypercube sampling strategy. An initial population of $N_p = 1000$ particles is sampled from the uniform prior $p_{\mathcal{X}}$. A monotone relaxation grid $\{\lambda_t\}_{t=0}^{T}$ is defined with $\lambda_0 = 0$ and $\lambda_T = 1$, such that $\mathcal{B}_{t+1} \subset \mathcal{B}_t$ for all t and $\mathcal{B}_T = \mathcal{B}_{\text{target}}$. Algorithm 4 is then run.

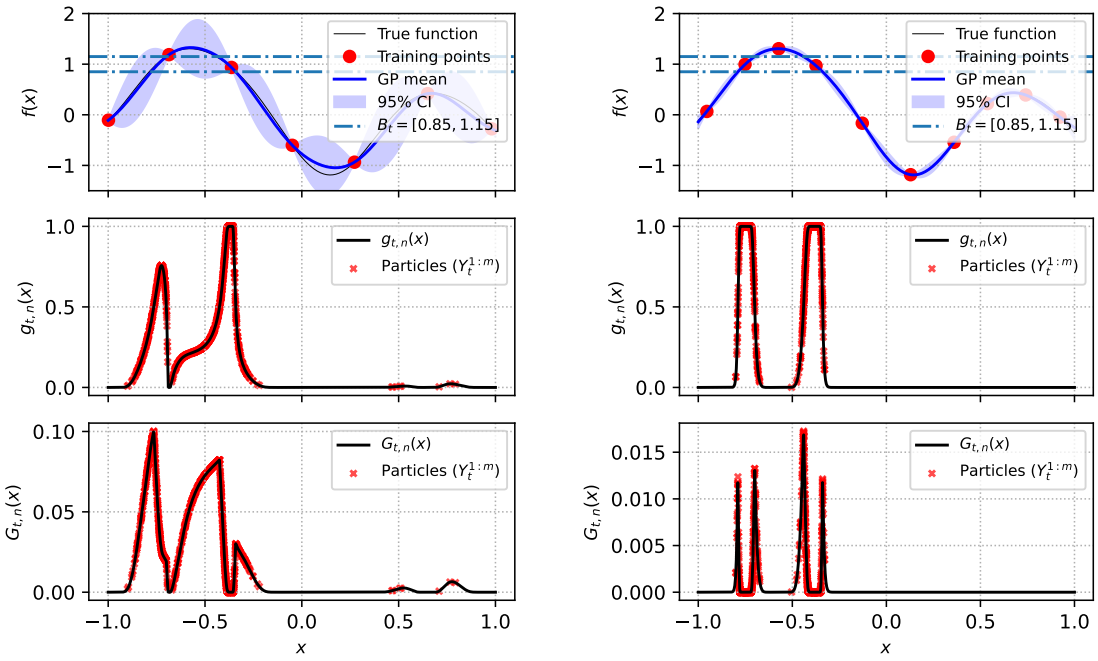

(a) 7 observations

(b) 10 observations

Figure 6.3: Final inversion set at $\lambda_t = 1.0$ obtained with Algorithm 4, for two initial designs ($n = 7$, left; $n = 10$, right). Each column displays, from top to bottom: the GP posterior (mean and 95% confidence interval), the estimated coverage function $g_{t,n}(x)$ (Eq. (6.5)), and the sampling criterion $G_{t,n}(x)$ (Eq. (6.8)). Red dots denote the initial design points, while red crosses correspond to the final particle population $Y_t^{(1:N_p)}$. For $n = 7$, the sampling criterion $G_{t,n}(x)$ is spread over the entire inversion set, whereas for $n = 10$, it concentrates in the vicinity of the intersections between the GP posterior mean and the bounds a_{target} and b_{target}.

Results (case $n = 7$). Figure 6.3 (left column) shows that, for $n = 7$, the GP posterior remains highly uncertain, as indicated by the wide 95% confidence interval in the top panel. Accordingly, the coverage function $g_{t,n}(x)$ (middle panel) is diffuse, with

extended regions of intermediate values, reflecting ambiguity in the classification of the target set.

This uncertainty propagates to the sampling criterion $G_{t,n}(x)$ (bottom panel), which is distributed over several regions instead of being concentrated near the inversion boundaries. In particular, high values of $G_{t,n}(x)$ are observed in regions where the GP posterior overlaps the target interval, even when the true function does not satisfy the constraint (e.g., $x \in [0.5, 1.0]$).

As a result, particles remain dispersed and do not concentrate in the target region, indicating that the current design is not sufficiently informative to characterize the set.

Results (case $n = 10$). Figure 6.3 (right column) shows that, for $n = 10$, the GP posterior uncertainty is significantly reduced. The coverage function $g_{t,n}(x)$ becomes sharper, with a clear transition between regions where $g_{t,n}(x) \approx 0$ and $g_{t,n}(x) \approx 1$, indicating improved classification of the target set.

Consequently, the sampling criterion $G_{t,n}(x)$ becomes localized near the inversion boundaries, with maxima located close to the intersections between the GP posterior mean and the bounds a_{target} and b_{target}. This indicates that the remaining uncertainty is confined to a narrow region.

The particle population accordingly concentrates in the admissible region and provides a consistent approximation of the set. In contrast to the case $n = 7$, the set is well identified.

Discussion. These results highlight the role of the initial design in set inversion with a fixed GP. For $n = 10$, the design is sufficiently informative to accurately characterize the set, whereas for $n = 7$, the lack of information leads to a diffuse approximation.

In this one-dimensional setting, the GP posterior can be directly visualized, allowing a qualitative assessment of the set reconstruction. Such validation is not available in higher dimensions ($d > 2$), where the assessment must rely on quantitative diagnostics.

This raises a practical question: how can one diagnose, under a given fixed experimental design, whether the estimated inversion set is reliable at the target level?

The following section introduces quantitative diagnostics to answer this question.

6.4 Set inversion uncertainty quantification

To quantify the quality of the inversion set in higher dimensions under a fixed design, three practical questions arise at a given relaxation level. First, how small is the relaxed inversion set under the input distribution? Second, is the GP accurate enough at this level? Third, is the particle approximation stable enough? This section introduces diagnostics that address these three questions.

6.4.1 Expected volume of the inversion set

We begin with the size of the relaxed inversion set. A natural quantity of interest is the probability mass defined in Eq. (6.2)

$$\alpha_t = \mathbb{P}_{\mathcal{X}}(\mathbf{\Gamma}_t) = \int_{\mathcal{X}} \mathbf{1}_{f(\mathbf{x})\in\mathcal{B}_t} \pi_{\mathcal{X}}(\mathbf{x}) d\mathbf{x}, \tag{6.10}$$

which is the true volume of the inversion set $\mathbf{\Gamma}_t$ under the input distribution $P_{\mathcal{X}}$, assumed to admit a density $\pi_{\mathcal{X}}$.

Remark. Strictly speaking, α_t is the probability mass of $\mathbf{\Gamma}_t$ under $P_{\mathcal{X}}$. We nevertheless use the term "volume" throughout this section, with the understanding that it refers to volume measured with respect to the input distribution. When $P_{\mathcal{X}}$ is uniform on $\mathcal{X}$, this coincides with the usual geometric volume up to a constant factor.

Under the GP model conditioned on the fixed design $\mathcal{D}_n$, the corresponding Bayesian estimate of Eq. (6.10) is

$$\alpha_{t,n} = \mathbb{E}_n[\alpha_t] = \int_{\mathcal{X}} g_{t,n}(\mathbf{x}) \pi_{\mathcal{X}}(\mathbf{x}) d\mathbf{x}, \tag{6.11}$$

where $\mathbb{E}_n(\cdot)$ denotes conditional expectation given $\mathcal{D}_n$, and $g_{t,n}(\mathbf{x})$ is the posterior coverage function from Eq. (6.5). The quantity $\alpha_{t,n}$ therefore represents the GP-based expected volume of the relaxed inversion set at level t, conditional on $\mathcal{D}_n$.

To connect this quantity with the SMC procedure, we normalize the target density introduced in Section 6.3 in Eq. (6.6) as

$$q_{t,n}(\mathbf{x}) = \frac{g_{t,n}(\mathbf{x})\pi_{\mathcal{X}}(\mathbf{x})}{\alpha_{t,n}}, \tag{6.12}$$

assuming $\alpha_{t,n} > 0$. We then obtain the recursive representation

$$\alpha_{t,n} = \alpha_{t-1,n} \mathbb{E}_{q_{t-1,n}} \left[\frac{g_{t,n}(X)}{g_{t-1,n}(X)} \right]. \tag{6.13}$$

Let $\mathbf{Y}_{t-1}^{1:N_p} = \{Y_{t-1}^{(i)}\}_{i=1}^{N_p}$ denote the particle population produced by the previous SMC stage. After reweighting, resampling, and move steps at level $t-1$, these particles are approximately distributed according to $q_{t-1,n}$. Replacing the expectation under $q_{t-1,n}$ by the corresponding empirical average yields the Monte Carlo estimator $\hat{\alpha}_t$ of $\alpha_{t,n}$ (Eq. (6.13)):

$$\hat{\alpha}_t = \hat{\alpha}_{t-1}\hat{p}_t, \qquad \hat{p}_t = \frac{1}{N_p} \sum_{i=1}^{N_p} \frac{g_{t,n}(\mathbf{Y}_{t-1}^{(i)})}{g_{t-1,n}(\mathbf{Y}_{t-1}^{(i)})}. \tag{6.14}$$

This recursion is initialized at level 0 by

$$\hat{\alpha}_0 = \frac{1}{N_p} \sum_{i=1}^{N_p} g_{0,n}(Y_0^{(i)}), \qquad Y_0^{(i)} \sim P_{\mathcal{X}}, \tag{6.15}$$

which is a Monte Carlo estimator of $\alpha_{0,n}$. In practice, the initial relaxation set is chosen wide enough so that $g_{0,n}(\mathbf{x}) \approx 1$ over most of the input space, and therefore $\alpha_{0,n}$ is close to one.

The quantity $\hat{p}_t$ estimates the mean weight ratio $\mathbb{E}_{q_{t-1,n}}[g_{t,n}(X)/g_{t-1,n}(X)]$, and can be viewed as an analogue of the conditional probability $P_{\mathcal{X}}(\mathbf{\Gamma}_t \mid \mathbf{\Gamma}_{t-1})$ in the ideal indicator-based SuS framework, where the coverage function reduces to the indicator $\mathbf{1}_{\mathbf{\Gamma}_t}$.

From a practical viewpoint, $\alpha_{t,n}$ and $\hat{p}_t$ play different roles. The quantity $\alpha_{t,n}$ indicates how large the relaxed set remains under the prior, whereas $\hat{p}_t$ measures how severe the transition from level $t-1$ to level t is.

The parameter $\hat{p}_t$ can therefore be monitored to tune the relaxation schedule. Very small values may lead to weight degeneracy and increased variance in the SMC procedure, whereas very large values indicate that the relaxation step is too mild and may result in unnecessary intermediate levels.

Remark. The final expected volume $\alpha_{T,n}$ also provides insight into the relevance of the relaxation strategy. If the event is not rare (i.e., $\alpha_{T,n}$ remains relatively large), the relaxation procedure may be unnecessary, and the expected volume can be estimated directly by Monte Carlo sampling under $P_{\mathcal{X}}$.

The next question is whether the current GP is accurate enough for the relaxed set under consideration. Rather than refining the design immediately, we first seek to quantify the GP-induced uncertainty affecting $\alpha_{t,n}$.

6.4.2 GP-induced uncertainty

We now isolate the uncertainty affecting the volume estimator $\alpha_{t,n}$ due to the GP approximation, assuming negligible SMC noise ($N_p \to \infty$). This allows us to assess the effect of the current design $\mathcal{D}_n$ alone.

The goal is to estimate, or at least upper-bound,

$$\mathbb{E}_n[(\alpha_t - \alpha_{t,n})^2],$$

the mean squared error of the Bayesian estimate of the inversion-set volume. Applying Minkowski's inequality, see (Vestrup, 2009; Vazquez and Bect, 2009), gives the conservative upper bound

$$\mathbb{E}_n\big[(\alpha_t - \alpha_{t,n})^2\big] \leq \left(\int_{\mathcal{X}} \sqrt{\nu_{t,n}(\mathbf{x})}\pi_{\mathcal{X}}(\mathbf{x})d\mathbf{x}\right)^2, \tag{6.16}$$

with $\nu_{t,n}(\mathbf{x}) = g_{t,n}(\mathbf{x})\big(1 - g_{t,n}(\mathbf{x})\big)$, where $\nu_{t,n}(\mathbf{x})$ is the variance of a Bernoulli variable with success probability $g_{t,n}(\mathbf{x})$. Large values of $\nu_{t,n}(\mathbf{x})$ correspond to locations where the GP remains uncertain about membership in the relaxed set.

To obtain a relative uncertainty measure, we consider the normalized root mean squared error

$$\frac{\sqrt{\mathbb{E}_n[(\alpha_t - \alpha_{t,n})^2]}}{\alpha_{t,n}}. \tag{6.17}$$

Using the same particle population $\mathbf{Y}_{t-1} = \{Y_{t-1}^{(i)}\}_{i=1}^{N_p}$, produced by SMC at level $t-1$ and approximately distributed according to $q_{t-1,n}$, we obtain the practical upper bound derived from Eqs. (6.16) and (6.17); see Appendix P.3 for details:

$$\frac{\sqrt{\mathbb{E}_n\big[(\alpha_t - \alpha_{t,n})^2\big]}}{\alpha_{t,n}} \leq \delta_t^{\mathcal{GP}}, \qquad \delta_t^{\mathcal{GP}} \approx \frac{1}{\hat{p}_t}\frac{1}{N_p}\sum_{i=1}^{N_p}\sqrt{\frac{g_{t,n}(Y_{t-1}^{(i)})\big(1 - g_{t,n}(Y_{t-1}^{(i)})\big)}{g_{t-1,n}^2(Y_{t-1}^{(i)})}}. \tag{6.18}$$

This bound is conservative and may overestimate the GP-induced uncertainty. Nevertheless, it is easy to interpret: small values of $\delta_t^{\mathcal{GP}}$ indicate that the GP provides a sharp probabilistic classification of the relaxed inversion set at level λ_t, whereas large values suggest that the inversion boundary remains poorly characterized and that additional model evaluations may be required.

The quantity $\delta_t^{\mathcal{GP}}$ can therefore be used to identify relaxation levels at which the GP model provides an accurate characterization of the inversion set, and to detect levels where additional evaluations are needed to reduce epistemic uncertainty.

6.4.3 SMC-induced uncertainty

The third question concerns sampling variability. Even with a fixed GP, $\hat{\alpha}_t$ is only an SMC approximation of $\alpha_{t,n}$. It is therefore affected by Monte Carlo noise arising from the particle procedure.

Following Bect et al. (2017), the coefficient of variation of $\hat{\alpha}_t$ due to SMC satisfies the recursive relation

$$(\delta_t^{\mathrm{SMC}})^2 = \frac{1}{N_p}\hat{\kappa}_t + \left(1 + \frac{1}{N_p}\hat{\kappa}_t\right)(\delta_{t-1}^{\mathrm{SMC}})^2, \tag{6.19}$$

where

$$\hat{\kappa}_t = \hat{p}_t^{-2}\frac{1}{N_p}\sum_{j=1}^{N_p}\left(\frac{g_{t,n}(\mathbf{Y}_{t-1}^{(j)})}{g_{t-1,n}(\mathbf{Y}_{t-1}^{(j)})} - \hat{p}_t\right)^2 \tag{6.20}$$

measures the variability of the normalized importance weights.

Large values of δ_t^{SMC} indicate either an insufficient number of particles or weight degeneracy between successive relaxation levels, resulting in increased sampling noise.

6.4.4 Diagnostic interpretation and workflow

The quantities $\hat{p}_t$, $\alpha_{t,n}$, $\hat{\alpha}_t$, $\delta_t^{\mathcal{GP}}$, and δ_t^{SMC} form a set of complementary diagnostics that quantify inversion quality at each relaxation level.

Given a fixed experimental design $\mathcal{D}_n$, Algorithm 4 is applied and these metrics are evaluated along the relaxation sequence.

Their interpretation is as follows and summarized in Table 6.1. The quantity $\hat{p}_t$ measures the severity of the transition from one level to the next. The quantity $\alpha_{t,n}$ is the GP-based expected volume of the relaxed set, and $\hat{\alpha}_t$ is its SMC approximation. The metric δ_t^{SMC} quantifies particle-induced sampling noise. The metric $\delta_t^{\mathcal{GP}}$ quantifies GP-induced uncertainty and indicates whether the inversion set at level λ_t is sufficiently characterized. Together, these quantities indicate both how small the relaxed set remains under the prior and how reliable its numerical approximation is.

In the following sections, design enrichment may be performed between two runs of Algorithm 4, leading to an updated design $\mathcal{D}_{n'}$.

The proposed diagnostics then enable a direct comparison of the inversion results and associated diagnostic metrics before and after metamodel refinement.

In the next section, we illustrate the behavior of these diagnostics using the same one-dimensional function introduced in Section 6.3.3.

Table 6.1: Summary of diagnostic quantities at relaxation level t.

Quantity	Meaning	Interpretation	Warning
$\alpha_{t,n}$ (Eq. (6.11))	Expected volume of the relaxed set under $P_{\mathcal{X}}$	Size of the relaxed inversion set	Small: rare set
$\hat{p}_t$ (Eq. (6.14))	Conditional transition coefficient (SMC)	Severity of level transition	Small: unstable
$\delta_t^{\mathcal{GP}}$ (Eq. (6.18))	Relative GP uncertainty on $\alpha_{t,n}$	GP accuracy at level t	Large: refine design
δ_t^{SMC} (Eq. (6.19))	Relative SMC uncertainty on $\hat{\alpha}_t$	Particle noise	Large: increase N_p

6.5 Numerical experiments

Experimental Setup In this section, we illustrate how the diagnostics introduced in Section 6.4 behave on the one-dimensional example introduced in Section 6.3.3. The experiments are designed to isolate three practical situations: insufficient GP accuracy, insufficient particle population, and an overly aggressive relaxation schedule.

We use the same one-dimensional test function and GP prior as in Section 6.3.3, based on seven input observations. An initial population of $N_p = 1{,}000$ particles is drawn from a uniform prior over $[-1, 1]$.

A monotone relaxation grid $\{\lambda_t\}_{t=0}^{T}$ is defined with $T = 20$, $\lambda_0 = 0$, and $\lambda_T = 1$, such that $\mathcal{B}_0 = [-2, 2]$, $\mathcal{B}_{t+1} \subset \mathcal{B}_t$, and $\mathcal{B}_T = [1.0, 1.1]$. Note that a sharper box is considered here to reduce the volume of the target set, to test the method in a more restrictive setting than in Section 6.3.3. At each level λ_t, we compute the GP-based expected inversion volume $\alpha_{t,n}$, its SMC approximation $\hat{\alpha}_t$, and the uncertainty metrics $\delta_t^{\mathcal{GP}}$ and δ_t^{SMC}. Their evolution is then monitored with λ_t.

Algorithm 4 is run along the full relaxation sequence, and $\hat{\alpha}_t$ is displayed together with conservative probability bounds around $\alpha_{t,n}$, derived from $\delta_t^{\mathcal{GP}}$ and δ_t^{SMC} using the Bienaymé-Chebyshev inequality with $k = \sqrt{20}$, corresponding to a conservative 95% probability bound (see Appendix P.3 for further details).

In the following, we empirically set a coefficient of variation threshold of 0.5 as an acceptable level for inversion quality, whether the uncertainty is GP- or SMC-induced. Throughout the experiments, inversion reliability refers to remaining below this threshold. For the transition coefficient, values of $\hat{p}_t$ below 0.1 are taken as a practical warning sign of potentially unstable SMC transitions.

When $\delta_t^{\mathcal{GP}}$ exceeds the enrichment threshold discussed below, the GP model is refined between two algorithm runs by adding new evaluations selected using the weighted mean squared error (WMSE) criterion (Eq. (6.8)) with $(\beta_1, \beta_2) = (0.5, 1.0)$.

Two thresholds are therefore used with different purposes. The value 0.5 serves as an acceptance threshold for inversion reliability, whereas the larger value 1.0 is used to identify clearly problematic relaxation levels at which enrichment should be targeted. In practice, model evaluations are added near a level λ_t such that $\delta_t^{\mathcal{GP}} \approx 1.0$. In some cases, the associated set at $\lambda_t = 1$, corresponding to the final target set $\mathcal{B}_T$, can also be considered.

We consider four configurations:

- the initial case from Section 6.3.3, without adding model evaluations;
- seven additional model evaluations, selected by the WMSE criterion near $\lambda_T = 1$;
- the same initial design, but with a reduced particle population $N_p = 100$;
- the same initial design and particle population, but with a light relaxation schedule $\lambda = \{0, 0.5, 1\}$.

This comparison shows how each configuration affects the diagnostics $\hat{p}_t$, $\delta_t^{\mathcal{GP}}$, and δ_t^{SMC}, and therefore clarifies the practical role of each metric.

First experiment: on the initial design Figure 6.4 shows the following behavior with respect to the threshold criteria defined in Section 6.5.

(i) The estimated volume $\hat{\alpha}_t$ decreases with λ_t, as expected from the progressive contraction of the relaxation sets.
(ii) The transition coefficient $\hat{p}_t$ remains above 0.1 at all levels, indicating stable SMC transitions.
(iii) The GP-induced uncertainty $\delta_t^{\mathcal{GP}}$ stays below 0.5 for $\lambda_t \leq 0.75$, but increases beyond this threshold at higher levels, showing a loss of accuracy of the GP near the target set.
(iv) The SMC-induced uncertainty δ_t^{SMC} remains below 0.1, with a moderate increase close to $\mathcal{B}_T$, suggesting that sampling noise remains limited.

Overall, the inversion is reliable up to $\lambda_t \approx 0.75$. Beyond this level, the accuracy is mainly limited by the GP approximation.

Second experiment: after additional evaluations After enrichment to $n = 14$, Figure 6.5 shows that $\delta_t^{\mathcal{GP}}$ remains below 0.5 over the entire relaxation path, with a maximum at $\lambda_t \approx 0.78$, and becomes negligible at $\lambda_T = 1.0$. The other metrics remain unchanged and satisfy the prescribed thresholds. The enriched design therefore ensures a reliable inversion across all levels. At $\lambda_t \approx 0.78$, where $\delta_t^{\mathcal{GP}}$ is maximal, uncertainty is concentrated near the inversion boundaries (Figure 6.6). The admissible region is correctly identified, but its boundaries remain diffuse. At the target level $\lambda_t = 1$, the coverage function becomes sharp and the particle population concentrates within $\mathcal{B}_T$, resulting in an accurate reconstruction of the inversion set.

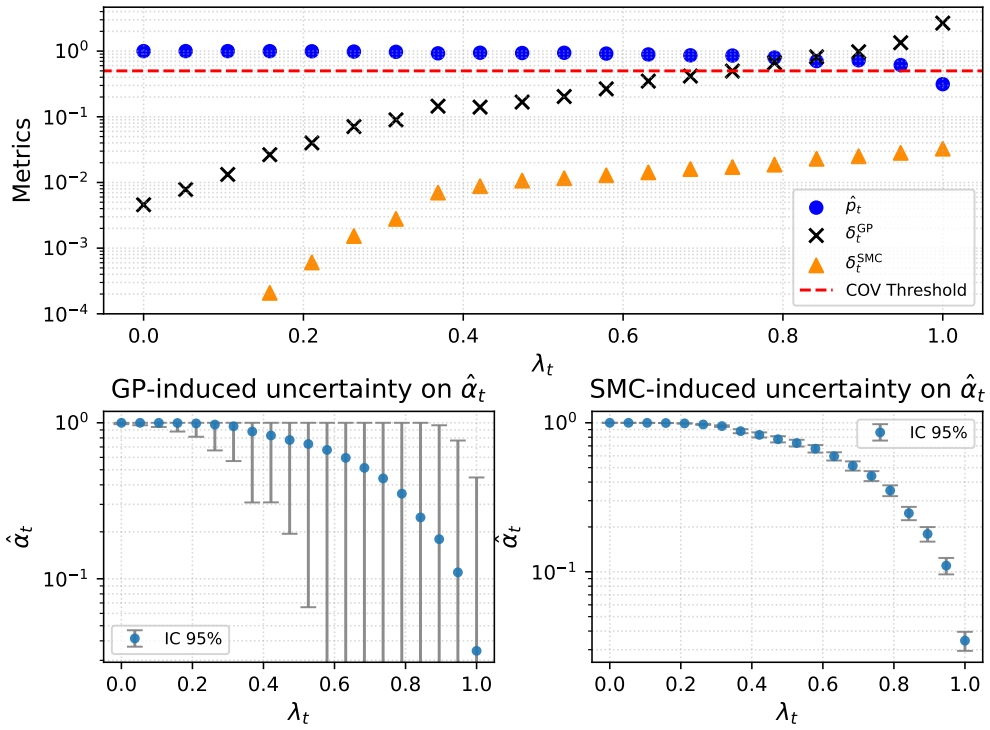

Figure 6.4: Evolution of the uncertainty metrics across 20 relaxation levels using Algorithm 4, with $N_p = 1000$ particles. The same initial design and test function as in Section 6.3.3 are used, with $n = 7$ observations. The top panel shows the evolution of the GP-induced uncertainty $\delta_t^{\mathcal{GP}}$ (black crosses), the SMC-induced uncertainty δ_t^{SMC} (orange triangles), and the transition coefficient $\hat{p}_t$, which reflects the smoothness of the transition between successive target densities, over the 20 subsets defined by $\lambda_0 = 0$ for $\mathcal{B}_0$ and $\lambda_T = 1$ for the target set $\mathcal{B}_T = \mathcal{B}_{\text{target}}$. The red dotted line indicates the threshold below which the coefficients of variation $\delta_t^{\mathcal{GP}}$ and δ_t^{SMC} are considered acceptable. The bottom panels show the evolution of $\hat{\alpha}_t$, the SMC approximation of $\alpha_{t,n}$, together with conservative uncertainty bounds derived separately from GP-induced uncertainty (left) and SMC-induced uncertainty (right), using the Bienaymé-Chebyshev inequality (see Appendix P.3).

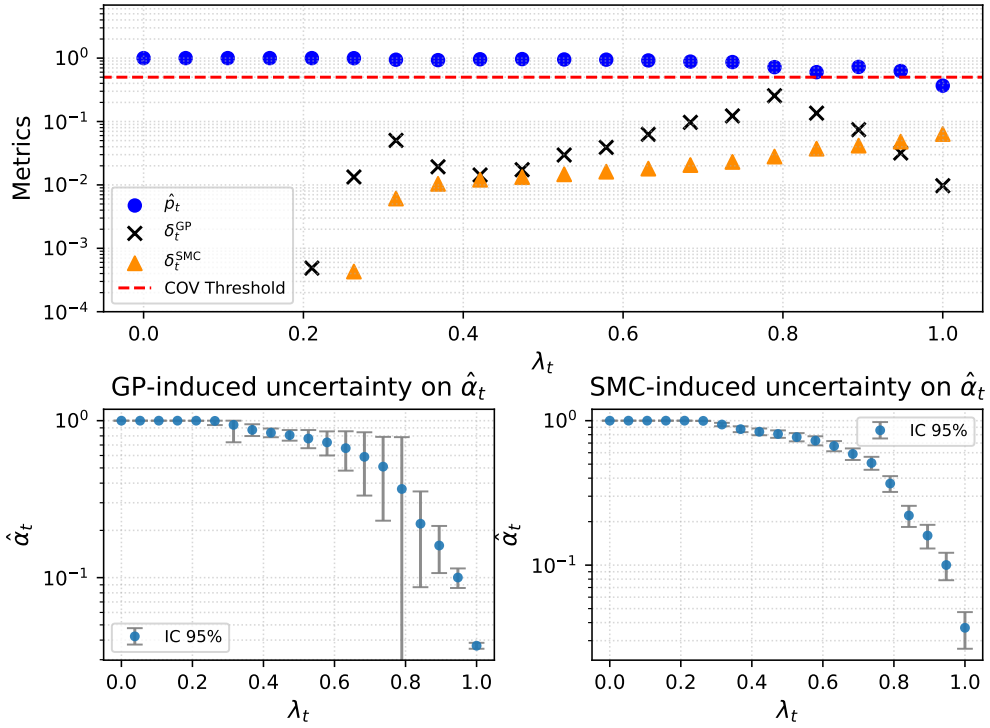

Figure 6.5: Evolution of the uncertainty metrics across 20 relaxation levels ($\lambda \in [0, 1]$) using Algorithm 4, with $N_p = 1000$ particles, after adding seven WMSE-selected evaluations (total $n = 14$). The description is identical to that of Figure 6.4. Compared to Figure 6.4, the GP-induced uncertainty at the final target set is negligible, indicating that the set boundaries are well identified by the GP.

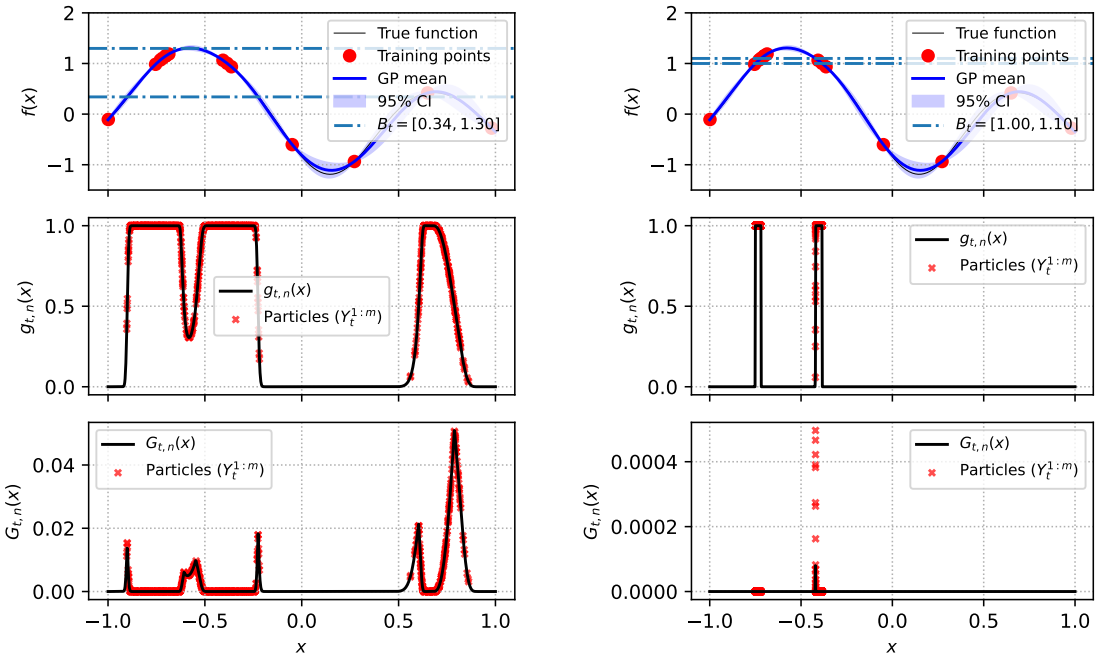

(a) Intermediate level, $\lambda_t = 0.78$

(b) Final level, $\lambda_t = 1.0$

Figure 6.6: Same description as Figure 6.3 but for an intermediate and final inversion sets ($\lambda_t = 0.78$ and $\lambda_t = 1.0$) obtained from the BSS set inversion with $n = 14$ observations. The graphical elements are the same as in Figure 6.3. At the intermediate level ($\lambda_t = 0.78$, $\mathcal{B}_t = [0.34, 1.30]$), GP uncertainty remains non-negligible near the set boundaries and the particles are more spread. At the final level ($\lambda_T = 1.0$, $\mathcal{B}_T = [1.0, 1.1]$), the GP uncertainty is reduced and the particles concentrate within the target inversion set.

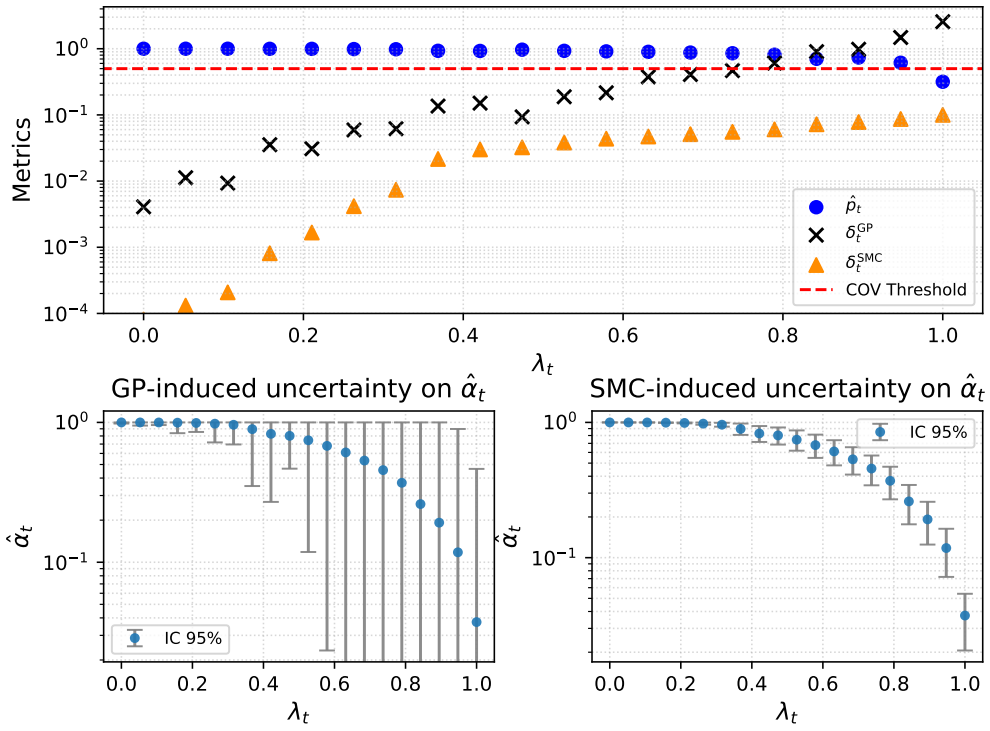

Figure 6.7: Evolution of uncertainty metrics during BSS set inversion (Algorithm 4) with 20 relaxation levels ($\lambda_0 = 0$ for the initial box and $\lambda_T = 1$ for the target set) and $N_p = 100$ particles, using the test function from Section 6.3.3 and the same design as in Figure 6.4. Graphical elements follow Figure 6.4. We observe that a low number of particles leads to an increase in SMC-induced noise compared to the case $N_p = 1000$ (Figure 6.4).

Third experiment: effect of particle population size Figure 6.7 shows an increase in the SMC-induced uncertainty δ_t^{SMC}, particularly at the final relaxation levels where particles concentrate in the target set. This is due to the reduced particle population. As a consequence, the estimator $\hat{\alpha}_t$ exhibits increased variance and tends to be overestimated compared to Figure 6.4. The other metrics remain essentially unchanged. This indicates that a reduced particle population primarily impacts the SMC approximation, especially at the final levels.

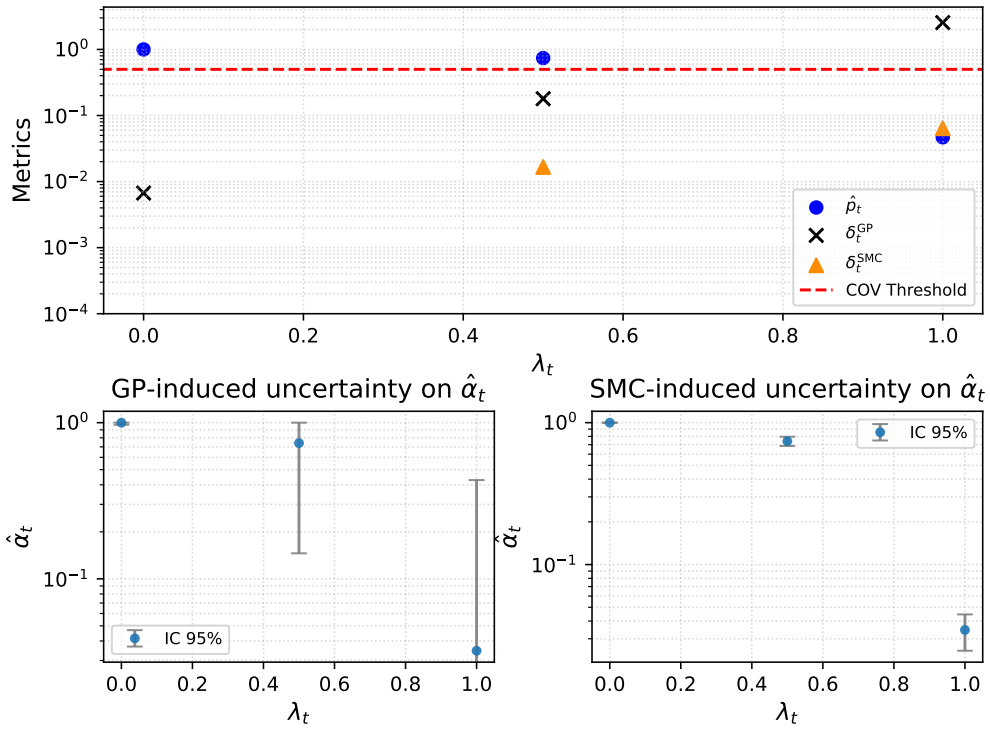

Figure 6.8: Evolution of uncertainty metrics during BSS set inversion (Algorithm 4) with three relaxation levels ($\lambda = 0, 0.5, 1$) and $N_p = 1000$ particles, using the same design as Figure 6.4. Graphical elements follow Figure 6.4. We observe that reducing the number of relaxation levels mainly leads to an increase in SMC-induced uncertainty compared to the case with 20 levels (Figure 6.4).

Fourth experiment: effect of the number of intermediate levels Figure 6.8 shows that the transition coefficient $\hat{p}_t$ exhibits larger variations, with a sharp drop during the final transition ($0.5 \to 1.0$), corresponding to a more severe transition between successive levels. The SMC-induced uncertainty δ_t^{SMC} increases significantly at the final level, due to the larger variability of the importance weight ratios. The other metrics remain essentially unchanged compared to Figure 6.4. This confirms that reducing the number of relaxation levels leads to unstable SMC transitions and increased sampling noise, due to weight degeneracy between successive levels. This highlights the need for a sufficiently fine relaxation schedule.

Discussion These experiments confirm the interpretation of the diagnostics introduced in Section 6.4. The first two experiments show that $\delta_t^{\mathcal{GP}}$ identifies relaxation levels where the GP is insufficiently informative and where enrichment is needed. The third experiment shows that δ_t^{SMC} reacts to an insufficient particle population, while $\delta_t^{\mathcal{GP}}$ remains essentially unchanged. The fourth experiment shows that $\hat{p}_t$ and δ_t^{SMC} reveal an overly coarse relaxation schedule through unstable transitions and increased sampling noise.

Taken together, the diagnostics play complementary roles. The coefficient $\hat{p}_t$ guides the choice of relaxation levels, $\delta_t^{\mathcal{GP}}$ assesses metamodel reliability and supports adaptive enrichment, and δ_t^{SMC} quantifies particle-induced sampling noise.

In the next section, the proposed framework is applied to two higher-dimensional and more complex problems: (i) the 4D Hartmann function, and (ii) a 3D TBM FE simulator for estimating surface settlements within a soil domain.

6.6 Case studies

6.6.1 Protocol

This section uses two case studies with complementary roles. The Hartmann 4 function serves as a controlled benchmark to illustrate how the diagnostics guide design enrichment in a moderate-dimensional setting. The tunnel FE model then illustrates how the same diagnostics can be used to assess, on a realistic engineering simulator, whether the current design is sufficient to characterize the admissible set at a given relaxation level.

The same setup as in Section 6.5 is used:
(i) independent GP metamodels with zero mean and a Matérn-5/2 covariance kernel are fitted for each output. When the simulator is multi-output, the coverage function $g_{t,n}(\mathbf{x})$ is computed as the product of the marginal posterior probabilities under the assumption of posterior independence between outputs (see Appendix P.2 for further details);
(ii) a monotone relaxation grid with 50 relaxation levels is defined from $\lambda_0 = 0$ to $\lambda_T = 1$, and a population of $N_p = 1000$ particles is sampled from a uniform prior over the input space;
(iii) a coefficient of variation below 0.5 is considered acceptable. Above this value, additional model evaluations are added using the WMSE criterion (Eq. (6.8)) with $(\beta_1, \beta_2) = (0.5, 1.0)$.
This protocol is applied to the two study cases considered: the Hartmann 4 function, commonly used as a benchmark for global optimisation problems, and the 3D FE simulator of tunnel excavation (Chapter 3).

6.6.2 Hartmann 4

We first illustrate the algorithm on a toy problem, namely the Hartmann 4 function, with a uniform prior on the input space $\mathbf{x} \sim \mathcal{U}([0,1]^4)$. The target set is defined as $\mathcal{B}_{\text{target}} = [-2.7, -2.6]$, while the initial relaxation set is $\mathcal{B}_0 = [-4, -1]$.

The objective is to determine whether the diagnostics correctly identify the relaxation levels at which the initial design becomes insufficient, and whether targeted enrichments improve the reliability of the inversion.

The study is conducted as follows:

1. An initial design of 40 simulations is generated (see Figure 6.9).
2. Algorithm 4 is run, and the resulting metrics are shown in Figure 6.10.
3. The relaxation level λ such that the GP uncertainty satisfies $\delta_t^{\mathcal{GP}} \geq 1.0$ is identified using Figure 6.10. At $\lambda = 0.75$, 40 additional simulations are added targeting this relaxation level.
4. Algorithm 4 is re-run with the updated GP model.
5. The same criterion is met at $\lambda = 0.85$, and another 40 simulations are added for the corresponding relaxation set.
6. Algorithm 4 is re-run with the updated GP model, and the resulting metrics are shown in Figure 6.11.
7. The final particle population is visualized using pairwise plots at a representative relaxation level, with colors indicating the logarithm of the posterior coverage function for membership in the corresponding relaxed set.

Remark. The objective here is not to optimize the design to reach the target set, but to analyze how the uncertainty diagnostics guide successive enrichments and indicate the remaining limitations of the current design.

Figure 6.10 shows the following behavior with respect to the threshold criteria defined in Section 6.6.1. The initial design of experiments is shown in Figure 6.9.
(i) The transition coefficient $\hat{p}_t$ remains above 0.1 for most relaxation levels, indicating stable SMC transitions. A decrease is observed near $\lambda_t \approx 0.9$, corresponding to a more severe transition towards the target set.
(ii) The GP-induced uncertainty $\delta_t^{\mathcal{GP}}$ remains below 0.5 for $\lambda_t \leq 0.6$, but increases for larger values of λ_t, reaching values close to 1.0 around $\lambda_t = 0.75$. Beyond this level, GP uncertainty dominates, leading to an uncertain inversion set.
(iii) The SMC-induced uncertainty δ_t^{SMC} remains low throughout, with a moderate increase as particles concentrate towards the target set. Sampling noise therefore does not limit the inversion.

As described in Section 6.6.1, additional evaluations are performed at $\lambda_t = 0.75$ (40 points) and $\lambda_t = 0.85$ (40 additional points) to reduce GP uncertainty in the critical regions.

After additional evaluations, Figure 6.11 shows that the GP-induced uncertainty $\delta_t^{\mathcal{GP}}$ is reduced compared to Figure 6.10 and remains below the threshold value of 0.5 up to $\lambda_t \leq 0.9$. The GP model is therefore sufficiently accurate to characterize the inversion boundaries over most of the relaxation path. The other metrics remain similar to those observed in Figure 6.10. The enriched design provides a reliable inversion up to $\lambda_t \approx 0.9$, beyond which GP uncertainty becomes non-negligible.

Figure 6.12 shows pairwise projections of the particle distribution corresponding to the relaxed set $\mathcal{B}_t = [-2.83, -2.3]$ at $\lambda_t = 0.9$. The particles form distinct clusters, with multiple disjoint regions along some input dimensions (e.g., X_2, and to a lesser extent X_4).

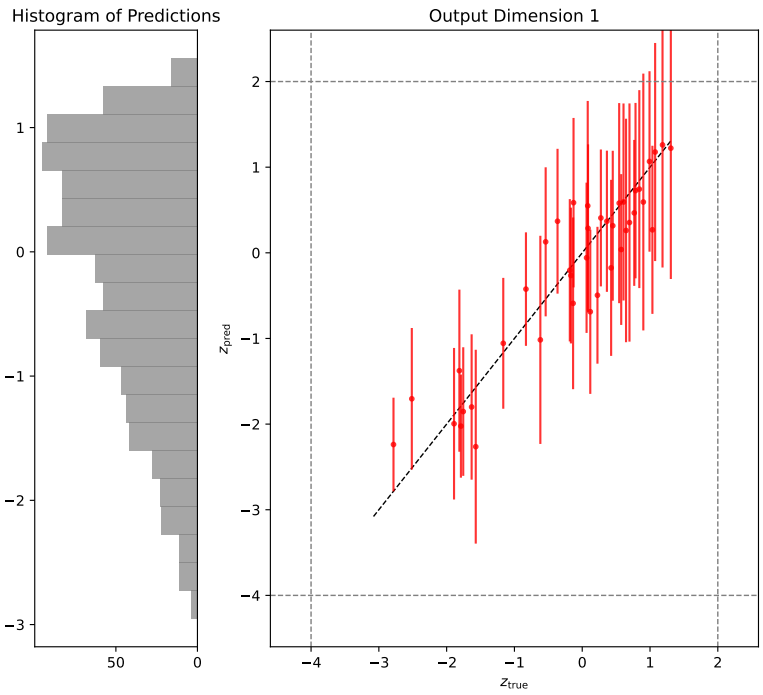

Figure 6.9: Initial design with 40 evaluations. The right panel shows the leave-one-out (LOO) validation of the GP model: red dots correspond to LOO predictions, with error bars representing the GP predictive uncertainty. The dashed line indicates $z_{\text{true}} = z_{\text{pred}}$. More details are given in Figure 4.10 in Chapter 4. The left panel shows the histogram of the initial particle distribution used to start the SMC procedure.

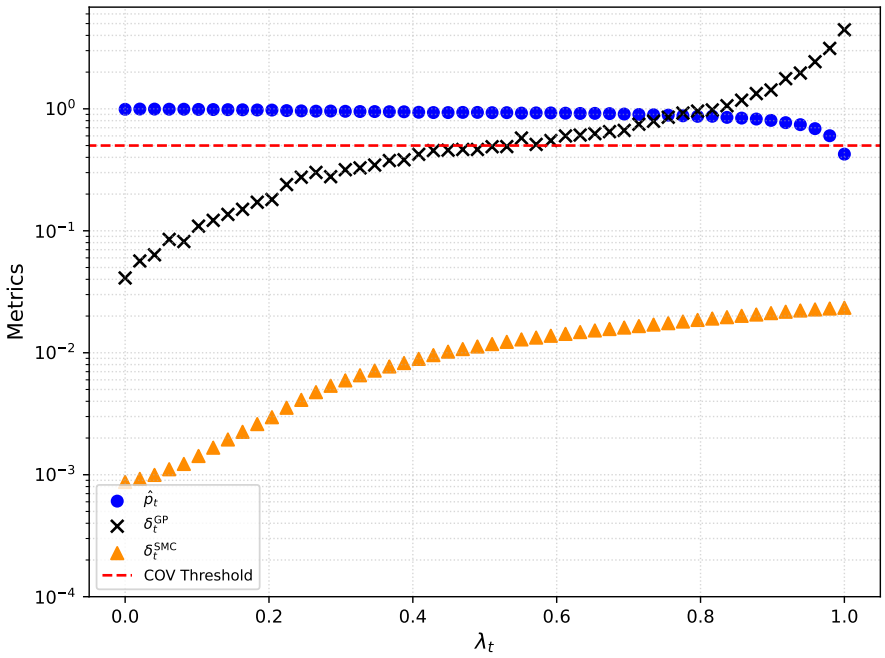

Figure 6.10: Evolution of the uncertainty metrics across 50 relaxation levels using Algorithm 4, with $N_p = 1000$ particles, and a GP conditioned on an initial design of 40 evaluations. The graphical elements follow the description provided for the top panel in Figure 6.4. $\delta_t^{\mathcal{GP}}$ remains below the acceptable threshold of 0.5 for $\lambda \leq 0.6$. At $\lambda = 0.75$, $\delta_t^{\mathcal{GP}}$ reaches values close to 1.0, highlighting this relaxation level as a candidate for design enrichment.

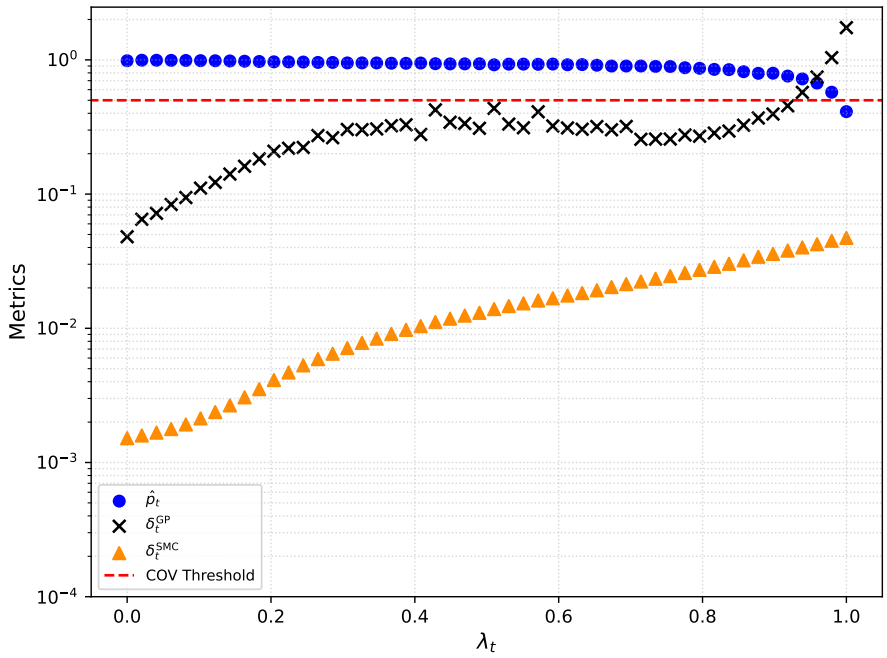

Figure 6.11: Evolution of the uncertainty metrics across 50 relaxation levels using Algorithm 4, with $N_p = 1000$ particles. The GP is conditioned on a total design of 120 evaluations: an initial design of 40 evaluations, followed by 40 evaluations targeting $\lambda_t = 0.75$, and 40 additional evaluations targeting $\lambda_t = 0.85$. The graphical elements follow the description provided for Figure 6.10. $\delta_t^{\mathcal{GP}}$ remains below the acceptable threshold of 0.5 for $\lambda_t \leq 0.9$.

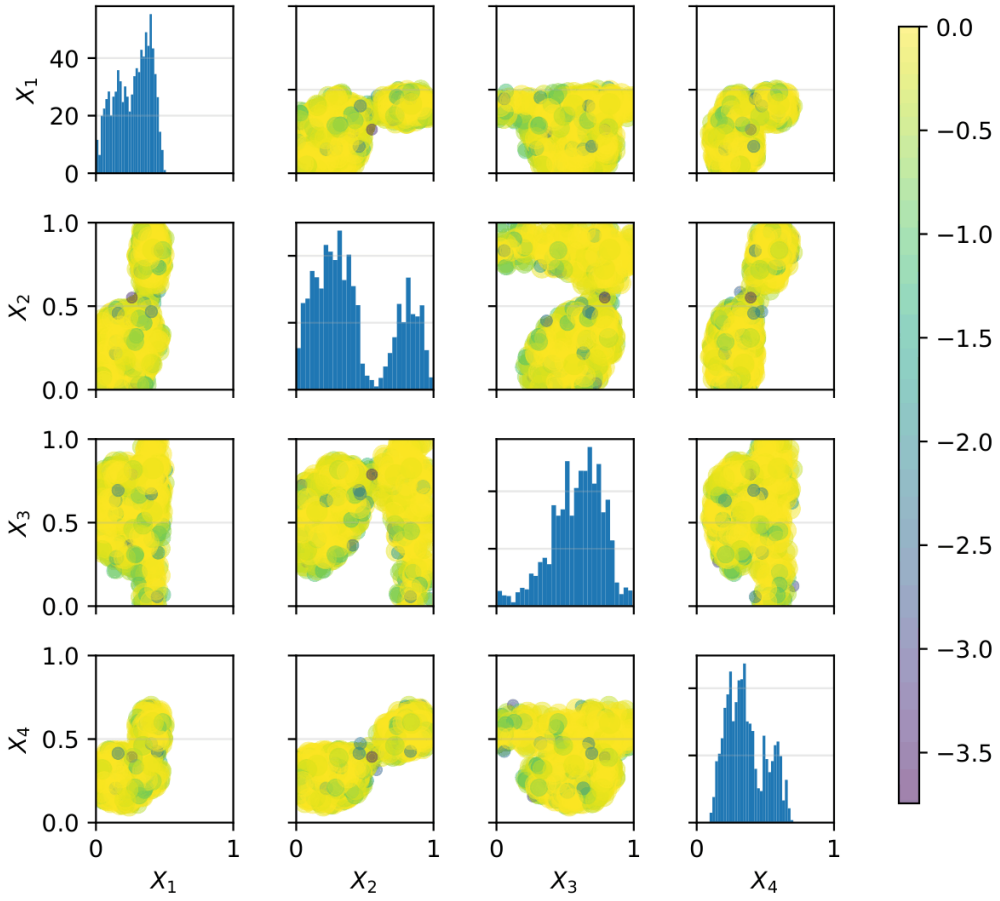

Figure 6.12: Pairwise particle plots illustrating the approximation of the inversion set $\mathbf{\Gamma}_t$ at relaxation level $\lambda_t = 0.9$ (see Figure 6.11), defined as $\mathbf{\Gamma}_t = \{\mathbf{x} \in \mathcal{X} : f(\mathbf{x}) \in \mathcal{B}_t\}$ with $\mathcal{B}_t = [-2.83, -2.3]$. The diagonal panels show the marginal distributions of each input variable X_i, while the off-diagonal panels show the joint distributions (X_i, X_j) for $i \neq j$. Particles are colored according to the log of the coverage function (Eq. (6.5)), reflecting the GP-induced uncertainty on membership in $\mathbf{\Gamma}_t$.

This indicates that different input configurations can produce outputs within the target interval, highlighting the non-uniqueness of the inverse problem. Despite the additional evaluations, the inversion of the final target set is not fully reliable, as shown in Figure 6.11. For the computational budget considered, the inversion at $\lambda_t = 0.9$ remains acceptable, but a more accurate characterization of $\mathcal{B}_t$ would require additional evaluations guided by the sampling criterion (Eq. (6.8)).

6.6.3 FE simulator - tunnel excavation

Numerical set-up This case study considers a calibration problem aimed at identifying the soil mechanical properties that reproduce the surface settlements observed along the monitored line (ML) at position y_{ML} (see Chapter 5). The tunnel geometry and TBM operational conditions (e.g., face pressure, grout injection pressure) are fixed, so that the inversion focuses exclusively on the geological parameters.

The objective is to determine the relaxation level λ_t beyond which the inversion set cannot be reliably characterized without additional evaluations of the 3D FE simulator (Chapter 3), using the experimental design introduced for the ML context (Chapter 4).

QoIs and target sets. The longitudinal QoIs (z_3, z_4) are excluded due to discrepancies between the simulation database and the monitoring data. The inversion is performed on two QoIs: the maximum surface settlement z_1 (mm) and the settlement trough width z_2 (m).

The target set is defined as

$$\mathcal{B}_{\text{target}} = [4.4, 4.6] \text{ mm} \times [36.5, 37.5] \text{ m}.$$

The initial relaxation set is defined from the QoIs distributions obtained in the initial design (Figure 4.9, Chapter 4):

$$\mathcal{B}_0 = [1.0, 25] \text{ mm} \times [25.0, 65] \text{ m}.$$

The problem is formulated in a multi-output setting. The corresponding coverage function and sampling criterion are defined in Appendix P.2.

Input parameters. Based on the global sensitivity analysis (Section 4.2.2, Chapter 4), the inversion focuses on the most influential parameters of the Saint-Ouen limestone (SO) and Beauchamp sand (SB) layers. The retained variables are the Young's moduli, friction angles, and horizontal earth pressure coefficients (K_{0x}, K_{0y}). Cohesion is fixed, as its influence is negligible within the considered ranges. The input parameters are modeled as independent uniform random variables:

$$\begin{aligned} E_{\text{SO}} &\sim \mathcal{U}(89.16, 354.84) \text{ MPa}, & E_{\text{SB}} &\sim \mathcal{U}(52.21, 207.79) \text{ MPa}, \\ \phi_{\text{SO}} &\sim \mathcal{U}(24.6, 45.5)^\circ, & \phi_{\text{SB}} &\sim \mathcal{U}(23.1, 42.9)^\circ, \\ K_{0x,\text{SO}}, K_{0y,\text{SO}} &\sim \mathcal{U}(0.10, 0.96), & K_{0x,\text{SB}}, K_{0y,\text{SB}} &\sim \mathcal{U}(0.10, 1.05). \end{aligned}$$

Remark. The remaining parameters are fixed to their mid-range values (Tables J.1-J.3, Appendix J).

Parameter vector. For Figures 6.14-6.15, the input vector is defined as

$$\boldsymbol{X} = (E_{\mathrm{SO}}, E_{\mathrm{SB}}, \phi_{\mathrm{SO}}, \phi_{\mathrm{SB}}, K_{0x,\mathrm{SO}}, K_{0x,\mathrm{SB}}, K_{0y,\mathrm{SO}}, K_{0y,\mathrm{SB}}).$$

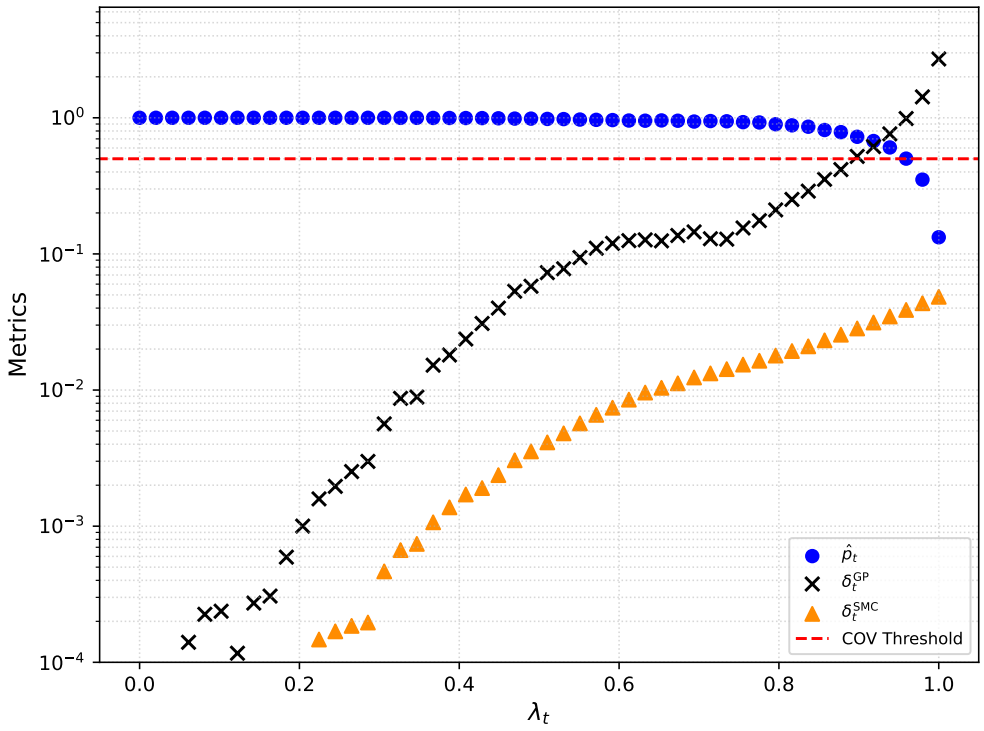

Figure 6.13: Evolution of the uncertainty metrics across 50 relaxation levels using Algorithm 4 ($N_p = 1000$), with a GP conditioned on an initial design of 366 evaluations (see Figure 4.10). The graphical elements follow the description provided for the top panel in Figure 6.10. The GP-induced uncertainty $\delta_t^{\mathcal{GP}}$ remains below the acceptable threshold of 0.5 for $\lambda \leq 0.9$ with the current design.

Results analysis Following the protocol of Section 6.6.1, Figure 6.13 shows the following behavior.
(i) The GP-induced uncertainty $\delta_t^{\mathcal{GP}}$ remains below the threshold value of 0.5 for $\lambda_t \leq 0.9$, corresponding to $\mathcal{B}_t = [4.06\mathrm{mm}, 6.64\mathrm{mm}] \times [35.4\mathrm{m}, 40.3\mathrm{m}]$. The inversion set is reliably characterized up to this level.
(ii) The conditional transition coefficient $\hat{p}_t$ remains above 0.1 and stable across relaxation levels. A decrease is observed for $\lambda_t \geq 0.9$, reflecting a more severe transition towards the target set $\mathcal{B}_T$.
(iii) The SMC-induced uncertainty δ_t^{SMC} remains below 0.1 throughout, with a progressive increase as particles approach $\mathcal{B}_T$. Sampling noise remains limited, indicating that the particle population is sufficient.

Figure 6.14 corresponds to the relaxation level $\lambda_t = 0.9$, for which the GP-induced uncertainty remains below the acceptable threshold of 0.5. At this level, the inversion

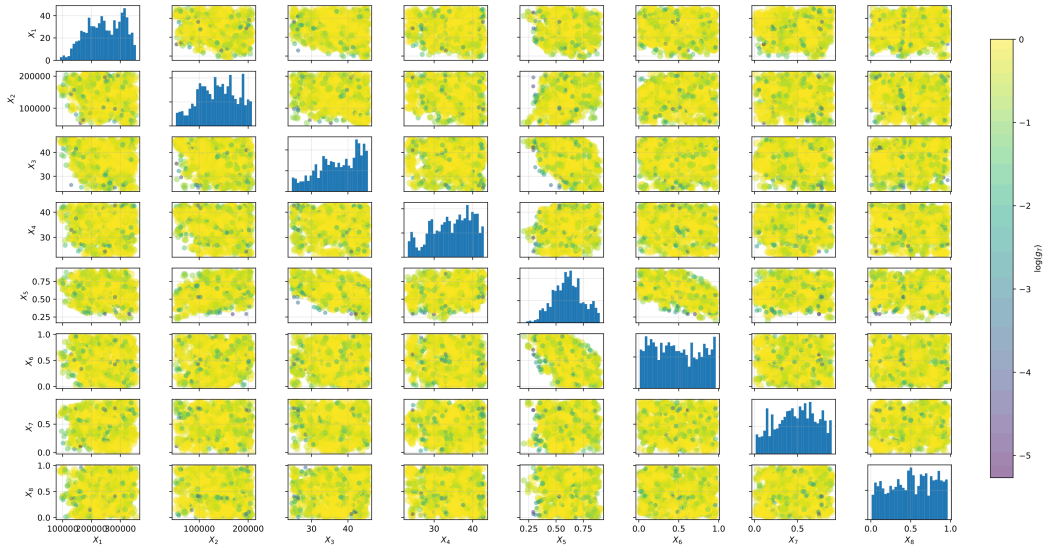

Figure 6.14: Pairwise particle plots illustrating the approximation of the inversion set $\mathbf{\Gamma}_t$ at relaxation level $\lambda_t = 0.9$ (see Figure 6.13), defined as $\mathbf{\Gamma}_t = \{\mathbf{x} \in \mathcal{X} : f(\mathbf{x}) \in \mathcal{B}_t\}$ with $\mathcal{B}_t = [4.06\text{mm}, 6.64\text{mm}] \times [35.4\text{m}, 40.3\text{m}]$. The graphical elements follow the description provided for Figure 6.12. For this relaxation level, the GP-induced uncertainty remains below the acceptable threshold of 0.5.

set is reliably characterized. The reduction of the input space remains limited, as most parameters still exhibit wide marginal distributions. The particle population shows little concentration in localized regions. A partial concentration is observed for $X_5 = K_{0x,\text{SO}}$, with values mainly in the range $0.5 - 0.75$, and interactions with other parameters. This behavior is consistent with the sensitivity analysis results reported in Section 4.2.2 (Chapter 4).

At $\lambda_t = 0.95$, the GP-induced uncertainty reaches the enrichment threshold ($\delta_t^{\mathcal{GP}} \approx 1.0$), indicating insufficient model accuracy at this level. The particle population is not degenerate, as indicated by a moderate transition coefficient ($\hat{p}_t \approx 0.5$), but the inversion boundaries remain poorly defined due to GP uncertainty. The admissible region is therefore only partially resolved. Nevertheless, the particle distribution provides qualitative insight into the regions of the input space that are compatible with the observations.

Figure 6.15 shows a clearer concentration of particles for X_1, X_2, X_3, X_4, and X_5, corresponding to $E_{\text{SO}}, E_{\text{SB}}, \phi_{\text{SO}}, \phi_{\text{SB}}$, and $K_{0x,\text{SO}}$. Particles cluster in regions associated with high values of Young's modulus and friction angle in the SO and SB layers. These configurations correspond to stiffer soil behavior and higher shear strength, leading to reduced surface settlements. In addition, $K_{0x,\text{SO}}$ concentrates in a narrower range ($0.5 - 0.6$) and exhibits interactions with $K_{0y,\text{SO}}$. Despite this structuring, the GP uncertainty remains high ($0.5 < \delta_t^{\mathcal{GP}} < 1.0$), especially near the inversion boundaries. The inversion set is therefore only partially resolved at this level.

Overall, the diagnostics indicate that the inversion is reliable up to $\lambda_t \approx 0.9$, but not for tighter relaxation levels closer to the target set. Additional evaluations are required to reduce GP uncertainty and refine the characterization of the inversion boundaries.

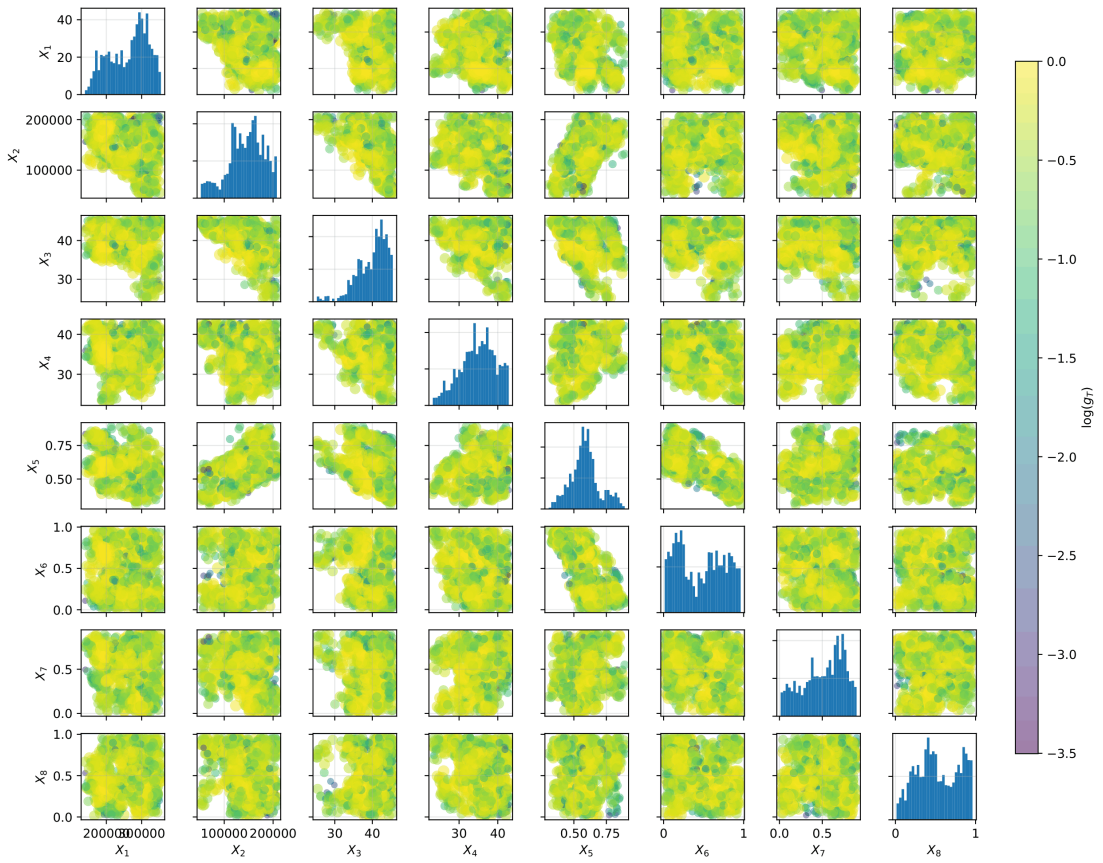

Figure 6.15: Pairwise particle plots illustrating the approximation of the inversion set $\mathbf{\Gamma}_t$ at relaxation level $\lambda_t = 0.95$ (see Figure 6.13), defined as $\mathbf{\Gamma}_t = \{\mathbf{x} \in \mathcal{X} : f(\mathbf{x}) \in \mathcal{B}_t\}$ with $\mathcal{B}_t = [4.23\text{mm}, 5.61\text{mm}] \times [35.9\text{m}, 38.9\text{m}]$. The graphical elements follow the description provided for Figure 6.14. At this relaxation level, the GP-induced uncertainty exceeds the acceptable threshold of 0.5.

6.7 Chapter conclusions

This chapter extends Bayesian subset simulation to set inversion problems. Starting from a target region in the output space, a sequence of relaxed sets is introduced, and a GP metamodel combined with SMC is used to progressively reconstruct the corresponding inversion sets in the input space.

The main contribution is the introduction of diagnostics that separate two sources of uncertainty under a fixed design: $\delta_t^{\mathcal{GP}}$, associated with the GP approximation, and δ_t^{SMC}, associated with the particle approximation. Combined with the transition coefficient $\hat{p}_t$, these quantities provide a practical framework to control the inversion process, by identifying unreliable relaxation levels, insufficient particle populations, and regions where additional evaluations are required.

The one-dimensional experiments confirm this interpretation: $\delta_t^{\mathcal{GP}}$ increases when the metamodel becomes insufficiently informative, δ_t^{SMC} reflects particle-induced variability, and $\hat{p}_t$ reveals overly abrupt transitions. The Hartmann 4 and tunnel FE case studies show how these diagnostics can be used in practice to delimit the range of reliably resolved relaxation levels and to guide targeted enrichment of the design.

The proposed GP-related bound, derived from Minkowski's inequality, is easy to evaluate but remains conservative. The approach relies on the quality of the GP posterior variance, so miscalibrated uncertainty may affect the characterization of the inversion sets.

Future work includes improving the calibration of GP uncertainty, quantifying the conservativeness of the proposed bound, and providing a more principled justification of the empirical threshold used for $\delta_t^{\mathcal{GP}}$.

Chapter 7

Conclusion and Perspectives

Contributions

This work addresses the calibration of three-dimensional numerical models of Tunnel Boring Machine (TBM) excavation using surface settlement monitoring data, with the objective of enabling their use for the analysis and control of settlements during construction. To this end, a Design and Analysis of Computer Experiments (DACE) framework is adopted throughout the study. This framework combines numerical simulation, quantification of numerical artefacts, metamodeling, global sensitivity analysis, and Bayesian set inversion.

3D finite element (FE) simulator and QoI definition. First, based on the review in Chapter 2, a parametric three-dimensional FE simulator is developed in Chapter 3. The model explicitly incorporates key operational parameters, including face pressure, grout injection pressure, shield conicity, shield-soil interaction, TBM weight and thrust, grout hardening, and lining installation. It is designed to reproduce the excavation process and predict the associated surface settlements for a given tunnel configuration.
The simulator outputs are post-processed and summarized through four settlement-related quantities of interest (QoIs), defined from a parametric representation combining the transverse formulation of (Wang, 2021) for z_1 (maximum surface settlement) and z_2 (radius of transverse influence), and a sigmoid model for the longitudinal evolution of z_3 (longitudinal slope at the inflection point) and z_4 (position of the longitudinal inflection point).
However, the computational cost of the simulator, of the order of 140 h per run for configurations complying with standard modeling recommendations, prevents its direct use for global sensitivity analysis, metamodeling, or calibration. In addition, the model involves a high-dimensional input space (66 parameters), most of which correspond to geotechnical properties subject to significant uncertainty, further complicating its practical use.

Accuracy-Cost Model Reduction (ACMR). To overcome these limitations, an Accuracy-Cost Model Reduction (ACMR) strategy is introduced in Chapter 4. This approach quantifies the numerical errors induced by modeling assumptions, in particular discretization and boundary truncation effects, through the construction of an empirical error model and extrapolation to an asymptotic reference solution.

This leads to reduced numerical configurations with a computational cost of approximately 15-30 h per simulation, corresponding to a reduction by a factor of about 5 to 9, while maintaining an acceptable level of accuracy for the quantities of interest.

Metamodel-based sensitivity analysis. Despite this reduction, the high dimensionality of the input space (66 parameters), primarily associated with the mechanical properties of the soil layers, makes direct GSA infeasible. A Sobol' analysis would have required 8704 simulations, corresponding to approximately 10^5 CPU-hours.
To overcome this limitation, Gaussian process (GP) metamodels were constructed for each QoI from 366 simulations (approximately five times the input dimension) and used to estimate Sobol' indices from conditional sample paths of the GP posterior. This approach enabled sensitivity analysis at an acceptable computational cost compared to direct simulation, while accounting for metamodel uncertainty (Marrel et al., 2009).

Sensitivity analysis results. In the context of multilayered soils, Sobol' indices show that the surface settlement response is mainly governed by the properties of the layers directly intersected by the TBM, namely the lateral earth pressure coefficients K_{0x} and K_{0y}, the Young's modulus E, the friction angle ϕ, and the cohesion c. In the specific geotechnical context of this study (two layers intersected), maximal settlements (z_1) and longitudinal QoIs (z_3 and z_4) tend to be more influenced by the upper layer (SO), whereas the transverse settlement width (z_2) appears to be more influenced by the properties of the lower layer (SB). Regarding TBM operation, grouting pressure affects all outputs, with a limited effect on z_2, while face pressure mainly influences the longitudinal slope z_3.

Monitoring data processing. To enable calibration with simulator QoIs, a processing pipeline was developed to transform noisy point monitoring data into QoIs consistent with the simulator outputs. A double-sigmoid formulation was introduced to describe the longitudinal settlement evolution. GP regression was used to reconstruct total settlement maps at successive TBM positions, from which a dynamic transverse representation was then derived. This dynamic transverse representation was then exploited to extract the observed QoIs.

Bayesian subset simulation (BSS) for set inversion. We then address calibration as a set inversion problem and reformulate BSS (Bect et al., 2017) to identify the set of input configurations consistent with observed QoIs. Starting from a target region in the output space, a sequence of relaxed sets is introduced, and a GP metamodel combined with Sequential Monte Carlo (SMC) sampling is used to progressively approximate the corresponding inversion set. The main contribution of this chapter lies in the introduction of diagnostics to quantify the reliability of the nested inversion sets. These include the GP-induced uncertainty $\delta_t^{\mathcal{GP}}$, introduced in this work, and the SMC sampling error δ_t^{SMC}, following Bect et al. (2017), as well as the conditional transition coefficient $\hat{p}_t$, which controls particle degeneracy between successive levels, and the SMC estimator of the expected volume $\hat{\alpha}_t$, which estimates the probability mass of the inversion set under the prior distribution. These quantities are further used to identify sets where the uncertainty

is acceptable for inversion and those where it remains too high and requires additional model evaluations.
The methodology is then illustrated on the Hartmann 4 function, showing the ability of the approach to address inverse problems with multiple solutions. It is then applied to the TBM case study using GP metamodels for the QoIs z_1 and z_2, based on monitoring data. The inversion results show that consistent input configurations can be identified for the relaxed target set $\mathcal{B}_t = [4.06, 6.64]$ mm $\times$ $[35.4, 40.3]$ m. However, this set remains relatively wide, and additional evaluations are required to target the narrower set $\mathcal{B}_{\text{target}} = [4.4, 4.6]$ mm $\times$ $[36.5, 37.5]$ m. These results suggest that the simulator admits input configurations compatible with the observed values of z_1 and z_2 simultaneously, at least for a relaxed target set.

Limitations

The proposed framework presents several limitations that should be acknowledged, as they define the scope of validity of the results and motivate the perspectives discussed in the following section.

FE simulator As the proposed simulator relies on a quasi-static formulation using a MC elastoplastic model under drained conditions with hydrostatic pore pressure and an effective stress formulation, it presents several limitations. First, pore pressure variations are not explicitly modeled, and hydromechanical coupling is neglected. This assumption is consistent with drained conditions but may be restrictive in low-permeability soils or when transient pore pressures affect the deformation response. Second, the MC model is limited by its assumption of constant elastic stiffness, with no account of stress- or strain-dependent stiffness. While useful in practice for its simplicity, it may lack accuracy when significant plastic strains develop (CFMS, 2023). More advanced models, such as the Hardening Soil model (Schanz et al., 2019) or its small-strain extension, provide a more realistic representation by capturing these stiffness variations (CFMS, 2023).
These limitations may explain the following observations encountered in this work: (i) A mismatch is observed in the longitudinal evolution of settlements between simulation and monitoring data, leading to discrepancies in the associated QoIs (z_3 and z_4). This discrepancy may result from neglecting time-dependent effects. (ii) The sensitivity analysis reveals a limited influence of face pressure on final settlement values, in contrast with field observations (Vanoudheusden, 2006) and previous FE studies (Kasper and Meschke, 2006a).

ACMR Although the ACMR methodology significantly reduces computational cost, it requires multiple evaluations of the FE simulator with varying modeling parameters (e.g., discretization, domain size) to fit the empirical error model and quantify numerical artefacts.
In addition, the ACMR framework assumes that the selected reduced configuration remains valid for the geotechnical conditions under which the empirical error model was fitted, and may not be directly transferable to significantly different soil conditions. In

other words, additional simulator evaluations are required, and the empirical error model must be refitted for different geotechnical conditions.
Finally, it is assumed that performing a design of experiments on the reduced model, through variations in soil properties, does not introduce additional numerical artefacts.

GP metamodel. The framework relies on GP metamodels, which assume stationarity of the simulator response (QoIs) and accurate calibration of the posterior variance (Williams and Rasmussen, 2006). Miscalibrated posterior variance, whether over- or under-estimated, directly affects the reliability of both the sensitivity analysis and the inversion results.
In addition, GP models may face limitations when dealing with a large number of evaluations, due to their cubic computational cost and memory requirements, which limit their scalability.

Inversion framework. The GP-induced uncertainty used to characterize the inversion set, $\delta_t^{\mathcal{GP}}$, derived from Minkowski's inequality, is known to be conservative. In this context, the empirical threshold value of 0.5 used for $\delta_t^{\mathcal{GP}}$ to assess whether the error is acceptable is not theoretically grounded. It is based on an empirical criterion for the acceptable relative uncertainty on the GP-based approximation of the probability mass of the inversion set.

Perspectives

The perspectives of this work are structured along two complementary axes: industrial perspectives related to the operational use of the proposed framework, and scientific perspectives addressing the main methodological limitations identified in this study.

Scientific perspectives.

Improving the modeling of longitudinal settlement evolution. Two main directions can be considered. First, improving the physical modeling by incorporating hydromechanical coupling to account for time-dependent effects (Kasper and Meschke, 2004; Ochmański et al., 2018), and by adopting more realistic constitutive models for soil behavior (Schanz et al., 2019). Second, explicitly accounting for model discrepancy within a Bayesian calibration framework (Kennedy and O'Hagan, 2001), for instance using recent approaches such as elastic Bayesian calibration (Francom et al., 2025).

Toward rigorous numerical design strategies for ACMR. The ACMR methodology provides practical guidelines for mesh and domain selection, but remains empirical and relies on one-at-a-time designs. Future work should aim at developing adaptive numerical design strategies within the ACMR framework to identify optimal accuracy-cost trade-offs with a minimal number of simulations. Bayesian approaches (Bect et al., 2021; Oates et al., 2025) offer promising perspectives for probabilistic numerical design with explicit control of numerical errors.

Consolidation of the BSS set inversion framework. Further work is required to quantify the impact of the conservativeness of the Minkowski-based bound on the GP-

induced error metric $\delta_t^{\mathcal{GP}}$. This would provide a more principled justification for the empirical thresholds used to assess inversion reliability.

Industrial perspectives.

Calibration on monitored sections. Calibration is first performed on well-instrumented sections using dense monitoring data and the BSS set inversion framework, which identifies the set of parameter configurations consistent with observations. This step provides a calibrated representation of the uncertainty on model parameters. For geotechnical contexts with similar characteristics, this information can then be reused to support predictive analyses.

Prediction of settlements under uncertainty. In a given geotechnical context, the parameter uncertainty identified during calibration is propagated through the numerical model to perform forward predictions. Given admissible parameters θ selected from the admissible set identified during calibration (or, in future work, from a probability distribution constructed on that set), settlement predictions are expressed as

$$z_{\text{pred}} = f(x_{\text{obs}}, x_{\text{tbm}}, \theta) + \varepsilon,$$

where ε accounts for residual uncertainties not already represented by θ, such as model discrepancy, metamodel approximation error, or unmodeled operational variability. This provides probabilistic estimates of surface settlements, such as confidence intervals or exceedance probabilities.

Multi-scenario operational decision support for TBM excavation. The predictive framework extends naturally to operational decision support by enabling the comparison of alternative TBM driving strategies prior to execution. For a scenario defined by a set of operational parameters $x_{\text{tbm}}^{(s)}$, the methodology yields a distribution of predicted settlements. This can be analyzed as an excursion set problem by estimating the probability $\Pr(z_{\text{pred}} > z_{\text{thr}})$ of exceeding a prescribed settlement threshold z_{thr}. Comparing these probabilities across scenarios allows operators to select strategies that balance excavation efficiency and surface risk control.

Appendices

Appendix A

Surface settlement and volume loss: Peck's formulation

Surface settlements induced by mechanized tunneling are commonly described using the empirical framework proposed by Peck (1969), in which the transverse settlement profile is approximated by a Gaussian distribution. Under greenfield conditions the vertical settlement $s(x)$ at a transverse distance x from the tunnel centerline is expressed as:

$$s(x) = s_{\max} \exp\left(-\frac{x^2}{2i^2}\right), \tag{A.1}$$

where $s_{\max}$ is the maximum settlement above the tunnel axis and i is the distance to the inflection point, which controls the width of the settlement trough (Figure A.1).

Peck's formulation remains a standard reference in preliminary design. Empirical correlations relate the trough width parameter i to the tunnel depth H_t, typically in the form $i = KH_t$, where K depends on soil conditions (O'reilly and New, 1982; Mair et al., 1993). Extensions have been proposed to account for more complex geological conditions (Zhou et al., 2024; Niu et al., 2023).

The maximum settlement is directly related to the ground volume loss per unit length of tunnel, denoted V_L. This quantity represents the normalized reduction of the tunnel cross-sectional area. For a tunnel of radius R_t and a uniform radial displacement u_s, the volume loss is

$$\Delta V = \pi R_t^2 - \pi(R_t - u_s)^2,$$

which leads to the normalized expression

$$V_L = \frac{\Delta V}{\pi R_t^2} = \epsilon_s(2 - \epsilon_s),$$

where $\epsilon_s = u_s/R_t$ is the radial strain.

In the small-strain regime ($u_s \ll R_t$), this simplifies to

$$V_L \approx 2\epsilon_s.$$

Under elastic conditions, the radial strain ϵ_s can be related to the stress state around the tunnel. For a circular cavity in a linear elastic medium subjected to an initial isotropic stress σ_0 and a support pressure p_0, the radial strain at the tunnel wall is expressed as:

$$\epsilon_s = \frac{\sigma_0 - p_0}{2G}$$

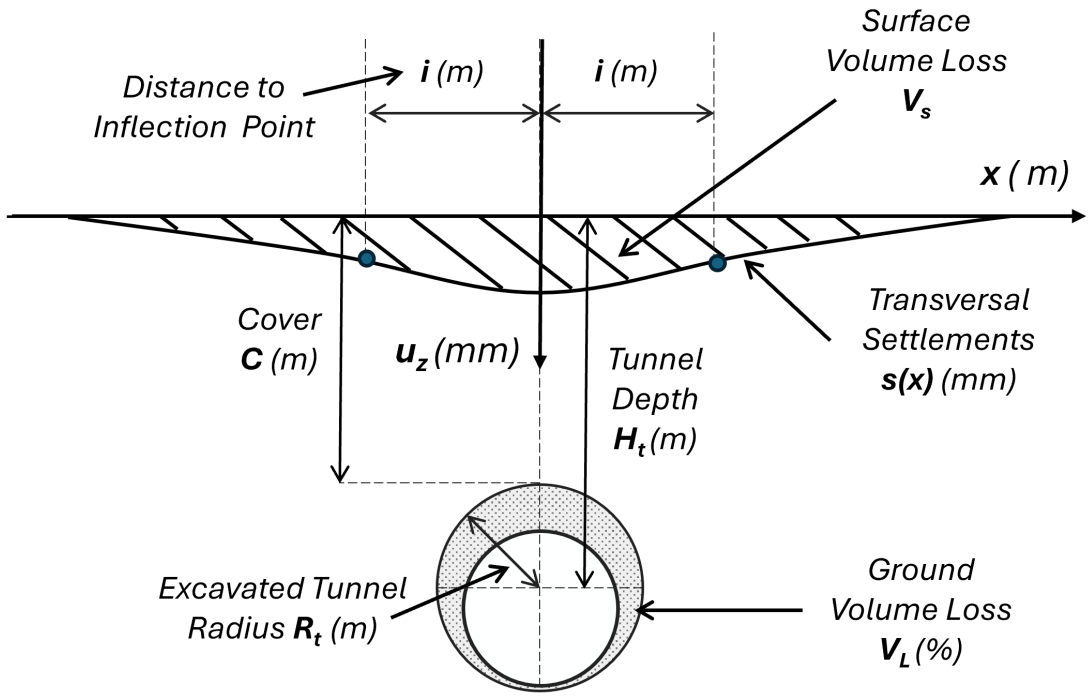

Figure A.1: Gaussian settlement trough after tunneling, adapted from Peck (1969).

where G is the shear modulus, defined by the Young's modulus E and Poisson's ratio ν as $G = \frac{E}{2(1+\nu)}$. More detailed expressions accounting for elastic and elastoplastic behavior can be found in Sagaseta (1998).

The surface settlement volume per unit tunnel length, denoted V_s, can be obtained by integrating Eq. (A.1):

$$V_s = \int_{-\infty}^{+\infty} s(x)dx = \sqrt{2\pi} i s_{\max}.$$

The relationship between V_s and the actual ground volume loss ΔV depends on drainage conditions (Cording, 1975). In undrained conditions, it is commonly assumed that $V_s \approx \Delta V$, whereas in drained conditions, internal soil rearrangements generally lead to $V_s < \Delta V$.

Assuming $V_s = \Delta V$, the maximum settlement can be expressed as

$$s_{\max} = \frac{V_L \pi R_t^2}{\sqrt{2\pi} i}.$$

This relation establishes a direct link between tunnel-scale deformation, through the volume loss V_L, and the resulting surface settlement profile.

Loganathan (2011) propose to decompose the volume loss into three components, corresponding to distinct zones around the tunnel and key deformation stages during which the construction process induces ground volume loss:

$$V_L = V_{\text{face}} + V_{\text{shield}} + V_{\text{tail}},$$

which correspond, respectively, to volume losses at the tunnel face due to the insufficient face pressure, around the shield due to its conicity, and in the tail void due to the annular gap between the tail and the lining (Figure A.2).

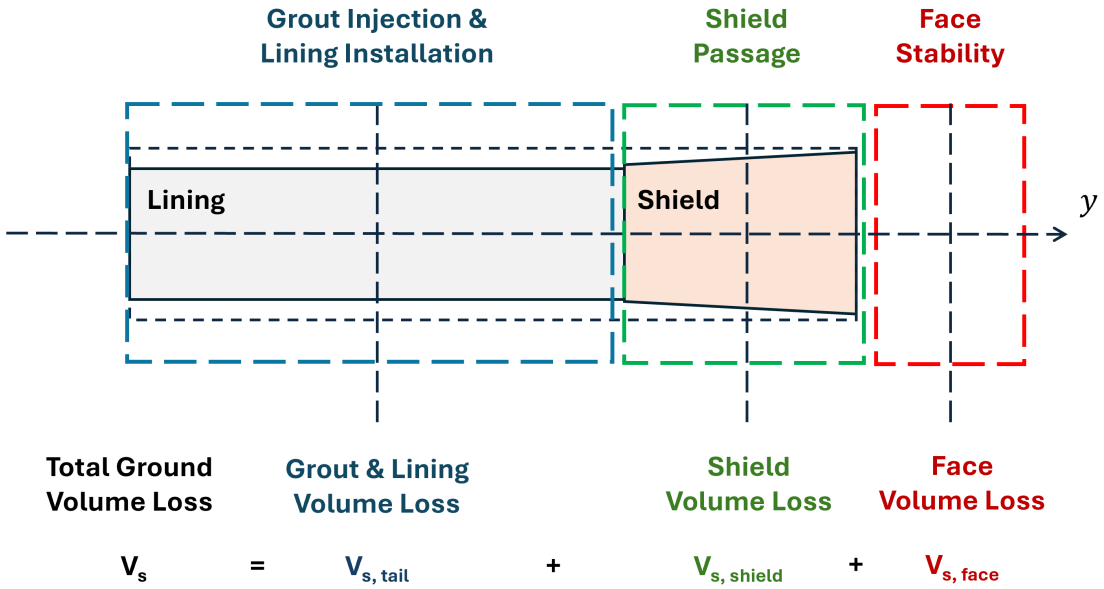

Figure A.2: Schematic illustration of ground volume loss mechanisms in EPB tunneling.

Appendix B

Influence of depth on settlement

The trough width parameter i is often related to the tunnel axis depth H_t. From field measurements in clay and granular soils, O'reilly and New (1982) proposed the following correlations

$$i = 0.43H_t + 1.1 \quad \text{(cohesive soils)},$$
$$i = 0.28H_t - 0.1 \quad \text{(granular soils)}.$$

For practical purposes, this relation is frequently simplified as Mair et al. (1993),

$$i = KH_t,$$

with $K \approx 0.5$, consistently with additional observations by Rankin (1988). These empirical laws are widely adopted for preliminary estimates of settlement troughs.

Using Peck-type profiles, the maximum surface settlement can be approximated by

$$s_{\max} = \frac{\pi}{2} \cdot \frac{V_L R_t^2}{i}.$$

The influence of the cover, defined as $C = H_t - R_t$, has been studied in detail (Vu et al., 2015). Here, we adopt the empirical expressions of O'reilly and New (1982) for $i(H_t)$ to evaluate the variation of $s_{\max}$ with the cover-to-diameter ratio C/D, assuming a constant tunnel radius of 3 m and a volume loss ratio $V_L = 0.5\%$.

As shown in Figure B.1, the results are consistent with Vu et al. (2015): the maximum transverse settlement decreases with increasing depth, highlighting the role of the cover-to-diameter ratio C/D. Beyond $C/D \approx 5$, the impact on surface displacements is negligible, in line with the definition of deep tunnels by Mair (2008).

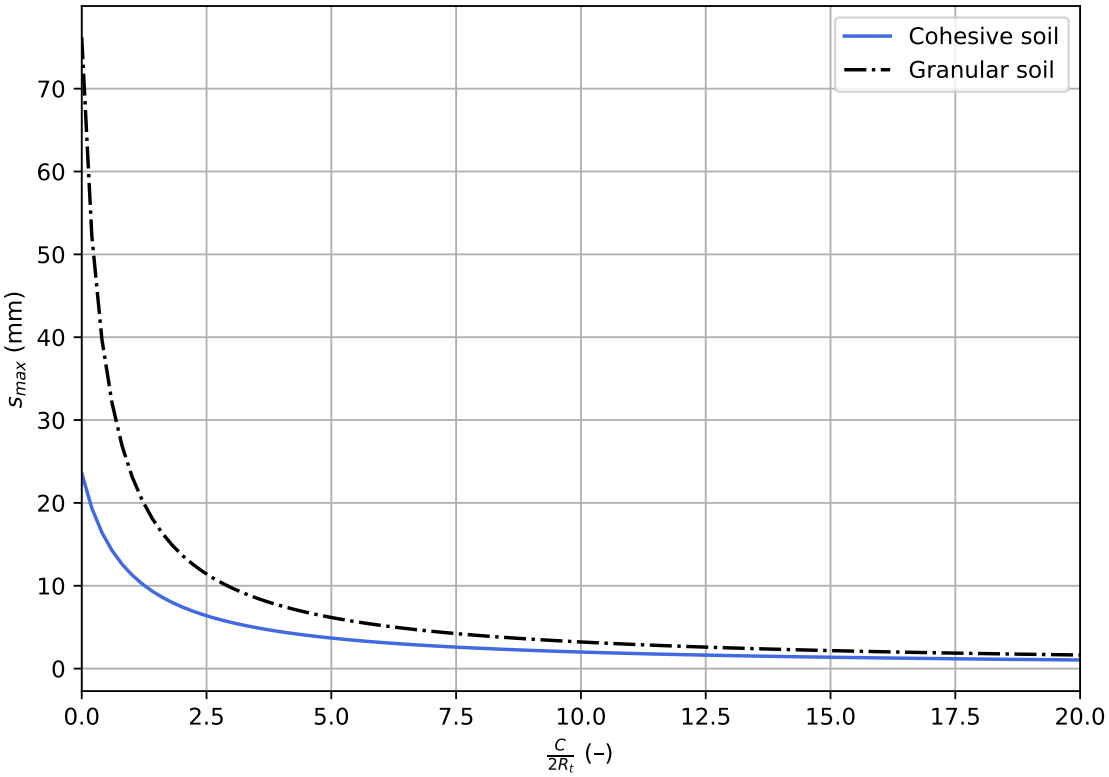

Figure B.1: Influence of tunnel depth on maximum settlement $s_{\max}$ as a function of the cover-to-diameter ratio C/D. For $C/D > 5$, the depth effect becomes negligible, which supports the classical definition of deep tunnels. Soil unit weight γ is not considered in this analysis.

Appendix C

K_0 estimation

Typical values of K_0 are derived from empirical or theoretical expressions. For normally consolidated soils ($K_0 < 1$), Jaky's relation (JAKY, 1944) is adopted,

$$K_0 = 1 - \sin\phi,$$

where ϕ denotes the soil friction angle. For overconsolidated soils ($K_0 > 1$), meaning that the horizontal stress exceeds the vertical stress, the expression proposed by Mayne and Kulhawy (1982) is often used:

$$K_0 = (1 - \sin\phi)OCR^{\sin\phi}, \qquad OCR = \frac{\sigma'_p}{\sigma'_z},$$

where σ'_p is the preconsolidation pressure, representing the maximum effective vertical stress reached during the soil's geological history.

When detailed site data are unavailable, an elastic plane-strain approximation may be adopted. For a linear elastic medium subjected to self-weight loading under zero lateral strain conditions, the at-rest coefficient may be approximated by

$$K_0 = \frac{\nu}{1 - \nu},$$

where ν is Poisson's ratio. This approximation corresponds to the elastic solution of the gravity problem without prescribing an empirical K_0 value.

Appendix D

On the limitations of the K_0 procedure for stress initialization

In urban or geologically complex contexts, a direct K_0 procedure may lead to unrealistic stress distributions. This occurs for example in the presence of inclined stratigraphy, localised surface loads, or non-horizontal water tables (Figure D.1).

A common alternative is the *geostatic step*, where gravity loading is applied numerically until equilibrium is reached. This approach ensures compatibility with heterogeneous stratigraphy, varying groundwater conditions, and soil-structure interaction. After the geostatic step, displacements are reset so that excavation starts from a strain-free state. Its main limitation is that the stress history cannot be represented by a single K_0 value.

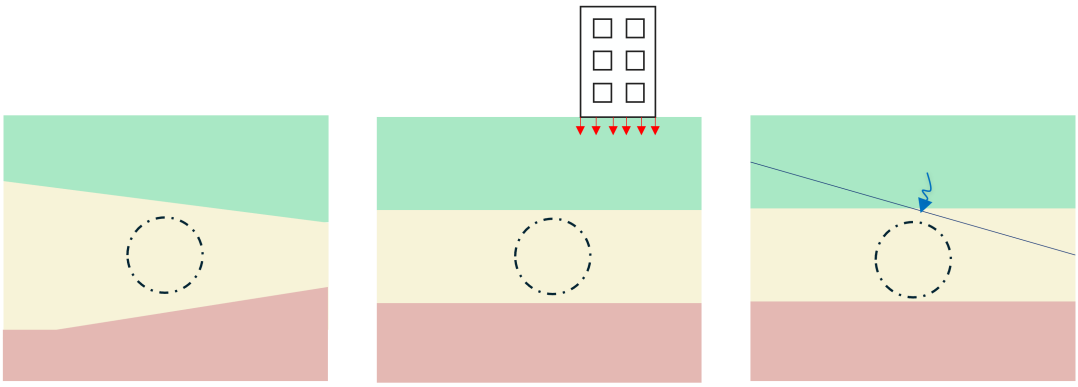

Figure D.1: Examples where a direct K_0 procedure is inadequate: (a) inclined stratigraphy, (b) surface structural load, (c) sloping water table.

When stratigraphy and groundwater are nearly horizontal, a two-step procedure is often adopted: a K_0 procedure under self-weight, followed by a geostatic step to incorporate local loads and boundary conditions. Displacements are then reset before excavation (Figure D.2).

Further details on these strategies are provided in Ochmański et al. (2018); CFMS (2023).

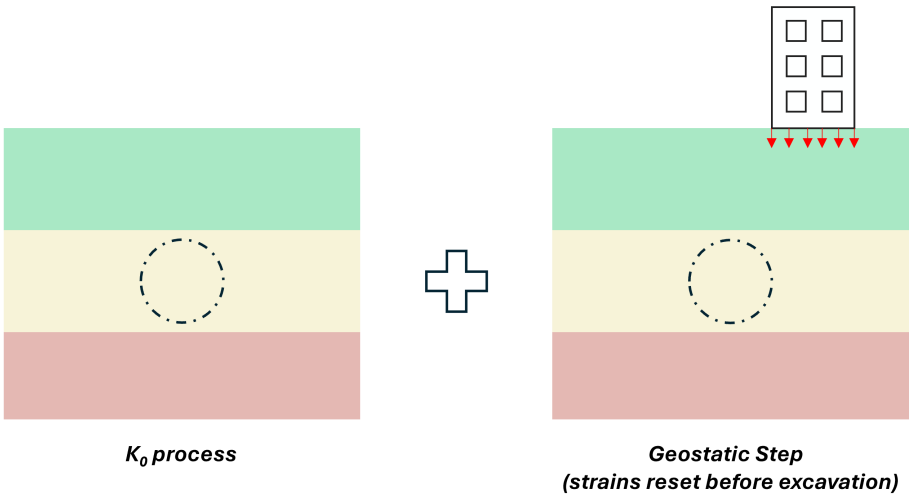

Figure D.2: Two-step initialization procedure: (i) computation of the K_0-based self-weight stress state; (ii) geostatic adjustment with local loads and boundary conditions, followed by displacement reset before excavation.

Appendix E

Stress initialization examples

The following examples illustrate typical stress initialization procedures using a K_0-approach. This method assumes horizontal stratification, hydrostatic pore pressure, and, where relevant, a uniform surface load. Vertical stresses are obtained from the self-weight of overlying layers, while horizontal stresses are deduced from the corresponding earth pressure coefficient K_0. Effective stresses are then corrected for pore water pressure according to the drainage conditions.

Figure E.1 shows a stratified soil profile under drained and undrained conditions with hydrostatic pore pressure. Each layer is characterized by a specific unit weight and K_0 value, from which the effective stress distribution is computed.

Figure E.2 adds a dry surface layer and an overconsolidated intermediate layer ($K_0 > 1$), illustrating the combined influence of unsaturation and stress history on the initial horizontal stresses.

Figure E.3 includes a uniform surface surcharge q_s. The surcharge increases the vertical stresses at depth and modifies the horizontal distribution through the K_0-relation. Effective stresses are again obtained by subtracting the hydrostatic pore pressure from the total stresses.

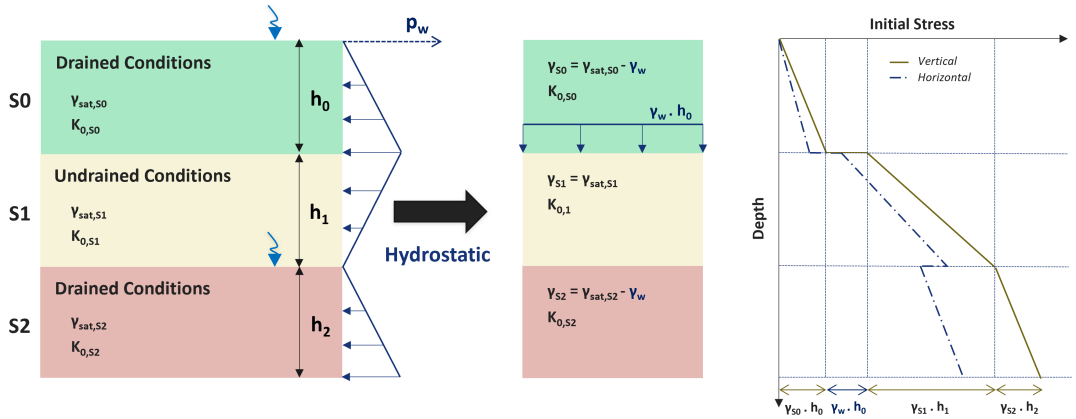

Figure E.1: Stress initialization in a stratified soil under drained and undrained conditions. Vertical stresses are derived from self-weight, and horizontal stresses from layer-specific K_0. Effective stresses account for hydrostatic pore pressure in saturated zones.

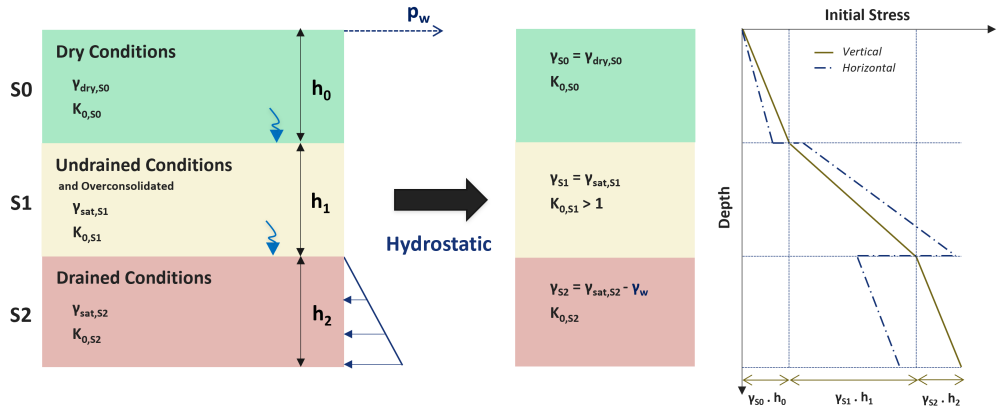

Figure E.2: Initial stress profile in a stratified deposit with a dry surface layer and an overconsolidated intermediate layer ($K_0 > 1$). Effective stresses are corrected using the hydrostatic pore pressure distribution.

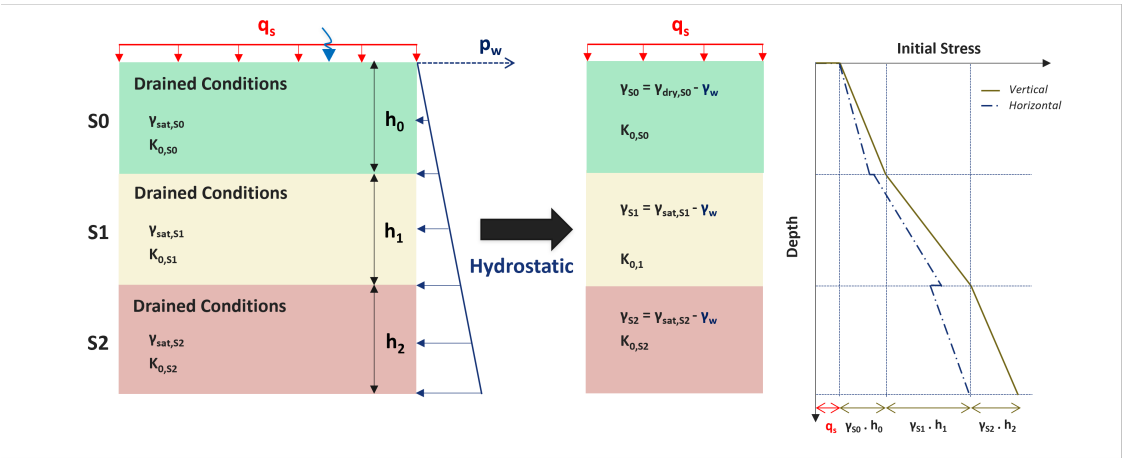

Figure E.3: Stress initialization with a uniform surface surcharge q_s. The surcharge is superimposed on self-weight stresses and transferred to horizontal stresses through the K_0-relation. Effective stresses are obtained by subtracting hydrostatic pore pressure.

Appendix F

Supplementary review of 3D FEM and FDM TBM excavation models

To complete the review of numerical models for TBM excavation, with a particular focus on the constitutive soil models adopted, Table F.1 summarizes a representative set of three-dimensional numerical studies published between 2002 and 2023. These contributions address tunneling in urban environments, with particular emphasis on the prediction of surface settlements. For each study, the table reports the numerical method, such as the finite element method (FEM) or finite difference method (FDM), the constitutive soil model, the treatment of stress-strain nonlinearity, and the consideration of pore-water pressures and hydromechanical coupling.

The majority of studies rely on the Mohr-Coulomb model, despite its well-known limitations in capturing soil behavior under complex loading conditions. Particular attention is paid to whether the analyses are performed under effective stress conditions (drained or undrained) and to how pore pressures are treated: either updated at each excavation step in partially coupled analyses, or fully coupled with mechanical equilibrium. When this information is not explicitly reported, the analyses are generally interpreted as undrained total-stress simulations, in which pore pressure effects are neglected.

Table F.1: Review of 3D numerical modeling of the TBM process and soil constitutive behavior.

Paper	FDM	FEM	Soil models	NL σ–ε*	Drained	HM*
Melis et al. (2002)	✓	✗	MC (1), MCC (2)	✓	✗	✗
Mroueh and Shahrour (2003, 2008)	✗	✓	MC (1)	✗	✗	✗
Jenck and Dias (2004)	✓	✗	MC (1)	✗	✓	✗
Kasper and Meschke (2006a,b); Meschke et al. (2011); Nagel and Meschke (2010)	✗	✓	MCC (2)	✓	✗	✓
Viggiani et al. (2004)	✓	✗	MC (1)	✗	✗	✗
Demagh et al. (2008)	✓	✗	MC (1)	✗	✓	✗
Migliazza et al. (2009)	✓	✗	MC (1)	✗	✓	✗
Lambrughi et al. (2012)	✓	✗	MC (1), MCC (2)	✓	✓	✗
Chakeri et al. (2013)	✓	✗	MC (1)	✗	✗	✗
Founta et al. (2013)	✗	✓	MC (1), DP (3)	✗	✗	✗
Mirhabibi and Soroush (2013)	✗	✓	MC (1)	✗	✗	✗
Mollon et al. (2013)	✓	✗	MC (1)	✗	✗	✗
Zhao et al. (2015)	✗	✓	HSS (5)	✓	✓	✗
Zhang et al. (2016)	✗	✓	MC (1), DP (3)	✓	✗	✓
Kavvadas et al. (2017)	✗	✓	MC (1)	✗	✗	✗
Litsas et al. (2017)	✗	✓	MC (1)	✗	✗	✓
Nematollahi et al. (2020)	✗	✓	MC (1)	✗	✓	✗
Ochmański et al. (2018)	✓	✗	HP (6) + ISC (7)	✓	✗	✓
Losacco and Viggiani (2019)	✗	✓	HP (6) + ISC (7)	✓	✗	✓
Miliziano and de Lillis (2019)	✗	✓	MC (1), HS (4)	✗	✓	✗
Nematollahi and Dias (2019)	✓	✗	MC (1), CY (8)	✓	✓	✗
Do et al. (2021)	✓	✗	MC (1), CY (8)	✓	✗	✗
Bahri et al. (2022)	✓	✗	MC (1)	✗	✗	✓
Tyrer et al. (2023)	✗	✓	MC (1), HS (4), HSS (5)	✓	✗	✗

Legend: NL $(\sigma$–$\varepsilon)$* = Soil strain-stress nonlinearity;
HM* = hydromechanical coupling (pore pressure / water flow);
MC (1) = Mohr-Coulomb (elastic-perfectly plastic, no hardening);

MCC (2) = Modified Cam Clay (critical state, isotropic hardening);
DP (3) = Drucker-Prager (approx. of Mohr-Coulomb);
HS (4) = Hardening Soil (nonlinear elastoplastic with shear/vol. hardening Schanz et al. (2019));
HSS (5) = HS Small Strain (small-strain stiffness; extension of HS);
HP (6) = Hypoplastic (no additive strain split; granular Von Wolffersdorff (1996), cohesive Mašín (2005));
ISC (7) = Intergranular Strain Concept (history variable; stiffness degradation Niemunis and Herle (1997));
CY (8) = Cap Yield (shear surface + hardening cap; compaction/vol. plasticity).

Appendix G

Shield-soil contact interface models

Contact interactions at the shield-soil interface are described by mechanical laws governing the normal and tangential behavior. Hard-contact formulation enforce non-penetration, but their abrupt pressure-displacement response may lead to convergence difficulties (Kavvadas et al., 2017; Ochmański et al., 2018).

To improve numerical stability, softened exponential pressure-overclosure law can be adopted. This law allow limited interpenetration (between soil mesh nodes and TBM mesh nodes) and provide a smooth increase in contact pressure, resulting in improved robustness and convergence. This formulation is implemented in ABAQUS and is commonly used in tunnel modeling (Zhao et al., 2015; Kavvadas et al., 2017; Ochmański et al., 2018; Losacco and Viggiani, 2019).

This contact law (exponential pressure-overclosure) is defined by parameters such as the contact pressure at zero clearance p_0 and the initial gap c_0, which control the shape of the pressure-displacement relationship. Figure G.1 compares the discontinuous response of the hard-contact law with the smooth behavior obtained using the exponential law.

Tangential behavior at the shield-soil interface may include frictional effects, commonly described using the Coulomb friction law (Kasper and Meschke, 2004; Meschke et al., 2011) or the Herzog friction law (Ochmański et al., 2018, 2020).

In practice, the interface is generally considered lubricated, and frictionless contact is therefore often assumed in numerical models (Losacco and Viggiani, 2019).

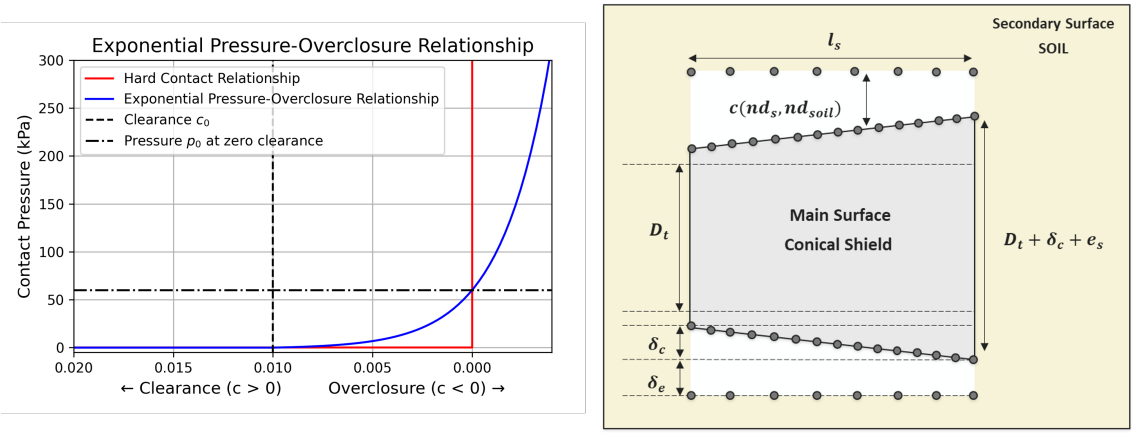

Figure G.1: Shield-soil contact law. Left: Comparison between a hard-contact law (red), characterised by a discontinuous pressure response, and an exponential pressure-overclosure law (blue), which provides a smooth increase in contact pressure as the clearance decreases. Right: Geometric parameters of the interface, including the mesh nodal clearance $c(nd_{\text{soil}}, nd_s)$, shield length l_s, tunnel diameter D_t, shield thickness e_s, conicity δ_c, and overexcavation δ_e.

Appendix H

Selection of operating pressures for TBM excavation

H.1 Face support pressure

Face support pressure is one of the most critical operational parameters in mechanised tunneling, as it directly controls the stability of the excavation face. Under undrained conditions, its selection often relies on the stability number (Broms and Bennermark, 1967; Peck, 1969), which provides a criterion for defining the required support pressure $p_f(z)$

$$N = \frac{\sigma_h(z) - p_f(z)}{c_u},$$

where $\sigma_h(z)$ is the total horizontal earth pressure, typically obtained from the initial stress state, and c_u is the undrained shear strength of the soil. Experimental and theoretical studies indicate that a critical stability number generally lies in the range $5 < N_c < 7$, beyond which face collapse becomes highly probable.

Alternative formulations, such as that proposed by Mair and Taylor (1992), use a stability criterion expressed in terms of a safety factor, for which maintaining values close to unity is recommended to avoid plastic collapse at the face.

In numerical simulations, a common practice is to set the average face pressure applied at the tunnel axis equal to the in-situ horizontal stress (Do et al., 2014), expressed as

$$p_{f,0} \approx \sigma_h(H_t) = K_0\, \sigma_v(H_t),$$

where K_0 is the coefficient of earth pressure at rest and $\sigma_v(H_t)$ the vertical stress at tunnel depth H_t. Under drained conditions, the effective vertical stress σ'_v is typically considered to compute the corresponding effective horizontal stress σ'_h.

While these simplified formulations are useful in practice, more advanced analytical and numerical approaches have been developed to evaluate face stability and support pressure requirements in both drained and undrained conditions; see for instance (Leca and Dormieux, 1990; Mollon et al., 2009, 2010, 2011; Ibrahim et al., 2015).

H.2 Grout injection pressure

The choice of grouting pressure is equally important, as it ensures proper annular gap filling and helps control ground deformations. A practical engineering criterion commonly used sets the injected grout pressure proportional to the soil overburden pressure at the tunnel crown (Do et al., 2014):

$$p_{0,g} \approx 1.2\,\sigma_v(z_{\text{crown}}),$$

where $\sigma_v(z_{\text{crown}})$ is the vertical overburden stress at crown level. Under drained conditions, the effective vertical stress σ'_v is typically used to compute the corresponding effective horizontal stress σ'_h.

Appendix I

Evolution of grout stiffness during hardening

The time-dependent evolution of grout stiffness is often described by empirical relations for the Young's modulus. A widely applied formulation CEB-FIB (1993); FIB (2013) expresses it as

$$E_g(t) = \beta_E(t)\, E_g^f, \tag{I.1}$$

with

$$\beta_E(t) = [\beta_{cc}(t)]^{0.5}, \quad \beta_{cc}(t) = \exp\left\{ s \left[1 - \left(\frac{28}{t} \right)^{0.5} \right] \right\},$$

where E_g^f is the final (28-day) modulus and s is a cement-dependent parameter (here $s = 0.38$).

For short-term analyses, Lambrughi et al. (2012) proposed an alternative expression tailored to the early hardening phase, with t expressed in hours. The Young's modulus $E_g(t)$ is defined with respect to a characteristic hardening time t_0 as

$$E_g(t) = \begin{cases} E_g^i, & t = 0, \\ E_g^f \left[1 - \exp\left(-0.2 \frac{t}{t_0} \right) \right], & 0 < t \leq t_0, \end{cases}$$

where E_g^i is the initial modulus at injection and E_g^f the final hardened modulus.

Appendix J

Tables of case study parameters

For all analyses conducted in this thesis, the proposed methods are evaluated on a geological profile representative of a tunnel section in Île-de-France. The ranges of geological parameters are based on Mollon et al. (2013); Phoon and Huang (2007); Phoon and Kulhawy (1999); Berthoz et al. (2020) and are selected to reflect typical variability observed in regional geotechnical conditions.

Operational parameter ranges and values (e.g., face pressure, grout pressure, shield conicity) are selected to ensure realistic excavation conditions and are also based on literature studies (Kavvadas et al., 2017; Ochmański et al., 2018).

The input space includes both geological and operational variables, as summarized in Tables J.1–J.3. In particular, Tables J.1 and J.2 describe geological properties representative of the Île-de-France context.

Soil Layers	**Water**	**Drained**	**Thickness**	**Saturated Unit Weight**
Notations	-	-	e_{geol}	γ
Units	-	-	m	kN/m^3
RB/AM	Yes	Yes	2.6-3.1	16-22
AA	Yes	Yes	5.2-7.8	16-22
CC	Yes	Yes	1.9-2.9	16-22
MPH	Yes	Yes	1.0-2.0	16-22
SO	Yes	Yes	8.7-13.3	15-21
SB	Yes	Yes	6.0-10.0	18-24
MC	Yes	Yes	13.6-20.4	17-23
CG	Yes	Yes	4.5-17.6	18-24

Table J.1: Geological Parameters (Geometric Properties)
Note: *RB: Fill, AM: Modern alluvium, AA: Ancient alluvium, MC: Marl and rubble mixture, SO: Saint-Ouen Limestone, SB: Beauchamp Sand, CC: Champigny Limestone, CG: Coarse Limestone, MPH: gypsiferous marl.*

Soil Layers	**Young Modulus**	**Poisson Ratio**	**Friction Angle**	**Cohesion**	**Earth Pressure Coefficient**
Notations	E	ν	ϕ	c	K_{0x}, K_{0y}
Units	MPa	-	$^\circ$	kPa	-
RB/AM	12.85-51.15	0.3	19.7-36.4	0.20-1.0	0.1-1.11
AA	78.32-311.68	0.3	25.9-48.0	2-8	0.1-0.84
CC	38.56-153.44	0.3	24.5-45.5	12-48	0.1-0.90
MPH	16.87-67.13	0.3	23.8-44.1	2-8	0.1-0.92
SO	89.16-354.84	0.3	24.6-45.5	10-40	0.1-0.96
SB	52.21-207.79	0.3	23.1-42.9	2-8	0.1-1.05
MC	131.33-522.67	0.3	21.0-38.4	8-32	0.1-1.05
CG	267.48-1064.0	0.3	24.5-45.5	40-160	0.1-0.90

Table J.2: Geological Parameters (Mechanical Properties)
Note: *RB: Fill, AM: Modern alluvium, AA: Ancient alluvium, MC: Marl and rubble mixture, SO: Saint-Ouen Limestone, SB: Beauchamp Sand, CC: Champigny Limestone, CG: Coarse Limestone.*

Table J.3: Global model parameters

Parameter	**Symbol**	**Value (Range)**	**Parameter**	**Symbol**	**Value (Range)**
Domain parameters			**TBM shield parameters**		
Total Width	X_{lim}	30-120 m	Overexcavation	δ_e	0-0.02 m
Total Length	Y_{lim}	40-170 m	Length	l_s	12 m
Total Height	Z_{lim}	35-70 m	Shield Conicity	δ_c	0.025 m
Surface Load	q_s	0-80 kPa	Shield Thickness	e_s	0.15 m
Tunnel Depth	H_t	19-24 & 32 m	Young Modulus	E_s	200 GPa
Water Level	z_w	0 m	Poisson Ratio	ν_s	0.3
			Shield Unit Weight	γ_s	70 kN/m^3
Excavation process			**Tunnel lining parameters**		
Soil Slice Length	l_e	2 m	Young Modulus	E_l	15-60 GPa
Total Excavation Length	L_t	10-120 m	Poisson Ratio	ν_l	0.2
Tunnel Diameter	D_t	9.9 m	Lining Thickness	e_l	0.323 m
Key Face Pressure	p_f^0	0-160 kPa	Lining Unit Weight	γ_l	31 kN/m^3
Gradient Face Pressure	p_f^{grad}	1-8 kPa/m			
Tail void grout backfilling			**Numerical parameters**		
Key Grout Pressure	p_g^0	0-100 kPa	Contact Pressure at Zero Clearance	p_0	60 kPa
Gradient Grout Pressure	p_g^{grad}	15-30 kPa/m	Contact Clearance	c_0	0.01 m
Length of Liquid Grout	l_g	0-6 m	Fine Material Coefficient	α_{fine}	0.25-2.7
Final Hardened Grout Young Modulus	E_g^f	0.1-4.5 GPa	Coarse Material Coefficient	α_{coarse}	0-0.25
Grout Hardening Unit Weight	γ_g	18 kN/m^3			
Length of Grout Hardening Process	l_h	6 m			

Appendix K

3D simulation results: surface settlement profiles

This appendix presents representative longitudinal and transverse settlement profiles extracted at mesh nodes along the monitored line (ML), as defined in Figure 3.1 of Chapter 3.

Transverse settlement profiles. The transverse settlement profile at the ML is defined as

$$s_v^t(x; y_k) := u_z(x, 0, 0; y_k), \tag{K.1}$$

where u_z is the vertical displacement, x the transverse horizontal coordinate, and y_k the TBM face position relative to the ML, with $y_k = 0$ at the intersection with the ML.

For a given simulation run, profiles $s_v^t(x; y_k)$ are evaluated at successive values of y_k, describing the evolution of surface settlements during TBM advance.

Longitudinal settlement profiles. The longitudinal settlement profile at the ML is defined as

$$s_v^l(y_k) := u_z(0, 0, 0; y_k), \tag{K.2}$$

corresponding to the settlement at the tunnel axis (x = 0) as a function of the TBM position.

Figure K.1 shows longitudinal settlement profiles obtained from different simulations. Settlements initiate before the TBM reaches the ML ($y_k < 0$) and progressively converge to a steady-state value after TBM passage ($y_k > 0$), resulting in an S-shaped evolution curve.

Figure K.2 presents transverse settlement profiles extracted from different simulations at comparable TBM positions. All profiles exhibit a maximum settlement at the tunnel axis, with settlements decreasing away from the center. Variations in amplitude and width reflect the influence of the input parameters.

Figure K.3 illustrates the evolution of $s_v^t(x; y_k)$ within a single simulation. As the TBM approaches the ML, the settlement amplitude and width increase. After passage, the profile stabilizes at a steady-state value.

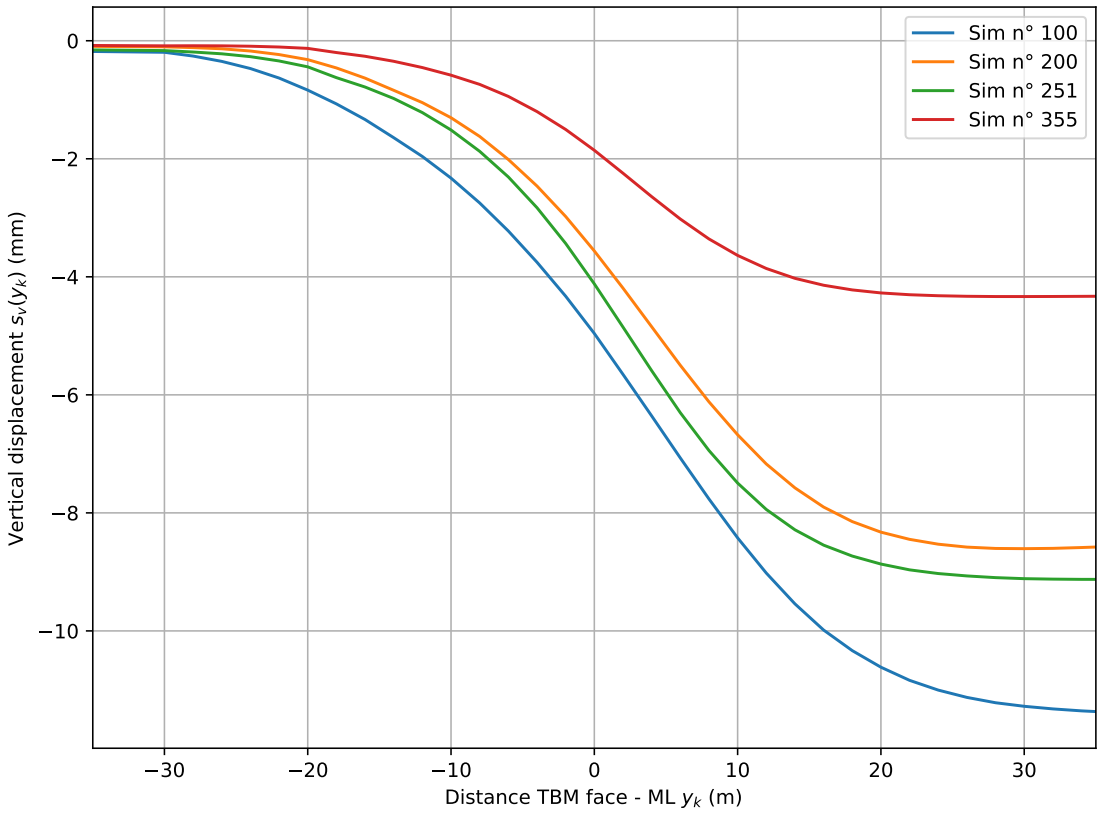

Figure K.1: Longitudinal settlement profiles s_v^l defined by Eq. (K.2), obtained from different simulations.

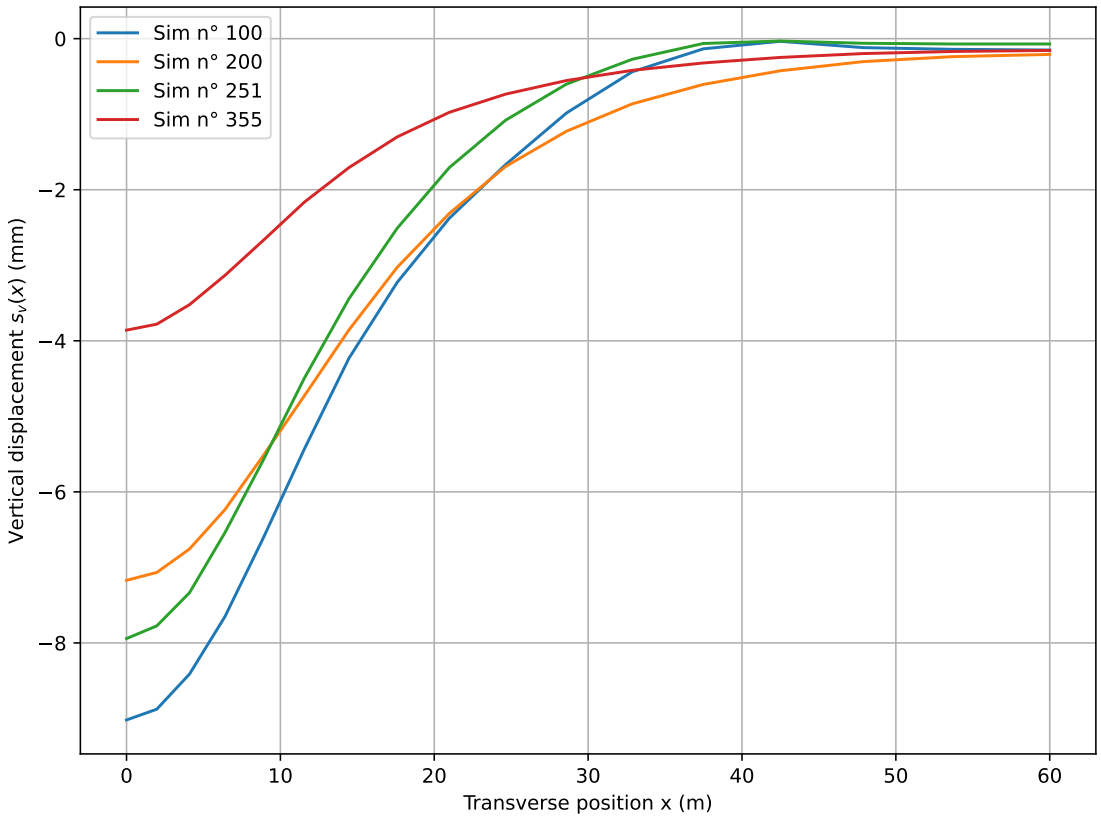

Figure K.2: Transverse settlement profiles s_v^t, defined by Eq. (K.1), obtained from different simulations.

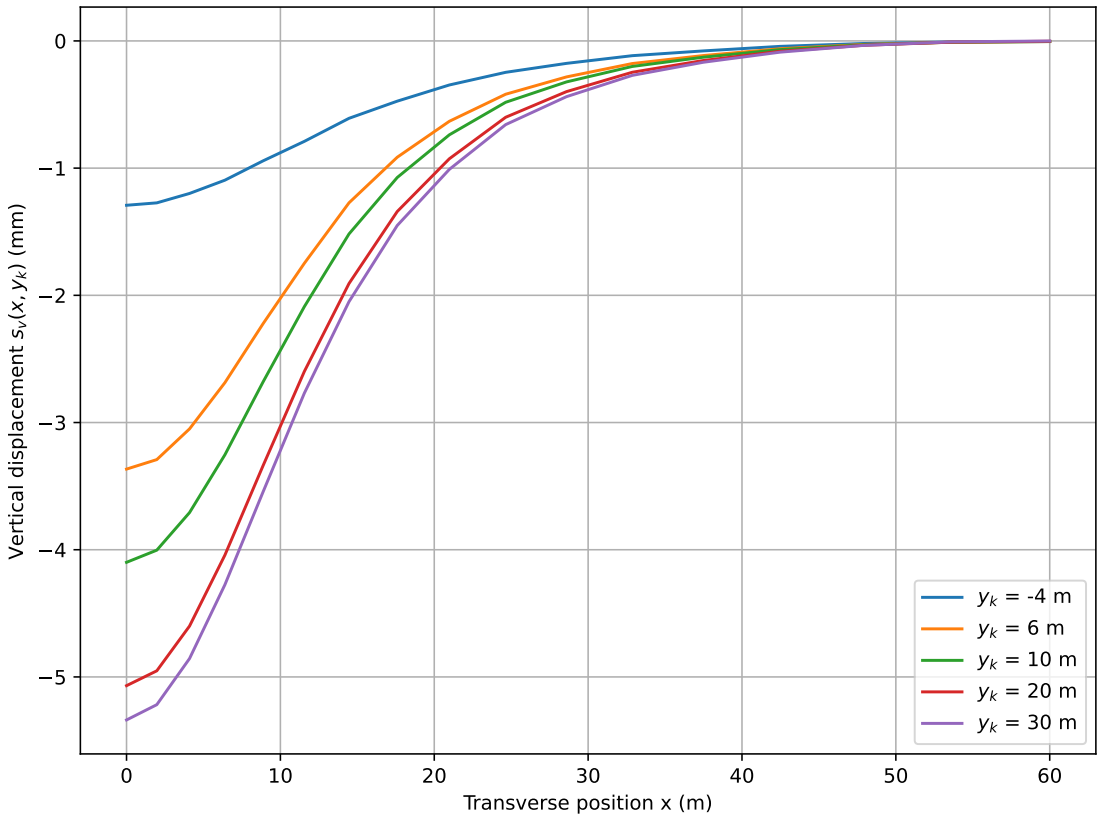

Figure K.3: Transverse settlement profiles s_v^t from a single simulation, evaluated at different TBM positions y_k.

Appendix L

Numerical fidelity framework

The numerical configuration parameters $\boldsymbol{\eta}$ are interpreted as defining different fidelity levels, following (Picheny and Ginsbourger, 2013; Stroh et al., 2022). We introduce an ideal high-fidelity simulator f_∞, corresponding to an infinitely refined mesh and an infinitely extended geotechnical domain, which is not accessible in practice.

For a given reduced configuration $\boldsymbol{\eta}$, the simulator output can be written as:

$$f(\mathbf{x}_p, \boldsymbol{\eta}) = f_\infty(\mathbf{x}_p) + \varepsilon(\mathbf{x}_p, \boldsymbol{\eta}), \tag{L.1}$$

where $\varepsilon(\mathbf{x}_p, \boldsymbol{\eta})$ denotes the numerical error induced by the numerical modeling choices. We assume that $\varepsilon(\mathbf{x}_p, \boldsymbol{\eta}) \to 0$ as the mesh is refined and the domain size increases.

In the following, we fix the geotechnical input configuration $\mathbf{x}_p$ and define:

$$\mathbf{z}(\boldsymbol{\eta}) = f(\mathbf{x}_p, \boldsymbol{\eta}), \qquad \mathbf{z}_\infty = f_\infty(\mathbf{x}_p), \tag{L.2}$$

where $\mathbf{z} \in \mathbb{R}^q$ denotes the vector of quantities of interest (QoIs). The error model is applied component-wise to each QoI.

We then introduce a parametric approximation of the numerical error:

$$\mathbf{z}(\boldsymbol{\eta}) = \mathbf{z}_\infty + \widehat{\boldsymbol{\varepsilon}}(\boldsymbol{\eta}) + \mathbf{r}(\boldsymbol{\eta}), \tag{L.3}$$

where $\widehat{\boldsymbol{\varepsilon}}(\boldsymbol{\eta})$ is a fitted model of the numerical error and $\mathbf{r}(\boldsymbol{\eta})$ is a residual term accounting for model mismatch.

Within the Accuracy-Cost Model Reduction framework, $\widehat{\boldsymbol{\varepsilon}}(\boldsymbol{\eta})$ is defined using the parametric forms introduced in Section 4.1, combining exponential decay for boundary effects and power-law behavior for discretization errors. The parameters of this model, together with $\mathbf{z}_\infty$, are estimated from numerical experiments conducted over a range of configurations $\boldsymbol{\eta}$. The resulting estimate of $\mathbf{z}_\infty$ defines a virtual high-fidelity reference, which enables the quantification of numerical errors associated with any admissible configuration.

However, the present formulation is local respect to the geotechnical configuration $\mathbf{x}_p$, and its validity for other geotechnical configurations is not guaranteed.

Appendix M

Full Sobol Indices Distribution per QoI

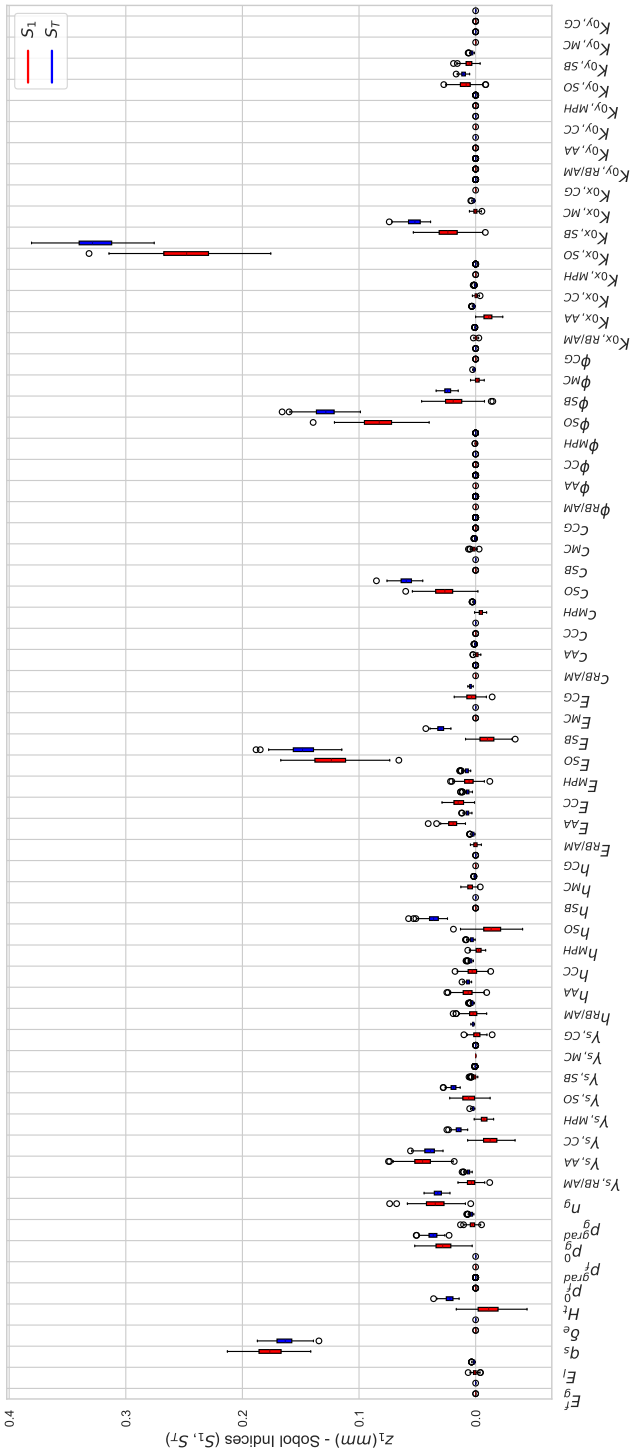

Figure M.1: Influence of the 66 input parameters on the maximum settlement value $z_1 = s_{\max}$. See Figure 4.11 for interpretation.

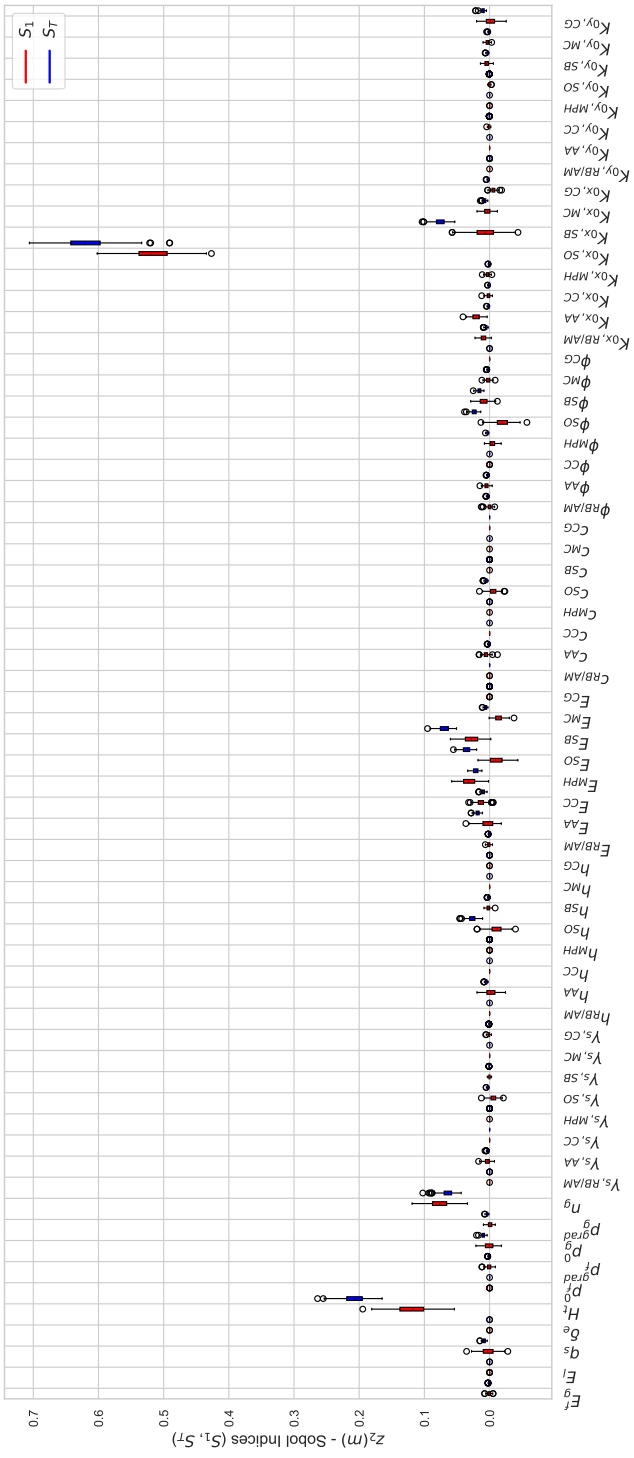

Figure M.2: Influence of the 66 input parameters on the transverse settlement width $z_2 = r_0$. See Figure 4.12 for interpretation.

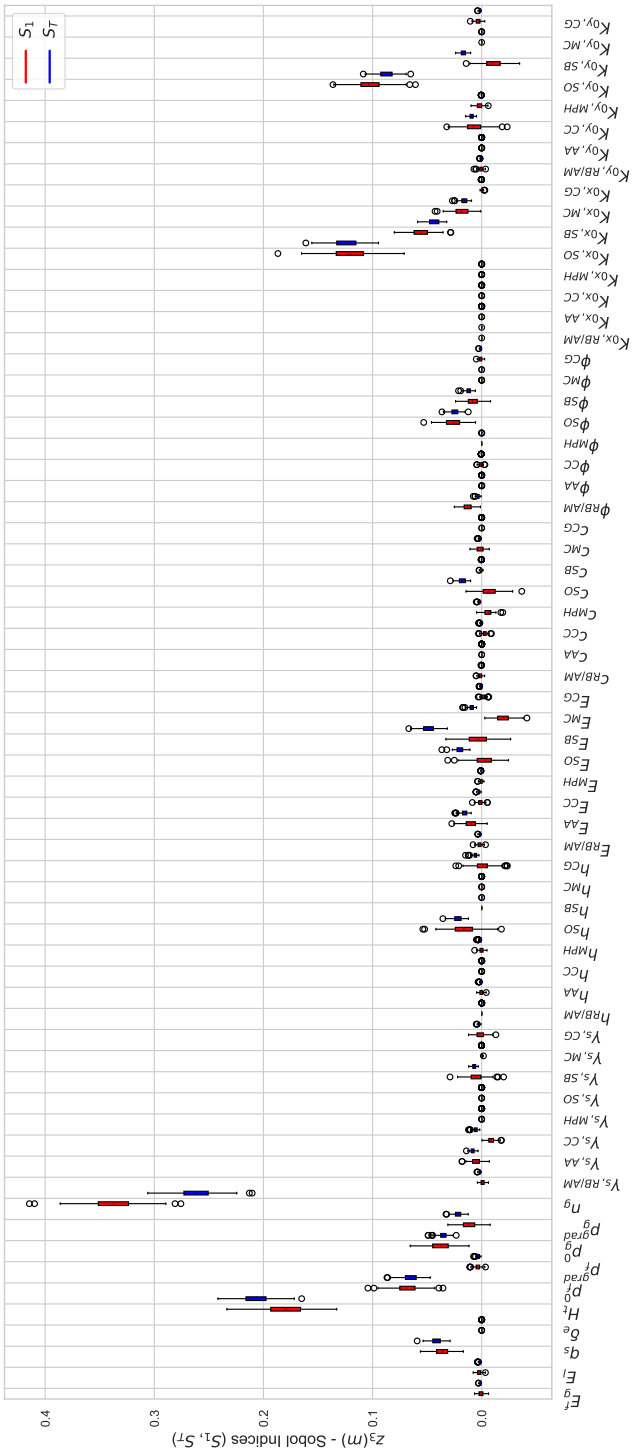

Figure M.3: Influence of the 66 input parameters on the longitudinal settlement steepness $z_3 = i_y$. See Figure 4.13 for interpretation.

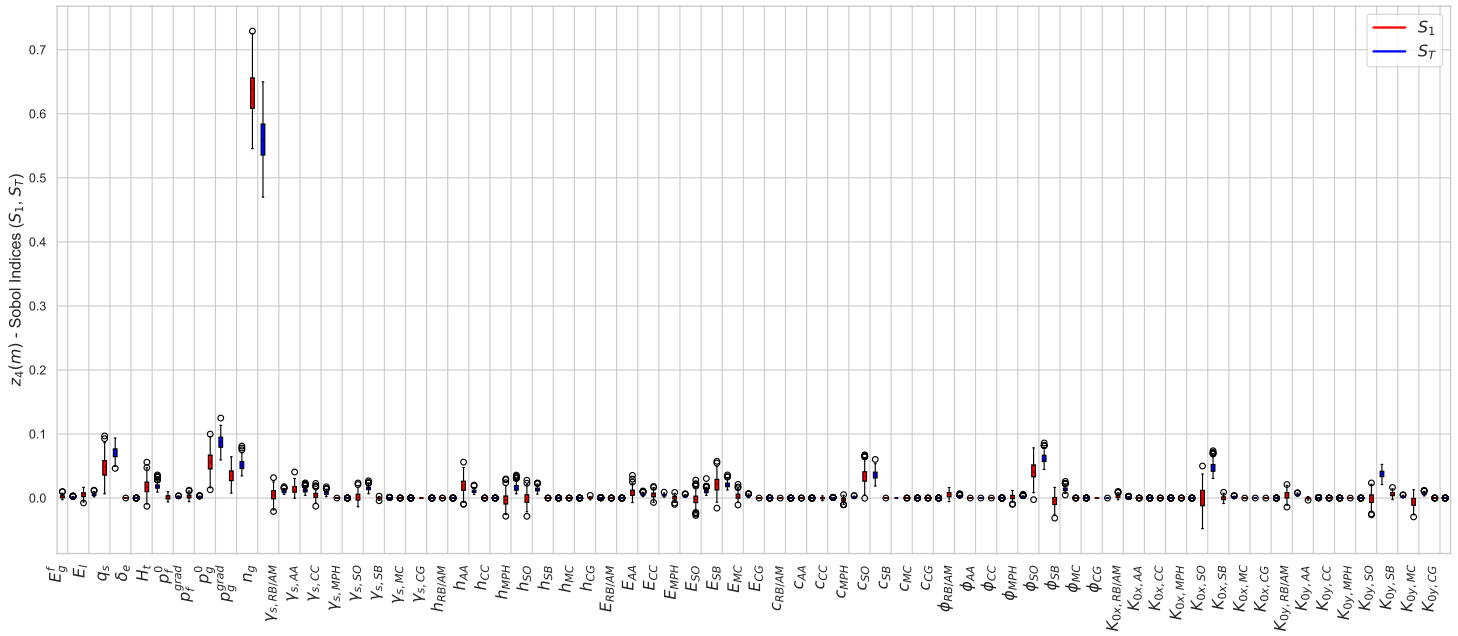

Figure M.4: Influence of the 66 input parameters on the longitudinal settlement inflection point $z_4 = y_0$. See Figure 4.14 for interpretation.

Appendix N

Robust regression framework

This appendix introduces the theoretical framework for the robust regression methods used in the estimation of longitudinal settlement model parameters. The following notations are used throughout this appendix and are consistent with those introduced in the main manuscript.

Notations

$x_i \in \mathbb{R}$, $y_i \in \mathbb{R}$: input and output observations
$\boldsymbol{\theta} \in \mathbb{R}^d$: parameter vector to be estimated
$f : \mathbb{R} \times \mathbb{R}^d \to \mathbb{R}$: parametric model
$e_i(\boldsymbol{\theta}) = y_i - f(x_i, \boldsymbol{\theta})$: residual
$\rho : \mathbb{R} \to \mathbb{R}_+$: loss function
$\psi(u)$: influence function (equal to $\rho'(u)$ when ρ is differentiable)
$w(u) = \psi(u)/u$ (defined for $u \neq 0$, extended by continuity at $u = 0$) : weight function
ε_i : measurement error (noise). Model error not explicitly considered here.

N.1 Ordinary least squares (OLS)

Consider the observation model

$$y_i = f(x_i, \boldsymbol{\theta}) + \varepsilon_i,$$

where the errors ε_i are assumed to be independent and identically distributed (i.i.d.) according to a Gaussian distribution $\mathcal{N}(0, \sigma^2)$.

Under these assumptions, the conditional probability density p of y_i given x_i is

$$p(y_i \mid x_i, \boldsymbol{\theta}) = \frac{1}{\sqrt{2\pi\sigma^2}} \exp\left(-\frac{(y_i - f(x_i, \boldsymbol{\theta}))^2}{2\sigma^2}\right).$$

Assuming independence of the errors, the log-likelihood of the dataset $\{(x_i, y_i)\}_{i=1}^n$ is given by

$$\log \mathcal{L}(\boldsymbol{\theta}) = -\frac{n}{2} \log(2\pi\sigma^2) - \frac{1}{2\sigma^2} \sum_{i=1}^{n} (y_i - f(x_i, \boldsymbol{\theta}))^2 .$$

Maximizing the log-likelihood with respect to $\boldsymbol{\theta}$ is equivalent to minimizing the sum of squared residuals. The maximum likelihood estimator (MLE) is therefore given by

$$\hat{\boldsymbol{\theta}}_{\text{MLE}} = \arg\min_{\boldsymbol{\theta}} \sum_{i=1}^{n} (y_i - f(x_i, \boldsymbol{\theta}))^2 ,$$

which coincides with the ordinary least squares (OLS) estimator.

While optimal under the Gaussian noise assumption, OLS is highly sensitive to outliers, as the quadratic loss assigns disproportionate weight to large residuals.

N.2 M-estimators

To mitigate the sensitivity of least-squares estimation to outliers, M-estimators (Huber, 1973; Fox and Weisberg, 2002; Filzmoser and Nordhausen, 2021) generalize the estimation procedure by replacing the quadratic loss with a function $\rho(\cdot)$ satisfying the following properties: (i) $\rho(u)$ is symmetric and non-negative, (ii) $\rho(u)$ is a non-decreasing function of $|u|$.

The M-estimator is defined as

$$\hat{\boldsymbol{\theta}} = \arg\min_{\boldsymbol{\theta}} \sum_{i=1}^{n} \rho(e_i(\boldsymbol{\theta})),$$

where $e_i(\boldsymbol{\theta}) = y_i - f(x_i, \boldsymbol{\theta})$.

The M-estimator is defined as a minimizer of the objective function

$$L(\boldsymbol{\theta}) = \sum_{i=1}^{n} \rho(e_i(\boldsymbol{\theta})),$$

and, for differentiable loss functions ρ, its gradient is given by

$$\nabla_{\boldsymbol{\theta}} L(\boldsymbol{\theta}) = -\sum_{i=1}^{n} \psi(e_i(\boldsymbol{\theta}))\, \nabla_{\boldsymbol{\theta}} f(x_i, \boldsymbol{\theta}) = -\sum_{i=1}^{n} w(e_i(\boldsymbol{\theta}))\, e_i(\boldsymbol{\theta})\, \nabla_{\boldsymbol{\theta}} f(x_i, \boldsymbol{\theta}),$$

where $\psi(u) = \rho'(u)$ when ρ is differentiable, and $w(u) = \psi(u)/u$ for $u \neq 0$, extended by continuity at $u = 0$.

Any interior minimizer $\hat{\boldsymbol{\theta}}$ therefore satisfies the first-order stationarity condition

$$\nabla_{\boldsymbol{\theta}} L(\boldsymbol{\theta})\big|_{\boldsymbol{\theta}=\hat{\boldsymbol{\theta}}} = 0,$$

which is typically solved approximately using iterative numerical optimization methods.

To achieve robustness against outliers, the loss function ρ should induce a bounded (or redescending) influence function $\psi(u)$ for large $|u|$, ensuring that extreme residuals have limited impact on the parameter estimates. Accordingly, the associated weight function $w(u)$ decreases as $|u|$ increases.

Common loss functions used for M-estimation, together with their corresponding influence and weight functions, are reported in Table N.1.

Remark. Other estimators, such as S- and MM-estimators or the Least Trimmed Squares (LTS) estimator, have also been proposed, although they are not used in this work. See Fox and Weisberg (2002); Filzmoser and Nordhausen (2021) for further details.

Table N.1: Comparison of common loss functions for M-estimation.

Loss Type	**Loss function** $\rho(u)$	**Influence** $\psi(u)$	**Weight** $w(u)$
L2 (OLS)	$\frac{1}{2}u^2$	u	1
Huber	$\begin{cases} \frac{1}{2}u^2 & \lvert u\rvert \le \delta \\ \delta(\lvert u\rvert - \frac{\delta}{2}) & \lvert u\rvert > \delta \end{cases}$	$\begin{cases} u & \lvert u\rvert \le \delta \\ \delta\text{sign}(u) & \lvert u\rvert > \delta \end{cases}$	$\begin{cases} 1 & \lvert u\rvert \le \delta \\ \delta/\lvert u\rvert & \lvert u\rvert > \delta \end{cases}$
Soft L1	$2\delta^2\left(\sqrt{1+(u/\delta)^2}-1\right)$	$\frac{2u}{\sqrt{1+(u/\delta)^2}}$	$\frac{2}{\sqrt{1+(u/\delta)^2}}$

Appendix O

RANSAC algorithm

This section presents the Random Sample Consensus (RANSAC) algorithm used to estimate model parameters from a dataset containing outliers. The method iteratively identifies subsets of observations (inliers) that are consistent with the assumed model, while discarding corrupted data.

Algorithm 5 RANSAC for Robust Regression

Require: Dataset $\mathcal{D} = \{(x_i, y_i)\}_{i=1}^{n}$, model $f(x, \boldsymbol{\theta})$, sampling proportion p, number of iterations n_{iter}, threshold δ
Ensure: Estimated parameters $\hat{\boldsymbol{\theta}}$

Initialize $\mathcal{I}_{\text{best}} \leftarrow \emptyset$
for $k = 1, \ldots, n_{\text{iter}}$ **do**
    Sample a subset $\mathcal{D}_s \subset \mathcal{D}$ with proportion p
    Fit $\boldsymbol{\theta}_{\text{cand}}$ using $\mathcal{D}_s$
    $\mathcal{I}_{\text{curr}} \leftarrow \{i : |y_i - f(x_i, \boldsymbol{\theta}_{\text{cand}})| < \delta\}$
    if $|\mathcal{I}_{\text{curr}}| > |\mathcal{I}_{\text{best}}|$ **then**
        $\mathcal{I}_{\text{best}} \leftarrow \mathcal{I}_{\text{curr}}$
    end if
end for
Refit $\hat{\boldsymbol{\theta}}$ using $\mathcal{I}_{\text{best}}$
return $\hat{\boldsymbol{\theta}}$

Appendix P

BSS for set inversion: additional details

P.1 Definitions and notation

General notation

Let $f : \mathcal{X} \to \mathbb{R}^q$, with $q \geq 1$, denote a deterministic simulator.

For $q = 1$, let $\mathcal{B} = [a, b] \subset \mathbb{R}$ and define the associated inversion set as

$$\mathbf{\Gamma} = \{\mathbf{x} \in \mathcal{X} \mid f(\mathbf{x}) \in \mathcal{B}\}.$$

For $q > 1$, the definition extends directly by considering a target box $\mathcal{B} \subset \mathbb{R}^q$. The only modification concerns the definition of the posterior coverage function; details are provided in Appendix P.2. For clarity, the exposition in this appendix focuses on the scalar-output case $q = 1$, except in Appendix P.2.

At stage t, the current design of experiments is denoted by

$$\mathcal{D}_n = \{(\mathbf{x}_i, f(\mathbf{x}_i))\}_{i=1}^n.$$

Each input $\mathbf{x}_i$ is referred to as a **design point**.

The Gaussian process (GP) posterior conditioned on $\mathcal{D}_n$ is denoted by $\xi_n = \xi(\cdot \mid \mathcal{D}_n)$, with posterior mean $m_n(\cdot)$ and standard deviation $\sigma_n(\cdot)$. The GP prior is written as

$$\xi \sim \mathcal{GP}\big(m(\cdot), k(\cdot, \cdot)\big).$$

To construct the inversion set progressively, we introduce a sequence of nested output intervals

$$\mathcal{B}_t = [a_{\lambda_t}, b_{\lambda_t}] \subset \mathbb{R}, \qquad \mathcal{B}_t \subseteq \mathcal{B}_{t-1},$$

and the corresponding inversion sets

$$\mathbf{\Gamma}_t = \{\mathbf{x} \in \mathcal{X} \mid f(\mathbf{x}) \in \mathcal{B}_t\}.$$

Levels of approximation

Three levels of approximation are considered:

(i) **True quantities**, defined with respect to the simulator f, such as $\mathbf{\Gamma}_t$ and the probability mass

$$\alpha_t = \mathbb{P}_{\mathcal{X}}(\mathbf{\Gamma}_t).$$

(ii) **GP-based quantities**, conditional on the design $\mathcal{D}_n$, such as the coverage function $g_{t,n}$ and the expected volume

$$\alpha_{t,n} = \mathbb{E}_n[\alpha_t].$$

(iii) **Sequential Monte Carlo (SMC) estimators**, computed from a particle system, such as $\hat{\alpha}_t$ and the transition coefficient $\hat{\rho}_t$.

These three levels correspond respectively to the target quantity, its metamodel-based approximation, and its numerical approximation.

Coverage function

Deterministic case

When the simulator f is deterministic, membership in the inversion set is binary and is described by the indicator function

$$\mathbf{1}_{\mathbf{\Gamma}_t}(\mathbf{x}) = \begin{cases} 1, & \text{if } f(\mathbf{x}) \in \mathcal{B}_t, \\ 0, & \text{otherwise.} \end{cases}$$

GP metamodel

When f is emulated by a GP conditioned on the design $\mathcal{D}_n$, membership becomes probabilistic. The inversion problem is then characterized through the posterior coverage function

$$g_{t,n}(\mathbf{x}) = \mathbb{P}\big(\xi(\mathbf{x}) \in \mathcal{B}_t \mid \mathcal{D}_n\big),$$

where the probability is taken with respect to the posterior distribution of the GP.

Under the GP posterior, $\xi(\mathbf{x}) \mid \mathcal{D}_n \sim \mathcal{N}\big(m_n(\mathbf{x}), \sigma_n^2(\mathbf{x})\big)$, the coverage admits the closed-form expression

$$g_{t,n}(\mathbf{x}) = \begin{cases} \Phi\left(\dfrac{b_{\lambda_t} - m_n(\mathbf{x})}{\sigma_n(\mathbf{x})}\right) - \Phi\left(\dfrac{a_{\lambda_t} - m_n(\mathbf{x})}{\sigma_n(\mathbf{x})}\right), & \text{if } \sigma_n(\mathbf{x}) > 0, \\ \mathbf{1}_{\xi(\mathbf{x}) \in \mathcal{B}_t} \quad \text{a.s.} & \text{if } \sigma_n(\mathbf{x}) = 0, \end{cases} \tag{P.1}$$

where Φ denotes the standard normal cumulative distribution function, and the equality holds almost surely (a.s.) under a noiseless GP assumption.

The function $g_{t,n}(\mathbf{x})$ acts as a probabilistic surrogate of $\mathbf{1}_{\mathbf{\Gamma}_t}(\mathbf{x})$, capturing the posterior uncertainty induced by the GP model.

Bayesian set estimator.

A pointwise Bayesian estimator of the inversion set is defined as

$$\hat{\mathbf{\Gamma}}_{t,n} = \{\mathbf{x} \in \mathcal{X} \mid g_{t,n}(\mathbf{x}) > 1/2\}.$$

This threshold corresponds to the Bayes classifier under a symmetric 0–1 loss.

Particle approximation

We consider a population of N_p **particles**

$$\mathbf{Y}_t = \{Y_t^{(i)}\}_{i=1}^{N_p},$$

defined on $\mathcal{X}$ and initially sampled from the input distribution $P_{\mathcal{X}}$ with density $\pi_{\mathcal{X}}$.

At stage t, the particle set is constructed so as to approximate samples distributed according to the target density

$$q_{t,n}(\mathbf{x}) \propto g_{t,n}(\mathbf{x})\pi_{\mathcal{X}}(\mathbf{x}).$$

Accordingly, the particle population $\mathbf{Y}_t$ provides a particle approximation of the distribution $q_{t,n}$.

GP specification

In all examples of this appendix, the GP prior uses a constant mean function and a Matérn covariance kernel with smoothness parameter $\nu = 5/2$.

P.2 Multi-output framework

Multi-output coverage

For $f : \mathcal{X} \to \mathbb{R}^q$, the target set is defined as

$$\mathcal{B}_t = \prod_{j=1}^{q} [a_{\lambda_t}^{(j)}, b_{\lambda_t}^{(j)}].$$

We assume independent GP posteriors for each component,

$$\xi^{(j)}(\mathbf{x}) \mid \mathcal{D}_n \sim \mathcal{N}\big(m_n^{(j)}(\mathbf{x}), (\sigma_n^{(j)}(\mathbf{x}))^2\big).$$

The posterior coverage per component is

$$g_{t,n}^{(j)}(\mathbf{x}) = \mathbb{P}(a_{\lambda_t}^{(j)} \le \xi^{(j)}(\mathbf{x}) \le b_{\lambda_t}^{(j)} \mid \mathcal{D}_n),$$

and, under the independence assumption,

$$g_{t,n}(\mathbf{x}) = \prod_{j=1}^{q} g_{t,n}^{(j)}(\mathbf{x}).$$

Remark. This formulation assumes posterior independence between the GP components, which is a modeling approximation. In practice, this corresponds to using independent GP models for each output component.

Multi-output sampling criterion

In the single-output case, the sampling criterion reads

$$G_{t,n}(\mathbf{x}) = \left(\tau_{t,n}(\mathbf{x})\right)^{\zeta_1}\left(\sigma_n^2(\mathbf{x})\right)^{\zeta_2}, \qquad \tau_{t,n}(\mathbf{x}) = \min\left(g_{t,n}(\mathbf{x}), 1 - g_{t,n}(\mathbf{x})\right).$$

For $q > 1$, we define the component-wise criterion

$$\phi_{t,n}^{(j)}(\mathbf{x}) = \left(\tau_{t,n}^{(j)}(\mathbf{x})\right)^{\zeta_1}\left(\sigma_n^{(j)}(\mathbf{x})\right)^{2\zeta_2}, \qquad \tau_{t,n}^{(j)}(\mathbf{x}) = \min\left(g_{t,n}^{(j)}(\mathbf{x}), 1 - g_{t,n}^{(j)}(\mathbf{x})\right),$$

and aggregate it using normalized weights $\bar{\omega}_j$ (default $\bar{\omega}_j = 1/q$):

$$G_{t,n}^{\mathrm{MO}}(\mathbf{x}) = \sum_{j=1}^{q} \bar{\omega}_j \phi_{t,n}^{(j)}(\mathbf{x}).$$

P.3 Theoretical proof

Estimation of $\delta_t^{\mathcal{GP}}$

Let α_t denote the true probability at stage t, and $\alpha_{t,n}$ its GP-based approximation. Using the definitions introduced above, we write

$$\alpha_t - \alpha_{t,n} = \int_{\mathcal{X}} \left(\mathbf{1}_{\mathbf{\Gamma}_t}(\mathbf{x}) - g_{t,n}(\mathbf{x})\right)\pi_{\mathcal{X}}(\mathbf{x})d\mathbf{x}.$$

Using Minkowski's integral inequality, we obtain the bound

$$\mathbb{E}_n\left[\left(\alpha_t - \alpha_{t,n}\right)^2\right] \leq \left(\int_{\mathcal{X}} \sqrt{\nu_{t,n}(\mathbf{x})}\pi_{\mathcal{X}}(\mathbf{x})d\mathbf{x}\right)^2, \tag{P.2}$$

where

$$\nu_{t,n}(\mathbf{x}) = g_{t,n}(\mathbf{x})\left(1 - g_{t,n}(\mathbf{x})\right)$$

denotes the posterior variance of the indicator function.

Recursive formulation

Let

$$q_{t-1,n}(\mathbf{x}) = \frac{g_{t-1,n}(\mathbf{x})\pi_{\mathcal{X}}(\mathbf{x})}{\alpha_{t-1,n}}$$

denote the intermediate density. Assuming $g_{t-1,n}(\mathbf{x}) > 0$ almost everywhere under $q_{t-1,n}$, we rewrite Eq. (P.2) as

$$\mathbb{E}_n\left[\left(\alpha_t - \alpha_{t,n}\right)^2\right] \leq \alpha_{t-1,n}^2 \left(\mathbb{E}_{q_{t-1,n}}\left[\frac{\sqrt{\nu_{t,n}(\mathbf{x})}}{g_{t-1,n}(\mathbf{x})}\right]\right)^2.$$

Dividing by $\alpha_{t,n}^2$ yields

$$\frac{\sqrt{\mathbb{E}_n\left[\left(\alpha_t - \alpha_{t,n}\right)^2\right]}}{\alpha_{t,n}} \leq \frac{\alpha_{t-1,n}}{\alpha_{t,n}}\mathbb{E}_{q_{t-1,n}}\left[\frac{\sqrt{\nu_{t,n}(\mathbf{x})}}{g_{t-1,n}(\mathbf{x})}\right].$$

Using the recursive identity

$$\alpha_{t,n} = \alpha_{t-1,n}\mathbb{E}_{q_{t-1,n}}\left[\frac{g_{t,n}(X)}{g_{t-1,n}(X)}\right],$$

we define

$$p_{t,n} = \mathbb{E}_{q_{t-1,n}}\left[\frac{g_{t,n}(X)}{g_{t-1,n}(X)}\right].$$

Replacing $p_{t,n}$ by its SMC estimate $\hat{p}_t$ leads to

$$\frac{\alpha_{t-1,n}}{\alpha_{t,n}} \approx \frac{1}{\hat{p}_t},$$

and yields the approximation

$$\delta_t^{\mathcal{GP}} = \frac{1}{\hat{p}_t}\mathbb{E}_{q_{t-1,n}}\left[\frac{\sqrt{g_{t,n}(\mathbf{x})(1-g_{t,n}(\mathbf{x}))}}{g_{t-1,n}(\mathbf{x})}\right].$$

This quantity provides an approximation of the theoretical upper bound on the relative posterior root mean squared error of $\alpha_{t,n}$.

SMC approximation

Using particles $\mathbf{Y}_{t-1} = \{Y_{t-1}^{(i)}\}_{i=1}^{N_p}$ distributed according to $q_{t-1,n}$, we obtain

$$\delta_t^{\mathcal{GP}} \approx \frac{1}{\hat{p}_t}\frac{1}{N_p}\sum_{i=1}^{N_p}\sqrt{\frac{g_{t,n}(Y_{t-1}^{(i)})(1-g_{t,n}(Y_{t-1}^{(i)}))}{g_{t-1,n}^2(Y_{t-1}^{(i)})}}.$$

Concentration inequality

Assuming $\alpha_{t,n} > 0$, Bienaymé–Chebyshev's inequality yields

$$\mathbb{P}\left(|\alpha_t - \alpha_{t,n}| \leq k\delta_t^{\mathcal{GP}}\alpha_{t,n} \;\middle|\; \mathcal{D}_n\right) \geq 1 - \frac{1}{k^2}.$$

Choosing $k = \sqrt{20}$ yields a conservative probability bound of 0.95 for the conditional inequality above. In practice, both $\alpha_{t,n}$ and $\delta_t^{\mathcal{GP}}$ are estimated using SMC particles, so this inequality should be interpreted as a conservative diagnostic bound rather than an exact finite-sample guarantee.

This result provides a conditional bound on the relative deviation of α_t around $\alpha_{t,n}$, where $\delta_t^{\mathcal{GP}}$ quantifies the uncertainty induced by the GP approximation.

Remark. A similar bound can be derived for the error induced by the SMC approximation.

P.4 Relaxation and stopping strategies

Selection of the relaxation levels

In BSS for set inversion, the relaxation levels $\lambda_0, \ldots, \lambda_T$ control the progressive refinement of the target sets $\mathbf{\Gamma}_t$.

In the original BSS algorithm (Bect et al., 2017), the relaxation level λ_t at stage $t \geq 1$ is selected using an adaptive rule. The objective is to choose λ_t such that a prescribed transition coefficient $p_0 \in (0, 1)$ is maintained between successive target densities.

This is achieved by solving

$$\frac{1}{N_p} \sum_{i=1}^{N_p} \frac{g_{t,n}(Y_{t-1}^{(i)}; \lambda_t)}{g_{t-1,n}(Y_{t-1}^{(i)})} = p_0,$$

where $g_{t,n}(\cdot; \lambda_t)$ denotes the posterior coverage function evaluated at the candidate relaxation level λ_t.

In the ideal indicator-based setting, this rule corresponds to selecting a $(1-p_0)$-quantile of the empirical distribution of weights. In practice, Bect et al. (2017) recommend $p_0 \in [0.1, 0.3]$.

In the context of set inversion, the same principle applies. The relaxation sequence may be stopped when no candidate λ_t yields a transition coefficient $\hat{p}_t$ within a prescribed range, which indicates that the GP model does not provide sufficient resolution of the coverage function at the corresponding level.

Stopping criteria for model refinement

Stopping criteria are required to assess whether the current GP model provides a sufficiently accurate characterization of the inversion set.

Following Moustapha et al. (2022), stopping criteria can be classified into three classes: (i) criteria based on the sampling criterion, (ii) criteria based on uncertainty or error estimates, and (iii) criteria based on the stabilization of estimated quantities.

Stability of the conditional probabilities

In BSS for set inversion, the expected volume $\alpha_{t,n}$ is expressed as a product of conditional expectations across relaxation levels. The stability of these quantities is therefore required for reliable estimation.

At stage t, the conditional probability is approximated using SMC particles $\{Y_{t-1}^{(i)}\}_{i=1}^{N_p}$, distributed according to $q_{t-1,n}$, as

$$\hat{p}_t = \frac{1}{N_p} \sum_{i=1}^{N_p} \frac{g_{t,n}(Y_{t-1}^{(i)})}{g_{t-1,n}(Y_{t-1}^{(i)})}.$$

After each enrichment of the design, the estimate $\hat{p}_t$ is updated. A stopping criterion is then defined as

$$\left| \hat{p}_t^{\text{new}} - \hat{p}_t^{\text{old}} \right| \leq \varepsilon,$$

where $\varepsilon > 0$ is a prescribed tolerance.

This criterion monitors the stability of the SMC estimator of

$$p_{t,n} = \mathbb{E}_{q_{t-1,n}} \left[\frac{g_{t,n}(X)}{g_{t-1,n}(X)} \right],$$

and ensures that the particle approximation of the ratio $g_{t,n}/g_{t-1,n}$ is sufficiently stable before proceeding to the next relaxation level.

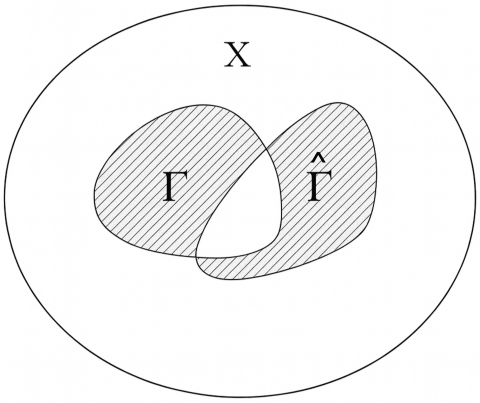

Figure P.1: Illustration of the symmetric difference $\mathbf{\Gamma}\Delta\hat{\mathbf{\Gamma}} = (\mathbf{\Gamma}\setminus\hat{\mathbf{\Gamma}})\cup(\hat{\mathbf{\Gamma}}\setminus\mathbf{\Gamma})$ between $\mathbf{\Gamma}$ and its estimator $\hat{\mathbf{\Gamma}}$, both subsets of $\mathcal{X}$. If $\mathbf{\Gamma} = \hat{\mathbf{\Gamma}}$, then $\mathbf{\Gamma}\Delta\hat{\mathbf{\Gamma}} = \emptyset$.

Misclassification-based criterion

The error induced by approximating the inversion set $\mathbf{\Gamma}_t$ by its estimator $\hat{\mathbf{\Gamma}}_{t,n}$ can be quantified through the probability of their symmetric difference,

$$\mathbb{P}_{\mathcal{X}}(\mathbf{\Gamma}_t\Delta\hat{\mathbf{\Gamma}}_{t,n}).$$

The local misclassification probability is

$$\tau_{t,n}(\mathbf{x}) = \min\big(g_{t,n}(\mathbf{x}), 1 - g_{t,n}(\mathbf{x})\big).$$

A global measure is obtained by averaging over the particle population $\{Y_{t-1}^{(i)}\}_{i=1}^{N_p}$, yielding

$$\tilde{\tau}_{t,n} = \frac{1}{N_p}\sum_{i=1}^{N_p}\tau_{t,n}(Y_{t-1}^{(i)}) \approx \mathbb{E}_{q_{t-1,n}}\big[\tau_{t,n}(X)\big]. \tag{P.3}$$

Using the recursive identity for $\alpha_{t,n}$, we obtain the approximation

$$\frac{\alpha_{t-1,n}}{\alpha_{t,n}} \approx \frac{1}{\hat{p}_t}.$$

This motivates the definition of the relative misclassification criterion

$$\beta_{t,n} = \frac{\tilde{\tau}_{t,n}}{\hat{p}_t}.$$

A stopping condition is then defined as

$$\beta_{t,n} \leq \eta,$$

where $\eta > 0$ controls the acceptable level of misclassification relative to the contraction of the target sets across relaxation levels.

This criterion provides a normalized measure of classification uncertainty, consistent with the SMC approximation under $q_{t-1,n}$.

P.5 Sampling criterion for GP metamodel

When a GP metamodel is used to approximate an expensive function, adaptive sampling strategies guide where to perform new evaluations. They are generally classified into two main families.

Maximal uncertainty reduction (MUR) This strategy selects the point that maximizes a measure of predictive uncertainty, denoted $G_{t,n}$:

$$x_{n+1} = \arg\max_{x \in \mathcal{X}} G_{t,n}(x).$$

Stepwise uncertainty reduction (SUR) This Bayesian decision-theoretic approach selects the point expected to minimize the posterior uncertainty after evaluation, denoted $J_{t,n}$:

$$x_{n+1} = \arg\min_{x \in \mathcal{X}} J_{t,n}(x).$$

SUR is well suited when the evaluation budget is limited (Bect et al., 2012), but is computationally demanding since each candidate requires assessing the impact of a hypothetical observation on the posterior uncertainty (Vazquez and Bect, 2009; Picheny et al., 2010; Bect et al., 2012, 2019; Azzimonti et al., 2021; Ait Abdelmalek-Lomenech et al., 2025).

These two families give rise to the functions $J_{t,n}$ and $G_{t,n}$, commonly referred to as sampling criteria. In the following, we focus on the misclassification-weighted mean squared error (MSE) criterion, a MUR-based strategy adapted to set inversion.

MSE criterion

A first strategy is to select the point with the highest posterior variance of the GP model,

$$G_{t,n}^{\mathrm{MSE}}(\mathbf{x}) = \sigma_n^2(\mathbf{x}).$$

Although this variance-based criterion improves the global accuracy of the metamodel, it does not explicitly target the boundary of the inversion set.

Misclassification criterion

To address this limitation, Bryan et al. (2005) introduced the probability of misclassification, which emphasizes regions where the classification is uncertain, that is, where $g_{t,n}(\mathbf{x})$ is close to $1/2$:

$$G_{t,n}^{\mathrm{MISS}}(\mathbf{x}) = \tau_{t,n}(\mathbf{x}) = \min\left(g_{t,n}(\mathbf{x}), 1 - g_{t,n}(\mathbf{x})\right).$$

Weighted MSE criterion

As a combination of variance-based and misclassification-based strategies, we consider the weighted MSE criterion

$$G_{t,n}^{\mathrm{WMSE}}(\mathbf{x}) = \left(\tau_{t,n}(\mathbf{x})\right)^{\beta_1} \left(\sigma_n^2(\mathbf{x})\right)^{\beta_2}, \tag{P.4}$$

where β_1 and β_2 control the relative importance of misclassification uncertainty and predictive variance.

In Figure P.2, we illustrate the sampling criterion $G_{t,n}^{\mathrm{WMSE}}(\mathbf{x})$ for different pairs of exponents (β_1, β_2). The exponent β_1 increases the focus on the decision boundary, while β_2 controls the influence of the GP predictive variance.

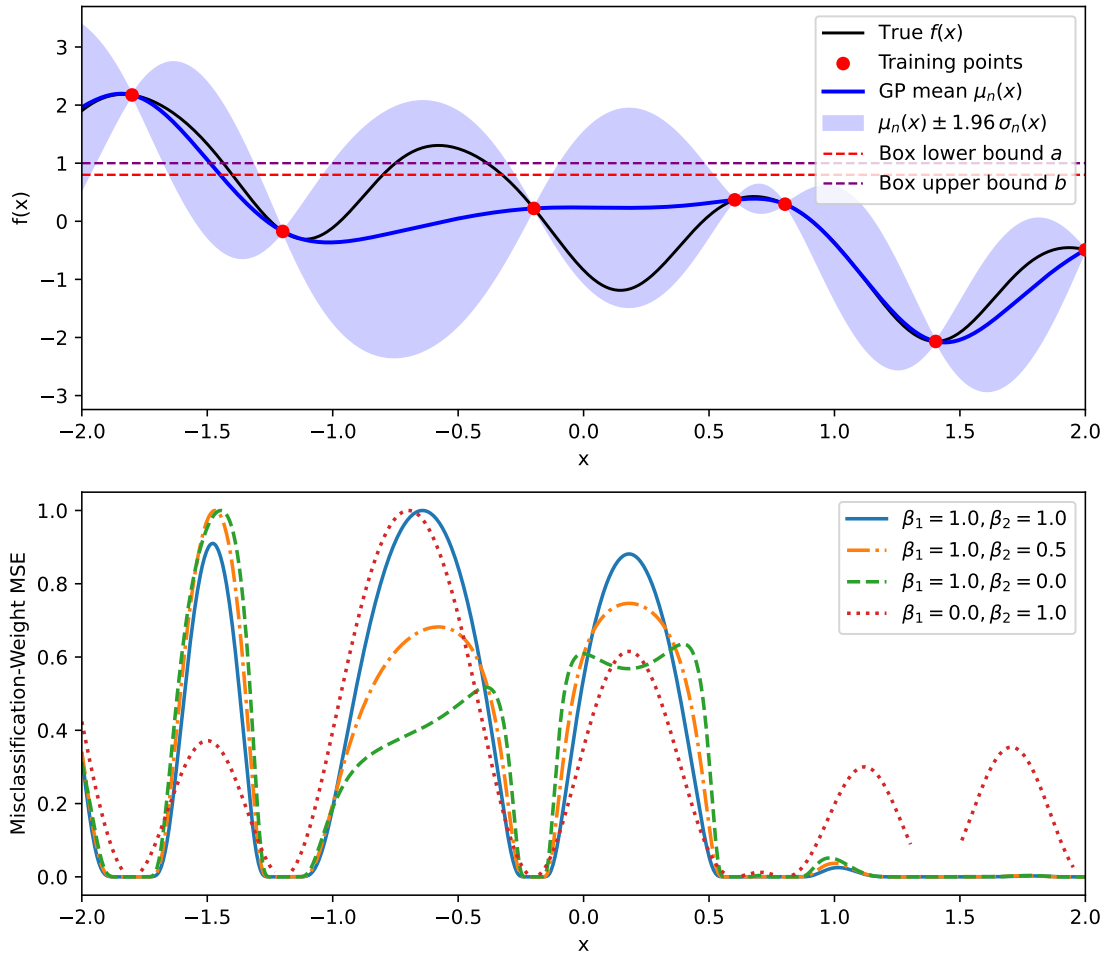

Figure P.2: Illustration of the sampling criterion $G_{t,n}^{\mathrm{WMSE}}(\mathbf{x})$ for different pairs of exponents (β_1, β_2). The top panel shows the GP metamodel with the target set to be inverted $B = [0.8, 1.0]$, and the bottom panel displays the corresponding values of $G_{t,n}^{\mathrm{WMSE}}(\mathbf{x})$. When $(\beta_1 = 0.0, \beta_2 = 1.0)$, the criterion highlights regions of high posterior variance. Conversely, $(\beta_1 = 1.0, \beta_2 = 0.0)$ concentrates on the decision boundary. Intermediate settings such as $(\beta_1 = 1.0, \beta_2 = 0.5)$ or $(\beta_1 = 1.0, \beta_2 = 1.0)$ provide a trade-off between exploration and boundary refinement. For visualization purposes, the bottom panel shows the normalized values of $G_{t,n}^{\mathrm{WMSE}}(\mathbf{x})$.

Batch weighted MSE criterion

To enable parallel evaluations, the weighted MSE criterion can be combined with a space-filling strategy. A common choice is the maximin criterion, which maximizes the minimum pairwise distance between selected points.

A batch of n_b points is constructed sequentially. The first point $\mathbf{x}_1^\star$ maximizes $G_{t,n}(\mathbf{x})$. Each subsequent point is defined as

$$\mathbf{x}_k^\star = \arg\max_{\mathbf{x}\in\mathcal{X}} \Big(G_{t,n}(\mathbf{x}) \cdot \min_{j<k} \|\mathbf{x} - \mathbf{x}_j^\star\| \Big), \qquad k = 2, \ldots, n_b.$$

Figure P.3 illustrates the points selected by this strategy.

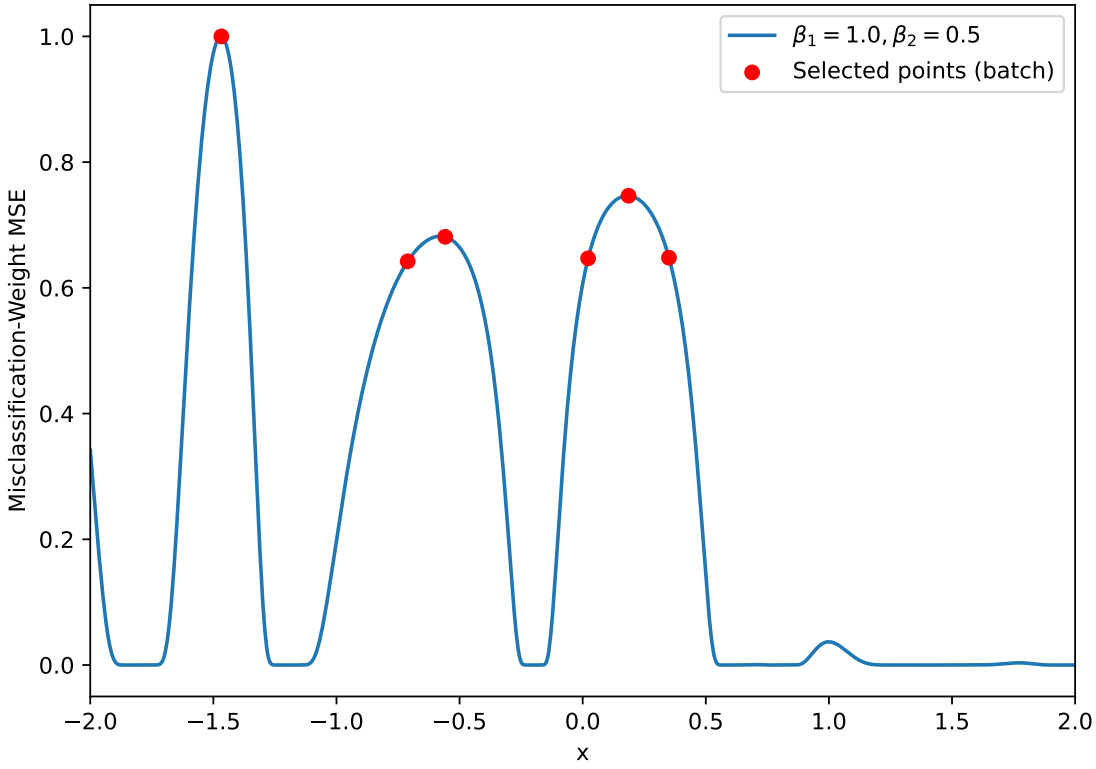

Figure P.3: Batch sampling using the $G_{t,n}^{\text{WMSE}}$ criterion with $(\beta_1 = 1.0, \beta_2 = 0.5)$ and a batch size of $n_b = 6$, in the same context as Figure P.2. The points correspond to the selected $\mathbf{x}_k^\star$. For visualization purposes, the panel displays normalized values of $G_{t,n}^{\text{WMSE}}(\mathbf{x})$.

Comparative analysis of MUR sampling criteria

To compare the impact of batch selection using the maximin strategy (see Section P.5) and of the choice of (β_1, β_2) in the sampling criteria defined by Eq. P.4, we monitor the evolution of the average misclassification score $\tau_{t,n}$ during the sequential refinement of the GP.

We consider the two-dimensional test problem shown in Figure P.4, where the objective is to invert the set $\mathcal{B} = [a, b] = [0.8, 1.0]$.

The analytical form of the test function is

$$f(\mathbf{x} = (x_1; x_2)) = \exp\left(1.8(x_1 + x_2)\right) + 3x_1 + 6x_2^2 + 3\sin(4\pi x_1). \tag{P.5}$$

A fixed uniform grid of 80×80 points over $[-1, 1]^2$ is used throughout the experiment. The initial GP design consists of 15 input points sampled over this domain. For each

sampling criterion, the mean misclassification score $\tau_{t,n}$ is evaluated on this grid as new evaluations of f are added.

Results are shown in Figures P.5 and P.6. The settings $(\beta_1, \beta_2) = (1.0, 0.5)$ and $(\beta_1, \beta_2) = (1.0, 1.0)$ lead to stable behavior on this multimodal problem.

In contrast, using $(\beta_1, \beta_2) = (1.0, 0.0)$, corresponding to $G_{t,n} = \tau_{t,n}$, produces noticeable jumps in the misclassification curve around 50 and 70 evaluations. These transitions likely correspond to the discovery of previously unexplored modes. Once these regions are identified, this configuration converges faster than $(\beta_1, \beta_2) = (1.0, 1.0)$.

Remark. The grid remains fixed and dense
in this example. In higher-dimensional settings, where particles concentrate in regions of high posterior probability, a criterion such as $G_{t,n} = \tau_{t,n}$ may lead to mode trapping.

Batch sampling improves performance during early iterations (up to about 50 evaluations), but becomes less effective afterwards, as the maximin strategy favours spatial coverage over local refinement.

Finally, the setting $(\beta_1, \beta_2) = (0.0, 1.0)$, corresponding to the MSE criterion, focuses exclusively on regions of high predictive variance. As a result, many evaluations are spent in regions that do not contribute to the inversion set, and convergence is not achieved within 90 evaluations.

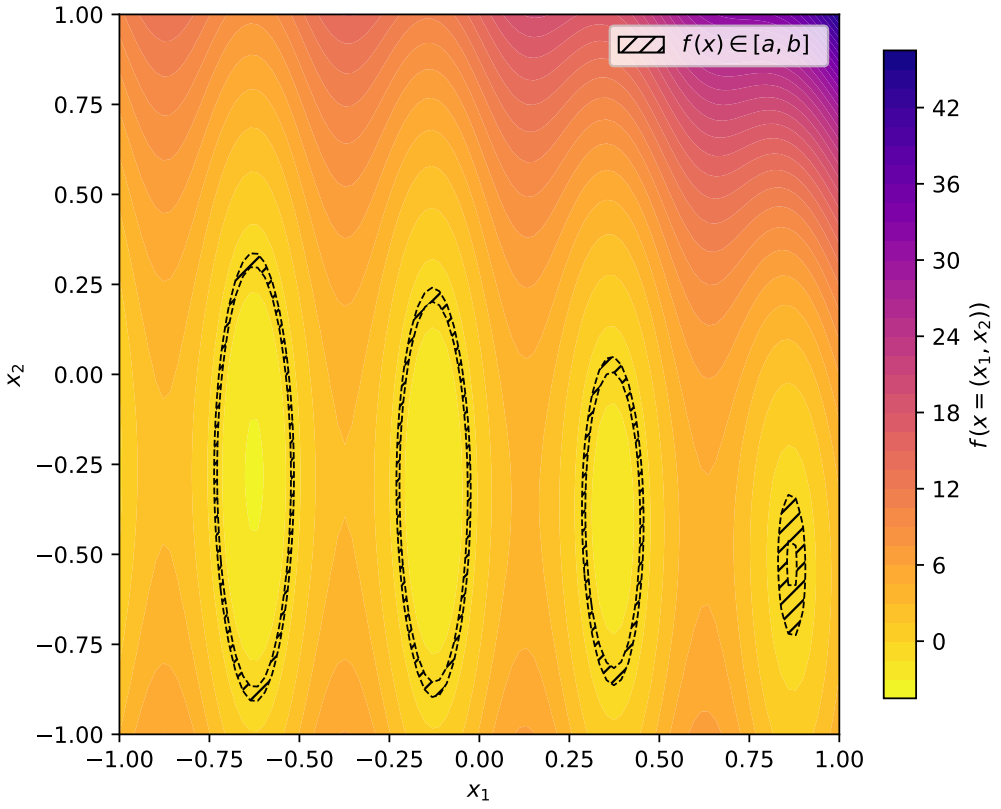

Figure P.4: Two-dimensional test function (color map) and target set $\mathcal{B} = [a, b] = [0.8, 1.0]$.

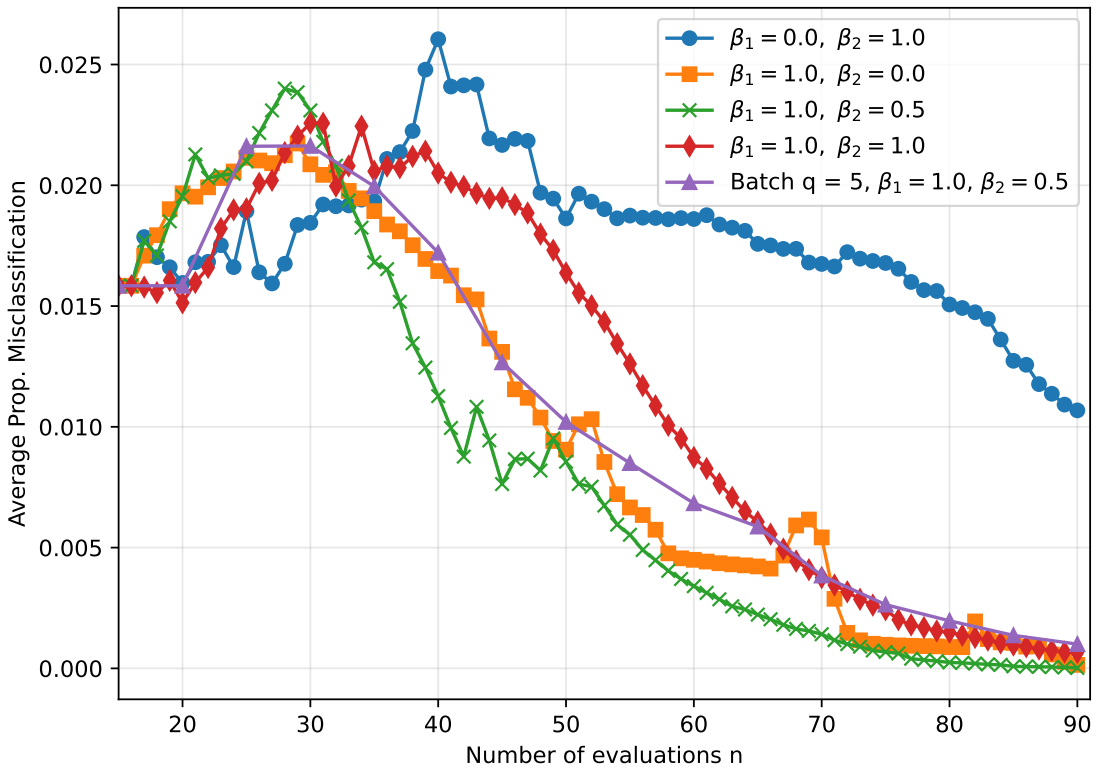

Figure P.5: Comparison of different $G_{t,n}^{\text{WMSE}}$ criteria on the test problem of Figure P.4. Starting from an initial design of 15 points, the GP is sequentially enriched, and the mean misclassification score $\tau_{t,n}(\mathbf{x})$ is monitored as a function of the number of evaluations for different (β_1, β_2) settings and with batch sampling.

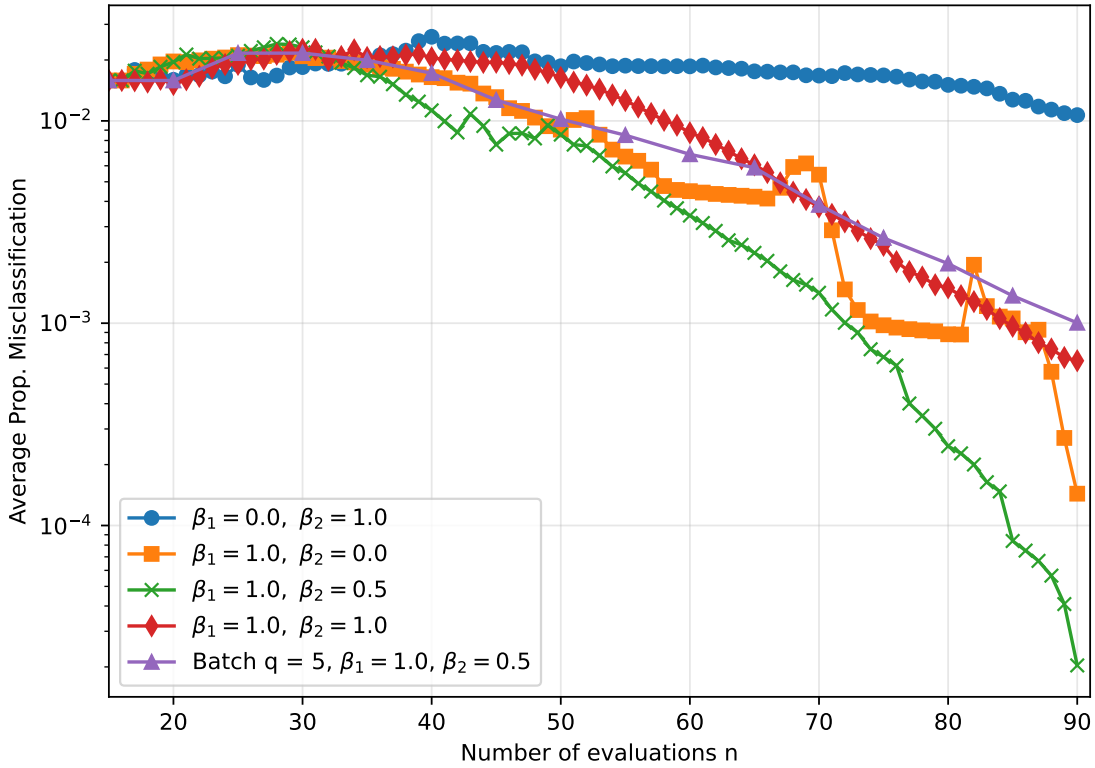

Figure P.6: Same comparison as in Figure P.5 but with a logarithmic scale for the misclassification score.

Bibliography

G. Abaqus. Abaqus 6.11. *Dassault Systemes Simulia Corporation, Providence, RI, USA*, 3, 2011.

M. Afifipour, M. Sharifzadeh, K. Shahriar, and H. Jamshidi. Interaction of twin tunnels and shallow foundation at zand underpass, shiraz metro, iran. *Tunnelling and Underground Space Technology*, 26(2):356–363, 2011.

AFTES. Recommandations relatives au choix des techniques d'excavation mécanisée. Version 1, Association Française des Tunnels et de l'Espace Souterrain, Paris, France, 2000. URL `https://www.aftes.asso.fr/`. Texte présenté par P. Longchamp et assisté par A. Schwenzfeier.

GT19R2F1 AFTES. Recommandations de l'aftes - méthodes d'auscultation des ouvrages souterrains. Technical report, AFTES, 2005.

N. Z. Ahmed, M. El-Shourbagy, A. Akl, and K. Metwally. Field monitoring and numerical analysis of ground deformation induced by tunnelling beneath an existing tunnel. *Cogent Engineering*, 8(1):1861731, 2021.

R. Ait Abdelmalek-Lomenech, J. Bect, V. Chabridon, and E. Vazquez. Bayesian sequential design of computer experiments for quantile set inversion. *Technometrics*, 67(1):112–121, 2025.

P. B. Attewell and J. P. Woodman. Predicting the dynamics of ground settlement and its derivitives caused by tunnelling in soil. *Ground engineering*, 15(8), 1982.

P. B. Attewell, J. Yeates, and A. R. Selby. *Soil movements induced by tunnelling and their effects on pipelines and structures*. Methuen, Inc., New York, NY, 1986.

S.-K. Au and J. L. Beck. Estimation of small failure probabilities in high dimensions by subset simulation. *Probabilistic engineering mechanics*, 16(4):263–277, 2001.

D. Azzimonti, D. Ginsbourger, C. Chevalier, J. Bect, and Y. Richet. Adaptive design of experiments for conservative estimation of excursion sets. *Technometrics*, 63(1):13–26, 2021.

M. Bahri, E. J. Mascort-Albea, R. Romero-Hernández, M. Koopialipoor, C. Soriano-Cuesta, and A. Jaramillo-Morilla. Numerical model validation for detection of surface displacements over twin tunnels from metro line 1 in the historical area of seville (spain). *Symmetry*, 14(6):1263, 2022.

J. Bect, D. Ginsbourger, L. Li, V. Picheny, and E. Vazquez. Sequential design of computer experiments for the estimation of a probability of failure. *Statistics and Computing*, 22 (3):773–793, 2012.

J. Bect, L. Li, and E. Vazquez. Bayesian subset simulation. *SIAM/ASA Journal on Uncertainty Quantification*, 5(1):762–786, 2017.

J. Bect, F. Bachoc, and D. Ginsbourger. A supermartingale approach to Gaussian process based sequential design of experiments. *Bernoulli*, 25(4A):2883–2919, 2019.

J. Bect, S. Zio, G. Perrin, C. Cannamela, and E. Vazquez. On the quantification of discretization uncertainty: comparison of two paradigms. *arXiv preprint arXiv:2103.14559*, 2021.

M. Beghoul and R. Demagh. Slurry shield tunneling in soft ground. comparison between field data and 3D numerical simulation. *Studia Geotechnica et Mechanica*, 41(3), 2019.

N. Berthoz, D. Branque, and D. Subrin. Déplacements induits par les tunneliers : rétro-analyse de chantiers en milieu urbain sur la base de calculs éléments finis en section courante. *Revue Française de Géotechnique*, page 1, 2020. doi: 10.1051/geotech/2020019.

E. Bilotta. Recent trends in monitoring tunnelling-induced displacements of structures. *Geotechnical Engineering Challenges to Meet Current and Emerging Needs of Society*, pages 113–124, 2024.

J.-B. Blanchard, R. Chocat, G. Damblin, M. Baudin, N. Bousquet, V. Chabridon, B. Iooss, M. Keller, J. Pelamatti, and R. Sueur. Fiches pédagogiques sur le traitement des incertitudes dans les codes de calcul. Technical report, EDF, 2023.

A. Bobet. Analytical solutions for shallow tunnels in saturated ground. *Journal of engineering mechanics*, 127(12):1258–1266, 2001.

R. B. J. Brinkgreve. Plaxis versión 8 manual de referencia. *Delft University of Technology & PLAXIS bv*, 2004.

B. B. Broms and H. Bennermark. Stability of clay at vertical opening. *Journal of the Soil Mechanics and Foundations Division*, 93(1):71–94, 1967.

B. Bryan, R. C. Nichol, C. R. Genovese, J. Schneider, C. J. Miller, and L. Wasserman. Active learning for identifying function threshold boundaries. *Advances in neural information processing systems*, 18, 2005.

F. Campolongo, J. Cariboni, and A. Saltelli. An effective screening design for sensitivity analysis of large models. *Environmental modelling & software*, 22(10):1509–1518, 2007.

CEB-FIB. *CEB-FIP model code 1990: Design code*. Thomas Telford Publishing, 1993.

T. B. Celestino, R. A. M. P. Gomes, and A. A. Bortolucci. Errors in ground distortions due to settlement trough adjustment. *Tunnelling and underground space technology*, 15 (1):97–100, 2000.

F. Cérou, P. Del Moral, T. Furon, and A. Guyader. Sequential Monte Carlo for rare event estimation. *Statistics and computing*, 22(3):795–808, 2012.

CFMS. Recommandations sur la modélisation numérique des ouvrages géotechniques. Technical report, CFMS, 2023.

H. Chakeri, Y. Ozcelik, and B. Unver. Effects of important factors on surface settlement prediction for metro tunnel excavated by EPB. *Tunnelling and Underground Space Technology*, 36:14–23, 2013.

R. Chen, P. Zhang, H. Wu, Z. Wang, and Z. Zhong. Prediction of shield tunneling-induced ground settlement using machine learning techniques. *Frontiers of Structural and Civil Engineering*, 13(6):1363–1378, 2019.

S.-L. Chen, S.-C. Lee, and Y.-S. Wei. Numerical analysis of ground surface settlement induced by double-o tube shield tunneling. *Journal of Performance of Constructed Facilities*, 30(5):04016012, 2016.

C. Y. Cheng, G. R. Dasari, Y. K. Chow, and C. F. Leung. Finite element analysis of tunnel–soil–pile interaction using displacement controlled model. *Tunnelling and Underground Space Technology*, 22(4):450–466, 2007.

Y.-H. Choi and S. S. Lee. Reliability and efficiency of metamodel for numerical back analysis of tunnel excavation. *Applied Sciences*, 12(14):6851, 2022.

G. W. Clough and E. Leca. EPB shield tunneling in mixed face conditions. *Journal of geotechnical engineering*, 119(10):1640–1656, 1993.

E. J. Cording. Displacement around soft ground tunnels-general report. In *Proc. 5th Pan-American Conf. on Soil Mechanics and Foundation Engrg., Buenos Aires, 1975*, pages 571–632, 1975.

R. I. Cukier, C. M. Fortuin, K. E. Shuler, A. G. Petschek, and J. H. Schaibly. Study of the sensitivity of coupled reaction systems to uncertainties in rate coefficients. i theory. *The Journal of chemical physics*, 59(8):3873–3878, 1973.

C. Currin, T. Mitchell, M. Morris, and D. Ylvisaker. A Bayesian approach to the Design and Analysis of Computer Experiments. Technical Report ORNL-6498, Oak Ridge National Laboratory, Oak Ridge, TN, sep 1988.

O. Deck and A. Singh. Analytical model for the prediction of building deflections induced by ground movements. *International Journal for Numerical and Analytical Methods in Geomechanics*, 36(1):62–84, 2012.

P. Del Moral, A. Doucet, and A. Jasra. Sequential Monte Carlo samplers. *Journal of the Royal Statistical Society Series B: Statistical Methodology*, 68(3):411–436, 2006.

P. Del Moral, A. Doucet, and A. Jasra. An adaptive sequential Monte Carlo method for approximate Bayesian computation. *Statistics and computing*, 22(5):1009–1020, 2012.

R. Demagh, F. EMERIAULT, and R. KASTNER. Modélisation 3D du creusement de tunnel par tunnelier à front pressurisé dans les sols surconsolidés. *Actes des journées scientifiques du LCPC*, pages 305–312, 2008.

R. Demagh, F. Emeriault, and F. Hammoud. 3D modelling of tunnel excavation using pressurized tunnel boring machine in overconsolidated soils. *Studia geotechnica et mechanica*, 35(2):3–17, 2013.

N.-A. Do, D. Dias, P. Oreste, and I. Djeran-Maigre. 2D numerical investigation of segmental tunnel lining behavior. *Tunnelling and Underground Space Technology*, 37:115–127, 2013.

N.-A. Do, D. Dias, P. Oreste, and I. Djeran-Maigre. Three-dimensional numerical simulation for mechanized tunnelling in soft ground: the influence of the joint pattern. *Acta Geotechnica*, 9:673–694, 2014.

N. A. Do, D. Dias, T. T. Vu, and V. K. Dang. Impact of the shield machine's performance parameters on the tunnel lining behaviour and settlements. *Environmental Earth Sciences*, 80(16):507, 2021.

S. El Jirari. *Modélisation numérique du processus de creusement pressurisé des tunnels*. PhD thesis, Université de Lyon, 2021.

FIB. *fib model code for concrete structures 2010*. John Wiley & Sons, 2013.

P. Filzmoser and K. Nordhausen. Robust linear regression for high-dimensional data: An overview. *Wiley Interdisciplinary Reviews: Computational Statistics*, 13(4):e1524, 2021.

V. Founta, J. Ninic, A. J. Whittle, G. Meschke, and J. Stascheit. Numerical simulation of ground movements due to EPB tunnelling in clay. In *Proceeding of the 3rd International Conference on Computational Methods in Tunnelling (Euro: Tun 2013)*, pages 97–108, 2013.

J. Fox and S. Weisberg. Robust regression. *An R and S-Plus companion to applied regression*, 91(6), 2002.

D. Francom, J. D. Tucker, G. Huerta, K. Shuler, and D. Ries. Elastic Bayesian model calibration. *SIAM/ASA Journal on Uncertainty Quantification*, 13(1):195–227, 2025.

N. Gilleron, E. Bourgeois, P. Chatellier, and A. Saïtta. An anisotropic model for the numerical analysis of tunneling-induced settlements in the paris area. *Geotechnical and Geological Engineering*, 39:3133–3146, 2021.

C. González and C. Sagaseta. Patterns of soil deformations around tunnels. application to the extension of madrid metro. *Computers and Geotechnics*, 28(6-7):445–468, 2001.

GPy. GPy: A Gaussian process framework in Python. `http://github.com/SheffieldML/GPy`, since 2012.

R. B. Gramacy. *Surrogates: Gaussian process modeling, design, and optimization for the applied sciences*. Chapman and Hall/CRC, 2020.

L. L. Gratiet, S. Marelli, and B. Sudret. Metamodel-based sensitivity analysis: polynomial chaos expansions and Gaussian processes. *arXiv preprint arXiv:1606.04273*, 2016.

A. Gretton, O. Bousquet, A. Smola, and B. Schölkopf. Measuring statistical dependence with Hilbert-Schmidt norms. In *International conference on algorithmic learning theory*, pages 63–77. Springer, 2005.

M. Hajjar, A. Nemati Hayati, M. M. Ahmadi, and S. A. Sadrnejad. Longitudinal settlement profile in shallow tunnels in drained conditions. *International Journal of Geomechanics*, 15(6):04014097, 2015.

J. Herman and W. Usher. SALib: An open-source Python library for sensitivity analysis. *The Journal of Open Source Software*, 2(9), jan 2017. doi: 10.21105/joss.00097. URL `https://doi.org/10.21105/joss.00097`.

P. J. Huber. Robust regression: asymptotics, conjectures and Monte Carlo. *The annals of statistics*, pages 799–821, 1973.

E. Ibrahim, A.-H. Soubra, G. Mollon, W. Raphael, D. Dias, and A. Reda. Three-dimensional face stability analysis of pressurized tunnels driven in a multilayered purely frictional medium. *Tunnelling and Underground Space Technology*, 49:18–34, 2015.

B. Iooss and P. Lemaître. A review on global sensitivity analysis methods. *Uncertainty management in simulation-optimization of complex systems: algorithms and applications*, pages 101–122, 2015.

T. Iwanaga, W. Usher, and J. Herman. Toward SALib 2.0: Advancing the accessibility and interpretability of global sensitivity analyses. *Socio-Environmental Systems Modelling*, 4:18155, May 2022. doi: 10.18174/sesmo.18155. URL `https://sesmo.org/article/view/18155`.

S. W. Jacobsz, J. R. Standing, R. J. Mair, T. Hagiwara, and T. Sugiyama. Centrifuge modelling of tunnelling near driven piles. *Soils and foundations*, 44(1):49–56, 2004.

J. JAKY. The coefficient of earth pressure at rest. *Journal of the Society of Hungarian Architects and engineers*, 1944.

J. P. Janin, D. F. R. H. Dias, F. Emeriault, R. Kastner, H. Le Bissonnais, and A. Guilloux. Numerical back-analysis of the southern toulon tunnel measurements: A comparison of 3D and 2D approaches. *Engineering Geology*, 195:42–52, 2015.

A. Janon, T. Klein, A. Lagnoux, M. Nodet, and C. Prieur. Asymptotic normality and efficiency of two Sobol index estimators. *ESAIM: Probability and Statistics*, 18:342–364, 2014.

L. Jaulin and E. Walter. Set inversion via interval analysis for nonlinear bounded-error estimation. *Automatica*, 29(4):1053–1064, 1993.

O. Jenck and D. Dias. Analyse tridimensionnelle en différences finies de l'interaction entre une structure en béton et le creusement d'un tunnel à faible profondeur: 3D-finite difference analysis of the interaction between concrete building and shallow tunnelling. *Geotechnique*, 54(8):519–528, 2004.

D. R. Jones, M. Schonlau, and W. J. Welch. Efficient Global Optimization of Expensive Black-Box Functions. *Journal of Global Optimization*, 13(4):455–492, 1998. doi: 10.1023/A:1008306431147.

J. P. Kaipio and E. Somersalo. *Statistical and computational inverse problems*. Springer, 2005.

T. Kasper and G. Meschke. A 3D finite element simulation model for TBM tunnelling in soft ground. *International journal for numerical and analytical methods in geomechanics*, 28(14):1441–1460, 2004.

T. Kasper and G. Meschke. On the influence of face pressure, grouting pressure and TBM design in soft ground tunnelling. *Tunnelling and underground space technology*, 21(2): 160–171, 2006a.

T. Kasper and G. Meschke. A numerical study of the effect of soil and grout material properties and cover depth in shield tunnelling. *Computers and Geotechnics*, 33(4-5): 234–247, 2006b.

M. Kavvadas, D. Litsas, I. Vazaios, and P. Fortsakis. Development of a 3D finite element model for shield EPB tunnelling. *Tunnelling and Underground Space Technology*, 65: 22–34, 2017.

M. C. Kennedy and A. O'Hagan. Bayesian calibration of computer models. *Journal of the Royal Statistical Society: Series B (Statistical Methodology)*, 63(3):425–464, 2001.

K. Khaledi, S. Miro, M. König, and T. Schanz. Robust and reliable metamodels for mechanized tunnel simulations. *Computers and Geotechnics*, 61:1–12, 2014.

C. Y. Kim, G. J. Bae, S. W. Hong, C. H. Park, H. K. Moon, and H. S. Shin. Neural network based prediction of ground surface settlements due to tunnelling. *Computers and Geotechnics*, 28(6-7):517–547, 2001.

D. Kim. Large deformation finite element analyses in TBM tunnel excavation: Cel and auto-remeshing approach. *Tunnelling and Underground Space Technology*, 116:104081, 2021.

K. Kovári. La sicurezza del sistema nel campo della costruzione di gallerie in aree urbane-l'esempio della galleria del zimmerberg. *Gallerie e grandi opere sotterranee*, 68:31–40, 2002.

Y. Koyama. Present status and technology of shield tunneling method in japan. *Tunnelling and Underground Space Technology*, 18(2-3):145–159, 2003.

B. Kratz, P. Jehel, and M. Tatin. 3D numerical simulation of TBM excavation for predicting surface settlements-state of the art. *Expanding Underground-Knowledge and Passion to Make a Positive Impact on the World*, pages 2757–2765, 2023a.

B. Kratz, P. Jehel, M. Tatin, and E. Vazquez. Kriging metamodels for 2D finite element simulations of the settlements induced by TBM excavation in urban areas. In *Congrès Français du Génie Civil 2023*, 2023b.

B. Kratz, P. Jehel, M. Tatin, and E. Vazquez. Parameter influence analysis in a 3D TBM model via sensitivity analysis and gp metamodels. *Computers and Geotechnics*, 189: 107650, 2026.

A. Lambrughi, L. M. Rodríguez, and R. Castellanza. Development and validation of a 3D numerical model for TBM–EPB mechanised excavations. *Computers and Geotechnics*, 40:97–113, 2012.

L. Le Gratiet. *Multi-fidelity Gaussian process regression for computer experiments*. PhD thesis, Université Paris-Diderot-Paris VII, 2013.

E. Leca and L. Dormieux. Upper and lower bound solutions for the face stability of shallow circular tunnels in frictional material. *Géotechnique*, 40(4):581–606, 1990.

K. M. Lee, R. K. Rowe, and K. Y. Lo. Subsidence owing to tunnelling. i. estimating the gap parameter. *Canadian geotechnical journal*, 29(6):929–940, 1992.

S.-Y. Lee, D.-H. Kim, and S.-S. Jeong. A study on the excavation damage zone (EDZ) under TBM advancement based on large deformation technique (coupled Eulerian-Lagrangian). *Journal of the Korean Geotechnical Society*, 32(12):5–13, 2016.

D. Litsas, P. Fortsakis, and M. Kavvadas. 3D simulation of mechanized tunnel excavation. In *3rd Arabian Tunnelling Conference & Exhibition*, 2015.

D. Litsas, P. Sitarenios, and M. Kavvadas. Parametric investigation of tunnelling-induced ground movement due to geometrical and operational TBM complexities. *Italian Geotechnical Journal-Rivista Italiana Di Geotecnica*, 51(4):22–34, 2017.

W. Liu, X. Wu, L. Zhang, J. Zheng, and J. Teng. Global sensitivity analysis of tunnel-induced building movements by a precise metamodel. *Journal of Computing in Civil Engineering*, 31(5):04017037, 2017.

W. Liu, X. Wu, L. Zhang, Y. Wang, and J. Teng. Sensitivity analysis of structural health risk in operational tunnels. *Automation in Construction*, 94:135–153, 2018.

N. Loganathan. *An innovative method for assessing tunnelling-induced risks to adjacent structures*. Parsons Brinckerhoff Incorporated New York, NY, USA, 2011.

N. Loganathan and H. G. Poulos. Analytical prediction for tunneling-induced ground movements in clays. *Journal of Geotechnical and geoenvironmental engineering*, 124(9): 846–856, 1998.

N. Losacco and G. M. B. Viggiani. Class a prediction of mechanised tunnelling in rome. *Tunnelling and Underground Space Technology*, 87:160–173, 2019.

S. M. Lundberg and S.-I. Lee. A unified approach to interpreting model predictions. *Advances in neural information processing systems*, 30, 2017.

N. M Saleh, A. M Adam, and W. A Dawood. Numerical assessment of laterally loaded pile-tunnel interaction. *Engineering Research Journal (Shoubra)*, 51(2):200–211, 2022.

E. Mahmoudi, R. Hölter, R. Georgieva, M. König, and T. Schanz. On the global sensitivity analysis methods in geotechnical engineering: a comparative study on a rock salt energy storage. *International Journal of Civil Engineering*, 17(1):131–143, 2019.

R. J. Mair. Tunnelling and geotechnics: new horizons. *Géotechnique*, 58(9):695–736, 2008.

R. J. Mair and R. N. Taylor. Prediction of clay behaviour around tunnels using plasticity solutions. In *Predictive soil mechanics: Proceedings of the Wroth Memorial Symposium held at St Catherine's College, Oxford, 27-29 July 1992*, pages 449–463. Thomas Telford Publishing, 1992.

R. J. Mair, R. N. Taylor, and A. Bracegirdle. Subsurface settlement profiles above tunnels in clays. *Geotechnique*, 43(2):315–320, 1993.

J. Man, T. Zhang, H. Huang, and D. Dias. Probabilistic analysis of tunnel face seismic stability in layered rock masses using polynomial chaos Kriging metamodel. *Journal of Rock Mechanics and Geotechnical Engineering*, 16(7):2678–2693, 2024.

A. Marrel, B. Iooss, B. Laurent, and O. Roustant. Calculations of Sobol indices for the Gaussian process metamodel. *Reliability Engineering & System Safety*, 94(3):742–751, 2009.

D. Mašín. A hypoplastic constitutive model for clays. *International Journal for numerical and analytical methods in Geomechanics*, 29(4):311–336, 2005.

P. W. Mayne and F. H. Kulhawy. Ko-ocr relationships in soil. *Journal of the Geotechnical Engineering Division*, 108(6):851–872, 1982.

M. Melis, L. Medina, and J. M. Rodríguez. Prediction and analysis of subsidence induced by shield tunnelling in the madrid metro extension. *Canadian Geotechnical Journal*, 39 (6):1273–1287, 2002.

G. Meschke, F. Nagel, and J. Stascheit. Computational simulation of mechanized tunneling as part of an integrated decision support platform. *International Journal of Geomechanics*, 11(6):519–528, 2011.

M. Migliazza, M. Chiorboli, and G. P. Giani. Comparison of analytical method, 3D finite element model with experimental subsidence measurements resulting from the extension of the milan underground. *Computers and Geotechnics*, 36(1-2):113–124, 2009.

S. Miliziano and A. de Lillis. Predicted and observed settlements induced by the mechanized tunnel excavation of metro line c near s. giovanni station in rome. *Tunnelling and Underground Space Technology*, 86:236–246, 2019.

A. Mirhabibi and A. Soroush. Effects of building three-dimensional modeling type on twin tunneling-induced ground settlement. *Tunnelling and underground space technology*, 38: 224–234, 2013.

S. Miro, D. Hartmann, and T. Schanz. Global sensitivity analysis for subsoil parameter estimation in mechanized tunneling. *Computers and Geotechnics*, 56:80–88, 2014.

S. C. Möller. *Tunnel induced settlements and structural forces in linings*. Univ. Stuttgart, Inst. f. Geotechnik Stuttgart, Germany, 2006.

G. Mollon, D. Dias, and A.-H. Soubra. Probabilistic analysis and design of circular tunnels against face stability. *International Journal of Geomechanics*, 9(6):237–249, 2009.

G. Mollon, D. Dias, and A.-H. Soubra. Face stability analysis of circular tunnels driven by a pressurized shield. *Journal of geotechnical and geoenvironmental engineering*, 136 (1):215–229, 2010.

G. Mollon, D. Dias, and A.-H. Soubra. Rotational failure mechanisms for the face stability analysis of tunnels driven by a pressurized shield. *International Journal for Numerical and Analytical Methods in Geomechanics*, 35(12):1363–1388, 2011.

G. Mollon, D. Dias, and A.-H. Soubra. Probabilistic analyses of tunneling-induced ground movements. *Acta Geotechnica*, 8:181–199, 2013.

M. D. Morris. Factorial sampling plans for preliminary computational experiments. *Technometrics*, 33(2):161–174, 1991.

M. Moustapha, S. Marelli, and B. Sudret. Active learning for structural reliability: Survey, general framework and benchmark. *Structural Safety*, 96:102174, 2022.

H. Mroueh and I. Shahrour. A full 3-d finite element analysis of tunneling–adjacent structures interaction. *Computers and Geotechnics*, 30(3):245–253, 2003.

H. Mroueh and I. Shahrour. A simplified 3D model for tunnel construction using tunnel boring machines. *Tunnelling and Underground Space Technology*, 23(1):38–45, 2008.

F. Nagel and G. Meschke. An elasto-plastic three phase model for partially saturated soil for the finite element simulation of compressed air support in tunnelling. *International journal for numerical and analytical methods in geomechanics*, 34(6):605–625, 2010.

M. Nematollahi and D. Dias. Three-dimensional numerical simulation of pile-twin tunnels interaction–case of the shiraz subway line. *Tunnelling and Underground Space Technology*, 86:75–88, 2019.

M. Nematollahi, H. Molladavoodi, and D. Dias. Three-dimensional numerical simulation of the shiraz subway second line–influence of the segmental joints geometry and of the lagging distance between twin tunnels' faces. *European Journal of Environmental and Civil Engineering*, 24(10):1606–1622, 2020.

A. Niemunis and I. Herle. Hypoplastic model for cohesionless soils with elastic strain range. *Mechanics of Cohesive-frictional Materials: An International Journal on Experiments, Modelling and Computation of Materials and Structures*, 2(4):279–299, 1997.

J. Ninić and G. Meschke. Model update and real-time steering of tunnel boring machines using simulation-based meta models. *Tunnelling and Underground Space Technology*, 45:138–152, 2015.

J. Ninić and G. Meschke. Simulation based evaluation of time-variant loadings acting on tunnel linings during mechanized tunnel construction. *Engineering Structures*, 135: 21–40, 2017.

G. Niu, X. He, H. Xu, and S. Dai. Tunnelling-induced ground surface settlement: A comprehensive review with particular attention to artificial intelligence technologies. *Natural Hazards Research*, 2023.

C. Noubissi, R. Taherzadeh, G. Puel, and F. Lopez-Caballero. An optimized methodology of back-analysis and sensitivity analysis for the settlement evaluation: Case study on a TBM on the metro line 12 extension in the paris region. *Computers and Geotechnics*, 167:106043, 2024.

J. E. Oakley and A. O'Hagan. Probabilistic sensitivity analysis of complex models: a Bayesian approach. *Journal of the Royal Statistical Society Series B: Statistical Methodology*, 66(3):751–769, 2004.

C. J. Oates, T. Karvonen, A. L. Teckentrup, M. Strocchi, and S. A. Niederer. Probabilistic richardson extrapolation. *Journal of the Royal Statistical Society Series B: Statistical Methodology*, 87(2):457–479, 2025.

M. Obel, M. A. Ahrens, and P. Mark. Metamodel-based prediction of structural damages due to tunneling-induced settlements. *ASCE-ASME Journal of Risk and Uncertainty in Engineering Systems, Part A: Civil Engineering*, 6(4):04020044, 2020.

R. F. Obrzud. On the use of the hardening soil small strain model in geotechnical practice. *Numerics in geotechnics and structures*, 16:1–17, 2010.

M. Ochmański, G. Modoni, and J. Bzówka. Automated numerical modelling for the control of EPB technology. *Tunnelling and Underground Space Technology*, 75:117–128, 2018.

M. Ochmański, R. L. Spacagna, and G. Modoni. 3D numerical simulation of consolidation induced in soft ground by EPB technology and lining defects. *Computers and Geotechnics*, 128:103830, 2020.

M. P. O'reilly and B. M. New. Settlements above tunnels in the united kingdom-their magnitude and prediction, 1982.

M. Panet and J. Sulem. *Le calcul des tunnels par la méthode convergence-confinement.* Presse des Ponts, 2021.

J. S. Park. *Tuning Complex Computer Codes to Data and Optimal Designs.* Ph.d. dissertation, University of Illinois at Urbana-Champaign, Champaign-Urbana, IL, 1991. Department of Statistics.

K. H. Park. Elastic solution for tunneling-induced ground movements in clays. *International Journal of Geomechanics*, 4(4):310–318, 2004.

B. B. Peck. Deep excavation and tunnelling in soft ground, state of the art volume. In *7th ICSMFE*, volume 4, pages 225–290, 1969.

S. J. Petit, J. Bect, P. Feliot, and E. Vazquez. Parameter selection in Gaussian process interpolation: an empirical study of selection criteria. *SIAM/ASA Journal on Uncertainty Quantification*, 11(4):1308–1328, 2023.

K. K. Phoon and S. P. Huang. Geotechnical probabilistic analysis using collocation-based stochastic response surface method, 2007.

K.-K. Phoon and F. H. Kulhawy. Characterization of geotechnical variability. *Canadian geotechnical journal*, 36(4):612–624, 1999.

V. Picheny and D. Ginsbourger. A nonstationary space-time Gaussian process model for partially converged simulations. *SIAM/ASA Journal on Uncertainty Quantification*, 1 (1):57–78, 2013.

V. Picheny, D. Ginsbourger, O. Roustant, R. T. Haftka, and N.-H. Kim. Adaptive designs of experiments for accurate approximation of a target region. *Journal of Mechanical Design*, 132(7), 2010.

F. Pinto and A. J. Whittle. Ground movements due to shallow tunnels in soft ground. i: Analytical solutions. *Journal of geotechnical and geoenvironmental engineering*, 140(4): 04013040, 2014.

D. M. Potts, L. Zdravković, T. I. Addenbrooke, K. G. Higgins, and N. Kovačević. *Finite element analysis in geotechnical engineering: application*, volume 2. Thomas Telford London, 2001.

L. Pronzato and W. G. Müller. Design of computer experiments: space filling and beyond. *Statistics and Computing*, 22:681–701, 2012.

W. J. Rankin. Ground movements resulting from urban tunnelling: predictions and effects. *Geological Society, London, Engineering Geology Special Publications*, 5(1):79–92, 1988.

T. Richa, T. Lamare, J.-M. Pereira, L.-M. Guayacán-Carrillo, G. Chapron, and F. Lanquette. Prévision en temps réel des tassements induits par le creusement au tunnelier, 2024.

B. Ring and M. Comulada. Practical numerical simulation of the effect of TBM process pressures on soil displacements through 3D shift iteration. *Underground Space*, 3(4): 297–309, 2018.

P. J. Roache. Perspective: a method for uniform reporting of grid refinement studies. *Journal of Fluids Engineering*, 116(3):405–413, 1994.

L. E. M. Rodriguez. *Estudio de los movimientos originados por la excavación de túneles con escudos de presión de tierras en lossue los tosquizos de Madrid.* PhD thesis, Ph. D. thesis. University of La Coruña, Spain, 2000.

J. Rohmer. Dynamic sensitivity analysis of long-running landslide models through basis set expansion and meta-modelling. *Natural Hazards*, 73(1):5–22, 2014.

R. K. Rowe and G. J. Kack. A theoretical examination of the settlements induced by tunnelling: four case histories. *Canadian Geotechnical Journal*, 20(2):299–314, 1983.

C. J. Roy and W. L. Oberkampf. A comprehensive framework for verification, validation, and uncertainty quantification in scientific computing. *Computer methods in applied mechanics and engineering*, 200(25-28):2131–2144, 2011.

J. Sacks, S. B. Schiller, and W. J. Welch. Designs for computer experiments. *Technometrics*, 31(1):41–47, 1989a.

J. Sacks, W. J. Welch, T. J. Mitchell, and H. P. Wynn. Design and analysis of computer experiments. *Statistical science*, 4(4):409–423, 1989b.

C. Sagaseta. Analysis of undrained soil deformation due to ground loss. *Geotechnique*, 37 (3):301–320, 1987.

C. Sagaseta. On the role of analytical solutions for the evaluation of soil deformation around tunnels. In *Application of Numerical Methods to Geotechnical Problems: Proceedings of the Fourth European Conference on Numerical Methods in Geotechnical Engineering Numge98 udine, Italy October 14–16, 1998*, pages 3–24. Springer, 1998.

A. Saltelli. Making best use of model evaluations to compute sensitivity indices. *Computer physics communications*, 145(2):280–297, 2002.

A. Saltelli, S. Tarantola, and K. P.-S. Chan. A quantitative model-independent method for global sensitivity analysis of model output. *Technometrics*, 41(1):39–56, 1999.

A. Saltelli, P. Annoni, I. Azzini, F. Campolongo, M. Ratto, and S. Tarantola. Variance based sensitivity analysis of model output. design and estimator for the total sensitivity index. *Computer physics communications*, 181(2):259–270, 2010.

T. J. Santner, B. J. Williams, W. I. Notz, and B. J. Williams. *The design and analysis of computer experiments*, volume 1. Springer, 2003.

T. Schanz, P. A. Vermeer, and P. G. Bonnier. The hardening soil model: Formulation and verification. In *Beyond 2000 in computational geotechnics*, pages 281–296. Routledge, 2019.

J.-F. Serratrice and J.-P. Magnan. Analyse et prévision des tassements de surface pendant le creusement du tunnel nord de la traversée souterraine de toulon. *Bulletin des laboratoires des Ponts et Chaussées*, 237(5):36, 2002.

W. Shang, Y. Li, H. Wei, Y. Qiu, C. Chen, and X. Gao. Prediction method of longitudinal surface settlement caused by double shield tunnelling based on deep learning. *Scientific Reports*, 14(1):908, 2024.

I. M. Soboĺ. Sensitivity estimates for nonlinear mathematical models. *Math. Model. Comput. Exp.*, 1:407, 1993.

M. L. Stein. *Interpolation of spatial data: some theory for Kriging*. Springer Science & Business Media, 1999.

R. Stroh, J. Bect, S. Demeyer, N. Fischer, D. Marquis, and E. Vazquez. Sequential design of multi-fidelity computer experiments: Maximizing the rate of stepwise uncertainty reduction. *Technometrics*, 64(2):199–209, 2022. doi: 10.1080/00401706.2021.1935324.

A. M. Stuart. Inverse problems: a Bayesian perspective. *Acta numerica*, 19:451–559, 2010.

K. Terzaghi. *Theoretical soil mechanics*. Wiley, 1943.

G. Tjie-Liong. Common mistakes on the application of Plaxis 2D in analyzing excavation problems. *International Journal of Applied Engineering Research*, 9(21):8291–8311, 2014.

J. Tyrer, C. Paraskevopoulou, R. Shah, R. Miller, and M. Kavvadas. Tunnelling with full-face shielded machines: A 3D numerical analysis of an earth pressure balance (EPB) excavation sequence using the finite element method (fem). *Geosciences*, 13(8):244, 2023.

E. Vanoudheusden. *Impact de la construction de tunnels urbains sur les mouvements de sol et le bâti existant. Incidence du mode de pressurisation du front*. PhD thesis, Insa Lyon, 2006.

E. Vazquez. GPmp: the Gaussian process micro package. https://github.com/gpmp-dev/gpmp, 2025. Version x.y.

E. Vazquez and J. Bect. A sequential Bayesian algorithm to estimate a probability of failure. *IFAC Proceedings Volumes*, 42(10):546–550, 2009.

A. Verruijt and J. R. Booker. Surface settlements due to deformation of a tunnel in an elastic half plane. *Géotechnique*, 46(4):753–756, 1996.

E. M. Vestrup. *The theory of measures and integration*. John Wiley & Sons, 2009.

G. Viggiani, F. M. Soccodato, et al. Predicting tunnelling-induced displacements and associated damage to structures. *Rivista italiana di geotechnical*, 4:11–25, 2004.

P. Virtanen, R. Gommers, T. E. Oliphant, M. Haberland, T. Reddy, D. Cournapeau, E. Burovski, P. Peterson, W. Weckesser, J. Bright, S. J. van der Walt, M. Brett, J. Wilson, K. J. Millman, N. Mayorov, A. R. J. Nelson, E. Jones, R. Kern, E. Larson, C. J. Carey, I. Polat, Y. Feng, E. W. Moore, J. VanderPlas, D. Laxalde, J. Perktold, R. Cimrman, I. Henriksen, E. A. Quintero, C. R. Harris, A. M. Archibald, A. H. Ribeiro, F. Pedregosa, P. van Mulbregt, and SciPy 1.0 Contributors. SciPy 1.0: Fundamental Algorithms for Scientific Computing in Python. *Nature Methods*, 17:261–272, 2020. doi: 10.1038/s41592-019-0686-2.

P.-A. Von Wolffersdorff. A hypoplastic relation for granular materials with a predefined limit state surface. *Mechanics of Cohesive-frictional Materials: An International Journal on Experiments, Modelling and Computation of Materials and Structures*, 1(3): 251–271, 1996.

T. E. Vorster, A. Klar, K. Soga, and R. J. Mair. Estimating the effects of tunneling on existing pipelines. *Journal of Geotechnical and Geoenvironmental engineering*, 131(11): 1399–1410, 2005.

M. N. Vu, W. Broere, and J. Bosch. Effects of cover depth on ground movements induced by shallow tunnelling. *Tunnelling and Underground Space Technology*, 50:499–506, 2015.

F. Wang. Empirical evidence for estimation of subsurface settlement caused by tunneling in sand. *Underground Space*, 6(5):577–584, 2021.

J. Wang, P. Zhou, Z. Song, S. Li, and Q. Zhang. A new calculation method for tunneling-caused stratum settlement. *KSCE Journal of Civil Engineering*, 26(6):2624–2640, 2022.

C. K. I. Williams and C. E. Rasmussen. *Gaussian processes for machine learning*, volume 2. MIT press Cambridge, MA, 2006.

M. Zerdia, M. Amrane, and R. Demagh. Impact of excavation phase shift on mechanized twin tunnels in soft ground: A 3D numerical study. *Indian Geotechnical Journal*, 54 (6):2096–2109, 2024.

Z. X. Zhang, C. Liu, X. Huang, C. Y. Kwok, and L. Teng. Three-dimensional finite-element analysis on ground responses during twin-tunnel construction using the urup method. *Tunnelling and Underground Space Technology*, 58:133–146, 2016.

C. Zhao, A. A. Lavasan, T. Barciaga, V. Zarev, M. Datcheva, and T. Schanz. Model validation and calibration via back analysis for mechanized tunnel simulations–the western scheldt tunnel case. *Computers and Geotechnics*, 69:601–614, 2015.

J. Zhou, X. Shi, K. Du, X. Qiu, X. Li, and H. S. Mitri. Feasibility of random-forest approach for prediction of ground settlements induced by the construction of a shield-driven tunnel. *International Journal of Geomechanics*, 17(6):04016129, 2017.

J. Zhou, H. Qi, K. Peng, Y. Zhang, and M. Khandelwal. Comprehensive review and future perspectives on prediction and mitigation of tunnel-induced ground settlement: A bibliometric analysis and methodological overview (2002–2022). *Tunnelling and Underground Space Technology*, 154:106081, 2024.